

**Rolling contact wear of hybrid ceramic bearings with
refrigerant lubrication**

ZULFIQAR AHMAD KHAN

**A thesis is submitted in partial fulfilment of the requirements of Bournemouth
University for the degree of Doctor of Philosophy**

March 2006

Bournemouth University

This copy of the thesis has been supplied on condition that anyone who consults it is understood to recognise that its copyright rests with its author and that no quotation from the thesis and no information derived from it may be published without the author's consent.

Abstract

Silicon nitride Si_3N_4 bearing elements have shown practical advantages over traditional steel elements due to their mechanical and physical properties. Leading technology and demands for high efficiency have caused loading bearing contacts in all kinds of machinery to be subjected to high speeds, high contact stresses and severe conditions of lubrication. In addition the introduction of a new generation of hydrocarbon refrigerants in various systems, where these rolling contact silicon nitride bearing elements are employed raises further demands to evaluate the rolling contact fatigue performance of these elements with refrigerant lubrication.

Obtaining material wear properties of these refrigerants used in mechanical applications is difficult due to high saturation pressure of the refrigerants. It is important to investigate the influence of these refrigerants as lubricants on the rolling contact fatigue performance of ceramic bearing elements. This research responds to the need for bench testing of rolling contacts using the new generation refrigerants as lubricants. A novel pressurised chamber was designed to achieve a liquid state of the refrigerant as fluid for the rolling contact fatigue experiments. A high-speed rotary Tribometer was used for rolling contact fatigue tests. Experimental study of the influence of the liquid refrigerant lubrication on rolling contact wear of the silicon nitride/steel elements is presented. Investigations of the lubricated contact of silicon nitride rolling elements using the pressurised chamber reveal that wear rate is affected by the nature and geometry of the induced defect.

A residual stress survey was also performed on failed ceramic elements. Analysing the relationship of residual stress with rolling contact fatigue is an important study which will provide guidelines on the design process and manufacturing of these elements. The residual stress field analysis shows that residual stresses are relieved due to sub-surface damage and are inversely related to stress cycles. Maximum tensile stresses at the edges of the contact path cause a weaker residual stress field at the sub-surface crack front.

Publications resulting from thesis

1. Khan, Z., Hadfield, M., Tobe, S., Wang, Y., *Manufacturing induced residual stress influence on the rolling contact fatigue life performance of lubricated silicon nitride bearing materials*. Materials and Design, 2005. (submitted)
2. Khan, Z., Hadfield, M., (2006). *Failure mechanisms of rolling contact silicon nitride bearing materials with refrigerant lubrication*. Gordon Research Conference on Tribology, Colby College Waterville, Maine, USA (Accepted)
3. Khan, Z., Hadfield, M., Shogo, T., Inaba, F., Wang, Y., (2006). *An experimental study of refrigerant lubricated ceramic rolling elements wear with ring crack defects*. STLE/ASME International Joint Tribology Conference, Hyatt Regency San Antonio, San Antonio Texas, USA (submitted)
4. Khan, Z., M. Hadfield, Y. Wang., (2005). *Rolling wear of silicon nitride bearing materials with refrigerant lubrication*. Mission of Tribology Research 14, Institution of Mechanical Engineers, London, UK, 14: 1-8
5. Khan, Z., Hadfield, M., Tobe, S., Wang, Y., *Residual stress variations during rolling contact fatigue of refrigerant lubricated silicon nitride bearing elements*. Ceramics International, 2004: (in press)
6. Khan, Z., Hadfield, M., Tobe, S., Wang, Y., *Ceramic rolling elements with ring crack defects - a residual stress approach*. Materials Science and Engineering A, 2005. 404: 221-226
7. Khan, Z., Hadfield, M., Wang, Y., *Pressurised Chamber Design for Conducting Rolling Contact Experiments with Liquid Refrigerant Lubrication*. Materials and Design, 2005. 26 (8): 680-689
8. Khan, Z., M. Hadfield (2004). *Design and Finite Element Analysis of a Novel Pressurised Chamber to Conduct Rolling Contact Experiments using Refrigerant Lubrication*. Presentation at Britain's Top Younger Scientists, Engineers and Technologist at the House of Commons, London, UK, L2-8
9. Khan, Z., M. Hadfield, Y. Wang., (2004). *Design of a Novel Pressurized Chamber to Assess in-use Durability Performance of Rolling Contact Elements Using Refrigerant Lubrication*. 4th Intl. Conf. Advanced Engineering Design, Glasgow Scotland, UK, ISBN 80-86059-41-3 (C3.01)
10. Khan, Z., M. Hadfield, Y. Wang., (2003). *Rolling Wear of Silicon Nitride Bearing Material in a Simulated Refrigerant Environment using a Novel Pressurised Chamber*. Tribology in Environmental Design, Bournemouth, UK, 2: 337-346

List of contents

Abstract.....	iii
List of publications	iv
List of figures.....	ix
List of tables.....	xvii
Acknowledgement	xx
Nomenclature.....	xxi
CHAPTER 1	1
1. INTRODUCTION	1
1.1. Background.....	3
1.2. Programme and Methodology.....	7
1.2.1. Aims and Objectives.....	7
1.2.2. Methodology.....	7
1.2.3. Novelty.....	8
1.3. Literature Review.....	8
1.4. Wear of Ceramics	14
1.4.1. Experimental Research	15
1.4.2. Theoretical Research.....	16
1.4.3. Refrigerants as Lubricants	20
1.4.4. Causes of Differences between CFC and HFC.....	21
1.5. State-of-the-Art	23
CHAPTER 2	24
2. TEST RIG DESIGN	24
2.1. Design of Environmental Chamber	24
2.1.1. Design Parameters	27
2.1.2. Pressurised Chamber – Design Concepts	28
2.1.3. Pressurised Chamber Testing.....	32
2.1.4. Seals.....	42
2.1.5. Test rig modifications	48
2.2. Hydrocarbon Refrigerants.....	50

2.2.1.	Refrigerant selection.....	51
2.2.2.	General Safety Issues.....	52
2.2.3.	Use of Components.....	57
2.2.4.	Installation.....	58
CHAPTER 3	62
3.	EXPERIMENTAL METHODOLOGY.....	62
3.1.	Test Materials.....	62
3.1.1.	Silicon Nitride Si ₃ N ₄ Sphere.....	62
3.1.2.	Steel Sphere.....	63
3.1.3.	Lubricants.....	64
3.2.	Sample Preparation.....	64
3.2.1.	Surface Ring Cracks.....	64
3.2.2.	Indents and Radial Cracks.....	65
3.2.3.	Surface inspection.....	65
3.3.	Test procedures.....	66
3.3.1.	Crack positioning.....	66
3.3.2.	Test rig.....	69
3.3.3.	Mounting specimen.....	69
3.3.4.	Preparing pressurised testing.....	69
3.3.5.	Discharging system.....	70
3.3.6.	Surface inspection.....	71
3.4.	Post-test Analysis.....	71
3.4.1.	Light Microscopy.....	71
3.4.2.	Digital Microscopy.....	72
3.4.3.	Scanning Electron Microscopy (SEM).....	73
3.4.4.	Atomic Force Microscopy (AFM).....	74
3.4.5.	Surface Mapping ZYGO.....	75
3.4.6.	Profilometer.....	77
3.4.7.	X-ray Diffractometer.....	77
3.4.8.	Replication.....	78

CHAPTER 4	79
4. RESIDUAL STRESS MEASUREMENTS	79
4.1. Introduction.....	79
4.2. Methodology	80
4.2.1. Background	80
4.2.2. Measuring Procedure	84
4.3. Residual Stresses.....	87
CHAPTER 5	89
5. ROLLING CONTACT FATIGUE EXPERIMENTAL RESULTS	89
5.1. Smooth specimens	89
5.2. Indents and radial cracks.....	90
5.3. Ring crack location	102
5.4. Ring crack geometry	107
5.5. State of the refrigerant	110
5.6. Crack propagation.....	113
5.7. Fatigue spall	116
5.8. Delamination.....	119
5.9. Surface wear.....	120
CHAPTER 6	125
6. RESIDUAL STRESS MEASUREMENT RESULTS.....	125
6.1. Residual Stress Results	125
6.2. Stress Cycles	129
6.3. Distance from Crack	130
6.4. Contact Path.....	134
6.5. Measuring Direction	135
6.6. RCF Spall.....	137
6.7. Secondary Cracks.....	144
6.8. Tensile residual stresses.....	147
CHAPTER 7	149
7. DISCUSSIONS AND CONCLUSION	149

7.1. RCF test discussions	149
7.2. Residual stress discussions	151
7.3. Conclusions.....	152
7.4. Future work.....	154
8. APPENDICES	155
9. REFERENCES	204
10. BIBLIOGRAPHY.....	211

List of figures

Figure 1.1 Slave Ball Contact Ellipse Measurement Geometric Method.....	15
Figure 2.1 Isometric View of the Pressurised Chamber	29
Figure 2.2 Cross-sectional View of the Pressurised Chamber.....	29
Figure 2.3 Isometric View of the Pressurised Chamber	30
Figure 2.4 Isometric View of the Pressurised Chamber	30
Figure 2.5 Isometric View of the Pressurised Chamber	31
Figure 2.6 Cross-sectional View of the Pressurised Chamber.....	31
Figure 2.7 FEA temperature model for cooling purpose	32
Figure 2.8 A section diagram of temperature model	32
Figure 2.9 Trial Test Rig.....	33
Figure 2.10 Clamped circular plate subjected to uniform surface pressure.....	36
Figure 2.11 TE92 Microprocessor Controlled Rotary Tribometer	41
Figure 2.12 Profile of a Typical Shaft Seal	43
Figure 2.13 Shaft seal used for the Pressurised Chamber outer shell view	44
Figure 2.14 Shaft seal used for the Pressurised Chamber lip view.....	44
Figure 2.15 Standard 'O' Ring.....	46
Figure 2.16 Housing Details for Dynamic Sealing.....	46
Figure 2.17 Radial Clearance for 'O' Ring.....	46
Figure 2.18 Housing Details for the Static Sealing	47
Figure 2.19 Modified Test rig coupled with pressurised chamber	48
Figure 2.20 Close up Modified Test rig coupled with pressurised chamber ...	48
Figure 2.21 Schematic of Rig for the High Speed Rotary Tribometer	49
Figure 3.1 Schematic of crack generating device	65
Figure 3.2 Schematic of the contact path offset from the tip.....	67
Figure 3.3 Schematic showing, (a) loading configuration; (b, c) ring crack positioning in the contact track; (d) indent positioning on contact track.....	68
Figure 3.4 Lower chamber part slides into upper chamber part	70
Figure 3.5 Test rig.....	70

Figure 3.6 Optical micrograph secondary fatigue crack propagation.....	72
Figure 3.7 Dye penetrant treated ceramic surface	72
Figure 3.8 Digital light micrograph of a spall	72
Figure 3.9 SEM micrograph for specimen 38.....	74
Figure 3.10 SEM micrograph for specimen 34.....	74
Figure 3.11 AFM micrograph of surface profile	75
Figure 3.12 Spall micrograph obtained by Zygo	76
Figure 3.13 Surface profile of the contact track obtained by a Profilometer...	77
Figure 3.14 Residual Stress Measurement Profile on Rint 2100 XG control engineering workstation.....	78
Figure 4.1 Plane-spacing diagram. (a) and (b) orientations of x-ray beams relative to specimen.	80
Figure 4.2 A schematic of Bragg's law	81
Figure 4.3 Raw data collected during RS measurement.....	83
Figure 4.4 Smoothing of RS data during measurement.....	84
Figure 4.5 3D image of ceramic ball showing surface diameter for RS measurement	85
Figure 4.6 3D sectional view of ceramic ball showing depth of RS measurement	85
Figure 4.7 Schematic of ceramic ball cylindrical volume taken for RS measurement	85
Figure 4.8 Rigaku Rint x-ray diffractometer with Rint 2100 XG control engineering workstation.....	87
Figure 4.9 Residual Stress Measurement Profile on Rint 2100 XG control engineering workstation.....	87
Figure 5.1 Light micrograph; smooth specimen 15.....	90
Figure 5.2 Saturation temperatures for R134a.....	91
Figure 5.3 Saturation temperatures for R600a.....	91
Figure 5.4 Surface damage resulting from ceramic-steel contact. (a) pre-test (b) fatigue spall and crack propagation (c, d) fatigue crack propagation	

(e, f) fatigue spall; Test 1	93
Figure 5.5 Surface damage resulting from ceramic-steel contact. (a) pre-test (b) fatigue spall; Test 2	94
Figure 5.6 Surface damage resulting from ceramic-steel contact in R134a environment; Test 3	95
Figure 5.7 Light micrograph showing fatigue crack propagation (specimen-4)	96
Figure 5.8 Light micrograph failure due to delamination (specimen-4).....	96
Figure 5.9 Light micrograph before test (specimen-5)	96
Figure 5.10 Light micrograph after failure (specimen-5)	96
Figure 5.11 Light micrograph for at 13 minutes test time (specimen-6)	97
Figure 5.12 Light micrograph at 14 minutes test time, lower indent (specimen-6)	97
Figure 5.13 Failure process of specimen 9; (a) 5 minutes (b) 8 minutes and (c) 9 minutes	98
Figure 5.14 Light micrograph showing failure in specimen 12.....	98
Figure 5.15 Fatigue crack propagation in specimen 12	98
Figure 5.16 Fatigue life performances of specimens 1, 4, and 5 at different indent loading	100
Figure 5.17 Fatigue life performances of specimens 6, 11 and 12 at different indent loading	101
Figure 5.18 Fatigue life performances for specimens 3, 4, 6, 11 and 12.....	101
Figure 5.19 Fatigue life performances of specimens 4, 6 ,8 and 11	102
Figure 5.20 Schematic showing, (a, b) ring crack positioning in the contact track	104
Figure 5.21 Light micrograph; induced ring crack and its positioning in the contact track in specimen 31.....	105
Figure 5.22 Light micrograph; secondary cracks initiation and propagation in specimen 31	105
Figure 5.23 Light micrograph; spall failure in specimen 31.....	105

Figure 5.24 Light micrograph; dark field showing crack position in contact path.....	106
Figure 5.25 Light micrograph; secondary crack initiation and propagation....	106
Figure 5.26 Fatigue life performances; influenced by ring crack position in the contact path	106
Figure 5.27 Fatigue life performance; as influenced by ring crack geometry .	107
Figure 5.28 Fatigue life performance; as influenced by ring crack geometry .	108
Figure 5.29 Light micrograph; secondary cracks (specimen-32)	109
Figure 5.30 Light micrograph; delamination and fatigue spall (specimen-32)	109
Figure 5.31 Light micrograph; secondary cracks (specimen-34)	109
Figure 5.32 Light micrograph; fatigue spall failure (specimen-34).....	109
Figure 5.33 Light micrograph; secondary cracks propagation (specimen-35)	110
Figure 5.34 Light micrograph; dark field, spall (specimen-35).....	110
Figure 5.35 Fatigue life performance; liquid and vapour state of refrigerant (specimens-16,18,19,20,25,26,27 and 28	111
Figure 5.36 Fatigue life performance; liquid and vapour state of refrigerant (specimens-18,19,23,24,27 and 28	112
Figure 5.37 Light micrograph; secondary crack initiation and propagation Specimen-21	113
Figure 5.38 Light micrograph; secondary crack propagation specimen-21	113
Figure 5.39 Light micrograph; secondary crack specimen 21	113
Figure 5.40 Light micrograph; secondary crack specimen 21	113
Figure 5.41 Light micrograph showing secondary crack initiation and propagation in specimen 35	114
Figure 5.42 Scanning electron micrograph showing delamination failure during rolling contact in specimen 35.....	114
Figure 5.43 Light micrograph; secondary cracks propagation specimen 20 ...	115
Figure 5.44 Light micrograph secondary cracks propagation specimen 20	115
Figure 5.45 Light micrograph; secondary crack initiation and propagation specimen 16	115

Figure 5.46 Light micrograph; secondary crack initiation and propagation specimen 16	115
Figure 5.47 Light micrograph; induced ring crack and its positioning in the contact track in specimen 31	116
Figure 5.48 Light micrograph; secondary cracks initiation and propagation in specimen 31	116
Figure 5.49 Scanning electron micrograph; fatigue spall failure in specimen 31	117
Figure 5.50 Scanning electron micrograph; fatigue spall failure in specimen 31	117
Figure 5.51 Scanning electron micrograph; spall specimen 17	117
Figure 5.52 Scanning electron micrograph; spall specimen 23	117
Figure 5.53 Scanning electron micrograph; spall fatigue specimen 25	118
Figure 5.54 Scanning electron micrograph; spall fatigue specimen 25	118
Figure 5.55 Scanning electron micrograph; sub-surface cracks in specimen 43	119
Figure 5.56 Light micrograph; secondary crack initiation and propagation in specimen 35	120
Figure 5.57 Scanning electron micrograph; delamination failure in specimen 35	120
Figure 5.58 Light micrograph; rolling contact wear due to secondary cracks specimen 20	121
Figure 5.59 Scanning electron micrograph; wear mechanism due to surface initiated cracks specimen 35	121
Figure 5.60 Atomic Force Micrograph surface profile; specimen 16.....	122
Figure 5.61 Contact path wear profile for specimen 46	123
Figure 5.62 Surface profile; spall specimen 17	123
Figure 5.63 3-dimensional surface profile; spall specimen 17	123
Figure 5.64 3-dimensional surface profile; spall specimen 28	124

Figure 5.65 Comparison of the fatigue spall characteristics of specimens 28 and 17	124
Figure 6.1 Showing residual stress measurement points	129
Figure 6.2 Compressive residual stress relation to RCF stress cycles.....	130
Figure 6.3 Residual stress measurement points, specimen 46	131
Figure 6.4 Compressive residual stress relative to distance from crack.....	132
Figure 6.5 Compressive residual stress relative to distance from ring crack ..	132
Figure 6.6 Residual stress measurement points	133
Figure 6.7 Residual stress measurement points for specimen 46	134
Figure 6.8 Residual stress measurement points for specimen 21	135
Figure 6.9 Residual stress measurement points for specimen 46	136
Figure 6.10 Residual stress measurement direction for specimen 24.....	138
Figure 6.11 3D surface profile of the spall fatigue specimen 24.....	138
Figure 6.12 Residual stress measuring points for specimen 33	139
Figure 6.13 3-dimensional surface profile of the spall fatigue specimen 33 ...	139
Figure 6.14 Residual stress measuring points for specimen 23	140
Figure 6.15 3-dimensional surface profile of the spall for specimen 23	140
Figure 6.16 Residual stress measurements for specimen 35	141
Figure 6.17 3-dimensional surface profile of the spall in specimen 35	141
Figure 6.18 Ceramic failed ball showing spall	142
Figure 6.19 Sub-surface compressive residual stress distribution.....	142
Figure 6.20 Residual stress measuring points for specimen 14.....	143
Figure 6.21 Residual stress measuring points for specimen 14.....	143
Figure 6.22 Residual stress measurements points for specimen 14.....	144
Figure 6.23 Residual stress measurements points for specimen 29.....	145
Figure 6.24 Residual stress measurements points for specimen 22.....	146
Figure 6.25 Residual stress measurements points for specimen 46.....	148
Figure 7.1 Schematic of the stress distribution in the contact circle	150
Figure 7.2 Residual stress measurements points	150
Figure.A1.1 Loading Configuration of Modified Four-Ball Machine.....	156

Fig.A1.2 Rolling Contact Fatigue Test Machine, High Speed Test Arrangement	156
Figure A1.3 Loading configuration of five-ball machine.....	157
Figure A1.4 Loading configuration of ball-on-plate machine	158
Figure A1.5 Loading configuration of ball-on-rod machine	158
Figure A1.6 Loading configuration for disc-on-rod machine.....	159
Figure A1.7 Loading configuration for contacting ring.....	160
Figure A2.1 Machining process (manual)	167
Figure A2.2 Spring-Energised Lip seal	174
Figure A2.3 Shaft Seal.....	174
Figure A2.4 Cross-section of a typical Shaft Seal.....	174
Figure A2.5 PTFE Rotary Shaft Seals.....	175
Figure A2.6 Diagrammatic representation of average roughness value, Ra (Courtesy RS online 2005).....	177
Figure A2.7 Flow chart indicating design routes according to safety standards	189
Figure A3.1 Buehler Vickers Indent generating device	200
Figure A3.2 Digital light microscope used for surface inspection.....	200
Figure A3.3 Optical microscope used for surface inspection.....	200
Figure A3.4 Hand free ball rotating manipulator	201
Figure A3.5 Hands-free ball rotating manipulator used on light microscope .	201
Figure A3.6 Vertical manipulator	201
Figure A3.7 Vertical manipulator used on light microscope.....	201
Figure A3.8 Angular manipulator.....	201
Figure A3.9 Angular manipulator use on light microscope.....	201
Figure A3.10 Determining height of the ball surface tip.....	202
Figure A3.11 The tip is offset by h from the top	202
Figure A3.12 Digital optical microscope.....	202
Figure A3.13 Jeol JSM 5300 scanning electron microscope.....	202
Figure A3.14 Agar sputter gold surface coater.....	202

Figure A3.15 Atomic force microscope	202
Figure A3.16 Specimen mounted on the AFM stage.....	203
Figure A3.17 AFM workstation.....	203
Figure A3.18 Zygo NewView 5000	203
Figure A3.19 Rigaku Rint x-ray diffractometer with Rint 2100 XG control engineering workstation.....	203

List of tables

Table 1.1 Summary of Materials Tested.....	10
Table 1.2 Population Fatigue Life Estimates.....	10
Table 1.3 Material Parameters	12
Table 1.4 Thermodynamic Functions of Refrigerant thermal decomposition.....	22
Table 2.1 Test and Fluids Characteristics	26
Table 2.2 Engineering Properties of 515-1000 Thermoplastic.....	35
Table 2.3 Technical Specification for Shaft Seals / Oil Seals	45
Table 2.4 PTFE Seals optimum Ra.....	47
Table 2.5 Rubber seals dynamic and static optimum Ra.....	47
Table 2.6 Polyurethane seals optimum Ra.....	48
Table 3.1 Typical Properties of Commercial Bearing Si ₃ N ₄	63
Table 3.2 Typical Properties of Commercial Steel Ball	63
Table 3.3 Typical Properties of Refrigerants used	64
Table 4.1 Measurement Conditions for Residual Stress.....	86
Table 4.2 Physical Constant for Residual Stress Measurement.....	86
Table 5.1 Test results for smooth specimens.....	89
Table 5.2 Test results for specimens with induced indents	92
Table 5.3 Test programme	99
Table 5.4 Test results at 2000 rpm spindle speed.....	103
Table 5.5 Test Programme (ring crack positioning as figure 4a)	104
Table 5.6 Test Programme (ring crack positioning as figure 4b).....	104
Table 5.7 RCF tested specimens with different ring crack geometry.....	107
Table 5.8 Test results with different refrigerant state	111
Table 6.1 Specimen RCF details for Residual Stress Measurement.....	126
Table 6.2 Residual Stress Values.....	127
Table 6.3 Residual Stress Values.....	128
Table 6.4 Residual stress measured values for RCF tested specimens	

(x = 0.1 mm)	129
Table 6.5 compressive residual stress values for Specimen 46	130
Table 6.6 compressive residual stress values for Specimen 46	133
Table 6.7 Compressive residual stress values for Specimen 21	135
Table 6.8 Compressive residual stress values for Specimen 46 with change in measuring direction.....	136
Table 6.9 Compressive residual stress for Specimen 24	137
Table 6.10 Compressive residual stress values for Specimen 33	138
Table 6.11 Compressive residual stress values for Specimen 23	140
Table 6.12 Compressive residual stress values for Specimen 35	141
Table 6.13 Compressive residual stress values for Specimen 14	143
Table 6.14 Compressive residual stress values for Specimen 29	144
Table 6.15 Compressive residual stress values for Specimen 22	147
Table 6.16 Residual stress values for Specimen 46	147
Table A2.1 Abbreviations.....	173
Table A2.2 Mechanical Properties of Polycarbonate	173
Table A2.3 Charging HC (R600a) into the System	183
Table A2.4 Charging HC (R600a) into the System – continued	185
Table A2.5 Important Properties of the R600a and R134a Refrigerants	185
Table A2.6 Application ranges for Hydrocarbon Refrigerants	186
Table A2.7 Physical Properties of R600a Refrigerant.....	186
Table A2.8 Compatibility of various lubricants with HC refrigerants.....	187
Table A2.9 Compatibility of Various Lubricants	188
Table A2.10 Flammability properties of Selected Hydrocarbon Refrigerants	190
Table A2.11 Installation/Charges Size Categories	190

Dedicated to my parents

The pillar of stability

Acknowledgements

I will take this opportunity to express my heartiest gratitude to Professor Mark Hadfield my supervisor. His continuous support, help and guidance was a strong source of inspiration, encouragement and confidence. He also provided an excellent opportunity for me to meet experts in the research area.

I would also like to thank Professor Shogo Tobe and Professor Fumio Inaba, Ashikaga Institute of Technology, Japan, for providing the facility to use surface analysis equipment and expertise during my investigation in Japan.

I am also thankful to Dr. Robert Bulpett, Experimental Technique Centre, Brunel University, for contributing and interpretation of scanning electron microscopy.

Dr. Rehan Ahmed, school of engineering and physical sciences, Heriot-Watt University, provided help in using surface mapping in his institute.

Jacqui Holmes provided enormous admin support during the period of my study. She is helpful and informative and is doing a fabulous job.

I would also like to thank technical staff in research lab, namely Peter Jones, Brian Wright and Ken Millard for their support and friendly attitude.

I should also mention my wife who contributed continuous support and encouragement.

Last but not least I appreciate help and support of colleagues and friends.

Nomenclature

ψ	angle between sample normal and diffraction plane normal
θ_0	angle of diffraction in a stress-free condition
L	applied load shaft load, in KN, known
A	area
S_2	area
Ω	area of the solid angle projected
d	atomic spacing
R	ball radius
σ	calculated stress
CFC	chlorofluorocarbon
C	chord Length
CRS	compressive residual stress
Y	constant related to crack geometry
ϕ	contact angle, 35.5°
P	contact load in KN, N
b	contact path radius
A	crack area
B	crack growth constant
$\frac{da}{dN}$	crack growth rate
σ_{cr}	critical stress
D	diameter of vessel
δ	displacement vector
u, v, w	displacement vector components in the x, y, z coordinate directions
V_{eff}	effective stress volume
EP	extreme pressure
P_f	failure probability
N	fatigue cycle

n	fatigue exponent, stress life exponent
F	force
F_b	forces on surface
FWHM	full width of half intensity method
ΔG	Gibb's free energy change
ΔH	Gibb's thermal change
σ	hoop stress
HC	hydrocarbon
HFC	hydrofluorocarbons
$\{\epsilon_0\}$	initial strain due to non uniform temperature distributions
IC	internal combustion
L	length of vessel
$[C]$	linear elastic modulus matrix
α	material coefficient for linear thermal expansion
C and n	material constants
$[D]$	material flexibility matrix
$[C]$	material stiffness matrix
$\sigma_{c,\max}$	maximum compressive stress
P_o	maximum contact pressure
p_0	maximum Hertzian contact pressure
$\sigma_{t,\max}$	maximum tensile stress
$K_{I,\max}$	Mode-I maximum stress intensity factor
$\Delta K_{I,\max}$	Mode-I maximum stress intensity range
E	Modulus of elasticity
MOR	Modulus of fracture
P	normal/tearing force
$\frac{\Delta N}{\Delta A}$	number of stress cycles per unit crack growth

$\Omega/4\pi$	orientation factor
ν	Poisson's ratio
ν_1	Poisson's ratio for ceramic ball
ν_2	Poisson's ratio for steel ball
p	pressure
PC	pressure chamber
R_1	radius of ceramic ball
r	radius of cylinder
R_2	radius of steel ball
RS	residual stress
RCF	rolling contact fatigue
M	slope of $(2\psi-2\theta)$
Ω	solid volume
ε	strain
U	strain energy for a three-dimensional linear elastic body
T	strained state reference temperature
σ	stress
K	stress constant
ΣY	summation of forces in y-axis
S	surface
S_1	surface
T	surface tractions
TRS	tensile residual stress
θ	the incident angle between the x-ray and the plane of the multilayer
n	the order of the reflection
λ	the wavelength
$\{\varepsilon_T\}$	thermal strain vector
T_0	unstrained state reference temperature

$\{F_b\}$	vector of body force components per unit volume
ε	vector of infinitesimal strains components
σ	vector of stress components
$\{T\}$	vector of surface traction components per unit area
t	wall thickness of vessel
m	Weibull modulus
σ_0	Weibull scale parameter
E_1	Young's modulus of elasticity for ceramic ball
E_2	Young's modulus of elasticity for steel ball
E^*	Young's modulus of elasticity for hybrid combination

CHAPTER 1

This chapter introduces background, objectives and methodology of the research. A comprehensive overview of the literature survey is provided in this chapter. The experimental research of performing rolling contact fatigue testing using various test rig is briefly described. The failure modes in rolling contact ceramic bearing elements are also described providing an initial understanding of the problem. The introduction of the new generation of refrigerants in the refrigeration systems have direct tribological effect on the durability of these elements. It was, therefore, important to assess the rolling contact wear mechanism of hybrid ceramic-steel contact with these refrigerants as lubrication. These refrigerants do not exist as liquid due high saturation pressure. A novel pressurised chamber was designed to achieve the required liquid state of refrigerants for lubrication. A brief description of the refrigerants used and the differences between HFC and HC are briefly discussed.

1. INTRODUCTION

When HFCs were substituted for CFCs to comply with the Montreal Protocol¹ severe wear was observed in the actual refrigeration compressors. The cause of this serious wear was believed to be the inferior *Extreme Pressure* (EP) or poor anti-wear capability of the new HFC refrigerant as the environment gas, compared to CFC-12 which is currently used. However, there are some cases where HFC shown extreme pressure or anti-wear capability by forming a fluoride layer on the sliding surface under severe conditions (Mizuhara et al. 1994). Although the HFC-134a had showed some capability of forming a fluoride layer on the sliding surface, it did not exhibit good lubricating quality. The reason for that is because the condition for the HFC to form a protective layer during sliding was more severe than we have in the actual compressors (Mizuhara and Matsuzaki 1994).

¹ 1987 Montreal Protocol on Substances that Deplete the Ozone Layer, United Nations Environment Program, (Adopted Sep. 1987, Enforced Jan. 1989, Revised June 1990).

It has been observed that HFC has shown poor lubricity (cause severe wear). Since the compressor design uses the gaseous phase of the CFC-12, therefore, the friction and wear behaviour of the parts in moving contact is affected when CFC-12 is replaced by HFC. The atmospheric effects of these environments have a direct affect on the durability of the bearing component of the refrigeration compressor. Therefore, the Tribology of the HFC system must be studied. It is necessary to modify the wear test conditions for the HFC refrigerant to get the good results from the actual compressor tests.

Dichlorodifluoromethane (CCl_2F_2 , CFC -12), which is currently widely used as a refrigerant, has been shown to exhibit some benefit as a high temperature boundary lubricant, (Murry et al. 1956). By regulating the use of CFCs with the object of protecting the ozone layer², CFC-12 will be replaced with tetrafluoroethane (CH_2FCF_3 , HFC -134a) R134a and 2-methyl propane (isobutane) ($CH(CH_3)_3$) R600a as an alternative refrigerant. The rapid change from chlorinated to non-chlorinated and natural refrigerants has put great demands on refrigeration compressor companies to develop new equipment designed for these environmentally friendly refrigerants. The use of the new alternative refrigerants in the compressors has been a major issue during recent years. For instance the combination of HFC refrigerant and Polyoester lubricant cause very poor anti-wear properties, (Jonsson et al. 1999). In this case the oxide film between the contact surfaces is not maintained properly and if the lubricant film is too thin the contact surfaces experience high wear rates.

Komatsuzaki and Homma (Komatsuzaki et al. 1987; Komatsuzaki et al. 1991) used a four-ball tester to evaluate the extreme pressure (EP) properties of pure refrigerants and oil refrigerant mixtures. They found that R-134a in Polypropylene glycol gave higher rates of wear than R-12 and R-22 in mineral oil.

² 1987 Montreal Protocol on Substances that Deplete the Ozone Layer, United Nations Environment Program, (Adopted Sep. 1987, Enforced Jan. 1989, Revised June 1990).

The wear was slightly lower when compared with samples tested in air. Mizuhara (Mizuhara and Matsuzaki 1994) studied the anti-wear properties of R-12, R-22 and R-134a in mineral oil showed that chloride and fluoride were present on the surface after wear tests. Randles and Heavers (Randles et al. 1996) carried out a systematic study on how the structure of ester lubricant influences their lubricating properties. They found that the wear rate in Falex and four-ball tests increased when branched acids were present.

The most important property of a lubricant is to form an oil film that separates the surfaces and prevents metal to metal contact. The expected life of a ball bearing is largely related to the film thickness on the bearing. A thin film will increase the number and severity of asperity contacts between the race and the roller or ball. Contact between the surfaces will cause local high stresses, increasing the risk of fatigue in the bearing material. Asperity contacts can also lead to wear of the bearing surfaces.

Refrigerant lubrication has a direct effect on the durability of the rolling element bearings within industrial compressors. In addition, refrigerants have evolved rapidly over the last decade due to sustainable development legislation. Therefore, the Tribology of the refrigerants [HC Hydrocarbon, (R600a, $CH(CH_3)_3$, 2 - Methyl Propane (Isobutane) and HFC tetrafluoroethane (CH_2FCF_3 , HFC -134a)] used in industrial application systems must be studied. The refrigerant dissolved in the oil brings about lubricating behaviour different from that in an ambient environment, especially for boundary lubrication (Itoh 1966; Hon-Ma et al. 1983). The lubricants are easily deteriorated in the presence of refrigerant because the two react chemically (Spauschus et al. 1961; Walker et al. 1962). The gas/liquid phase transition has a significant influence on the wear mechanisms of traditional lubricants and is therefore a useful experimental study (Ciantar 2001).

1.1. Background

Hybrid (ceramic/steel) design is considered a critical technology for high-speed turbine engine and precision machine tool rolling element-bearing applications.

Hybrid ceramic bearings used in a refrigerant environment are an attractive design solution for automotive applications (air conditioning systems). Traditional bench testing of refrigerants as a lubricant is difficult due to their gaseous phase at standard atmospheric conditions. Pressurising the concentrated contact test is therefore necessary to evaluate the system in a liquid state and therefore simulate the practical application. This research is also looking at the wear mechanism simulation in pressurised environment using refrigerants as lubricants. R600a and R134a are used to investigate the influence of these lubricants on the rolling contact wear.

It was necessary to simulate an actual operating condition for rolling contact hybrid ceramic-steel ball-bearings with refrigerant as lubrication. A novel pressurised chamber was designed and manufactured. Rolling contact hybrid ceramic-steel tests can be performed with refrigerant in liquid state without generating severe frictional heat. TE92 Microprocessor Controlled Rotary Tribometer offers facilities to run high and low load tests over a wide range of speeds, coupled with the latest control and instrumentation. The test rig was fitted to the Rotary Tribometer with the novel pressurised chamber. The pressurised chamber offers controlled conditions of temperature(s) and pressure(s). Making it possible to obtain saturated liquid state of the refrigerant as fluid at operating conditions. The tests were conducted using HC (R600a) and HFC (R134a) refrigerants as lubrication.

Fatigue crack propagation is always involved with rolling wear. Many studies have been completed to relate crack propagation behaviour with wear performance. The rolling and sliding wear processes have attracted the interest of many researchers over the past few decades (Suh 1977; Kato 1990). The bulk of that research was focused on the experimental aspects of wear. Only a few attempts have been made to develop analytical models for predicting the wear process. The importance of determining analytical models for wear mechanisms has been discussed (Braza 1989) and wear modes must be described mechanistically to better understand how they occur and to develop formulae for wear material removal. Fracture mechanics has been applied to the analysis of wear modes in a number of studies (Fleming et al. 1977) and (Rosenfield 1980). They analysed a subsurface crack parallel to the

surface of a half-plane subjected to a Hertzian surface load. The stress intensity factors at the crack tips were calculated from an approximate stress field induced by the contact load in a crack-free half-plane. Also, several attempts have been made to explain the ceramic wear mechanisms (Braza 1989; Keer et al. 1990) and (Thomsen et al. 1996). In the case of brittle materials, cracks may occur on the surface due to tension or subsurface cracks parallel to the contact path due to shear. Friction in rolling and sliding contact can arise from asperity interlock, adhesion or abrasion by debris trapped between the contacting surface and viscous drag of the lubricant.

Many experimental and analytical studies have confirmed that ceramic bearing elements typically fail by crack propagation from existing surface cracks. Failure modes of ring, radial and lateral pre-cracked ceramic elements have been extensively studied in the past (Hadfield et al. 1993a; Hadfield et al. 1993b; Hadfield et al. 1995). The results revealed that the artificially produced cracks failed in a non-catastrophic spalling mode. Recent experiments (Wang et al. 2000; Wang et al. 2000a; Wang et al. 2000b) on 'natural' ring cracks were carried out using a recently developed technique involving location/orientation determination of a crack. The 'natural' ring crack initiated failure depends on location/orientation of a crack within the contact path. The spalling fatigue failure only occurs in a few crack positions. A more recent experimental observation (Wang et al. 2001) on ring crack propagation has shown that fatigue spalling processes are involved in fatigue crack propagation from existing surface cracks as well as the formation of the secondary surface cracks. Hence the spalling fatigue life cannot be simply determined in terms of crack propagation rates from the existing surface crack; the subsequent surface damage is also critical in the whole life prediction. It is crucial to understand the influences on rolling wear and to develop a life prediction methodology.

Since it is known that failure initiates from surface cracks, a fracture mechanics approach can offer a significant advantage over the statistical approach in accurately predicting the bearing element life. Most fracture mechanics evaluations provide conservative results, since limiting assumptions are typically made for key parameters. However, some important parameters used in the fracture analysis are

known to vary significantly, these variables and their behaviour can be well-monitored and predicted by simulating the experimental conditions by pressurising the system. For the rolling wear, however, since the failure mechanism and criteria are not fully understood, a more widely applicable understanding of rolling wear from surface defects is still under development. The proposed research seeks to develop techniques to predict rolling wear in the liquid/gaseous phase refrigerant environment using detailed experimental observations.

Since these rolling contact bearing elements are subjected to high cyclic contact stresses the surface and sub-surface residual stresses are highly important in establishing a relationship to fatigue life performance. An understanding of residual stress within complex materials is needed to evaluate the effect of the manufacturing process, characterise failure modes and evaluate the in-service loading conditions of the concentrated rolling contacts (Hadfield et al. 1998). The finishing process parameters have influences on the residual stresses (Kang et al. 2002). It is important to carry out an assessment of residual stresses induced during the manufacturing process and in-service conditions to make suggestions on the design parameters related to residual stress. Analysing the relationship of residual stresses with rolling contact fatigue is an important study which will provide guidelines on the design, process and manufacturing of these elements. The residual stress value within the silicon nitride will vary due to primary processing (hot isostatically pressing) and surface finishing methods (Hadfield and Tobe 1998). In respect to surface finishing methods there is significant pressure to accelerate material removal rates to reduce product costs. In addition to traditional grinding and lapping methods new processes such as magnetic force (Kato et al. 1980) and tribochemically (Kang et al. 1996) assisted processes have been considered for silicon nitride materials. It is therefore necessary to monitor residual manufacturing stresses within the finished silicon nitride bearing elements.

In this research experimental residual stress measurements of silicon nitride are presented. Residual stress measurements were performed on refrigerant lubricated RCF (rolling contact fatigue) failed bearing elements with ring crack defects. A

feature of this study is the small irradiation volume of 0.0942 mm^3 which enabled residual stress measurements of specific points on the rolling contact path. X-ray methodology for residual stress measurement is used during this research.

1.2. Programme and Methodology

1.2.1. Aims and Objectives

This project is concerned with experimental bench testing using a novel environmental chamber to simulate operational conditions without generating severe frictional heat of rolling contact fatigue from surface cracks. In this way the prevailing wear mechanisms of silicon nitride/steel concentrated contacts will be evaluated.

Objectives:

- (1) Design and manufacture an environmental chamber for the TE92 Rotary Tribometer.
- (2) Investigate wear mechanisms in pressurized refrigerant lubrication rolling contact.
- (3) Understand the prevailing wear mechanisms of hybrid contacts in a pressurized refrigerant environment from physical experiments.
- (4) Measure the residual stresses in failed specimens due to rolling contact with refrigerant lubrication.
- (5) Interpret the residual stress relationship to fatigue life of the rolling contact bearing elements.

1.2.2. Methodology

The work is concerned, principally with an experimental investigation of rolling wear of hybrid ceramic bearings with refrigerant lubrication. Surface analysis for identifying various failure mechanisms is undertaken. The experimental part is performed using an environmental chamber that can provide various testing conditions. The research is supplemented by residual stress investigation on the

failed specimen. A relationship of residual stress to fatigue life of the rolling contact bearing elements with refrigerant lubrication is established.

1.2.3. Novelty

The novelty of the proposed research is to test wear properties of ceramic bearing elements with pressurised liquid refrigerant lubrication using in-house designed environmental chamber. Another novelty of the proposed research is to measure and investigate the residual stress relationship to fatigue life. The residual stress measurement is performed sub-surface at a depth of 30 μm . A feature of the research is a small irradiation volume through which the residual stress measurements have been performed.

1.3. Literature Review

Several investigators, prompted by the increasing application of silicon nitride in bearing systems, have documented the wear, friction, and fatigue behaviour of these materials. Bhushan Sibly (Bhushan et al. 1981) and Morrison (Morrison 1982) have provided detailed reviews. In highly stressed bearings, the ceramic containing assemblies will require internal geometry modifications to provide fatigue lives equivalent to all steel bearings. Direct substitutions of ceramic elements increase contact stresses, reducing fatigue life. Bearings containing ceramic can provide improved lives where temperature, corrosion, lubricant compatibility, electrical isolation and high inertial element loads reduce steel bearing life (Lucek et al. 1990). Far fewer investigations have evaluated the tribological behaviour of silicon nitride in rolling contacts. Dry rolling wear rates were measured on silicon nitride (Kato et al. 1986; Kim et al. Oct 1986). In pure rolling, wear rates of 2×10^{-14} to 4×10^{-14} cubic metres/metre were obtained at peak contact stresses 2 to 3 GPa. A variety of solid high temperature lubrication schemes were evaluated in both pure rolling and rolling/sliding conditions (Wedevan 1988). Performance of three silicon nitride materials rolling against cast iron in mineral oil was evaluated (Braza 1989). Hot

pressed silicon nitride wore at 3×10^{-17} cubic metres/metre at 1.4 GPa peak contact stress. All three investigators above used test rigs of their own design.

Rolling contact fatigue tests conducted at high stress with high asperity to elastohydrodynamic film thickness ratios were used to initiate surface fatigue, subsurface fatigue and wear at asperity contacts. In use, bearing wear is also accentuated by these high stress and boundary lubrication conditions. These standardized methods offer a uniform method of screening rolling bearing materials for both wear and fatigue under accelerated rolling contact conditions.

Materials tested (Lucek and John 1990) are given in table 1.1. All have been used in rolling-element bearings. Fatigue test lives were analysed by Weibull statistical methods described by (Johnson 1964) to treat suspended tests. Linear regression analyses provided a conservative estimate of population characteristics. For HIP (Hot isostatically pressed) material (E) and the sintered-HIP material (B) insufficient failures occurred to estimate fatigue life statistics.

The Weibull population life statistics for the several materials tested are shown in table 1.2³. Even at the increased test loads, all of the nitride materials compare favourably to the M50 steel. The Hot Isostatically Pressed materials show a greater magnitude of improvement in calculated life over the hot pressed materials available for the last decade. Reliability as assessed by Weibull slopes is nominally equivalent to steel. Failure mode and wear performance varies significantly among the materials.

³ Source of data, Lucek (1990)

Table 1.1 Summary of Materials Tested⁴

Materials	Letter Designation	Densification Route	Sintering Additives	Hardness (Vickers)
Sialon	A	Pressureless Sintering	Y 203 7% Al ₂ O ₃ 5%	13.5
Silicon Nitride	B	Sinter + HIP	Y 203 5% Al ₂ O ₃ 2%	15.6
Silicon Nitride	C	Hot Pressing	MgO 1%	16.4
Silicon Nitride	D	Hot Isostatic Pressing	MgO 1%	18.1
Silicon Nitride	E	Hot Isostatic Pressing	MgO 1%	16.5

Table 1.2 Population Fatigue Life Estimates⁵

Material	10% Life* (L ₁₀)	Weibull Slope	Magnitude of Test (n)	Fatigue Test (r)
M-50 Steel	3.32	1.57	32	11
Sialon (A)	1.66	1.09	13	13
Sinter-HIP (B)	>3.36	1.39	11	0
Hot Pressed (C)	0.58	0.59	20	20
HIP (D)	4.08	1.26	20	14
HIP (E)	>10.1	2.03	14	1

Wear performance differences between materials C, D, and E are not significant. No wear performance advantage can be ascribed to the tungsten containing material (D). The relative wear performance of the sintered, sintered-HIP and low additive content material follows the hardness trends shown.

The high value of Young's modulus of ceramics over steel causes high contact stresses in bearings having ceramic elements. Therefore, the Hot Isostatically Pressed silicon nitride is the best choice for ceramic rolling element bearings. Due to low density, high temperature strength and hardness, ceramics are one of the superior materials. It is known, however, that at low temperature, ceramics are more brittle than steel. The values of fracture toughness and bending strength of ceramics are lower when compared to hardened bearing steel. Therefore, brittleness, cost of

⁴ Lucek, John W (1990)

⁵ Lucek, John W (1990)

product, reliability and reproducibility are the most current areas of focus (Katz et al. 1985). Much of the data available for hybrid silicon nitride reveals that spalling is the major failure mode just as in steel material. The laboratory test data obtained using an RCF (Rolling Contact Fatigue) tester at high contact stresses (> 6 GPa) clearly shows a special mode of failure: fatigue cracking at the edge of the rolling track. Lucek (Lucek and John 1990), Baumgartner (Baumgartner et al. 1975) and Katz (Katz et al. 1991) have attributed this failure to the high tensile stress at the edge of a Hertzian contact. A similar finding has been reported by Duffy (Duffy 1991) for the track edge cracking on silicon nitride rings in full ceramic ball bearings under a maximum contact stress of 4.2 GPa. The authors consider that the failure in a ceramic rolling element is indicated by the first appearance of a macro crack in the rolling body, such as the RCF test rod, even though the formal failure is indicated by the appearance of macro-spalling (Chiu 1999). In ceramics it is well established that tensile stress is the main critical factor of causing Mode I fracture and most failures are initiated from the flaws within the ceramic itself. The flaws in the ceramic material, however, are randomly distributed with respect to their size and number. The following are some of the known formulations for the probability of ceramic failure.

Fast Fracture

The probability of ceramic failure by fast fracture is non-zero at the first application of load, depending on the magnitude of the stress level. Modulus of fracture (MOR) is a common technique for evaluating strength against the fast fracture. Tests involve static bending of bar specimens. First, for fast fracture, the failure probability of a component is an exponential function of a volume integration of stress (σ) to the power of Weibull modulus m , i.e.

$$P_f = 1 - \exp\left[- \int \left(\frac{\sigma}{\sigma_0}\right)^m dV\right] = 1 - \exp\left[-V_{eff} \frac{\sigma_{max}^m}{\sigma_0^m}\right] \quad (1.1)$$

Where V_{eff} is the effective stress volume, defined by

$$V_{eff} = \int \left(\frac{\sigma}{\sigma_{max}} \right)^m dV \quad (1.2)$$

For the two baseline ceramics the values of m and σ_0 have been presented in table 1.3 (Chiu 1999), which are calculated from Weibull plots obtained based on the MOR bending data using three-point (TSN-03H) and four-point bending tests (NB-200).

Table 1.3 Material Parameters⁶

Material Type	Unit	TSN-03H	NBD-200
Cyclic Fatigue - Fatigue Exponent (n)	-	25.88	54.34
Crack Growth Parameter (B)	MPa ² cycles	4.33x10 ¹²	20.3x10 ¹²
Fast Fracture - Method of Testing	-	3-Pt Bending	4-pt Bending
Characteristic Strength σ_θ	MPa	1050	900
Effective Volume, $V_{eff, MOR}$	Mm ³	1.602	12.26
Weibull Modulus (m)	-	10.27	9.7
Scale Parameter σ_0	MPa	1098	1154

Alternatively, the Batdorf theory (Batdorf et al. 1974; Batdorf et al. 1978) can be applied as in (Nemeth et al. 1992), which results in a new scale parameter $\sigma_{b,0}$ where the subscript b denotes Batdorf, as opposed to Weibull in the above formulation. For the Batdorf theory the Equation-1 has the following form:

$$P_f = 1 - \exp \left\{ - \int \left[\int \left(\frac{\Omega}{4\pi} \right) dn_v \left(\frac{\sigma_{cr}}{d\sigma_{cr}} \right) \right] dV \right\} \quad (1.3)$$

where Ω is the area of the solid angle projected onto a unit radius sphere in the principal stress space containing all of the crack orientation for which the effective stress is greater than or equal to the critical stress σ_{cr} . Chao and Shetty (Chao et al. 1991) found that for silicon nitride, fracture initiating cracks nucleated at pores and oriented perpendicular to the maximum principal stress direction during loading.

⁶ Source of Data Chiu (1999)

Therefore, the orientation factor $\frac{\Omega}{4\pi}$ can be set equal to unity for both uniaxial and biaxial loading. With this important simplification, Equation 1.3 can be reduced to Equation 1.1.

Cyclic Fatigue

Crack Growth measurement for silicon nitride by H. Kobayashi (Kobayashi 1992)

shows that the crack growth rate $\frac{da}{dN}$ is governed by $K_{I,\max}$ rather than its range,

i.e., $\Delta K_{I,\max}$ (as in the Paris Law). Thus the crack growth rate $\left(\frac{da}{dN}\right)$ may be approximated by a power function of the equivalent Mode I maximum stress intensity factor $K_{I,\max}$, i.e.

$$\frac{da}{dN} = CK_{I,\max}^n, K_{I,\max} = Y\sigma\sqrt{A} \quad (1.4)$$

Where A is the crack area, Y is a constant related to crack geometry. For ring cracks, $Y = \frac{2}{\sqrt{\pi}}$. C and n are material constants, which are called "crack growth parameter" and "fatigue exponent," respectively.

Note that in a Hertzian stress field, the stress σ is not uniform. For silicon nitride ceramics, the values of the fatigue exponent 'n' is very large as shown in the Table-2.

The crack growth rate $\frac{da}{dN}$ can vary very strongly with A and σ as the crack grows.

In the range of small values of crack size A (within which the stress σ is nearly a constant), the number of stress cycles per unit crack growth, i.e., $\frac{\Delta N}{\Delta A}$, is much

larger than when A is large. Therefore, it is possible to assume that in Equation 1.4, the stress σ is constant the same as the initial nominal stress at the flaw location.

Following (Sturmer et al. 1992), the integration of the above formula with respect to the cycle N results in the following formula for volume flaw analysis, for the probability of fracture (or macro cracking) after sub critical crack growth,

$$P_f = 1 - \exp \left[-\sigma_0^{-m} \int \sigma^m \left(1 + \sigma^2 \frac{N}{B} \right)^{\frac{m}{(n-2)}} dV \right] \quad (1.5)$$

$$B = \frac{2}{CY^2(n-2)K_{lc}^{n-2}} \quad (1.6)$$

As suggested (Nemeth and Gyekenyesi 1992), the constant B in the above formula can be obtained from the cyclic fatigue test under uniaxial stress, such as the rotating beam fatigue test.

Critical Stress of Rolling Contact

The rolling contact body is assumed to consist of many subsurface material elements, each is subject to time-dependent three-dimensional contact stress during the passage of a rolling contact load. At each relative position of contact load, the stresses due to the load consist of three normal stresses and three shear stress components. These six components combined with the hoop or residual stress acting on the ring can be used to determine three principal stresses according to the theory of elasticity. For a ceramic material element under the passage of a contact load, the critical stress is assumed to be the greatest tensile principal stress the material element has experienced due to the moving contact load. For certain cases, where the principal stress field in the material element at all relative locations to the load is compressive to all three components, the critical stress of the material element due to the particular moving load would be zero (Chiu 1999).

1.4. Wear of Ceramics

Wear scars on steel loading balls were measured optically but measurement of diameter reduction with a micrometer proved as accurate and more repeatable. Width of the scar was calculated as shown in Fig. 1.1, (Lucek and John 1990).

$$C = 2\sqrt{R^2 - b^2} \quad (1.7)$$

where C = Chord Length

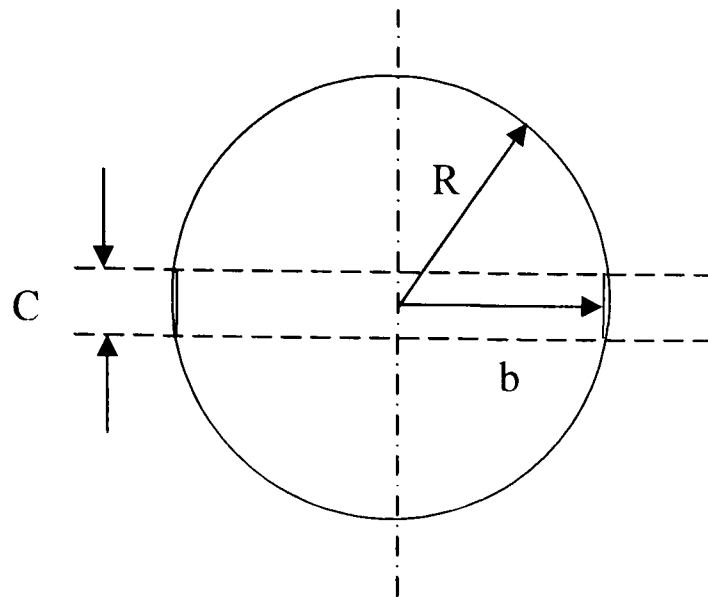


Figure. 1.1 Slave Ball Contact Ellipse Measurement Geometric Method

1.4.1. Experimental Research

Many Rolling Contact Fatigue (RCF) test machines (see appendix 1) are in use to study the wear performance of materials and lubricants in rolling contact. In rolling contact, surface and subsurface initiated fatigue is observed due to repeated loading. At a critical number of fatigue cycles the break-up of the material surface results in the formation of small pits, also known as pitting or spalling. Several investigators, prompted by the increasing application of silicon nitride in bearing systems, have documented wear and fatigue behaviour of these materials (Lucek and John 1990). Investigations have shown that, except for very specialized conditions of load or local chemistry, solid or liquid lubrication is required to effectively utilize silicon nitride in wear applications. Dry rolling wear rates on silicon nitride were measured by (Kato et al. 1986; Kato et al. 1988). Generally, wear occurs either by mechanical or chemical means and has six principal, quite distinct phenomena that have one thing in common, removal of material from the rubbing surfaces, (Bhushan 2002). These types of wear mechanisms are adhesive wear, abrasive wear, fatigue wear, impact wear, corrosive wear, electrical-arc-induced wear and fretting and fretting corrosion.

1.4.2. Theoretical Research

Wear

Ajayi and Ludema (Ajayi et al. 1988) reviewed the microstructural wear mechanisms of silicon nitride ceramics. Fisher (Fisher et al. 1985) has studied the Tribology of silicon nitride sliding couples in several environments. Sutor (Sutor 1984) has reported the Tribology of silicon nitride and steel couples at elevated temperature. These investigations have shown that, except for very specialized conditions of load or local chemistry, solid or liquid lubrication is required to effectively utilize silicon nitride in wear applications. Miyoshi (Miyoshi 1989) has shown that amorphous carbon films on ceramics can provide low sliding friction coefficients in several tribological environments.

The predominant fatigue failure mechanism in silicon nitride ceramics involves the slow growth of circumferential cracks from the rod surface at the edges of the wear track, outside the contact ellipse. These cracks are driven by the tensile stresses at the edge of the contact ellipse. The applied tensile stress in this test (Lucek and John 1990) exceeds the bulk tensile strength of the material. Because the stress field surface is localized, the cracks grow in stable mode until material in the compressive contact zone becomes sufficiently unsupported to spall out, leaving a pit. The appearance of the pit is similar to that obtained in metallic fatigue testing but originates from tensile crack growth. The sinter-HIP and higher purity, tungsten free, HIP silicon nitride (E) materials offer superior fatigue performance.

Rolling contact wear is the most common type of failure mechanism found at the rolling contact path. Preliminary work was reported by (Scott et al. 1971) using a modified four-ball machine to assess hot-pressed silicon nitride as rolling bearing elements. Un-lubricated contact was reported at 1500 rpm spindle speed at various temperatures with 5.8 GPa contact stresses. Lubricated contact was studied at ambient temperature with 7.7 GPa contact stresses. During un-lubricated contact the wear was 0.6 mg in 30 minutes with modest surface quality on the contact path. With lubrication the upper ball failed after 20 seconds showing wear and fracture.

An upper silicon nitride ball was used with En31 steel lower balls which increased failure time to 70 seconds.

Allen (Allen 1994) presented a study of the effect of composition and physical properties of silicon nitride on rolling wear and fatigue performance using a ball-on-rod machine. Three commercial bearing materials were tested at contact stresses of 6.4 GPa. Wear and fatigue properties were compared to physical properties and composition. It was evident that high fracture toughness was required for fatigue life and wear resistance. Grain boundary composition had no influence on the wear mechanisms of HIPed (hot-isostatically pressed) silicon nitride.

Akazawa and Kato (Akazawa et al. 1988) studied the wear properties of silicon nitride in dry rolling-sliding contact using a ring on roller machine. With no lubrication and 1.1 GPa contact stresses showed thin flake-like wear particles rich in oxygen and varying according to the roughness of the contact surfaces. Braza (Braza 1989) carried out rolling-sliding tests to assess wear mechanisms. This involved a large diameter iron and a small diameter silicon nitride roller with an internal steel pin lubricated with standard lubricant oils. Three types of silicon nitride, hot-pressed, pressure-less sintered and reaction bonded, were tested at comparatively lower contact stresses of 1.37 GPa. Wear rate for the reaction type bonded was higher, wear mode observed was 'grain pullout'. The other two types had similar wear rate with 'submicron chipping' type wear. Rolling contact friction co-efficient was 0.0056, similar for each type. Dry rolling tests on several ceramics by Kim (Kim 1986) concluded that silicon nitride wear was the least under such conditions. A ring-o-disc testing machine was used. The maximum contact stresses were 2.5 to 5 GPa. An unsuccessful attempt was made to co-relate mechanical properties to wear rate, suggesting a combination of material properties and roughness was needed. Brittle fracture was observed to be the main mode of failure (Kim 1986).

Transient wear of lubricated silicon nitride in rolling contact was reported by Chao (Chao and Shetty 1991; Chao 1998). A ball-on-rod machine was used with 5 to 6.5 GPa maximum contact stresses. Wear rate was influenced by surface roughness.

Spalling

Spalling is the most common type of failure mechanism in rolling contact fatigue. The spalling phenomenon in silicon nitride is comparable to steel and silicon nitride is, therefore, considered the best candidate material to substitute steel in bearing elements. Ceramics, like SiC have low fracture toughness and fail into catastrophic fracture or severe wear by micro-fracture.

Rolling contact fatigue performance of hot-pressed silicon nitride using a rod type machine was reported (Lucek and John 1990). Maximum contact stress was 6.4 GPa with synthetic turbine oil at ambient temperature to provide boundary lubrication. The specimen speed was set to 3600 rpm. The failure mechanism involved slow growth of a circumferential crack from the contact path edges due to tensile stresses. Spalling occurred when material was insufficiently supported in the compressive zone.

A five-ball fatigue test machine was employed to investigate the fatigue life of hot-pressed silicon nitride balls (Parker et al. 1975). The ball diameter was 12.7 mm with lubricated contact, with maximum contact stresses ranging from 4.3 to 6.2 GPa, shaft speed of 9600 rpm and contact angle of 30°. Test specimens failed only into fatigue spall similar to that found on steel elements. The fatigue life of ceramic-steel contact was comparable to that of steel-steel contact. There was no evidence of edge cracking on or near the spall on the contact path.

A disc-on-rod machine was used to investigate the failure modes of hot-pressed ceramic (Lucek et al. 1978). The test loads were 4.1 to 5.5 GPa. The specimens failed into non-catastrophic spall failure. Roughness (R_a) of the test rods used was 0.1 μm for standard tests and non-standard tests were conducted with various ceramic grades, lubricants and roughness (Hadfield and Stolarski 1995). The results have shown that under various tribological conditions silicon nitride failure occurred in non-catastrophic mode.

Silicon nitride hybrid ball-bearing elements of 12.7 mm diameter with M50 steel rings and a brass cage were used (Morrison 1982). The range of contact pressure

during the tests was 1.95 to 2.44 GPa, lubricant film parameter was approximately 3.5 for the tests. The investigations showed evidence of spall without silicon ball fracture. Statistical analysis shows that bearing life varies according to a power law model.

Dynamic and static load rating of silicon nitride bearing elements were analysed (Fujiwara 1989). The ball on plate machine was used. Steel balls revolving around an inner race were loaded against a flat test piece. The maximum contact stress was 6.4 GPa with 1400 rpm rotational speed with turbine mineral oil as lubricant. Spalling was the only long-term failure mode, two other modes of failure were also identified after short time as 'cave-in' and 'peeling'.

An extensive testing of silicon nitride with perfect and artificially pre-cracked bearing elements was presented (Hadfield 1995; Hadfield and Stolarski 1995; Hadfield et al. 1995). A four ball modified test rig was employed for conducting rolling contact fatigue tests. The maximum contact stress was 6.4 GPa with 5000 rpm spindle speed with high viscosity mineral oil, low viscosity synthetic oil and high penetration kerosene as lubricants. Spalling was observed as non-catastrophic failure mechanism. The failure mechanisms were influenced by lubrication fluids.

Rolling contact fatigue performance of 11 silicon nitride bearing materials was studied (Burrier 1996). Tests were conducted using a ball-on-rod machine. The contact stresses were 5.93 GPa with rod rotation of 3600 rpm. Spalling was observed as failure mode. Silicon nitride material can exhibit a wide range of rolling contact fatigue endurance. Under relatively high stress conditions, fatigue durability increased as the microstructure inclined dramatically toward finer, more equiaxed grains with uniform and minimum distribution of second phases.

Delamination

Investigations on delamination failure of rolling contact ceramic bearing elements with perfect and artificially pre-cracked specimens were carried out (Hadfield et al. 1993a; Hadfield et al. 1993b; Hadfield 1994; Hadfield and Stolarski 1995). The steel-ceramic contact was used to simulate a hybrid bearing system. The pre-induced

cracks were in the ring form, radial or lateral. Various tribological and high compressive stress conditions resulted in delamination failure. Delamination failure was classified by the crack location and subsequent propagation. Specimens with ring cracks were failed into spall fatigue. Lateral and radial crack failure was observed in three ways. (1) radial crack induced spalling and (2) delamination and (3) radial crack-induced bulging. The types of lubricant influenced failure mechanisms since lubricant penetration into cracks produces significant hydrostatic pressure.

Surface delamination occurred due to adjacent radial crack propagation and joining. Fatigue striations were found in the delamination area which exhibited compressive residual stresses. Ferrous debris accumulated during bulging that originated from the steel surfaces was trapped under the ball surface. Steel debris suspended in the pressurised lubricant was forced up through the ball surface.

A recent study (Hadfield 1998) has shown no evidence of ring cracks developing into conics but only delamination. These ring cracks were found on the surface and were not artificially induced. The critical depth of these ring cracks ranges between 5 to 20 μm . Porosity had dominant influence on wear and performance.

1.4.3. Refrigerants as Lubricants

Due to environmental impact legislation, refrigerants have evolved to include Hydro fluorocarbons (HFC) such as R134a and Hydrocarbons (HC) such as R600a. Obtaining material wear properties of the refrigerants used in mechanical applications is difficult due to the high saturation pressure of the refrigerants. It is important to assess the in-use durability performance of these products from a sustainable development viewpoint. This research responds to the need for bench testing of rolling contacts using the new generation refrigerants as lubricants.

Refrigerants have evolved rapidly over the last decade due to sustainable development legislation (ACRIB October, 2000). Refrigerant lubrication has a direct effect on the durability of the rolling element bearings within industrial compressors. Therefore, the Tribology of the refrigerants (HC and HFC) used in industrial

application systems must be studied. The refrigerant dissolved in the oil varies the lubricating properties, the extent of the variation depends on the environmental condition of the fluid i.e. pressure and temperature, etc. especially for boundary lubrication (Itoh 1966; Hon-Ma and Komatsuzaki 1983). The lubricants easily deteriorate in the presence of refrigerant because the two react chemically (Spauschus and Doderer 1961; Walker and Levy 1962).

Komatsuzaki (Komatsuzaki and Homma 1991) used a four-ball tester to evaluate the Extreme Pressure (EP) properties of pure refrigerants and oil refrigerant mixtures. They found that R-134a in Polypropylene glycol gave higher rates of wear than R-12 and R-22 in mineral oil. Although the HFC-134a had shown some capability of forming a fluoride layer on the sliding surface, it did not exhibit good lubricating quality. Because the condition needed for the HFC to form a protective layer during sliding is more severe than in the actual compressors (Mizuhara and Matsuzaki 1994). The gas/liquid phase transition has a significant influence on the wear mechanisms of traditional lubricants and is therefore a useful experimental study (Ciantar 2001).

1.4.4. Causes of Differences between CFC and HFC

Investigations were made on the surfaces of the iron ring and the bronze disc (Mizuhara and Matsuzaki 1994). Chlorine was found on the worn surface of the bronze but not on the iron ring, which experienced less wear. This may lead to the suggestion that for the formation of a lubricating film in the refrigerant environment active fresh surface is needed. It may also be assumed that the *Cl* more reacts with *Pb* than *Fe*.

Mori (Mori et al. 1991) reported that chemisorption was not apparent when it was exposed to a fresh surface under a very low pressure. This meant that the factors that activated the decomposition of refrigerant on a fresh surface were necessary to form a lubricating film.

The Gibb's free energy changes, (ΔG), of the refrigerant's thermal decomposition, are positive values (Chen et al. 1975; Chen et al. 1976), as shown in Table-1.4.

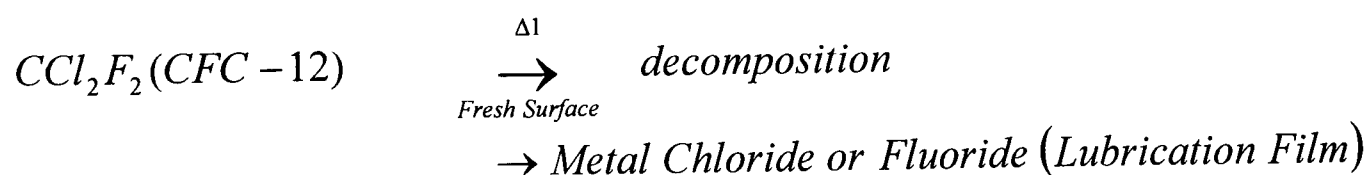
Table. 1.4 Thermodynamic Functions of Refrigerant thermal decomposition⁷

Reactions	Thermodynamic Function (KJ/mole)			
	298.15°K/25°C		700°K/426.85°C	
	ΔG	ΔH	ΔG	ΔH
$CCl_2F_2=C+Cl_2+F_2$	1125.5	1210.2	1100.5	1212.8
$CCL_2F_2=C+_2ClF$	1021.9	1109.6	903.2	1110.7
$CH_2FCF_3=2C=H_2+2F_2$	2169.1	2329.6	1948.0	2339.0
$CH_2FCF_3=2C+2HF+F_2$	1619.8	1784.5	1393.8	1791.9

This shows that thermal decomposition cannot occur even at 700°K/426.85°C, HFC-134a does not decompose up to 1170°K/896.85°C, Millward (1973) and CFC-12 does not decompose up to 770°K/796.85°C⁸.

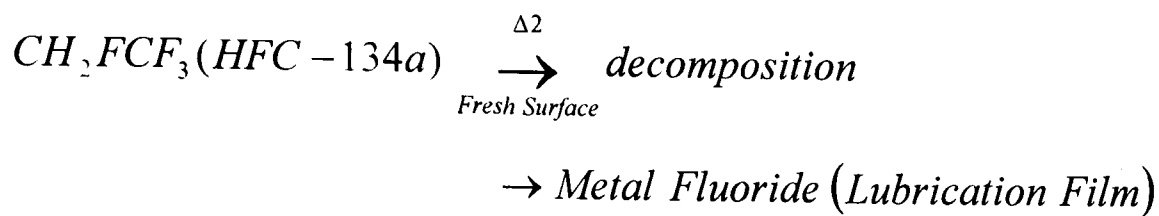
It is obvious from Mori's test conditions (Mori et al. 1991) that the authors ran more severe experiments that could have generated more frictional heat. It is reasonable to conclude that both high frictional heat and exposed fresh surface were necessary to decompose the refrigerant on the sliding surface. However, both refrigerants HFC-134a and CFC-12 require different decomposition temperatures.

To chemisorb on the fresh surface, the dissociation of molecules on the surface was required. The dissociation energy of the C-Cl bond (326.5 KJ/mole) was lower than C-F (485.6 KJ/mole). Thus, CFC-12, having C-Cl bonds, decomposed at lower frictional heat ($\Delta 1$), and protected the fresh surface under moderate sliding conditions. In contrast, HFC-134a required higher heat ($\Delta 2$) and did not decompose at the same temperature as CFC-12, and in turn, could not form a lubricating layer. This simple scheme is shown in Figure 1.2, (Mizuhara and Matsuzaki 1994).



⁷ Chen (1975, 1976)

⁸ "DAIFRON Gas Technical Information: K-2I," Daikin Industries Ltd. (1984).



$\Delta 1 < \Delta 2$: required frictional heat

Figure. 1.2 Schematic diagram of the lubrication film formation

It is possible that fluorine from CFC-12 formed a fluoride but this did not occur with the fluorine from HFC-134a. Oku et al (1989) reported that the *C-Cl* bond in the CFC acts as a trigger for the *C-F* decomposition during the reductive dehalogenation of the CFCs.

1.5. State-of-the-Art

This research responds to the need to assess rolling contact fatigue of hybrid ceramic-steel contact with liquid refrigerants as lubrication. The refrigerants in question do not exist as liquid at ordinary pressure and temperature conditions. Testing rolling contact without a liquid phase of refrigerant will generate excessive frictional heat and will not simulate actual operational conditions. Therefore, a novel pressurised environmental chamber was designed to achieve a liquid state of the refrigerant as lubricant without generating severe frictional heat by controlling the pressure/temperature condition of the refrigerant.

The induced cracks on the ceramic bearing elements influence failure mechanism. The geometry of the ring crack its positioning and orientation on the contact path is also very important. The maximum impact loading for generating ring crack was 2.88 KN. The radius of the induced ring crack ranges from 0.21 mm while contact circle radius 0.22 mm at 6 GPa Hertz contact stress. The surface analyses were performed by state-of-the-art equipment including AFM, Zygo, Profilometer and SEM etc. Residual stress analysis is an important feature of this research. Since these rolling contact bearing elements are subjected to high cyclic contact stresses the surface and sub-surface residual stresses are highly important in establishing a relationship to fatigue life performance.

CHAPTER 2

This research responds to the need for bench testing of rolling contacts using new generation refrigerants acting as a lubricant. A novel pressurised chamber is designed to achieve a liquid state of the refrigerant as a lubricant for rolling contact durability experiments. Design parameters such as material selection criteria, three-dimensional finite element stress analysis and detailed design of the pressurised chamber are presented. Sealing techniques are described. A cooling system used to control the temperature and pressure of the pressurised chamber is described. A high-speed rotary Tribometer is used for rolling contact durability tests. Test rig modifications are provided in this chapter. Refrigerants and related health and safety issues are briefly described.

2. TEST RIG DESIGN

2.1. Design of environmental chamber

Owing to the environmental damage caused by containing chlorine, CFCs were substituted as refrigerant to comply with the Montreal Protocol. Mixing of the lubricating oils with the refrigerants means changing the tribological properties of the lubricant. The properties of the CFCs are known, and it is also known that they act as an Extreme Pressure (EP) additive. The properties of the other refrigerants like Hydrofluorocarbon (HFC) 134a and Hydrocarbons, however, are unknown and their effect on the failure mechanism during rolling contact of ceramic bearing elements must be investigated. A series of extreme pressure tests was run on TE 92HS High Speed Microprocessor Controlled Rotary Tribometer (HSMCRT) in order to develop this research. A properly sealed Pressurised Chamber was designed and fitted with the TE 92 HSMCRT to introduce a liquid state refrigerant environment. Design of the pressurised chamber is described (Khan et al. 2005) and detailed 2-dimensional drawings are provided in appendix 2.

The research of improving the lubricants by using EP agents has an important role, since the high speed rotating machines need better lubricating conditions for better performance. Hon-Ma and S. Komatsuzaki (Hon-Ma et al. 1983) have been involved in a similar type of research. They examined the anti-seizure and anti-wear properties of R-12 (CFCs) refrigerant oils in gaseous state. Both of the properties were examined by conducting experiments in a modified four-ball friction-testing machine. The refrigerant was found to be effective under EP and improved the anti-seizure and anti-wear properties of the lubricant. They made changes to the basic friction-testing machine by introducing a pressurised chamber and a mechanical seal on the rotating shaft in order to avoid any leakage from the gaseous environment.

The analysed experimental details are:

Induced R-12 pressure	49.1 MPa
Lubricating oil temperature	25.1 °C
Lubricating oil quantity	110 g
Rotating time	10 min
Rotating speed	600 rev/min

In a similar study (Komatsuzaki et al. 1987), they reduced the pressure from 49.1 to 0.5 MPa inside the PC since the former temperature was too high for the mechanical seal to sustain. They carried out their tests at three different levels of pressures 0.098, 0.294 and 0.491 MPa. At higher pressure, the wear was less. They concluded from both studies that R-12 when used as an EP agent, improved the anti-seizure and anti-wear properties of the lubricant. The best lubricating conditions prevailed when the lubricating oils were moderately mixed with the refrigerant. However, this type of refrigerant had to be abandoned as it contained chlorine atoms. Therefore, it became evident and equally important that new refrigerants should be tested. In the following years, Komatsuzaki and Homma (Komatsuzaki et al. 1991) presented a new study stating that formation of metal chlorine and/or fluorine on the sliding surface(s) in the R-12 refrigerant environment acted as an EP or anti-wear agent causing good lubrication.

When mixed with lubricants HFC-134a did not positively affect the sliding surface(s) and it was concluded that HFC-134a did not exhibit lubricating qualities. Therefore, a need for new research arises to find ways of improving test facilities to simulate rolling contact fatigue testing with liquid refrigerant lubrication without generating severe frictional heat.

It is necessary to build a PC to provide a controlled atmosphere with respect to temperature and pressure while conducting tests on a four-ball PLINT machine. The advantage with the new PC is that it can be fitted with shaft rotation as high as 5,000 rpm, as compared to the 600 rpm, Komatsuzaki chamber. The new chamber has a cylindrical structure that reduces its dimensions, increases safety and a new smaller shaft seal replaces the mechanical seal. Some of the Pressurised Chamber PC test characteristics are tabulated as follows in Table 2.1.

Table 2.1 Test and Fluids Characteristics

Characteristics	Rolling test
Inside Pressure	3-4 bar
Refrigerant temperature	30 °C (Max)
Shaft Speed	Up to 5,000 rpm
Refrigerant state	Liquid/gaseous

The inside pressure is kept 3-4 bar in order to achieve the liquid state of the refrigerant subject to the pressure enthalpy chart Appendix-2. The lubricant temperature is ~25 °C. The rest of the characteristics are PLINT standard values described in the following section. Since the previous studies have shown HFC-134a is not a favourable EP agent, the new research is focused on investigating the effects of Hydrocarbon Refrigerants.

2.1.1. Design Parameters

The material selection for the design of the pressurised chamber was based on mechanical and thermal properties. Cast aluminium alloy (LM 13 – TF7) was selected for the design and manufacture. The operating temperatures and pressures for the pressurised chamber are 25°C and 3 bar/0.3MPa (maximum) respectively. The elastic limit of cast aluminium alloy is 280 MPa and tensile strength is 360 MPa. Poisson's ratio and Young's modulus are 0.36 and 88.5 GPa respectively. Thermal conductivity of the material is 220 W/m. K, while thermal expansion is 24 μ strain/K. Details of material specifications are provided in Appendix 2.

The pressurised chamber will be mounted on the Rotary Tribometer detail is provided in section 2.1.3. The Rotary Tribometer has an upper column which includes spindle of the machine see Figure 2.11. This spindle/shaft of the machine provides facility of fixing upper ball through a collet. The lower part of the machine supports the cup which is the housing to the lower three balls to simulate ball bearing. The lower part of the Rotary Tribometer moves vertically up and down aided by pneumatic system. This movement helps to dismount the cup for cleaning, adding lubricant and putting lower balls. Once these are added into the cup, the cup is then placed on the lower part through its guides. The lower part should then be actuated to move up so that the upper fixed ball held in the spindle of the upper part of the machine should come in contact with lower three balls in the cup. The load is also applied through this contact and is measured see details in section 2.1.3.

The pressurised chamber, therefore, should be designed in two separate parts. One part mounted on the upper column of the machine to house upper fixed ball. Second part of the pressurised chamber should be mounted on the lower part of the machine to house the lower three balls assembly. Therefore, they should be called upper and lower part of the pressurised chamber. This arrangement will provide facility to fix/remove upper ball in/from the spindle of the machine and load/unload lower balls in the steel cup of the lower part of the machine while pressurised chamber is mounted on the machine. When the lower and upper balls are engaged the two parts

of the pressurised chamber provide a coupled arrangement of a closed and sealed chamber such that no leakage of pressure or refrigerant takes place. When the test is stopped the lower part of the pressurised chamber slides out of the upper part of the pressurised chamber, as an integral part of the lower part of the machine, thus providing access to the inside of the chamber for taking upper and lower balls to record surface information.

2.1.2. Pressurised chamber – design concepts

Functional/operational complexity, controlled cooling system, machining complexity, material and final product cost put enormous constraints on the final design of the pressurised chamber. Three design concepts were developed through CAD system. The design criteria for all the three chambers are identical except for the option of cooling method. The internal and external dimensions, material and two parts chamber concept were the criteria of development. Machining complexity and manufacturing costs were among the factors that helped in the selection of final product. The simple cooling arrangement and its efficiency were also taken into considerations for selecting the final product to undergo commissioning. Details of the three various designs are provided below. The external cooling design was chosen for commissioning purpose and thus as the final product. The ease of machining, low cost and external cooling were the deciding factors. A cooling system employed an external coolant pipe wrapped around the surface of the pressurised chamber that carried coolant from and to the sink. This arrangement provided economical and efficient cooling system for the modified test rig see Figure 2.21.

External Cooling Design – Final Design

This design was chosen due to low machining cost and complexity, efficient and simple cooling system. Cooling was carried out through an external coolant pipe

wrapped around the surface of the chamber. The assembly statistics¹ are shown in Appendix 2. Detailed 2D drawings are also provided in Appendix 2.

The pictorial and the cross-sectional views are shown in Fig. 2.1 and Fig. 2.2 respectively.

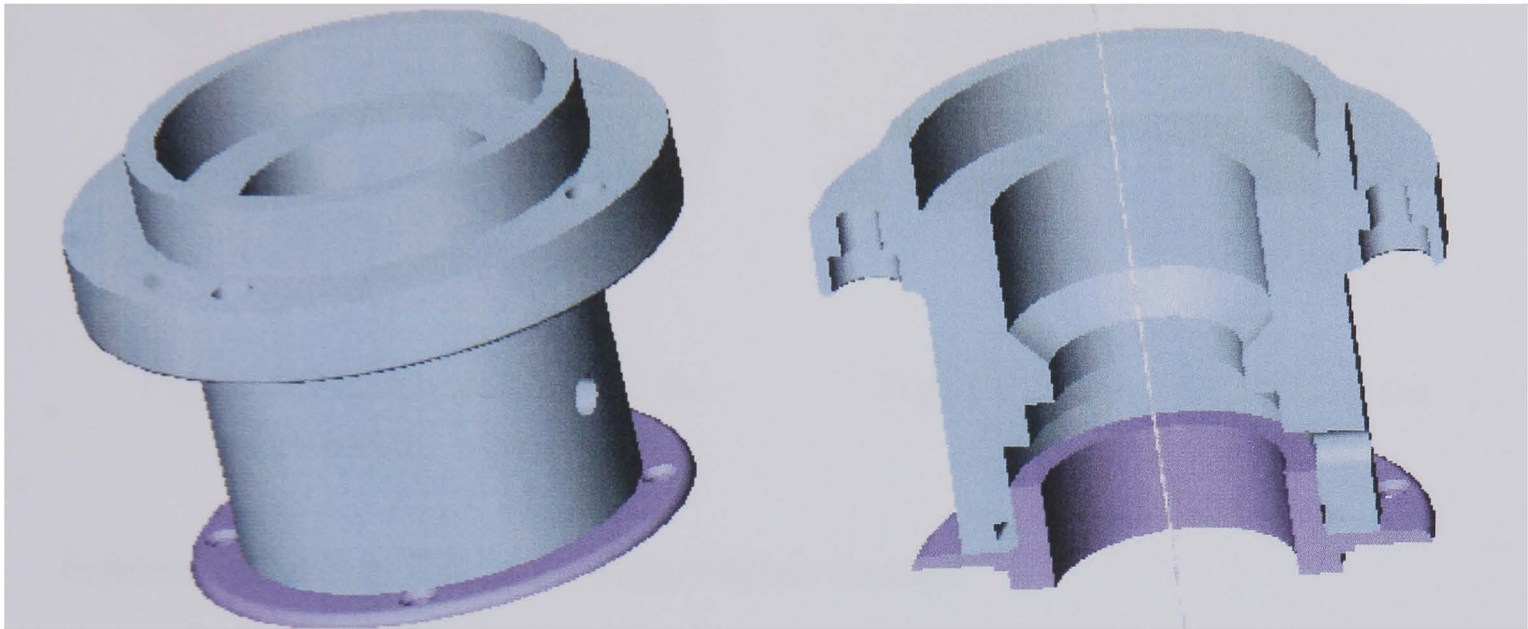


Figure 2.1 Isometric View of the Pressurised Chamber

Figure 2.2 Cross-sectional View of the Pressurised Chamber

Cooling Fin Design – Alternative Design

In this design fins are generated on the circumferential area of the chamber. These fins help increase the contact area. This design also has cooling performed by an external source i.e. blowing cool air on the exposed surface of the chamber. The only design difference between this and the external cooling design described above is the increased surface area. The assembly statistics² are shown in Appendix 2.

The pictorial and the cross-sectional views are shown in Fig. 2.3 and Fig. 2.4 respectively. This design could not qualify the selection criteria due to machining complexity and product cost.

¹ Components of suppressed sub-assemblies are excluded from these statistics.

² Components of suppressed sub-assemblies are excluded from these statistics.

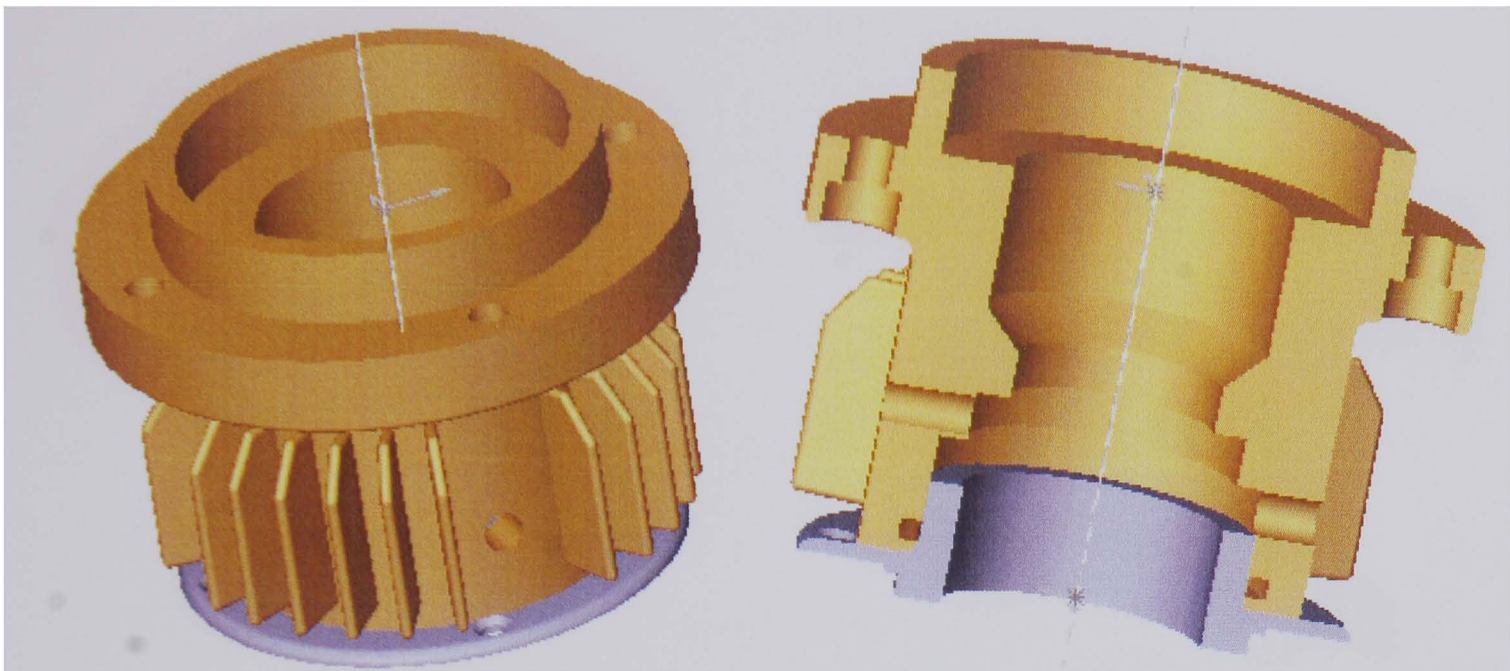


Figure 2.3 Isometric View of the Pressurised Chamber

Figure 2.4 Isometric View of the Pressurised Chamber

Internal Cooling Design – Alternative Design

This design is based on the concept of a water cooling jacket as in the automotive IC (internal combustion) engines. The water jacket is designed for the purpose of cooling the inside atmosphere by means of running coolant. An entry and exit port helps the coolant flow in and out from the pressurised chamber body. The assembly statistics³ are provided in Appendix 2.

The pictorial and the cross-sectional views are shown in Fig. 2.5 and Fig. 2.6 respectively. Again the machining complexity and cost were the factors for abandoning this design.

Thermal analysis of the pressurised chamber

Design and finite element stress analysis for the pressurised chamber are presented (Khan et al. 2004).

In the FEA the process needs defining constraints, loads, materials and running analyses. The transition to performing thermal analyses is straight forward as there is a direct correlation between stress and thermal analysis.

³ Components of suppressed sub-assemblies are excluded from these statistics.

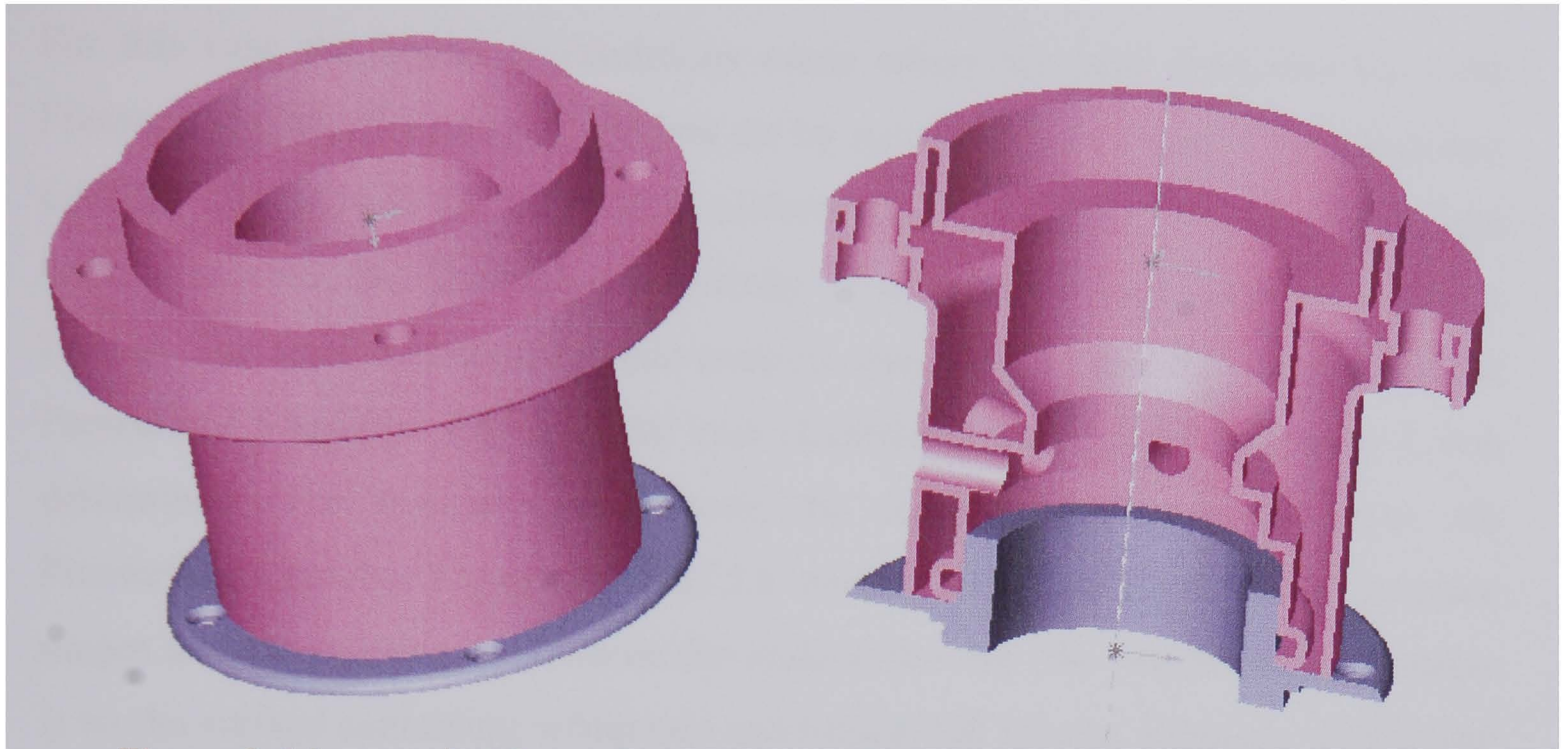


Figure 2.5 Isometric View of the Pressurised Chamber

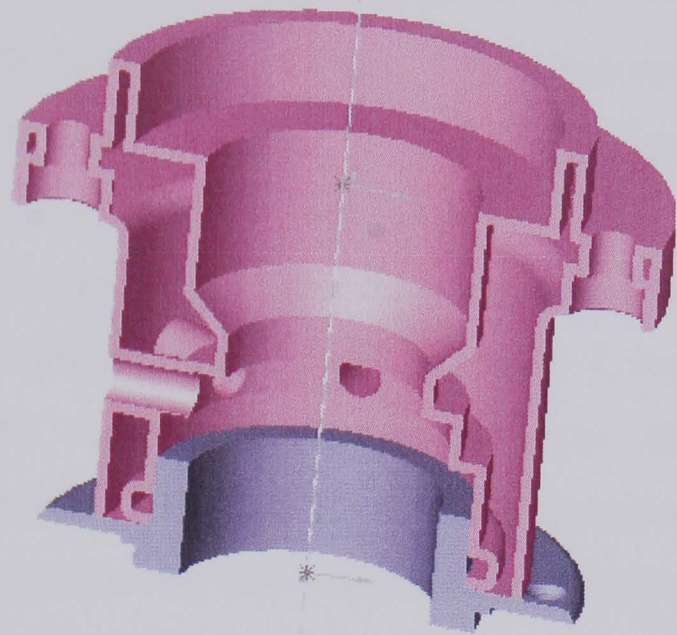


Figure 2.6 Cross-sectional View of the Pressurised Chamber

In a stress analysis loads (N) are applied to the model, in thermal analysis the equivalent is a thermal load measured in Watts. In stress analysis boundary conditions are applied (constraints) which restrict the movement of the model, in thermal analysis the equivalent boundary constraints are either temperature °C or convection coefficient W/m^2K . Ansys Workbench utility provides plugin for Solidworks and ProE. The CAD model is transported into Workbench where thermal gradients are applied to calculate heat distribution for thermal analysis.

The first step was to define the thermal loads on the Pressurised Chamber. Thermal loads are heat sources applied to the model. In the case of the Pressurised Chamber the heat sources was the frictional heat generated due to rolling contact, which applied heat to the internal surface of the Pressurised Chamber below the shaft seal. The internal surface was chosen a heat load Q of 25×10^5 mW for design temperature of 40 °C was applied. The maximum operating temperature conditions of the pressurised chamber is 30°C. The internal bulk temperature is taken by a thermocouple that is mounted inside the chamber. Inside operating temperatures of the chamber can also be recorded by measuring the corresponding pressure of the liquid refrigerant. The maximum operating pressure of the Pressurised Chamber for liquid R600a refrigerant is 3 bar (maximum).

For this case the boundary conditions occur where the heat dissipates from the Pressurised Chamber into the ambient air by means of convection. The convection option is chosen with all the external surfaces selected and a convection coefficient 0.03 is entered, the thermal conductivity is 115-119 W/m.K (aluminium alloy LM13). The final definition for this analysis was to determine the material for the Pressurised Chamber. The material cast aluminium alloy LM13 Appendix 2 was determined. The resultant plot shows the temperature distribution over the Pressurised Chamber Figures 2.7 and 2.8 where the colours show the temperature ranges and the values are shown on the scale to the left. The maximum temperature is on the surface containing refrigerant and rolling ball bearing elements. The lowest 30° C temperature is near the shaft seal and the upper part was heated 36-38° C by conduction.

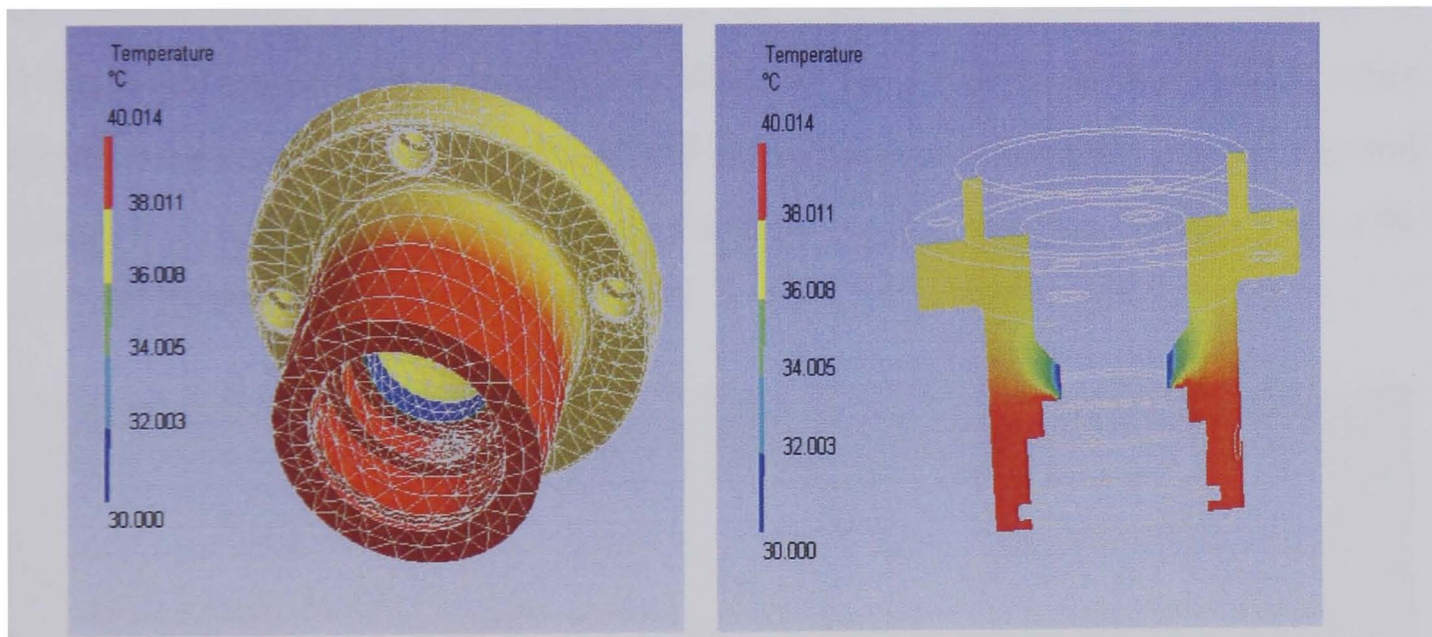


Figure 2.7 FEA temperature model for cooling purpose

Figure 2.8 A section diagram of temperature model

2.1.3. Pressurised Chamber Testing

The arrangement of the trial rig for pressurised chamber before commissioning is shown in the Figure 2.9. The rig was constructed for the pressurised chamber to be fitted and pressurised with air and then refrigerant. The idea was to check for any pressure leaking and provide facility of viewing liquid refrigerant through a

transparent window. The details of charging air and HC/HFC refrigerant and the variation in the temperature and pressure are recorded in Appendix A2.3.

The pressurised chamber is fitted with two clamps/plates, one on the top to simulate vertical column of the Rotary Tribometer and one at the bottom of the chamber to simulate the lower cup housing of the Rotary Tribometer see Figure 2.9. The top clamp is a transparent polycarbonate⁴ plate to provide facility to view the state of the gaseous vapour through it. The bottom clamp consists of steel plate only. Both these clamps are bolted together by eight studs. The circuit has a charging line fitted with refrigerant supply. As well as a shut-off valve and a pressure gauge. There is also a vacuum / discharge line which can be connected to a vacuum pump when the system needs to be vacuumed. The same line may be connected to a recovery cylinder when the refrigerant is discharged.

A compound gauge reads the pressure of the system. The pressurised chamber is also fitted with a temperature gauge to read the temperature of the system. After successful commissioning the pressurised chamber was removed from this rig and coupled with Rotary Tribometer for simulating rolling contact fatigue tests with liquid refrigerant lubrication section 2.1.5.

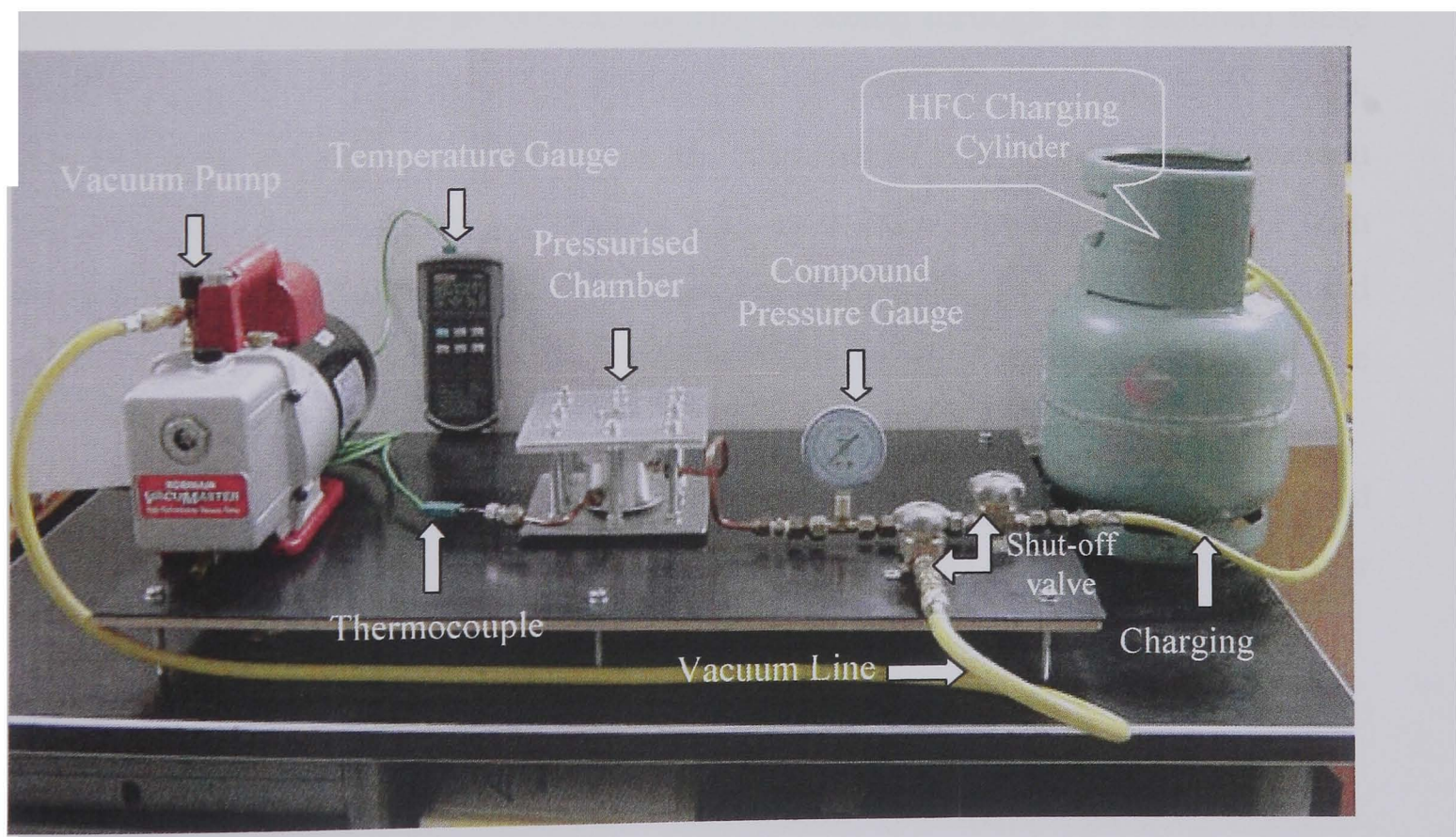


Figure 2.9 Trial Test Rig

Top and Bottom Plates

Prior to commissioning a trail rig was constructed to evaluate functions of various parts of the rig Figure 2.9. The Pressurised Chamber was provided with circular plates on both top and bottom, both plates provide sealing for the chamber and simulate modified test rig. The lower plate was steel. The upper plate was polycarbonate. This is because transparent polycarbonate plate provides facility to see through the chamber.

The Pressurised Chamber average wall thickness is 19 mm while the average radius is 30 mm for the upper part. For the pressurised Chamber $\frac{r}{t} = 1.58$, therefore, can

be classified as thick walled. Equations for design of thin-walled pressure vessels can be used to design thick-walled pressure vessels. However, several guidelines need to be considered. First, include generous safety factors in the design to allow for the geometrical differences at the joint of the end-plate and the cylinder, (in this case upper and lower plates were used for test rigs on top and at bottom of the Pressurised Chamber for sealing purpose and to simulate the test rig before commissioning, these plates were clamped and the upper plate was a transparent polycarbonate plate so as to provide facility of seeing through the chamber) these differences can cause maximum stresses, many times the nominal hoop stress, depending on the plate-to-wall joint design. Also, the ratio of wall thickness to mean radius should not exceed approximately 1:10 to avoid a triaxial stress state – with stresses acting in three directions – which can reduce the ductility of plastics and most other materials. And, of course, the modulus must be selected carefully. The ratio of wall thickness to mean radius of the Pressurised Chamber is 1.9:6.

From design view point this is safe, however, for many designs to support a load perpendicular to the plate. The illustrations give stress and deflection equations for several common plate configurations.

⁴ Appendix 2, A2.2. Mechanical properties of polycarbonate

Again, these equations are valid when working with a homogeneous, isotropic material, and when deflection is less than about one-half of the plate thickness.

A flat plate of uniform thickness is used on both sides of the Pressurised Chamber. The upper plate is transparent 515-1000 thermoplastic having the following material data shown in Table 2.2. The cylindrical pressurised vessel is fabricated by clamping two plates together. The thickness of plates on both sides is calculated for a maximum 5 bar pressure acting inside the pressurised chamber. The minimum required thickness of the plates on both sides is calculated to ensure that the operating stress is no more than 50% of the material's yield strength.

Table 2.2 Engineering Properties of 515-1000 Thermoplastic⁵

Class	Thermoplastic
Family	Polycarbonate
Chem.type	PC
Supplier	Comalloy International
Note	Polycarbonate with high strength/modulus
Features	High strength; High modulus
Uses	High strength, High modulus applications
Properties ⁶	EF 3.24 GPa; E 3.23 GPa; TSY 51.7 MPa; FYS 115.8 MPa

The calculations were performed on the polycarbonate that computes the stresses and displacement of a clamped circular plate under a uniformly distributed load. The maximum pressure for design was 5 bar. The values of the relating parameters are shown next page. Figure 2.10 shows a clamped circular plate with radius r_0 subjected to uniform pressure. The plate deflection, which is directly proportional to the pressure p , is thus expressed by

$$w = \frac{pr_0^4}{64D} \left[\frac{r^4}{r_0^4} - 2 \frac{3+\nu}{1+\nu} \frac{r^2}{r_0^2} + \frac{5+\nu}{1+\nu} \right] \quad (2.1)$$

Where

⁵ Source of data 'Engineering Plastics & Composites 2nd Edition'

⁶ See Appendix 2, Table A2.1 for Property abbreviations, Table A2.2 for Mechanical properties of polycarbonate

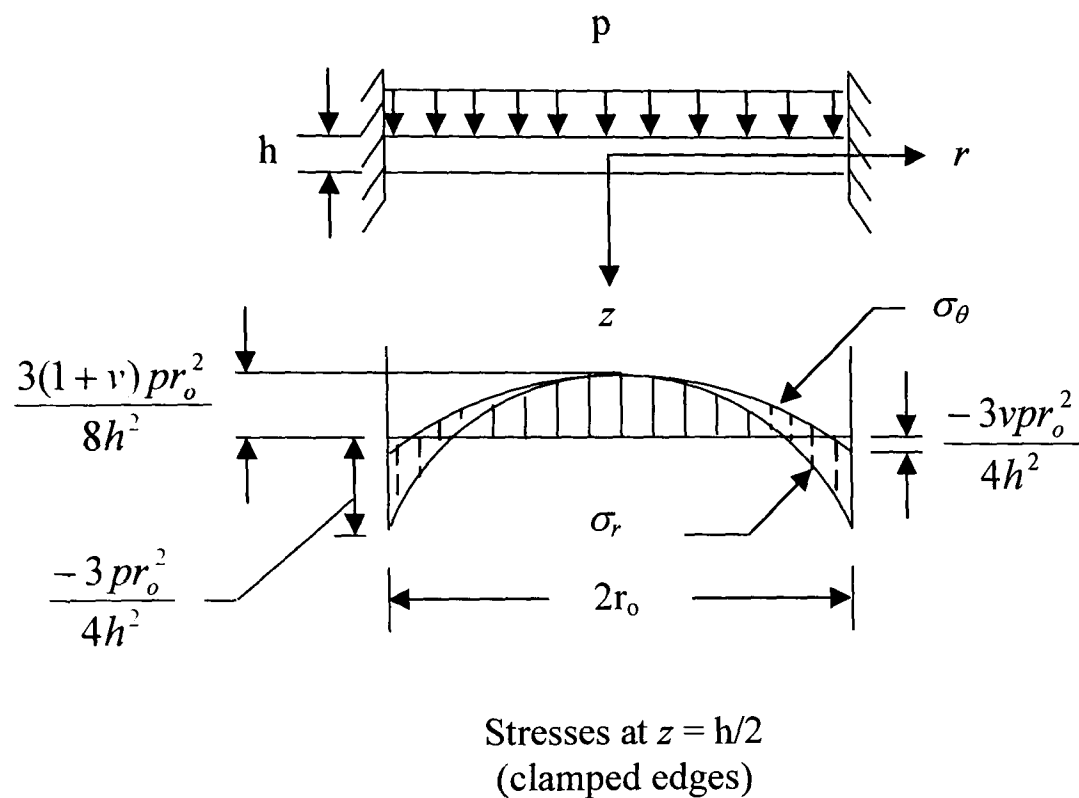


Figure 2.10 Clamped circular plate subjected to uniform surface pressure

- w deflection
 p uniform load
 r_o radius of the plate
 D is the bending/flexural rigidity of the plate defined as follows

$$D = \frac{Eh^3}{12(1-\nu^2)}$$

- E Young's modulus
 h thickness of the plate
 ν Poisson's ratio

(r, θ, z) polar cylindrical coordinate

The maximum deflection occurs at the centre of the plate and is given by

$$w_{\max} = \frac{5 + \nu}{1 + \nu} \frac{pr_o^4}{64D} \quad (2.2)$$

Hence from equations (2.1) and (2.2), together with the boundary conditions,

$$\text{At } r = r_o : w = 0 \text{ and } dw/dr = 0$$

The deflection of the plate is expressed by

$$w = \frac{p}{64D} (r_o^2 - r^2)^2 \quad (2.3)$$

$$w(r) = \frac{pr_o^4}{64D} \left[1 - \left(\frac{r}{r_o} \right)^2 \right]^2 \quad (2.4)$$

again, the deflection is directly proportional to the applied pressure p . The maximum displacement occurs at the centre of the plate as

$$w_{\max} = w(r = 0) = \frac{pr_o^4}{64D} \quad (2.5)$$

for upper polycarbonate plate the values are as follows:

Uniform load $p = 5$ bar

Radius $r_o = 0.29$ m

Thickness $h = 0.06$ m

Young's modulus $E = 3.23$ GPa

Poisson's ratio $\nu = 0.3$

Unit of displacement $w =$ m

$$w_{\max} = 0.000865 \text{ m} \approx 8.65 \times 10^{-4} \text{ m}$$

The Lower steel plate was Low Alloy Steel, 0.40C 300M, Quenched & Tempered with Modulus of Elasticity 200 – 210.3 GPa. Again the maximum design load was 5 bar, other parameter are given below.

Uniform load $p = 5$ bar

Radius $r_o = 0.22$ m

Thickness $h = 0.02$ m

Young's modulus $E = 200$ GPa

Poisson's ratio $\nu = 0.3$

Unit of displacement $w =$ m

$$w_{\max} = 0.000125 \text{ m} \approx 1.25 \times 10^{-4} \text{ m}$$

Both plates are safe to use with the defined thickness. If high pressure is required simply the thickness of the plates could be increased. However the actual pressure inside the Pressurised Chamber does not exceed 3 bar.

w_{\max} in Equation (2.5) is substantially smaller than w_{\max} for a simply supported plate (the ratio being $1/4$ for $\nu = 1/3$).

The distribution of the bending moments (M_r , M_θ) and, hence the stresses are determined using Equation (2.3) into Equation (2.6).

$$M_r = -D \left(\frac{d^2 w}{dr^2} + \frac{\nu}{r} \frac{dw}{dr} \right) \quad (2.6a)$$

$$M_\theta = -D \left(\frac{1}{r} \frac{dw}{dr} + \nu \frac{d^2 w}{dr^2} \right) \quad (2.6b)$$

$$Q_r = D \frac{d}{dr} \left(\frac{d^2 w}{dr^2} + \frac{1}{r} \frac{dw}{dr} \right) \quad (2.6c)$$

Q shear force

The stresses are then given by Equations (2.7)

$$\sigma_r = \frac{M_r z}{h^3 / 12} \quad (2.7a)$$

$$\sigma_\theta = \frac{M_\theta z}{h^3 / 12} \quad (2.7b)$$

as

$$\sigma_r = \frac{3pz}{4h^3} \left[(1+\nu)r_o^2 - (3+\nu)r^2 \right] \quad (2.8a)$$

$$\sigma_\theta = \frac{3pz}{4h^3} \left[(1+\nu)r_o^2 - (1+3\nu)r^2 \right] \quad (2.8b)$$

The maximum stresses are given by

$$(\sigma_r)_{\max} = \frac{3pr_o^2}{4h^2} \quad (2.9a)$$

occurring as the edge $r = r_o$ at $z = -h/2$

$$(\sigma_r)_{\max} (\text{poly}) = 8.76 \text{ MPa (poly - polycarbonate)}$$

$$(\sigma_r)_{\max} (\text{steel}) = 45.38 \text{ MPa}$$

$$(\sigma_\theta)_{\max} = \frac{3(1+\nu)}{8} \frac{pr_o^2}{h^2} \quad (2.9b)$$

occurring as the centre $r = 0$ at $z = -h/2$

$$(\sigma_\theta)_{\max} (\text{poly}) = 5.69 \text{ MPa}$$

$$(\sigma_\theta)_{\max} (\text{steel}) = 29.49 \text{ MPa}$$

The stress distributions are shown in Figure 2.10 for a clamped plate. Note that the solution is based on the assumption that its edges are fully constraint against any linear or angular displacements.

In order to assess the magnitude of plate deflection, consider the extreme case when pressure p is increased such that yielding is initiated. According to the maximum shear stress theory, this occurs at the edges when $(\sigma_r)_{\max} = Y$, where Y is the yield strength of the plate material, so that

$$Y = \frac{3}{4} \frac{pr_o^2}{h^2} \quad (2.10)$$

hence

$$p = \frac{4Yh^2}{3r_o^2} \quad (2.11)$$

at this value of p , the central deflection given by Equation (2.5) is

$$(w_{\max})_{\text{yielding}} = \frac{Yh^2r_o^2}{48D} = \frac{1-\nu^2}{4} \left(\frac{Y}{E} \right) \left(\frac{r_o}{h} \right) r_o \quad (2.12)$$

$$(w_{\max})_{\text{yielding}} \text{ poly} = 5.1 \times 10^{-5} \text{ m}$$

$$(w_{\max})_{\text{yielding}} \text{ steel} = 2.8 \times 10^{-5} \text{ m}$$

For plates of $r_o/h \approx 10$, the maximum deflection is less than 5% of the plate thickness, a result justifying use of this bending theory for thin (and even moderately thick plates) without much error. For thicker plates of all round clamped edge, deflection given by Equations 2.3 and 2.5 is found to be less than that in practice.

This is due to the fact that the condition of a clamped edge cannot be fulfilled as well as the neglect of shear stress deformation in developing Equation 2.3.

High Speed Microprocessor Controlled Rotary Tribometer

The TE92 Microprocessor Controlled Rotary Tribometer offers facilities to run high and low load tests over a wide range of speeds, coupled with the latest control and instrumentation. The body of the machine is of cylindrical steel fabrication inside which is located the test chamber, the loading piston, the drive spindle and the associated bearings. The bearings are lubricated for life with greases.

The drive motor is mounted outside the cylinder on a tensioning plate. For high-speed tests the motor is directly connected to the drive spindle by means of a smooth drive belt. For low speed tests, an electromagnetic clutch is mounted directly on the drive spindle and power transmitted from the motor by means of a toothed drive belt. This clutch arrangement is designed to give an identical performance to that achieved with an A.C. motor and thus allow low speed tests to be run with the correct start-up characteristics.

The lower race assembly is carried on the load piston. End load is applied to the piston by means of a loading arm mounted at the lower end of the cylindrical body. For high-speed tests the lower test assembly, consisting of the high speed rolling contact race, the oil bath and heater block, are mounted directly on the load piston. For low speed test, the assembly, consisting of the ball cup, oil bath, torque arm and heater block, are mounted on a thrust bearing located on top of the load piston thus allowing rotation of the test assembly to allow torque measurement.

The equipment consists of a bench-mounting test and control interface. The user's PC is connected via the serial to the micro-controller interface. The Plint COMPEND control software is then installed on the PC.

The core of the machine is two rigid vertical columns, which ensures accurate location of drive spindle with respect to the normal loading axis. The test adapters are mounted on a cross beam which is guided by linear bearings on the columns and

loaded by a pneumatic actuator. The actuator assembly included an in-line force transducer measurement for direct feedback control of load.

The test adapters are mounted on a thrust bearing and rotational movement is restricted by the strain gauge transducer, thus giving direct friction torque readout. The adapters also include integral electrically heated supports for tests up to 200°C. The COMPEND software is designed for easy user access to all test set-up parameters through menu-led utilities and a control panel generated on a monitor. The software includes an 8-channel chart recorder simulation for data output to a printer. At the end of the test the data may be manipulated for calculation or graphical presentation on the integrated spreadsheet software programme (Borland Quattro Pro).

Tests are defined by a series of steps, each step containing load, temperature and speed set-points, data recording and alarm level information. Set-points may be adjusted by step change or ramp. The test sequence is followed unless interrupted by the operator or an alarm. The Figure 2.11 shows the TE92 Microprocessor Controlled Rotary Tribometer.

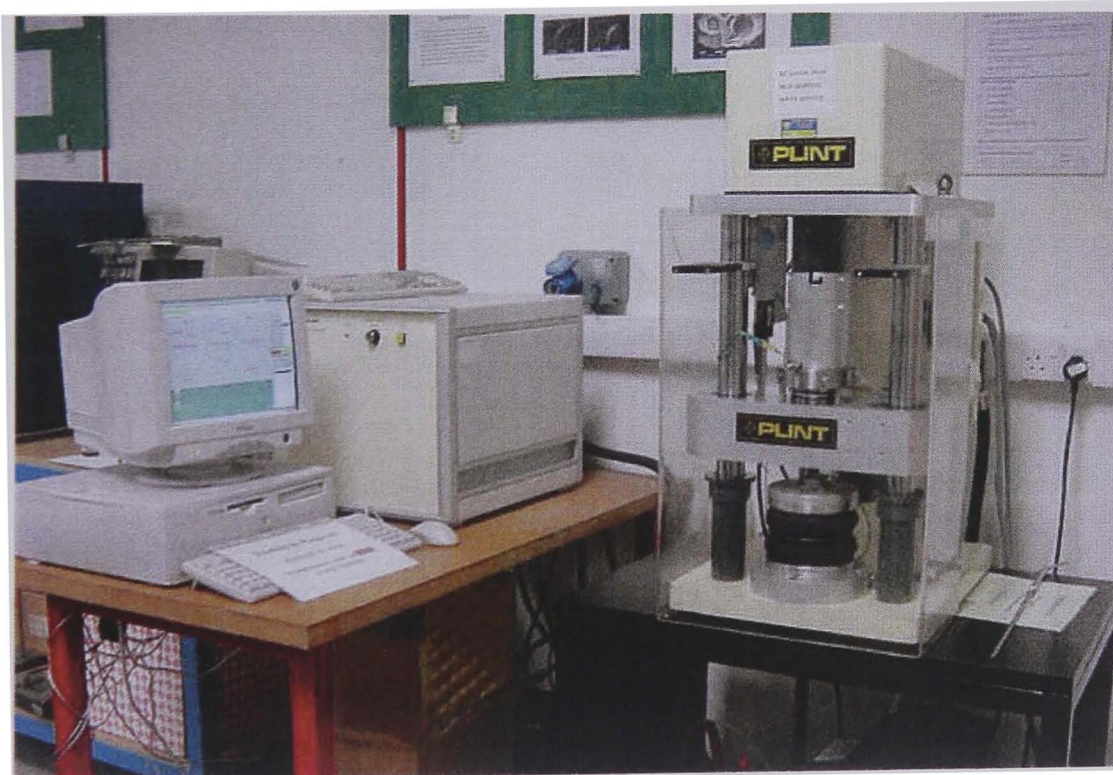


Figure 2.11 TE92 Microprocessor Controlled Rotary Tribometer

2.1.4. Seals

Shaft Seals

At first glance, there are almost as many seal designs as there are applications. In practice there are only a few principles to apply to any application design and thereafter the constraints of material choice, production technique and acceptable cost designate a suitable seal. Refinements to various aspects of seal geometry, material properties and housing designs can however have a significant effect on the performance and capability of the seal. When selecting a seal the following should be given consideration before final selection is made.

- Environmental Serviceability
- Simple Installation
- Operational Reliability
- Tolerance to the sealing media
- Frictional requirements
- Ability to function within a temperature range
- Good sealing at low and high pressures
- Resistance to extrusion between mating parts

Consideration and evaluation of these demands within the seals operating conditions is important as are the influencing factors of pressure, temperature, speed and surface finish.

Shaft seals also known as oil seals, are ideal for excluding dirt, dust, water or any other contaminant whilst retaining lubricant in rotary shaft equipment. They are generally used as a means of protecting the bearings of rotating shafts. These seals are:

- replaceable without damage to the housing bore
- do not need for circlips, sealants or retaining plate

However, they are not suitable for high-pressure unless positively retained.

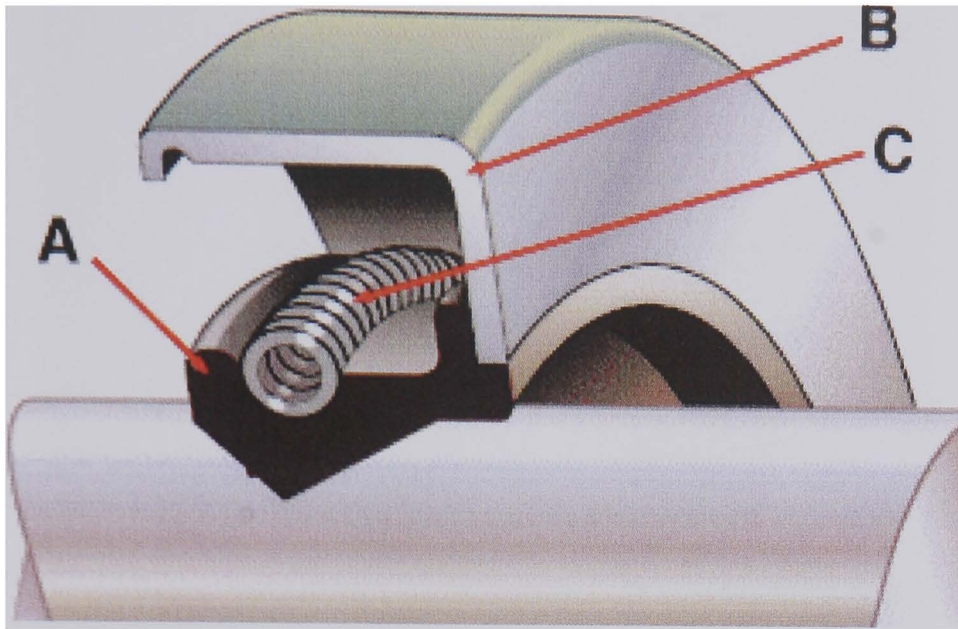


Figure 2.12 Profile of a Typical Shaft Seal

A dynamic radial seal creates a barrier between surfaces in relative motion. One is usually stationary while the other rotates. This three-quarter view of a cutaway seal Figure 2.12 shows the most common components found in a shaft seal.

- A. The flexible material component of the seal which produces the lip. In this design there is only one lip, the primary sealing lip.
- B. The outer shell of the seal holds the seal in place.
- C. The garter spring (found in most seal designs) is a coiled wire spring that provides a controlled radial load over time.

A spring-energised lip seal is shown in Figure A2.2, Appendix 2. During this research customised manufactured shaft seals were used shown in Figures 2.13 and 2.14.



Figure 2.13 Shaft seal used for the Pressurised Chamber outer shell view



Figure 2.14 Shaft seal used for the Pressurised Chamber lip view

The technical specifications for the shaft seal are provided in Table 2.3. Radial contact pressure of radial lip seals with PTFE lips, produces a sealing action on the shaft. The basic design of the seal consists of an outer PTFE lip, secondary elastomer seal and metal retaining ring. The metal case and seal lip are sealed by axial pre-tensioning of the elastomer static seal and in special cases by a solid sealant which is temperature and chemically resistant. A typical shaft seal is shown

in Figure A2.3, and a cross-section of the same is shown in figure A2.4, Appendix 2. More details on PTFE Rotary Shaft Seals are provided in Appendix 2 and Figure A2.5.

Table 2.3 Technical Specification for Shaft Seals / Oil Seals⁷

Pressure Rating	10 bar max
Shaft speed	5000 rev/min
Material	Nitrile
Shaft tolerance	H11
Housing tolerance	H8

'O' Ring

'O' rings were used between mating surfaces lower and upper parts of Pressurised Chamber and between lower part of Pressurised Chamber and steel cup housing see Figure 2.21. A standard 'O' ring geometry is shown in Figure 2.15. The standard metric 'O' rings BS 4518 are specified by the internal diameter ID, with a tolerance of $\pm 0.15 - 0.3$ mm and cross-section 'W', with a tolerance of $\pm 0.08 - 0.1$ mm. The housing details for dynamic sealing are shown in Figure 2.16. The 'O' rings may be used with or without back-up rings. In the event of using a back-up seal the pressure range is increased. The selection of 'O' ring depends on the gland depth 'T' that includes radial clearance 'E' where applied see Figure 2.17. Housing details for a static seal are shown in Figure 2.18. For static sealing the groove depth 'H' and groove width 'K' are taken into account. For pressure P1, Dia. D1 should be tolerated to fit the 'O' ring ID. For pressure P2, Dia D2 should be tolerated to fit the 'O' ring OD (outer diameter). Housing details are given in Figure 2.18 for static sealing. In order to choose a cross-section 'W' for the 'O' ring the groove depth 'H' and groove width 'K' must be defined.

⁷ Manufacturer's specs as requested

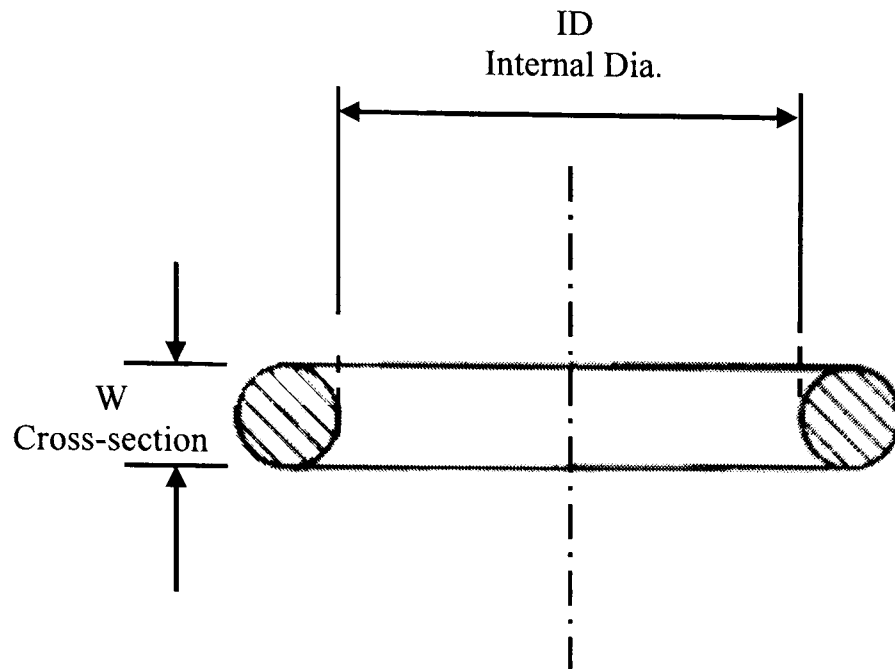


Figure 2.15 Standard 'O' Ring

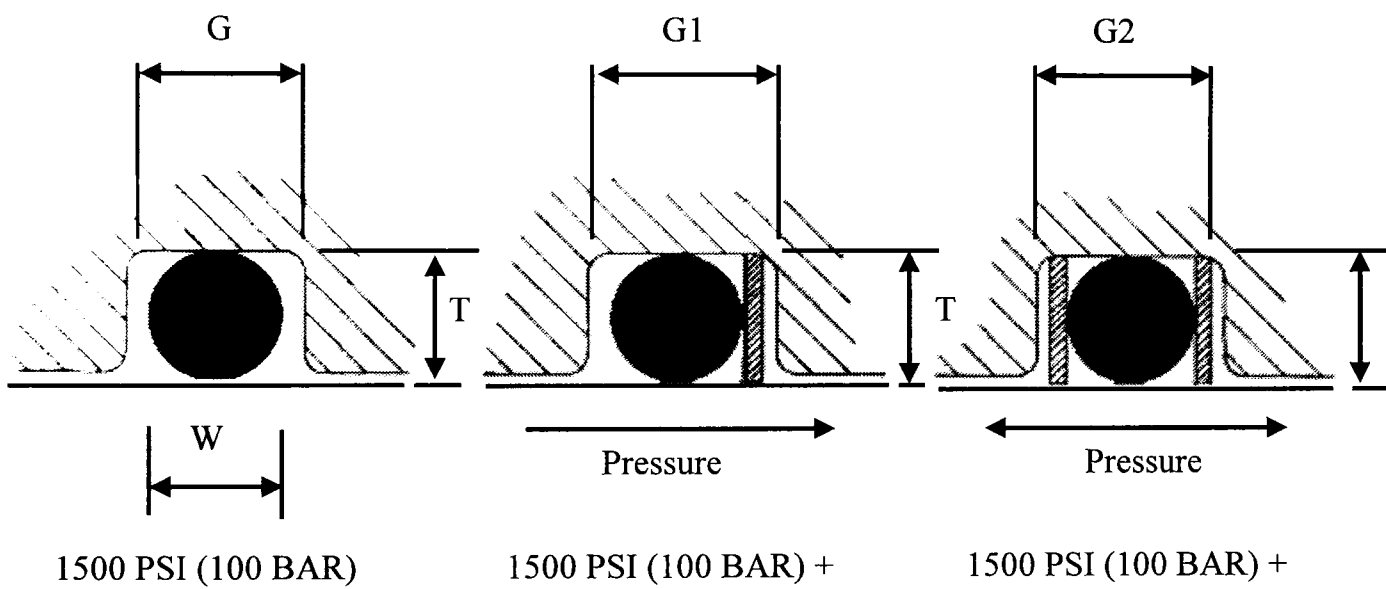


Figure 2.16 Housing Details for Dynamic Sealing

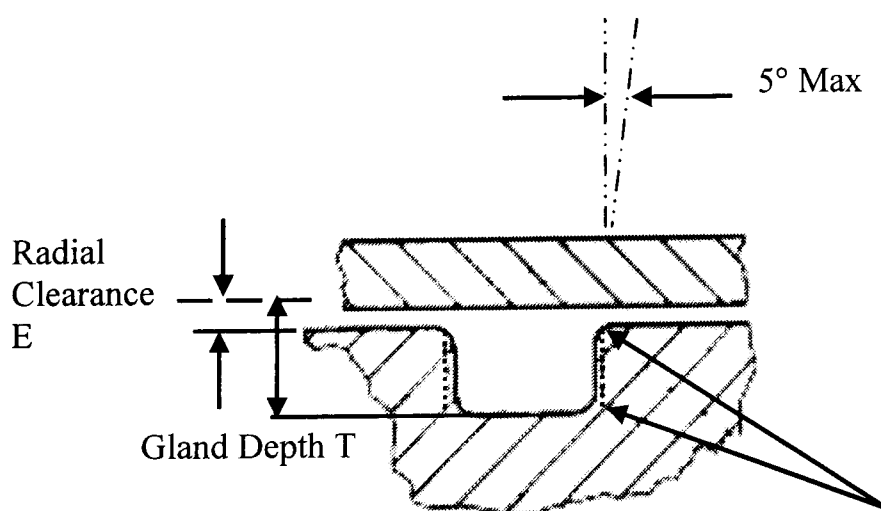


Figure 2.17 Radial Clearance for 'O' Ring

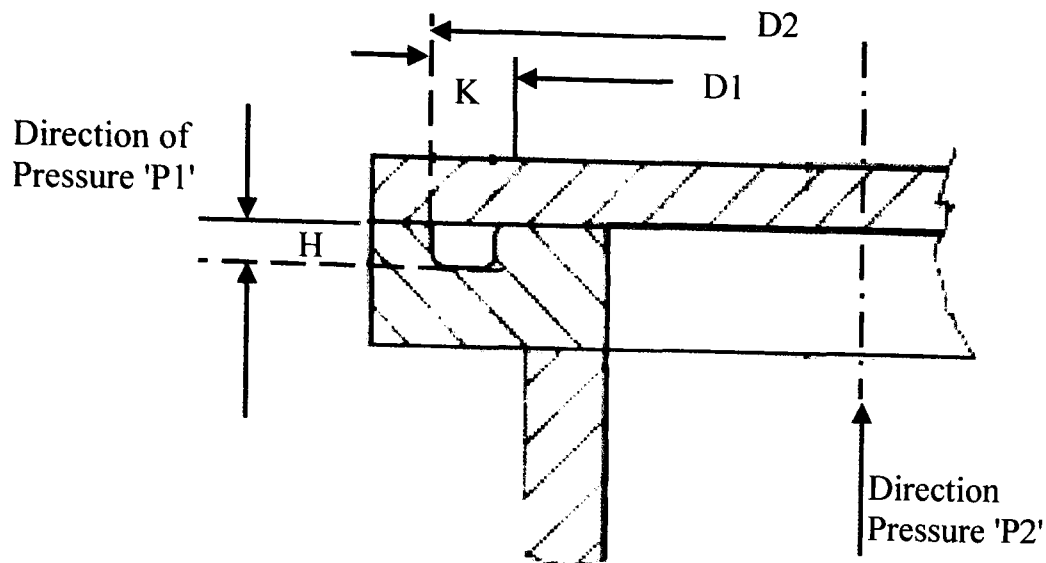


Figure 2.18 Housing Details for the Static Sealing

The optimum values of surface roughness for various seal types are summarised below in the Tables 2.4, 2.5 and 2.6. More details on 'O' rings are provided in Appendix 2.

Table 2.4 PTFE Seals optimum Ra⁸

Seal type	Ra (0.1 - 0.25 μm)		Rsk	
	PTFE	> 0.3 μm	< 0.1 μm	-1
Effect	Depend upon Rsk (skewness)	Friction and wear increases	Higher leakage, little wear	Higher friction and wear

Table 2.5 Rubber seals dynamic and static optimum Ra (RS online 2005)

Seal type	Ra (0.1 - 0.25 μm)			
	Dynamic			Static
Rubber seal	Up to 0.4 μm	> 0.4 μm	< 0.05 μm	< 0.8 μm
Effect	Slight increase in wear	Wear leakage and friction increases	High friction and wear	-

⁸ RS Online 2005

Table 2.6 Polyurethane seals optimum Ra (RS online 2005)

Seal type	Ra ($< 0.25 \mu\text{m}$)	Axial scores
Polyurethane	$> 0.3 \mu\text{m}$	$< 0.05 \mu\text{m}$
Effect	Expect high wear and leakage	Do not affect seal performance

2.1.5. Test rig modifications

It was necessary to simulate the actual operating condition for rolling contact hybrid ceramic-steel ball-bearings with refrigerant as lubrication. After the design, manufacture and successful commissioning of the pressurised chamber it was coupled to the Rotary Tribometer. With a purpose-built modified test rig rolling contact hybrid ceramic-steel tests can be performed with liquid refrigerant as lubrication without generating severe frictional heat. The pressurised chamber offers controlled conditions of temperature(s) and pressure(s) making it possible to obtain a saturated liquid state of the refrigerant as fluid at operating conditions. Figure 2.19 shows the modified test rig with cooling system, vacuum system and charging system. Figure 2.20 shows a close up of the test rig coupled with pressurised chamber.

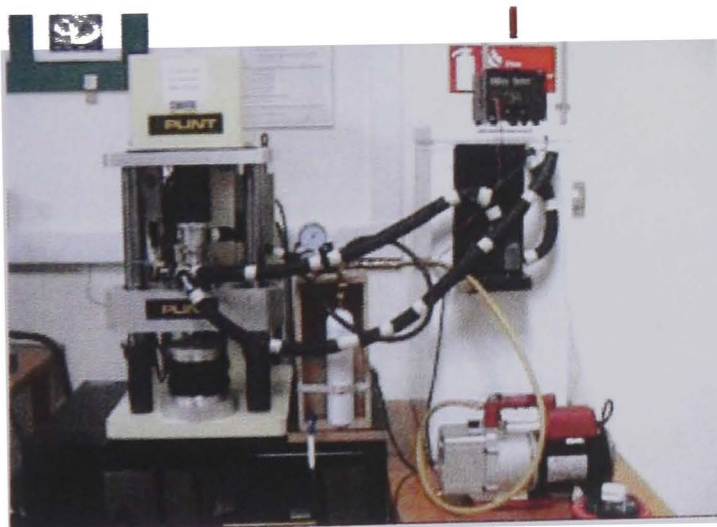


Figure 2.19 Modified Test rig coupled with pressurised chamber



Figure 2.20 Close up Modified Test rig coupled with pressurised chamber

Figure 2.21 is a schematic diagram of the modified test rig. The pressurised chamber is shown as added onto the Rotary Tribometer. The lower part of the pressurised

chamber is mounted on the steel cup and provided with an 'O' ring at the base. The seal prevents any leakage of the refrigerant from the system through the contact faces of the lower part of the chamber and the steel cup. The upper chamber is mounted on to the Rotary Tribometer column and slides onto the lower part. Upper part has an 'O' ring which prevents leakage through the mating surfaces of upper and lower chamber parts.

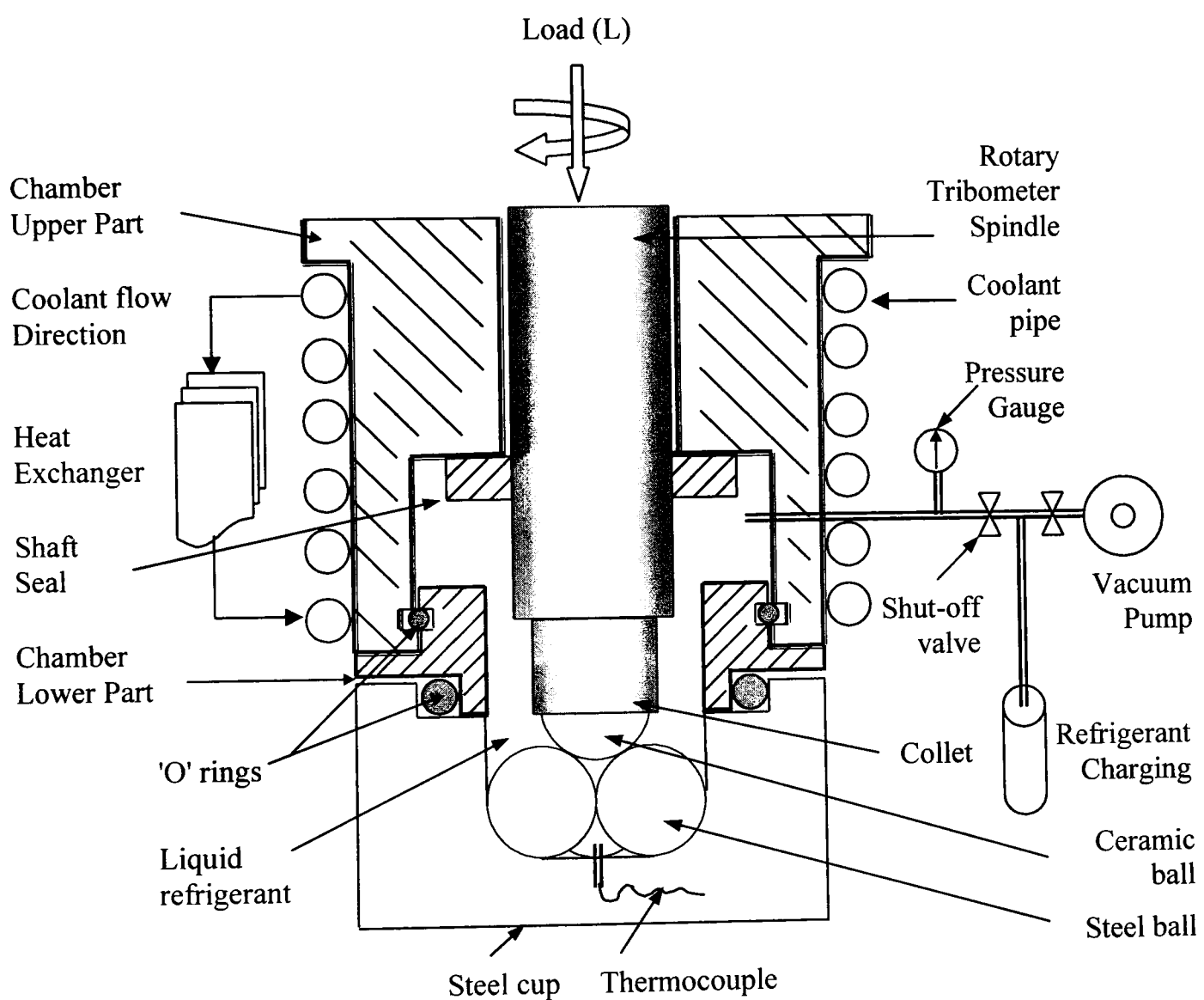


Figure 2.21 Schematic of Rig for the High Speed Rotary Tribometer

The steel cup has a thermocouple and is used to monitor bulk temperature of the system. The test rig has refrigerant charging and a vacuum system both separated by shut-off valves. The charging line has a compound pressure gauge to monitor the pressure. The vacuum line is supported by a vacuum pump and is used to vacuum

the chamber prior to refrigerant charging. A shaft seal is mounted on the spindle of the Rotary Tribometer and prevents refrigerant leakage through the matting surfaces of spindle and upper chamber. Coolant is circulated on the surface of the pressurised chamber by a peristaltic pump for cooling purposes.

2.2. Hydrocarbon Refrigerants

With the introduction of the revised EU Ozone Depleting Substances Regulation in October 2000 and the introduction of a Climate Change Policy by the UK Government in November 2000, it is considered likely that more refrigeration system designers and users will be turning to alternative refrigerants such as hydrocarbons. The increased application of this technology will bring with it many technical and safety issues. People working in this industry have relatively little practical or theoretical knowledge about hydrocarbon refrigerants. It is therefore in the interests of the industry to make as much technical and safety information as possible as available. Much of the knowledge and expertise already exists, and ACRIB (Air Conditioning and Refrigeration Industry Board) has brought this together into a comprehensive guide by reference to the range of detailed documentation available, as well as some of the basic information necessary for engineers working with refrigeration systems using hydrocarbons ACRIB (2001).

The new generation of environmentally acceptable hydrocarbon products is gaining widespread acceptance for many applications, both commercial and domestic. They do not pose any threat to the ozone layer and have a very low impact on global warming. The UK Government's Climate Change Policy has focused many researchers' minds on global warming and its causes and, while the refrigeration and air-conditioning industry is not a major contributor, hydrocarbons offer us the opportunity to reduce this contribution.

Hydrocarbons are, in general, very good refrigerants and are becoming more widely used in many applications. They have advantages over halo-carbon type refrigerants:

- Zero ozone depletion potential
- Very low global warming potential

- Good performance characteristics

R600a is pure iso-butane, and is primarily for new domestic type equipment. It operates at significantly lower pressures than R12 or R134a, so its use requires modifications to components. It is not designed to be used in existing R12 or R134a systems.

The important properties of R600a as a refrigerant are listed in Appendix 2, A2.5.

2.2.1. Refrigerant selection

Refrigerant selection is generally based on matching refrigerant vapour pressures to operating conditions, although this is not always the case. Refrigerants should also be selected so that they contribute to good system efficiency. With respect to blended refrigerants, these should only be selected when the effect of temperature glide and composition shift is not an issue. As a general guidance on refrigerant selection, Appendix 2, Table A2.6 provides indication as to the application ranges and equivalent fluorinated refrigerants where HCs could be employed.

When using hydrocarbon refrigerants it is essential to use refrigerant grade products only. Commercial grade hydrocarbons contain significant quantities of sulphur, water and other impurities and could contribute to oil degradation, shorten the compressor life and invalidate any warranties. Also, unlike commercial LPG, hydrocarbon refrigerants are not odourised. Another problem with commercial LPG is that the composition of any specific hydrocarbon can be variable thus drastically changing the properties of the refrigerant from cylinder to cylinder.

Refrigerant properties

Refrigerant properties are necessary to describe the operating characteristics of the refrigerant within a system. In particular, physical properties of refrigerants are useful for determining the applicability of a refrigerant under design operating conditions. Thermodynamic and transport properties are necessary for predicting system behaviour and performance of components. Basic properties are provided in Appendix 2, Table A2.7.

Lubricants

Hydrocarbon refrigerants possess full compatibility with nearly all lubricants commonly used within refrigeration systems. Good miscibility is maintained with most lubricants under all operating conditions. Due to the particularly good solubility with mineral oils, it may be necessary to use a lubricant with lower solubility or increased viscosity to compensate for possible thinning under situations where high solubility could occur.

Lubricants containing silicon or silicate (often used as anti-foaming additives) are not compatible with hydrocarbon refrigerants and should not be used. Appendix 2, Table A2.8 details the various lubricants and their compatibility characteristics.

Materials

Virtually all common elastomer and plastic refrigeration materials used as 'O' rings, valve seats, seals and gaskets are compatible with hydrocarbon refrigerants. These include Neoprene, Vitons, Nitrile rubbers, HNBR, PTFE and Nylon. Materials that are not compatible and should not be used in hydrocarbon refrigeration systems are EPDM, natural rubbers and silicon rubbers.

2.2.2. General Safety Issues

All hydrocarbon refrigerants are highly flammable but non-toxic. This gives them an "A3" classification according to BS EN378 Part 1. References should be made to this standard which details the requirements for the safe use of flammable refrigerants in commercial and industrial applications⁹.

Allowable Refrigerant Charge

The limiting factor associated with the use of hydrocarbon refrigerants is the refrigerant charge size, the occupancy category and the room size. The charge size requirements according to annex C of BS EN378 Part 1 are detailed in Appendix 2,

⁹ For more detailed information on these safety requirements refer to the Institute of Refrigeration Safety Code for A3 refrigerants.

Table A2.9 BS 4434 (1995), BS 5345 (1976), (1998) and BS EN 378 (2000). Systems with charge sizes of 0.15Kg or less can be installed in any size of room. Systems with charge size of more than 0.15kg room size should be such that a sudden loss of refrigerant shall not raise the mean concentration in the room above the practical limit (approximately 0.008kg/m^3).

The general approach to safe design of systems containing hydrocarbon refrigerants is detailed in Appendix 2, Figure A2.2. This flow chart provides general guidance to the appropriate measures associated with a specific refrigerant charge size and the locations where they are permitted.

Flammable Properties of Hydrocarbons

Appendix 2, Table A2.10 provides property data relevant to hydrocarbon refrigerants. These values are necessary in the design stage when determining maximum refrigerant charge, ventilation flow rates and maximum allowable temperatures of components.

Safety Standards and Codes of Practice

There are a number of codes and safety standards that are appropriate to the use of flammable refrigerants and related equipment. The selection of appropriate document is not always obvious and therefore the objective of this section is to provide a degree of clarity in this area. These standards and codes were set up in February 2001. Checks should be made to make sure that they are still current.

The following documents deal with subjects that are mainly related to pressure issues in commercial and industrial systems.

- BS 4434 (Withdrawn)
- BS EN 378
- Institute of Refrigeration Code of Practice for A3 Refrigerants

Requirements for small hermetic and domestic refrigeration systems are detailed as follows.

- BS EN 60335-2-24

- BS EN 60335-240
- BS EN 60335-2-89 (Draft at time of publication)

BS EN 60335-2-24 applies to systems that use up to 150g of flammable refrigerants. Regardless of the type of system, standards also exist for the refrigeration compressors:

- pr EN 12693 (Draft at time of publication)
- BS EN 60335-2-34

Where very small quantities of refrigerants are being employed, it is appropriate to consider standards that deal with hazardous areas. These standards are aimed directly at very large commercial and industrial type applications where flammable materials are used and provide a general approach to risk assessment and design of such environments.

- BS EN 1127-1

In particular, the most fundamental difference between systems using flammable refrigerants and non-flammable refrigerants is the use of suitable electrical equipment that will not pose a risk in the event of a release. Whilst, there are several methodologies to deal with such electrical apparatus, the following standards provide information on the general approach for using electrical equipment in any potentially flammable areas.

- IEC 60079-0
- BS EN 60079-10
- BS EN 60079-11
- BS EN 60079-14
- BS EN 60079-15

Finally, it is expected that the engineers involved in the design, construction and maintenance of refrigerating systems be competent. Competency in this context is defined in a draft standard.

- pr EN 13313 (draft at time of publication)

Design

Specific design requirements are generally applied to a system based on the refrigerant charge size and location. If manufacturer's data is not available, charge sizes can be approximated from internal system volumes and refrigerant densities based on design operating temperatures. Below is an explanation of the rules governing equipment design.

Refrigerant Charge

The equivalent hydrocarbon charge of a CFC or HCFC system will be approximately 40% to 50% of the mass. Under no circumstances should the system be overcharged.

Categories

The various requirements are denoted with the following categories, depending upon whether or not they apply to the corresponding categories. Occupancy types as defined in Appendix 2, Table A2.11 are as follows.

Occupancy Category A - Rooms, parts of buildings or buildings where people may sleep, people are restricted in their movements or an uncontrolled number of people are present or where any person has access without being personally acquainted with the general safety precautions (e.g. hospitals, prisons, courts, theatres, supermarkets, lecture halls, public transport termini, hotels, dwellings, restaurants).

Occupancy Category B - Rooms, buildings or parts of buildings where only a limited number of people may assemble, some being necessarily acquainted with the general safety precautions of the establishment (e.g. business or professional offices, small shops, small restaurants, laboratories, places for general manufacturing and where people work).

Occupancy Category C - Rooms, buildings or parts of buildings where only authorised persons have access, who are acquainted with general and special precautions of the establishment and where manufacturing, processing or storage of materials or products takes place.

Construction

Allowable Charge Size (All)

If the charge is more than 0.15kg, then a sudden loss of refrigerant should not raise the mean concentration in the room above the practical limit (0.008kg/m³). The room volume governs the total charge size. This can be determined by Equation 2.5.[Acib 2000].

$$M_r = 0.2(LFL)V_{room} \quad (2.13)$$

where

M_r = maximum allowable refrigerant charge per separate circuit (kg)

V_{room} = room volume (m³)

LFL = Lower Flammability Limit of refrigerant¹⁰ (kg/m³)

Similarly, the minimum room volume for a specific refrigerant charge is determined by Equation 2.6.

$$V_{room} = \frac{M_r}{0.2(LFL)} \quad (2.14)$$

Avoidance of Stratification (All)

In the event of "catastrophic" leak it is possible that stratification of refrigerant can occur, resulting in the formation of flammable concentrations at low level. In order to prevent this from occurring the fan provided with the refrigerating system should be able to provide a minimum air flow, as detailed in Equation 2.7, BS EN 378 (2000). This only applies to equipment that contains refrigerant charges above 150g. The fan operates only during the compressor on-cycle since the probability of a catastrophic leak during off-cycle is negligible.

$$\dot{V}_{air} = C \frac{M_r}{(LFL)} \quad (2.15)$$

where

¹⁰ Appendix 2, Table A2.10

\dot{V}_{air} = Minimum air flow rate from the fan (m^3/h)

The constant C, depends upon the origin of the air flow:

C = 17, when the evaporator fan on an air conditioning unit provides the airflow into the room, or,

C = 20, when the condenser fan on the refrigerating unit is providing the airflow into the room.

The different constants result from the effectiveness of fan mixing, primarily due to the velocity of the discharged air.

Maximum Refrigerant Charge (All)

The maximum allowable refrigerant charge for specific installation types, subject to other requirements is as follows:

- Direct expansion system in human occupied space is limited to A1-A3, B1-B4 and C1-C6.
- Indirect system in a human occupied space will be limited to A1-A5, B1-B6 and C1-C6.
- Systems with a high-pressure side (but not air-cooled condenser) in a machinery room will be limited to A1-A5, B1-B6 and C1-C7.
- Systems with all refrigerants containing parts in a machinery room or in open air shall be limited to A1-A5, B1-B6 and C1-C8.

Type of System (A4, A5, B6, C6)

The type of refrigerant charge can only be used within an indirect type refrigerating system.

Combustible Materials (All)

Materials used to construct the refrigerating system should not be combustible.

2.2.3. Use of Components

Pressure Relief (A3-5, B3-B6, C3-C8)

These systems must use some type of pressure relief device in addition to a fused plug. The discharge capacity of a pressure relief device shall be established in accordance with pr EN 122284. It is preferable to use an automatic pressure relief valve on the high side, vented to the low side before other pressure relief/bursting disc devices discharge refrigerant to the atmosphere.

Pressure Switches (A3-A5, B3-B6, C3-C8)

These systems must use low and high-pressure switches located on the suction and discharge sections of the systems.

Vibration Elimination (All)

If the equipment is solidly mounted then vibration eliminators to the suction and discharge lines should not under normal circumstances be required. If the compressor is mounted on rubber or spring mounts it may be advisable to install vibration eliminators to the suction and discharge line.

Pipe Connections (All)

Eliminate flared connections or compression fittings whenever possible. Use brazed joints only.

Charging (A4, A5, B4-B6, C4-C8)

Where reasonably practicable, charging points for systems shall be in the open air. Where this is not practicable they shall not be cited near exit passageways.

Other System Components (All)

Other system mechanical components such as pressure vessels, compressors, heat exchangers, piping and fittings should conform to the requirements of the relevant standards.

2.2.4. Installation

General

Minimum Room Volume (All)

Systems, or parts of a system should not be located within a space or room where its volume is such that an entire refrigerant leak would cause a refrigerant/air mixture

of a concentration higher than one-fifth of the Lower Flammability Limit (LFL) of the refrigerant Equation 2.20. If this is not possible and the installation is in a machinery room then the use of a refrigerant leak detector and mechanical ventilation should be employed (See sections 2.2.4.3, 2.2.4.4 and 2.2.4.6).

Floor Voids (All)

If equipment that could release its charge is installed in a room with a floor void, certain precautions should be taken. Where sources of ignition exist within the floor void, then it should either be sealed or the space ventilated. In particular, precautions should be made against refrigerant collecting in drains.

Refrigeration Piping

Refrigerant Piping (A4, A5, B4-B6, C4-C8)

Systems with these charge sizes cannot have piping passing through rooms that do not contain machinery as a part of the same refrigeration system. Where impractical this requirement can be overcome by using a sheath around the pipe work, with each end vented to the rooms containing the refrigerating machinery or to the outside.

Piping Duct Services (All)

Piping ducts must not contain any other pipe work or electrical wires or cables unless protection is provided to prevent damage due to interaction between services. Piping through ducts shall not contain any mechanical connections or other line components. Any ducts through which refrigerant piping passes must be vented to the atmosphere.

Piping Through Walls, Floors, Ceiling and Roof Spaces (All)

Piping passing through fire resisting walls and ceilings shall be so sealed as not to allow spreading of fire to neighbouring rooms. Pipe ducts and shafts shall be shut off from other rooms in such a way as to resist the spread of fire. Piping through false ceilings is permitted provided that the false ceiling is not completely sealed.

Pipe-work Routing Arrangements

The route of the piping should be as short as possible.

Machinery Rooms

Machinery rooms for systems using flammable refrigerants shall be designed to prevent the ignition of an explosive refrigerant/air mixture. There should be warning notices stating that smoking, naked lights or flames are prohibited. Fire extinguishers should be used in accordance with local fire authority.

Ventilation

Where the refrigerant charge of a single refrigerating circuit exceeds the mass in Equation 2.19 a machinery room using hydrocarbons must employ mechanical ventilation capable of providing the minimum ventilation rate. The minimum ventilation rate depends upon the type of electrical protection with the machinery room. Where the electrical installation is protected according to section 2.2.4.6 the mechanical ventilation rate should be equivalent to at least 10 room volume changes per hour, BS 4434 (1995).

Where the electrical installation does not conform to section 2.2.4.6 the minimum ventilation rate is defined by Equation 2.8, BS 5345 (1976).

$$\dot{V}_{\min} = \frac{M_r}{t_r (SF)(LFL)} \quad (2.16)$$

where

\dot{V}_{\min} = Minimum volume flow rate of extract on fan (m^3/hr)

M_r = Largest mass of refrigerant within any single circuit of any refrigerating system (kg)

t_r = Minimum release time of refrigerant following a catastrophic leak (typically 0.17 hr)

SF = Safety factor (0.5)

LFL = Lower Flammability Limit of refrigerant (kg/m^3)

In all cases a refrigerant detector should be linked into the initiation of mechanical ventilation. The location of the sampling point should be at low level (where heavier than air refrigerants are used). The ventilation must either be running continuously

or use a refrigerant detector starting device set at 20% of the LFL. Lower ventilation rates can be initiated upon detection of lower refrigerant concentrations.

Refrigerant Detection

Refrigerant vapour detectors shall be provided to activate an alarm. Points should be located so that they provide rapid signals in the event of a leak, and that the effect of air movement does not inhibit their effectiveness. A detector can normally cover an area of about 36 m² provided it is mounted at floor level, BS 4434 (1995).

Sources of Ignition

Precautions should be taken to avoid the possibility of direct sources of ignition from exposed electrical contacts. Electrical items that have potential to produce electrical sparks during normal operation should receive particular attention to eliminate them as potential sources of ignition. The following methods can be applied:

- Insulate terminals
- Locate within IP65 enclosure
- Replace with solid state type component
- Replace with Ex type component
- Locate externally

Providing such items only comprise of solid state parts or have casings which are solid encapsulated or otherwise sealed to at least IP54 or are located externally to the casing of the refrigerant containing parts then adequate precautions as required above are normally achieved.

Pipe work Installation

The following should be installed in accordance with the BRA (British Refrigeration Association) (April 2000) and BRA (February 2000): Copper Tubing, Copper to copper Pipe-work Fittings, Swaged Joints, Installation of line components, Pipe-work Support Methods for Copper Pipe-work, Tube bending, Brazing of pipe-work.

CHAPTER 3

This chapter presents an introduction to the properties of the test materials, and lubricants used during rolling contact fatigue testing. Specimen preparation, crack inducing and positioning of crack into contact path is described. Rolling contact fatigue tests are performed using a pressurised chamber. The chamber had to be vacuumed prior to charging with refrigerants. The surface inspection was performed during testing using light microscopy. Post test surface analysis techniques such as SEM, AFM, ZYGO, and Profilometer are described. X-ray diffractometer for measuring residual stresses in the rolling contact ceramic ball bearings is also described in this chapter.

3. EXPERIMENTAL METHODOLOGY

The specification relating to experimental research and methodology is presented in this chapter. The properties of the materials and lubricants are provided.

3.1. Test Materials

During this research the following materials were tested.

3.1.1. Silicon Nitride Si_3N_4 Sphere

α and β are the two crystallographic forms of pure silicon nitride both have hexagonal structure. The α -phase has a unit cell approximately double the size of the β -phase. The silicon nitride materials are classified into sintered, hot-presses, reaction bonded and hot iso-statically pressed (HIP), according to the processing techniques of solidifying. NBD-200 is a “Magnesia” doped material. It is Hot Isostatically Pressed (HIP) and meets the demanding requirements of ball-bearing and check valve applications.

Due to the HIP processing, the silicon nitride has zero porosity, fine grain microstructures, minimal level of dopant, and appropriate levels of strength,

hardness, toughness, and rolling contact fatigue behaviour and works exceptionally well in ball-bearing and check-valve applications.

The dopant or “sintering aid” is the controlling factor concerning corrosion resistance. Magnesia based silicon nitrides are highly inert in most liquids and gases. Typical physical and mechanical properties are listed in Table 3.1.

Table 3.1 Typical Properties of Commercial Bearing Si_3N_4

Grade (Manufacturer)	NBD-200
Material Fabrication Process	Hot-Isostatic Pressing
Density (g / cm^3)	3.16
Young's Modulus (GPa)	320
Poisson Ratio	0.26
Fracture Toughness ($\text{MPa}\cdot\text{m}^{1/2}$)	5.46
Hardness (Vickers Indentation) (GPa)	16.6 (at 10 kg)
Thermal Expansion Co-efficient ($10^{-6} / \text{K}$), 20 - 800 °C	2.9
Thermal Conductivity (Watt / m K)	29.3 (at 20 °C)

3.1.2. Steel Sphere

The steel ball is carbon chromium steel. The properties of the steel ball are given in the following Table 3.2.

Table 3.2 Typical Properties of Commercial Steel Ball

Diameter	12.7 mm
Surface Roughness (Ra)	0.02 μm
Hardness (Hv)	839
Elastic Modulus	210 GPa
Poisson Ratio	0.3

3.1.3. Lubricants

Due to environmental impact legislation, refrigerants have evolved to include Hydro fluorocarbons (HFC) such as R134a and Hydrocarbons (HC) such as R600a. Obtaining material wear properties of these refrigerants used in mechanical applications is difficult due to the high saturation pressure of the refrigerants. It is important to assess the in-use durability performance of these products from a sustainable development viewpoint. This research responds to the need for bench testing of rolling contacts using the new generation refrigerants as lubricants. Typical properties of the refrigerants used during rolling contact fatigue testing are provided in Table 3.3.

Table 3.3 Typical Properties of Refrigerants used¹

Property on a weight basis	R600a	R134a
Boiling point, °C, at 1 atmosphere	-11.8	-26.1
GWP ²	<4	420
ODP ³	0	0
Viscosity of liquid at 30°C, centipoises	0.14	0.20

3.2. Sample preparation

3.2.1. Surface Ring Cracks

An artificial surface ring crack is produced on the ceramic ball surface. The defect is induced with the help of a crack generating device (CGD). A schematic of a CGD⁴ is shown in Figure 3.1. The purpose of the defect is to shorten the experimental time and observe failure mechanism due to the particular geometry of the induced defect. The swing angle (angle of impact), impact force and crack geometry are known. The

¹ Source of data (Acirib 2000)

² GWP (global warming potential) is relative to carbon dioxide = 1

³ ODP (ozone depletion potential) is relative to R12 = 1

⁴ Earlier used by P Zhao

arc length of the ring crack and angle are measured. The embedded area of the ring crack is also known.

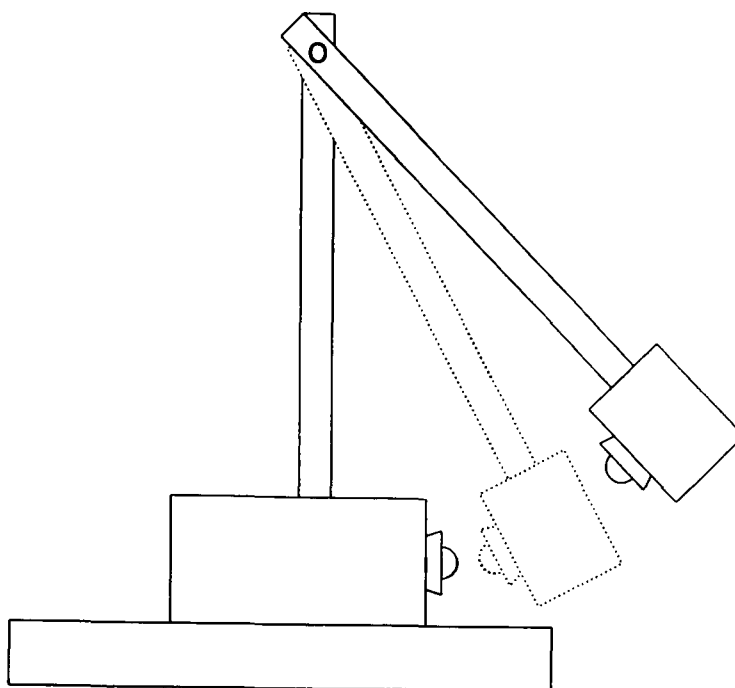


Figure 3.1 Schematic of crack generating device

3.2.2. Indents and Radial Cracks

Surface indents are generated by a Buehler Vickers indenting machine shown in Figure A3.1. A special holder was designed and produced to clamp the ball into the holder for indenting purposes shown in Figure A3.2. The load in kg_f for generating indents and geometry is known.

3.2.3. Surface inspection

Surface inspection is performed to obtain ring crack and indent defects geometry characteristics. This analysis is performed by using digital and Olympus BX60 optical light microscopy. A digital light microscope is shown in Figure A3.2. An optical microscope is shown in Figure A3.3. It is very important that all specimens under inspection should be clean to a very high standard. Cleaning is achieved by using an ultrasonic bath. The specimen is immersed into acetone and put in an ultrasonic bath for a few minutes. The specimen is dried by a blower so as the acetone is vaporized uniformly without leaving any traces of the liquid. The specimens are handled by a pair of prongs or forceps. Microscopy inspection is

strictly performed without touching the specimen to avoid contamination. Therefore, various manipulators are designed and produced to handle the specimen during microscopy inspection. These manipulators are shown in Figures A3.4 to A3.9.

3.3. Test procedures

3.3.1. Crack positioning

The ball positioning is very important as defect orientation is critical in the contact track and has direct influence on the fatigue life. To study the failure mechanisms driven by a particular defect in the ceramic ball surface, locating the defect into the contact path is very important. Once the defect is located into the contact path its orientation is important to failure mechanisms.

The probability of the crack to be in the contact area may be calculated as follows

$$\rho = \frac{A}{A_o} \quad (3.1)$$

where ρ is the probability of contact, A is the area of track and is given by

$$A = 4\pi a R_1 \sin \varphi \quad (3.2)$$

where a is the contact radius, R_1 is the radius of the ceramic ball, φ is the contact angle and is 35.5° . A_o is the area of the ball surface and is given by

$$A_o = 4\pi R_1^2 \quad (3.3)$$

$R_1 = 6.35$ mm, $a = 0.21$ mm, $\varphi = 35.3^\circ$, hence $\rho = 0.02$. From these results it can be seen that the probability of the induced defect being in the contact area is only 2%. Therefore, the defect positioning into the contact path is important.

The upper ball must be positioned such that the induced defect remains in the contact path. This position is calculated as

$$h = R_1 - (R_1 - \cos \varphi) \quad (3.4)$$

Where h ($h = 1.17$ mm) is the centre of the contact path from the tip of the ball surface as held in the collet. Figure 3.2 shows a schematic of the contact path

offsetting from the tip of the ball surface. Positioning of the defect into 0.21 mm contact path is sensitive. The defect is observed and positioned under the optical microscope. The position is marked. The ball is then positioned into a manipulator held in the collet over a surface plate Figure A3.10, and the height of the ball surface is determined by using a height gauge. The defect is then offset by 1.17 mm carefully without disturbing the required position of the defect into the contact path Figure A3.11. After accurate positioning of the defect into the contact path the ball is then pressed into the collet using a press.

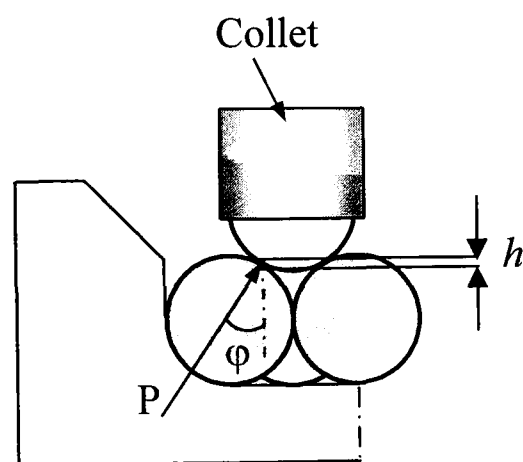


Figure 3.2 Schematic of the contact path offset from the tip

Contact stresses were calculated using classical Hertz elastic contact stress formulae (circular point contacts) (Johnson 1985).

$$P = \frac{L}{3 \cos \phi} \quad (3.5)$$

$$R \equiv \left(\frac{1}{R_1} + \frac{1}{R_2} \right)^{-1} \quad (3.6)$$

$$E^* = \left(\frac{1 - \nu_1^2}{E_1} + \frac{1 - \nu_2^2}{E_2} \right)^{-1} \quad (3.7)$$

radius of contact circle

$$a = \left(\frac{3PR}{4E^*} \right)^{\frac{1}{3}} \quad (3.8)$$

Maximum contact pressure

$$P_o = \left(\frac{3P}{2\pi a^2} \right) = \left(\frac{6PE^{*2}}{\pi^3 R^2} \right)^{\frac{1}{3}} \quad (3.9)$$

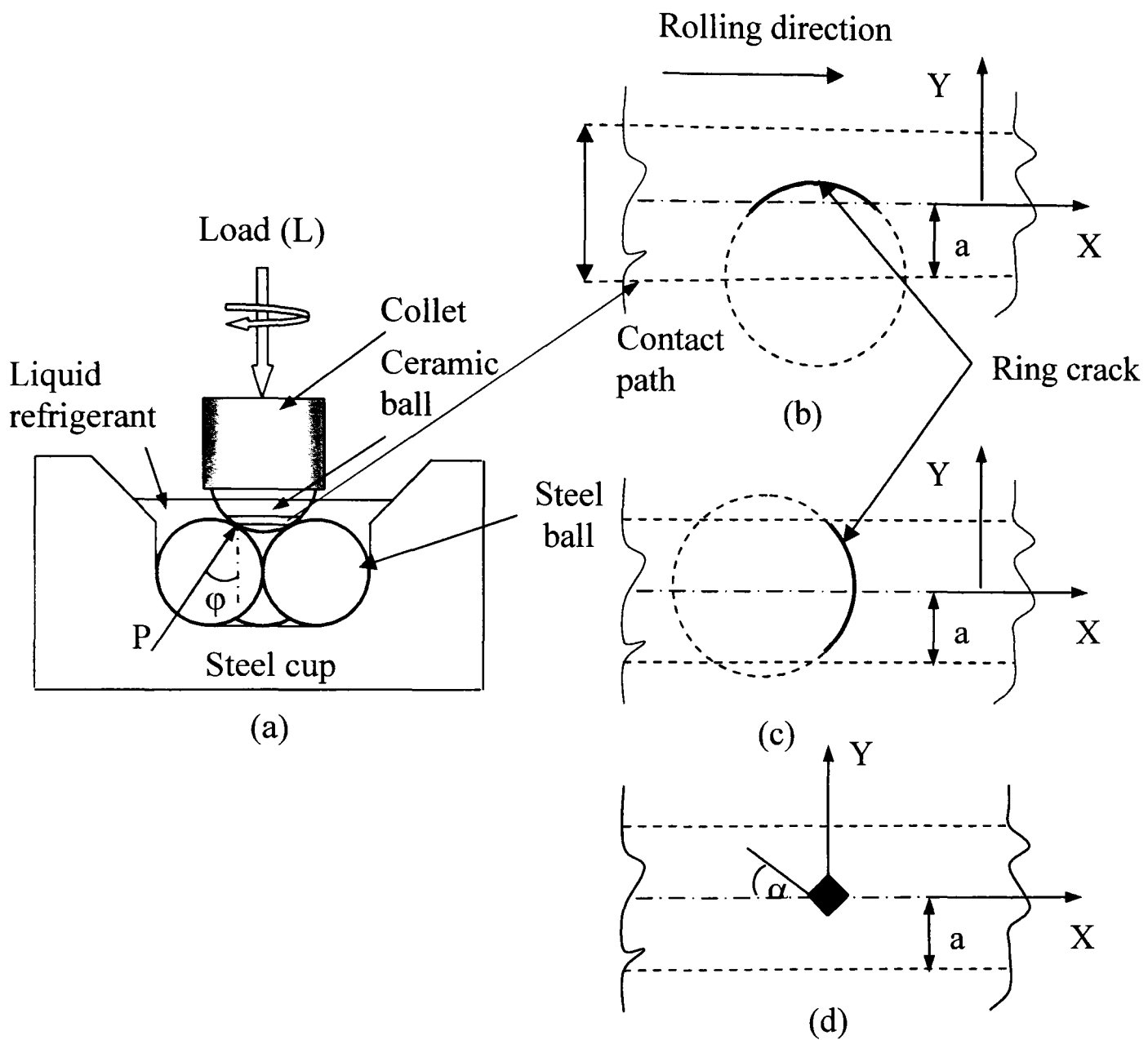


Figure 3.3 Schematic showing, (a) loading configuration; (b, c) ring crack positioning in the contact track (Wang 2000); (d) indent positioning on contact track

3.3.2. Test rig

Rolling contact fatigue tests are performed using the test rig described in Chapter 2. Tests follow a defined series of steps, each step containing shaft load, spindle speed and pressurised chamber temperature. The test sequence is continued unless interrupted by an operator or failure. This machine, coupled with a pressurised chamber, simulates rolling element bearing and precisely defines the contact load. The machine assembly simulates angular contact rolling element bearing. The stationary steel cup represents a bearing outer race, three lower balls represent the rolling elements within a bearing race and the upper ball represents the inner race.

3.3.3. Mounting specimen

After positioning the surface defect on the ceramic ball and press fitting, the upper ball is fitted into the drive spindle through a collet such that it should touch the lower three balls in the steel cup. The cup is thoroughly cleaned with acetone before the lower balls are loaded into the steel cup. The contact surfaces are separated by lubricating film.

3.3.4. Preparing pressurised testing

When the upper ceramic ball mounting has been completed the required load is applied. The lower pressurised chamber assembly (2) Figure 3.4 containing the steel cup and lower steel balls lifts up and slides into the upper chamber part (1), thus applying load and closing the chamber. The chamber is provided with a thermocouple (3); bulk temperature of the pressurised environment is monitored. The chamber temperature is kept low by coolant circulated through the cooling line (4). Once the load has been applied the pressurised chamber should be leak free. Prior to tests the pressurised chamber is thoroughly checked for any leakage by pressurising it with air. The pressurised chamber is then vacuumed to a pressure of -1 bar so as to eliminate any traces of air. A vacuum system (2) Figure 3.5 is employed to perform vacuuming on the pressurised chamber. The refrigerant is charged into the pressurised chamber through the charging system (3) and the

pressure of the refrigerant is constantly monitored by a compound gauge (4). At the same time the cooling system (1) is started by turning the power supply (7) of the pump (8) on. The cooling fluid starts circulating through the cooling lines (5) and (6). The temperature of the pressurised chamber is monitored, and once the saturation conditions of the refrigerant are reached, further refrigerant charging should be stopped. The tests are run, temperature and pressure conditions are recorded while the test is running.



Figure 3.4 Lower chamber part slides into upper chamber part

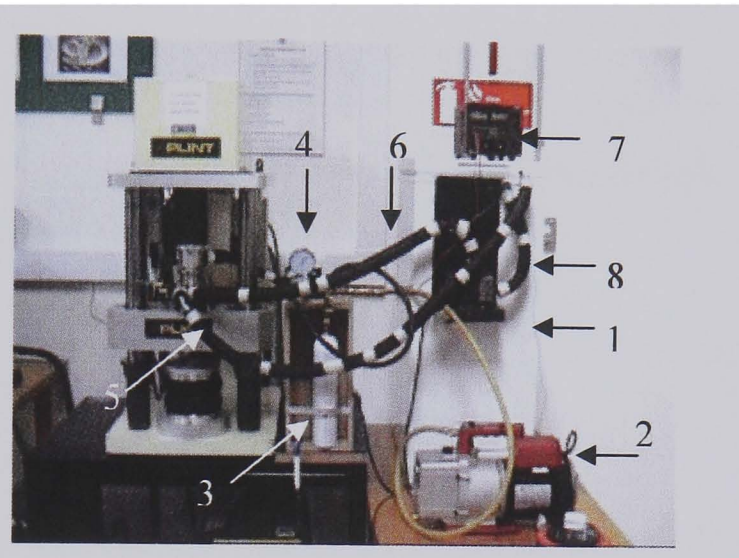


Figure 3.5 Test rig

3.3.5. Discharging system

Once the time step set for the test has been reached, or failure has occurred the test will stop. The test is also stopped intermittently to perform surface inspection at various test intervals. The vacuum line connected to the discharging or recovery line and the refrigerant is removed carefully. During this operation the electrical appliances coupled to the test rig are turned off. The recovery is followed by vacuuming. This makes sure that traces of refrigerant are removed from the pressurised chamber and associated lines to a safe level. The compound pressure gauge and temperature gauge are checked for the temperature and pressure conditions. The rig is then safe and the specimen can be removed for surface inspection.

3.3.6. Surface inspection

After the pressurised chamber has been vacuumed it is safe to open the chamber and take the specimen for surface inspection. The refrigerant system is shut off and isolated from the pressurised chamber through a stop valve. The cooling system is also stopped. The spindle load is then relieved and the pressurised chamber is opened. The collet assembly is taken off the machine spindle and the ceramic ball is pushed out from the collet. The ceramic ball is thoroughly cleaned in the acetone and dried using a blower. The steel cup is inspected for any surface damage and is replaced when necessary. Preliminary surface inspection is performed using an optical microscope. This inspection is important in order to establish whether the specimen has failed or the test should be continued.

3.4. Post-test Analysis

3.4.1. Light Microscopy

Optical microscope Olympus BX 60 with Sony Trinitron colour video monitor and Sony colour video printer is used for preliminary surface analysis. Turn on the power of the equipment in sequence - Light microscope, monitor and the printer. Put the sample in the manipulator. Clamp the manipulator on the stage holding specimen Figures A3.5, A3.7 and A3.9 showing use of various manipulators in conjunction with optical microscope. Adjust lower magnification - focus and locate defect. Use dark and light fields. Identify failure modes in the specimens. Use menu - Description, Scale, Area and Angle etc. Print photos of the different failure modes. Turn off the equipment - reverse order as to turning on. Surface defect information is obtained directly from the display monitor. Illuminated light intensity, dark field and Nomarsky interference are examples of light microscope techniques.

A micrograph for specimen 21 after 17 hours of test time with refrigerant lubrication is shown in Figure 3.6. Non destructive test (NDT) dying is employed for micro surface cracks to enhance visibility and surface details. The specimen is thoroughly cleaned and immersed in fluorescent penetrant post-emulsifiable solution for 30 to

45 minutes. The specimen is then immersed in diethyl glycol mono-butyl ether to clean the surface of any traces of penetrant followed by a gentle flow of tap water. Figure 3.7 shows a light micrograph with dye treatment.

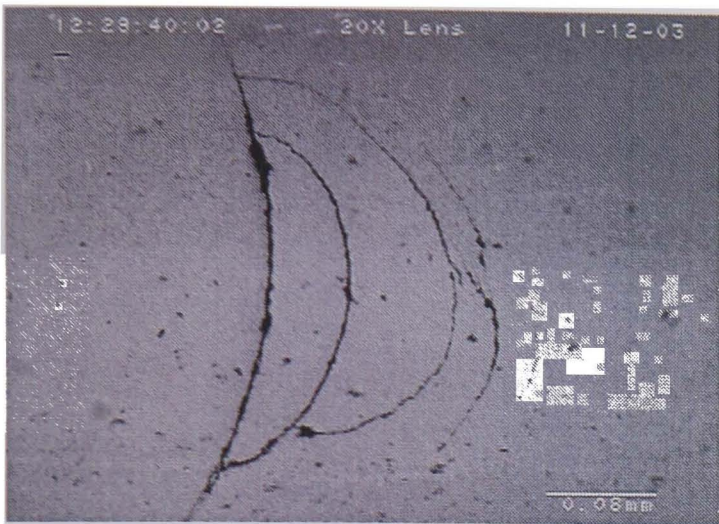


Figure 3.6 Optical micrograph secondary fatigue crack propagation

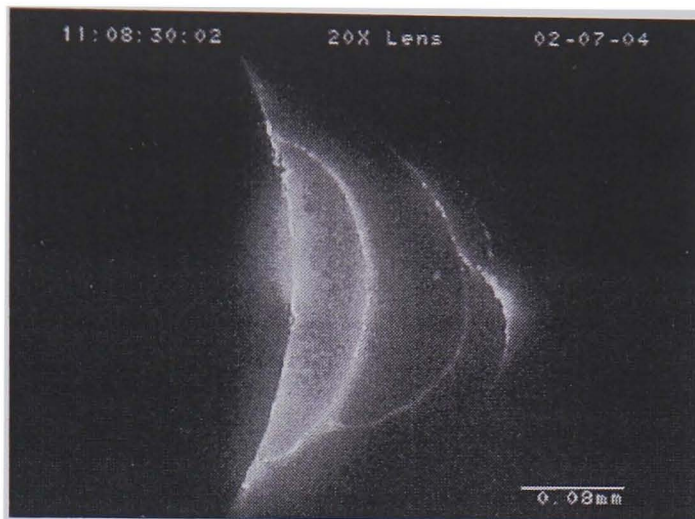


Figure 3.7 Dye penetrant treated ceramic surface

3.4.2. Digital Microscopy

Figure A3.12 showing a digital microscope. This microscope employs various magnification attachments. A micrograph obtained using digital microscope is shown in Figure 3.8.

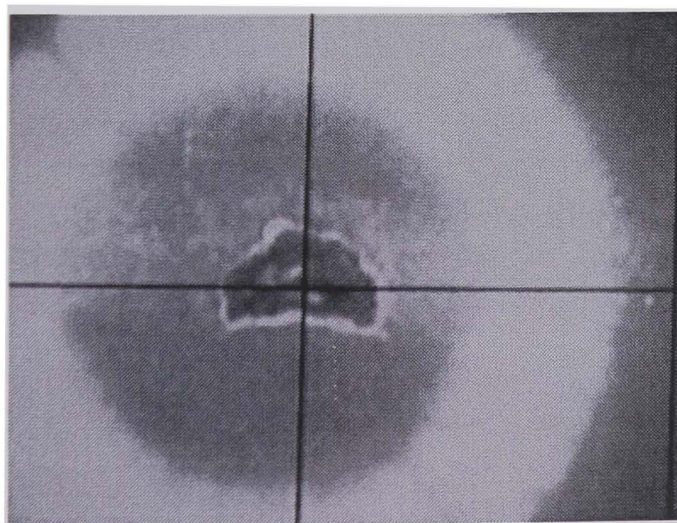


Figure 3.8 Digital light micrograph of a spall

3.4.3. Scanning electron microscopy

A Jeol JSM 5300 scanning electron microscope was used for surface analysis. High resolution and large depth of field are features of SEM analysis. Magnification of X30, 000 are available for ceramic ball samples. SEM has five distinct systems (1) electron gun source (2) condenser (3) scanning (4) detection and (5) display. Figure A3.13 shows a Jeol JSM 5300 scanning electron microscope.

Ceramic materials have low conductivity and therefore require conductive coating. Agar sputter coater Figure A3.14 was used for the purpose of coating. The standard coating for the ceramic surfaces is based on a five minute sputter application of gold. This produces a thickness of approximately 60 nm on a smooth surface. The distance between gold target and the sample is approximately 10 mm. The voltage for coating is 1.2 kV. The sample is placed in the coating chamber and the chamber is vacuumed to 0.1 millibar. This vacuum is continued for at least 15 seconds. Argon gas is then released and the vacuum is decreased, this is followed by an increase in the vacuum to 0.1 millibar, gold coating is performed for 5 minutes. The specimen is kept in a desiccator for about 20 minutes before performing SEM analysis.

The coated specimen is mounted on a metallic stub. Distance between the SEM electron gun and the sample during imaging is not relevant but distance between the sample and the final lens is normally 39 mm. For SEM examination the accelerating voltage is usually 20kV, sometimes reduced to 10kV but any change from normal should have been noted. The spot size or beam diameter is always small for imaging. Figure 3.9 and 3.10 show images obtained from an SEM examination.

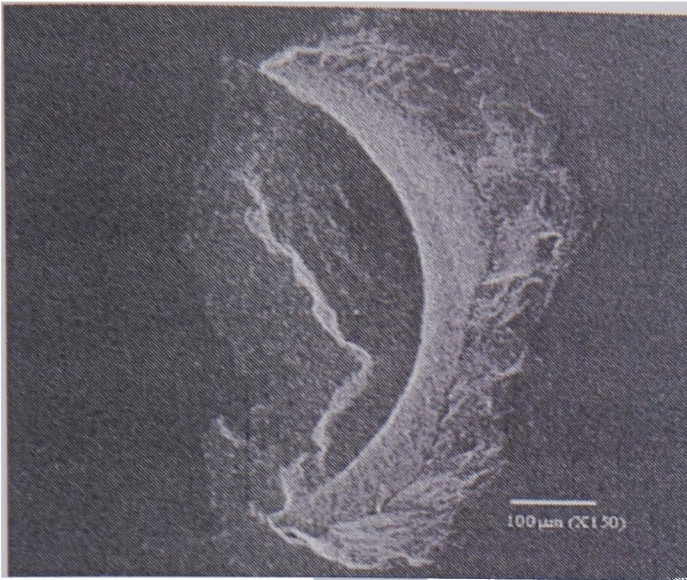


Figure 3.9 SEM micrograph for specimen 38

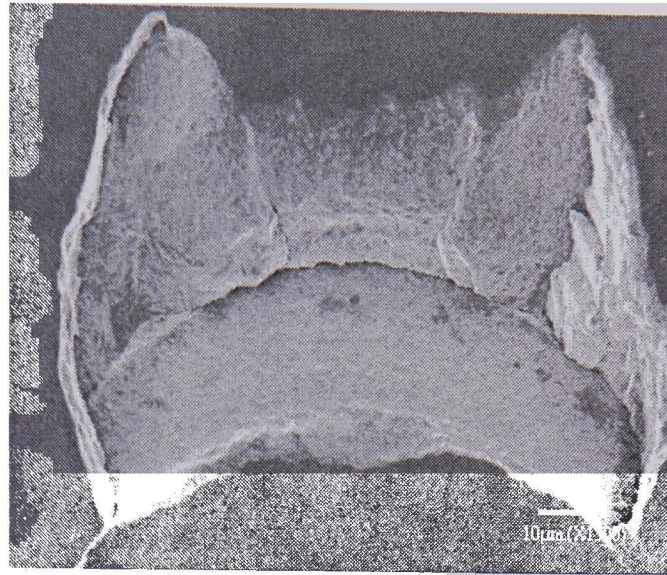


Figure 3.10 SEM micrograph for specimen 34

3.4.4. Atomic force microscopy (AFM)

Atomic force microscopy is contact type surface analysis. This research employed AFM analysis on failed rolling contact ceramic bearing elements to investigate the surface roughness and investigation of wear mechanisms. AFM model SPI-3700 made by Seiko precision was used for surface analysis. The resolution Z-axis (vertical direction) is 0.1 nm, horizontal direction 0.5 nm, moving range of stage is 200 mm. Atomic Force Microscope is shown in Figure A3.15. Figure A3.16 shows specimen mounting on the AFM stage. The surface topography is scanned through a stylus held in a probe. The location of the probe relative to the specimen is set by a laser beam. The quality of the stylus is also checked and is replaced if needed. The scanning is transferred through a workstation to a display monitor. Surface roughness measurements on a specified square area are performed. AFM workstation is shown in Figure A3.17. The surface image and details of the surface roughness measurements are then saved and printed as hard copy. The AFM surface profile for failed specimen 16 is shown in Figure 3.11. The scan area for the analysis is $30 \times 30 \mu\text{m}^2$. The average roughness on the surface was recoded to be $0.3 \mu\text{m}$.

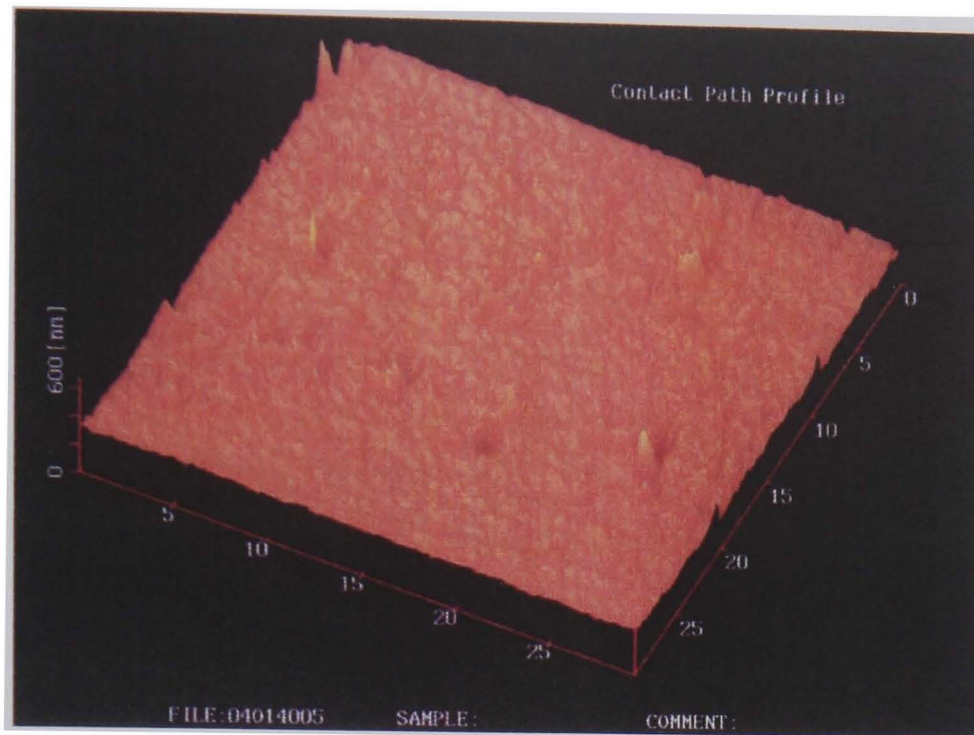


Figure 3.11 AFM micrograph of surface profile

3.4.5. Surface mapping

Surface mapping using Zygo was performed during this research. Zygo provides the facility of non-contact analysis. Zygo surface mapping is precise, no contact, 3-D surface metrology. The NewView 5000 3-D Surface Profilers have proved to be an invaluable tool in precisely characterising and quantifying surface texture, step heights, and critical dimensions.

The NewView 5000 is based on a scanning white-light interferometer, a traditional technique in which a pattern of bright and dark lines (fringes) result from an optical path difference between a reference and a sample beam. Incoming light is split inside an interferometer, one beam going to an internal reference surface and the other to the sample. After reflection, the beams recombine inside the interferometer, undergoing constructive and destructive interference and producing the light and dark fringe pattern. In the NewView 5000, a precision vertical scanning transducer and camera together generate a three-dimensional interferogram of the surface, processed by the computer and transformed by frequency domain analysis resulting in a quantitative 3-D image.

The vertical resolution is 0.1 nm. The vertical measuring range is 1 nm to 100 μm . surface roughness and spall details of the failed specimens are obtained by using Zygo analysis. The spall depth, angle of the crack relative to surface and spall exposed surface topography are also obtained by using Zygo. Figure A3.18 shows New View. Figure 3.12 shows a surface profile

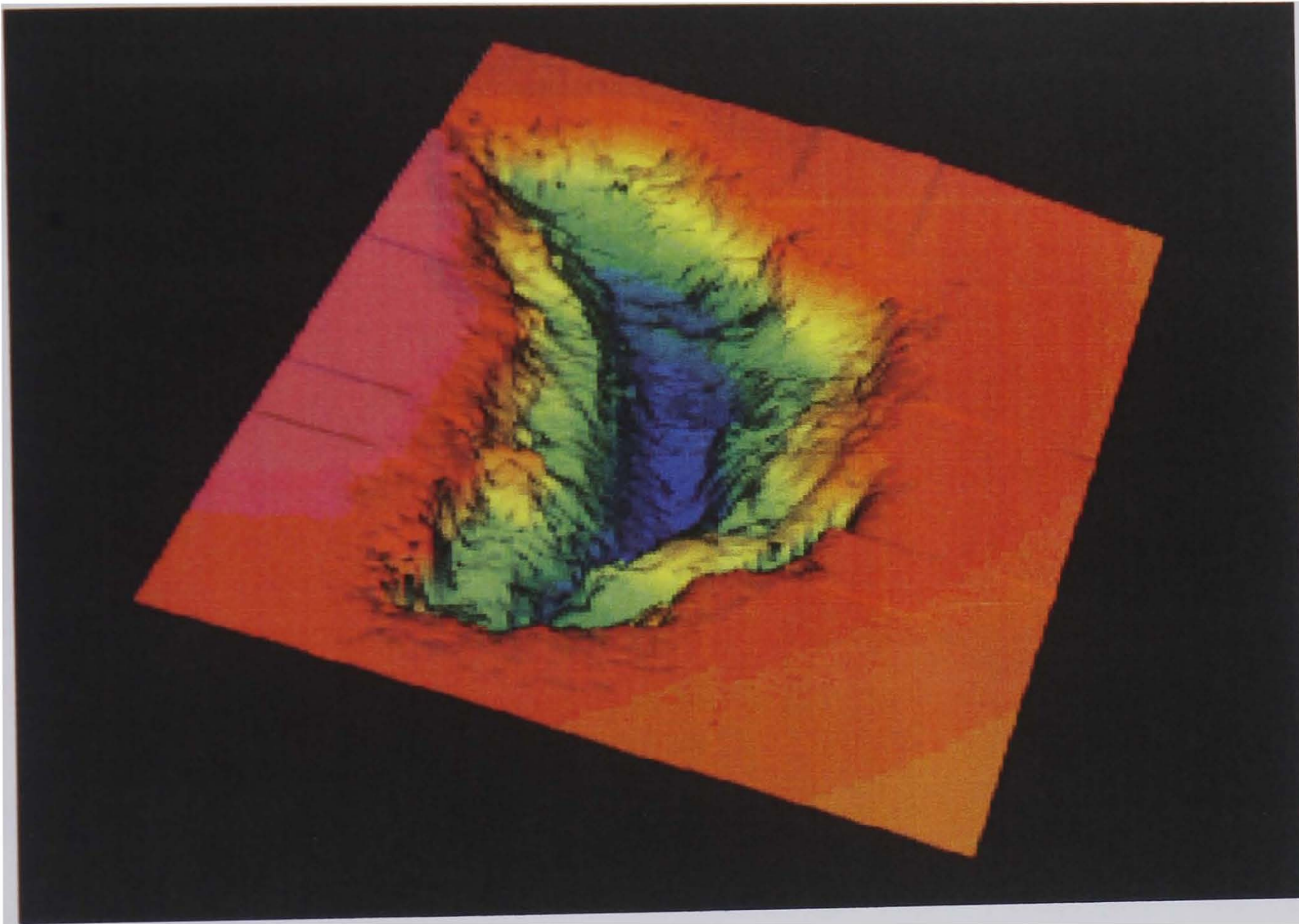


Figure 3.12 Spall micrograph obtained by Zygo

3.4.6. Profilometer

A Profilometer was employed during this research to probe the contact path profile, investigate the wear behaviour and surface texture. A Profilometer performs contact type surface analysis. The probe radius is $5\ \mu\text{m}$. The traverse speed v is $0.3\ \text{mm/s}$. Probe tip material is sintered carbide. Figure 3.13 shows a surface graph of the contact path obtained using a Profilometer for specimen 46.

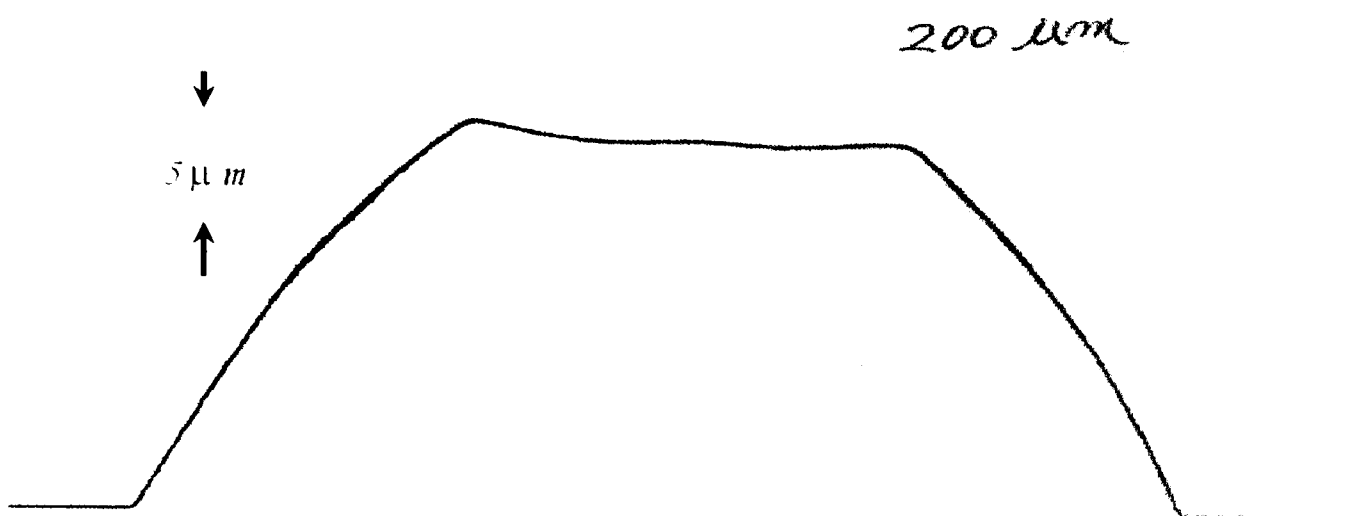


Figure 3.13 Surface profile of the contact track obtained by a Profilometer

3.4.7. X-ray diffractometer

Residual stress measurements were performed by a Rigaku Rint X-ray diffractometer. An engineering workstation Rint 2100 XG control was used to control machine parameters. The x-ray tube voltage was $40\ \text{kV}$, tube current was $200\ \text{mA}$ and power of $8.0\ \text{kW}$ was used. 2θ peak was 125° . A scanning range of 120° start and 130° stop was selected with a step angle of 1° and sampling time of 100 seconds. An incident beam of x-ray Cr K-Alpha1 was radiated through a collimator. The collimator diameter chosen was $2\ \text{mm}$. The incident x-ray beam penetrated the sub-surface within the material to a depth of $30\ \mu\text{m}$. Thus the stress measurement is taken from a cylindrical volume of irradiation $0.0942\ \text{mm}^3$ within the material.

Figure A3.19 shows Rigaku Rint x-ray diffractometer and its Rint 2100 XG control engineering workstation. Figure 3.14 shows the residual stress measurement profile during measurement on the workstation.

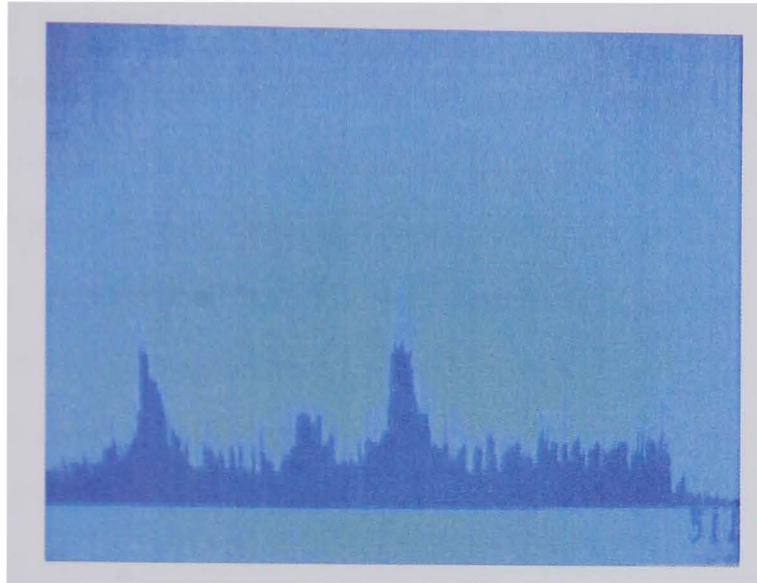


Figure 3.14 Residual Stress Measurement Profile on Rint 2100 XG control engineering workstation

3.4.8. Replication

Metallic replicas are produced by a stamping method for concave or convex surface texture. This research also employed the method of metallic replication. The advantage of replication is the convenience of use with optical microscopy or any other surface analysis. The flat surface of the replica around the area of interest make replica mounting easy.

CHAPTER 4

This chapter presents a brief introduction to the background of x-ray principles for measuring residual stresses. Residual stresses were measured on rolling contact fatigue failed lubricated specimens. The measuring procedure is described in this chapter. X-ray diffractometer for measuring residual stresses in the rolling contact ceramic ball bearings is briefly described in this chapter. The x-ray method makes use of calculating stresses from known strain. The strain is known from the relationship of the x-ray wavelength (monochromatic), the deflection angle and the inter-planner in the ceramic elements. Post test surface analysis techniques such as SEM, AFM, ZYGO, and Profilometer were employed to obtain surface characteristics. The residual stress measurements were performed at sub-surface levels. The feature of this study is the small volume of irradiation through which the measurements were performed.

4. RESIDUAL STRESS MEASUREMENTS

4.1. Introduction

Residual stress measurements help in understanding the relationship between residual stresses and rolling contact fatigue, the relationship of fatigue crack propagation and variations in the compressive residual stresses. Analysing the relationship of residual stresses with rolling contact fatigue is an important study which will provide guidelines on the design, process and manufacturing of these elements. The ceramic rolling contact bearing elements were pre-cracked with ring cracks the geometry of the induced defects being then known. The residual stress measurements were performed at various positions on the contact path relative to the induced defect.

4.2. Methodology

4.2.1. Background

In principle the x-ray method is useful in any crystalline material that has had some application to stress measurement in engineering ceramics and geology, its major use is the measurement of residual stress in metals and alloys (Cullity 1996).

The standard diffractometer method is usually called two exposure method, because two plane-spacing measurements are made, one of d_n at $\psi = 0$ and one of d_i at $\psi = 45^\circ$, shown in figure 4.1.

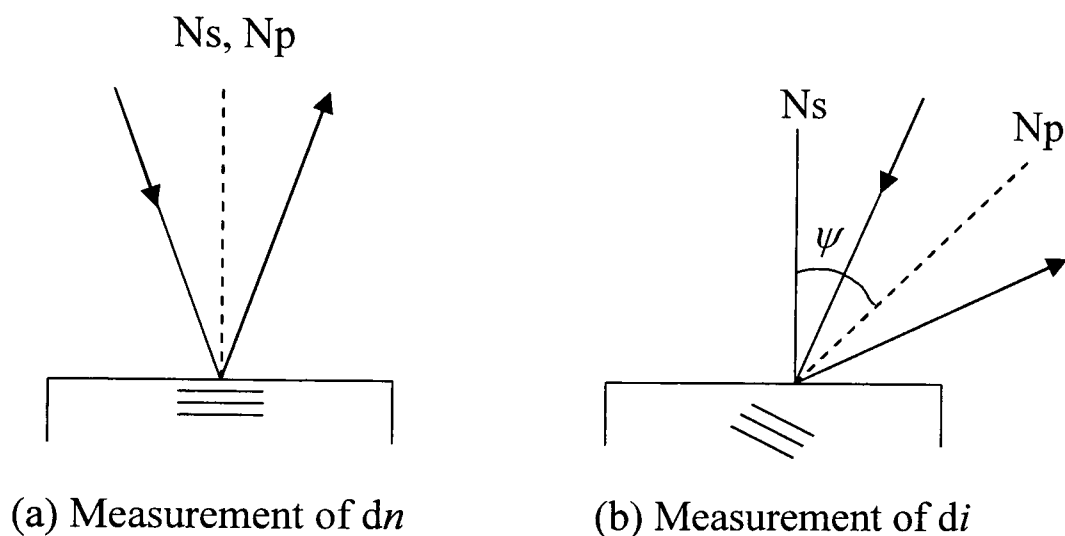


Figure 4.1 Plane-spacing diagram. (a) and (b) orientations of x-ray beams relative to specimen.

When x-ray radiations are passed through matter, interaction with electrons in the atom results in scatter of the radiation. If however the structure is crystalline and the distances between the atoms are of the same magnitude as the x-ray wavelength, constructive and destructive interference will take place. This will result in diffraction where x-rays are emitted at characteristic angles based on the spaces between atoms organised in crystalline structures called planes. Crystals may have more sets of planes passed through their atoms. The interplanar distance is specific and gives rise to a characteristic angle of x-rays being diffracted. The relationship between atomic spacing d , wavelength and angle was solved by Bragg's equation. If the illuminating wavelength is known (depends upon the type of X-ray tube and

monochromator used) and the angle can be measured, using a diffractometer, then the interplanar distance can be calculate using Bragg's equation.

$$n\lambda = 2d \times \sin \theta \quad (4.1)$$

A schematic of Bragg's principle is shown in figure 4.2.

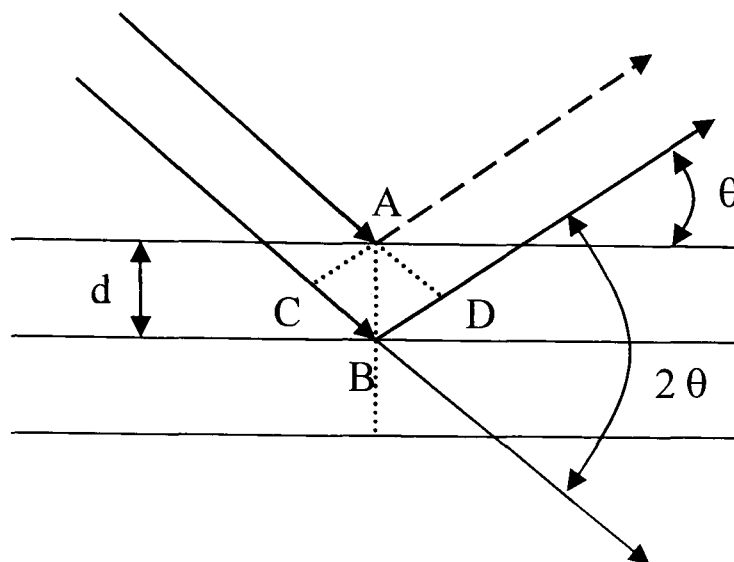


Figure 4.2 A schematic of the Bragg's law

The strain can be determined, either by a calculation involving the mechanically measured elastic constants of the material, or by a calibration method involving measurement of the strains produced by known stresses. However, stress is not measured directly by x-ray method. It is always strain that is measured, the stress is then measured indirectly by calculation or calibration. The strain is calculated from the equation 4.2.

$$\varepsilon = \frac{\Delta d}{d} = \cot \theta_0 \Delta \theta \quad (4.2)$$

The various methods of stress measurement differ only in the kind of strain gauge used. In the x-ray method, the strain gauge is the spacing of the lattice planes. In principle, the x-ray method is useful in any crystalline material. While it has had some application to stress measurement in ceramics and rocks, its major use is the measurement of residual stress in metals and alloys (Cullity 1978).

Stress can be calculated from the following relationship as follows.

$$\sigma = \left(\frac{E}{1+\nu} \frac{\partial(\varepsilon)}{\partial(\sin^2 \psi)} \right) = - \left(\frac{E \cot \theta_0}{2(1+\nu)} \frac{\partial(\theta)}{\partial(\sin^2 \psi)} \right) \quad (4.3)$$

where

$$K = - \left(\frac{E \cot \theta_0}{2(1+\nu)} \right) \quad (4.4)$$

and

$$M = \frac{\partial(\theta)}{\partial(\sin^2 \psi)} \quad (4.5)$$

then equation 3 may be re-written as

$$\sigma = KM \quad (4.6)$$

The “ K ” value is usually referred to as stress constant or elastic constant and has been measured on several materials. During this research the K value for silicon nitride is taken as $-954 \text{ MPa degree}^{-1}$. The variable M is the slope of $(2\psi-2\theta)$ and expresses strain. This value can be measured by peak shift of the diffraction profile found from each ψ angle. The calculated value of the stress is thus a product of K and M . The diffraction peak position can be computed in several ways. The FWHM is employed when stress in metallic material is measured. Since silicon nitride has many diffraction planes, a cluster of more than one peak could be found. In this case it is difficult to identify the background profile of x-ray, which means the FWHM method is not available. However, peak top method is employable. The peak top method makes use of a quadratic equation that approximates the peak profile and the centre of the peak is then calculated. This research employed peak top method for all measurements. Figure 4.3 shows 10 peaks of RS measurements. In this instance the sampling time was set to 100 seconds. The step angle was 0.1° , scan range was $120-130^\circ$, while scan axis was 2θ which needed to be set before measurements started. θ was 62.702° and sample rotation was 0. In order to determine peak top the highest peak is selected. The peak top is taken for measurement. In Figure 4.3 the peaks are not uniform and a step could be seen to the right of the high peak. In this case the calculation of peak top is not possible unless a uniform peak is available.

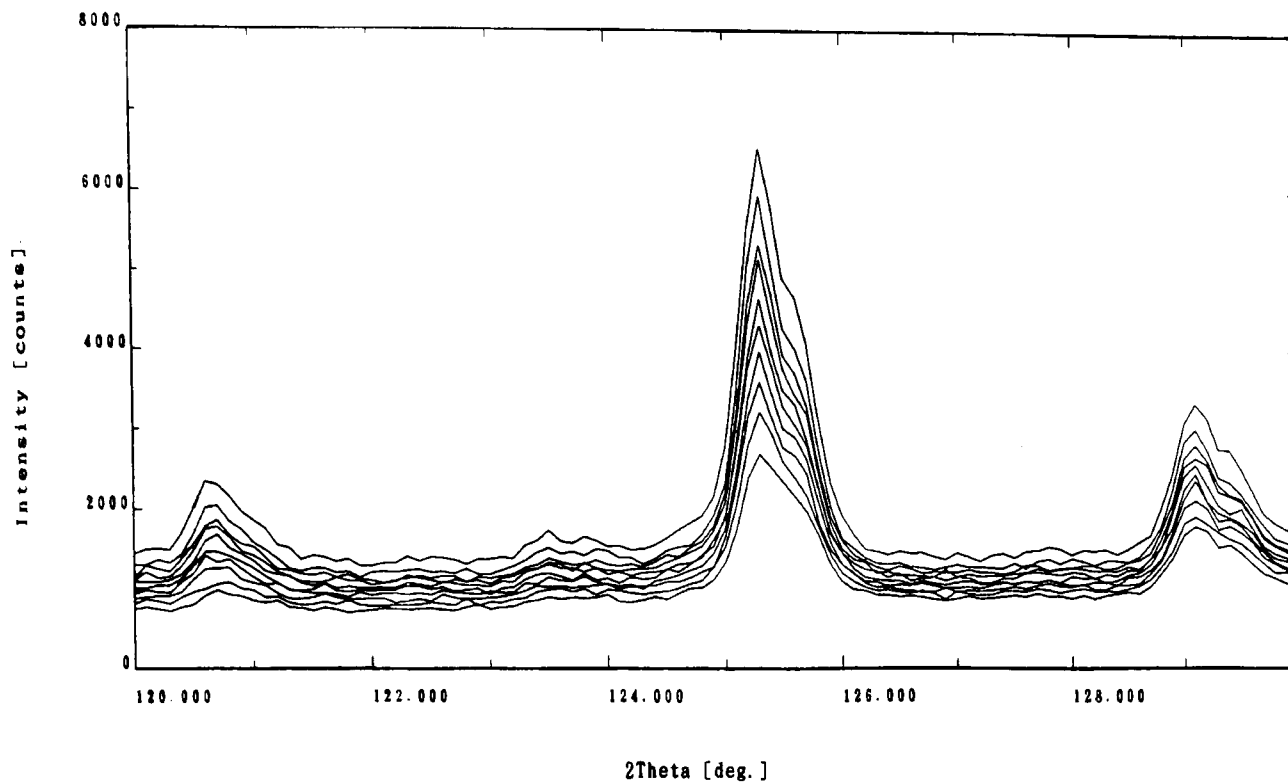


Figure 4.3 Raw data collected during RS measurement

The data smoothing helps to obtain uniform peak. The process of smoothing data from raw data collected is shown in Figure 4.4 below. In this case 10 section counts and 7 points were considered for measurement. The monochromatic source position was $K - \cos(2\theta M)^{-2}$, 2θ are set prior to any measurement, K and M are calculated as shown above. Linear absolute co-efficient is 1. The peak is now uniform in Figure 4.4 comparing to the peak in Figure 4.3.

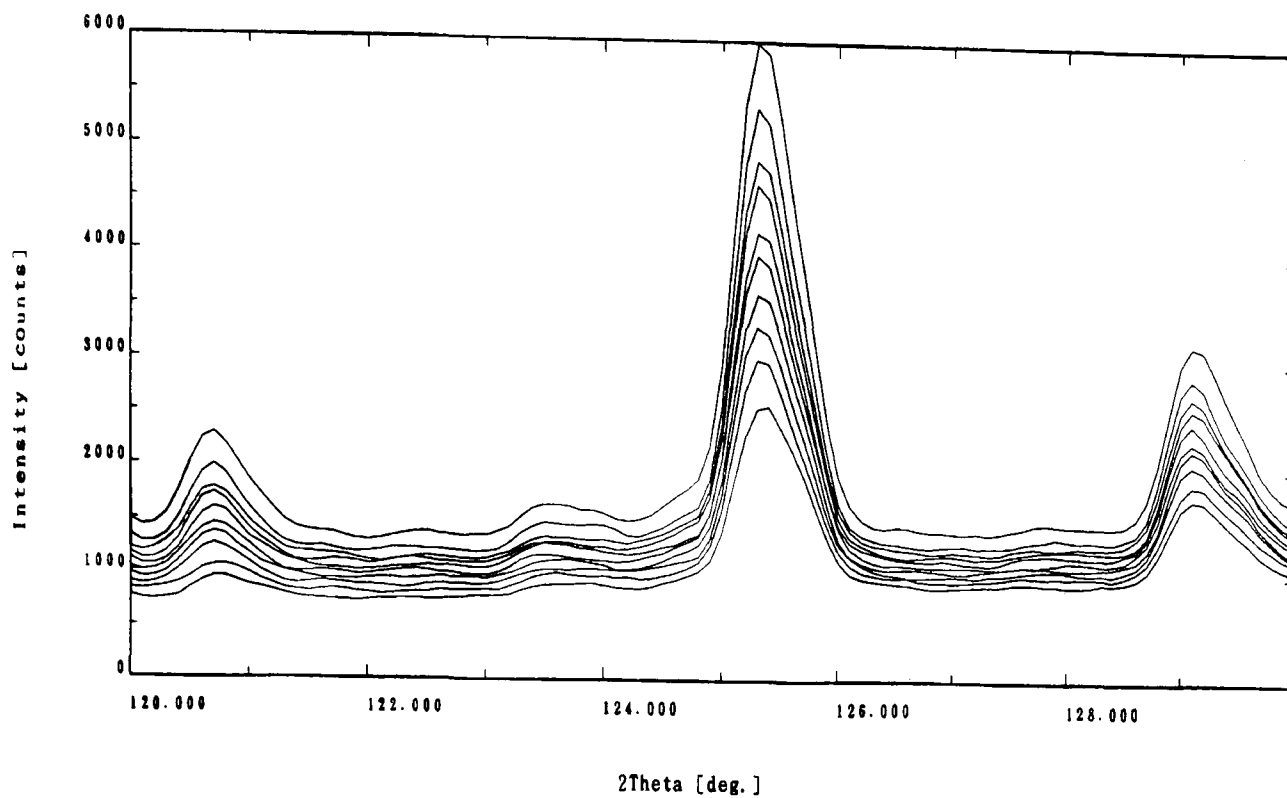


Figure 4.4 Smoothing of RS data during measurement

4.2.2. Measuring Procedure

Figure 4.5 shows ball surface diameter through which residual stress measurements are performed. Figure 4.6 is a section of the ball and shows sub-surface depth through which residual stress measurements were performed for one point. Figure 4.7 is a schematic showing cylindrical volume for RS measurements. Young's modulus for silicon nitride was taken as 27.4×10^4 MPa, and Poisson ratio as 0.26. The measurement conditions and the physical constant for performing residual stress measurement are given in table 4.1 and table 4.2 respectively.

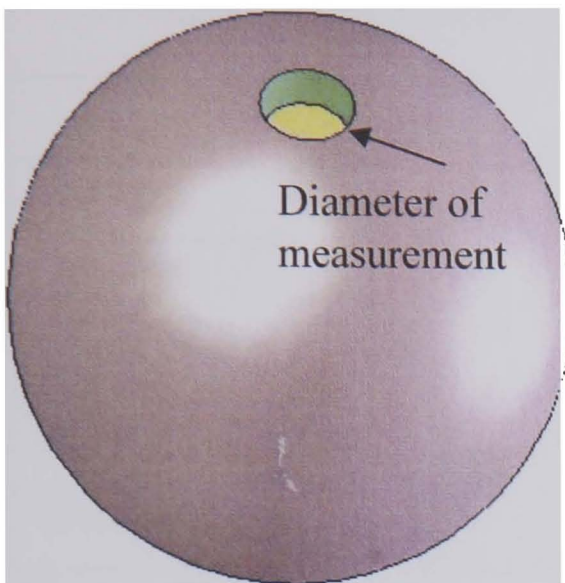


Figure 4.5 3D image of ceramic ball showing surface diameter for RS measurement

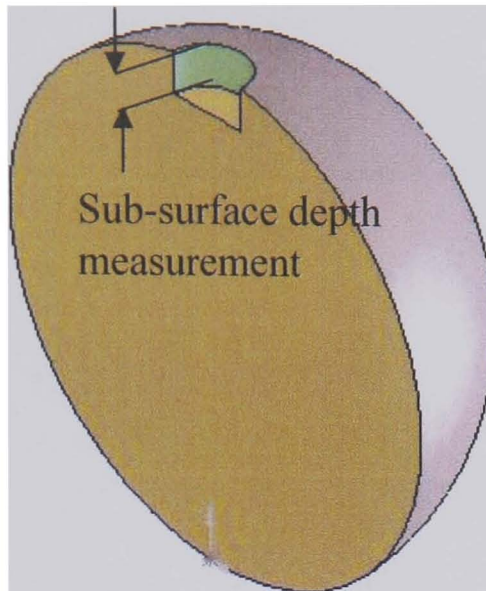


Figure 4.6 3D sectional view of ceramic ball showing depth of RS measurement

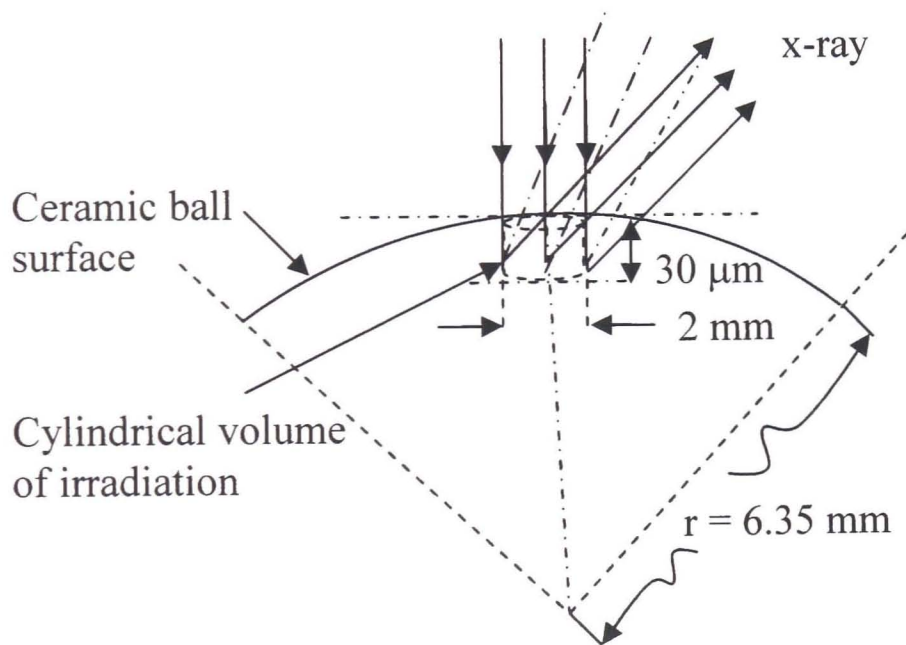


Figure 4.7 Schematic of ceramic ball cylindrical volume taken for RS measurement

Table 4.1 Measurement Conditions for Residual Stress

x-ray	<i>Cr K-Alpha 1</i>
Voltage	40 kV
Current	200 mA
Attachment	Special stress attachment
Filter	K-beta filter
Collimator	2.0 mm
Sampling time	100.00 sec
Step angle	0.100°
Scan axis	2θ
Scan range	120 - 130°
θ	62.702°
Sample rotation	0.00°

Table 4.2 Physical Constant for Residual Stress Measurement

Sample	<i>Si₃N₄</i>
Young's modulus	274×10 ³ MPa
Poisson's ratio	0.26
Stress constant	-953.50 MPa/deg
Wave length	2.29 Ang
Peak 2θ	125.4°
<i>Peak search method</i>	Peak top

Figure 4.8 showing Rigaku Rint x-ray diffractometer and its Rint 2100 XG control engineering workstation. Figure 4.9 showing the residual stress measurement profile shown during measurement on the workstation.

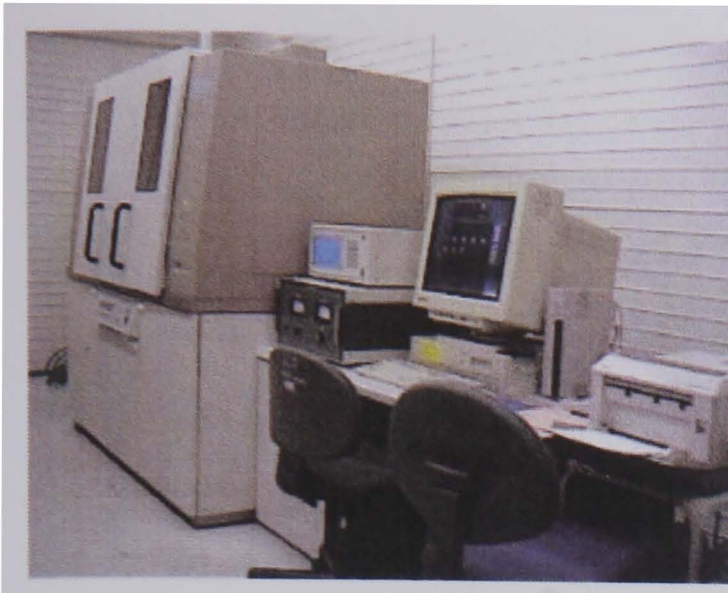


Figure 4.8 Rigaku Rint x-ray diffractometer with Rint 2100 XG control engineering workstation

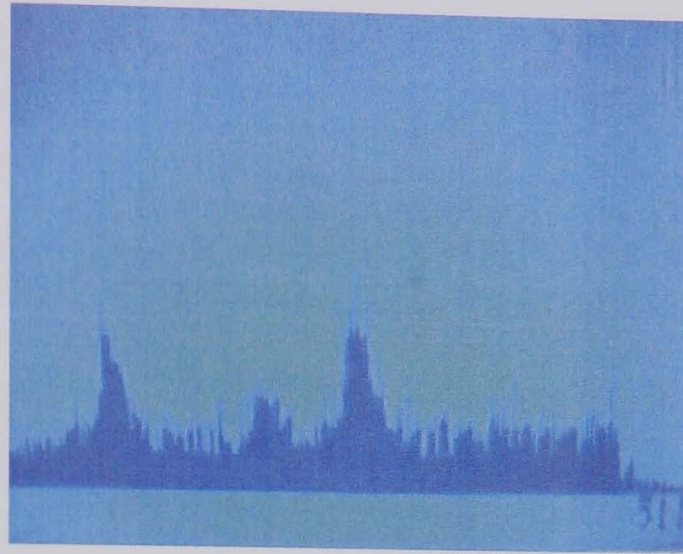


Figure 4.9 Residual Stress Measurement Profile on Rint 2100 XG control engineering workstation

4.3. Residual Stresses

In-service metallic residual stresses are referred to as shake-down stresses and are described by (Johnson 1985). In ceramics it has been found that residual stresses enhance the rolling contact fatigue life (Hadfield et al. 1998). During this research the rolling contact bearing elements were pre-cracked with ring cracks that had known geometry. The influence of the geometry, orientation and positioning of these ring cracks on the rolling contact fatigue life have been studied in recent researches (Hadfield 1998; Wang et al. 2000a). It is acknowledged that residual stresses during rolling contact is beneficial in that the fatigue strength is enhanced due to material shakedown (Hadfield and Tobe 1998).

The elastic deformation is continued in the elastic region of Hook's law and a steady plastic failure happens. When the metal is deformed plastically, the distortion of lattice planes usually takes place such that the spacing for any particular set of planes or from one part of the grain to another part of the grain varies. This phenomenon is also observed when an artificial defect is induced in the rolling contact bearing elements, while inducing ring cracks. This non uniform micro-strain causes a broadening of the corresponding diffraction line. On the other hand when a polycrystalline piece of metal is subject to elastic deformation such that the strain is

uniform over relatively large distances, the stress free value of the lattice spacing in the constituent grains changes to a new value corresponding to the value of applied stress level. This lattice spacing is equal from one grain to another for any particular set of planes similarly oriented according to the stress. Both kinds of strains are superimposed in plastic deformation of metals. The diffraction lines are both broadened and shifted, because both the lattice spacing from grain to grain and their mean value deviate from that of non-deformed metals. When a ring crack is induced due to impact loading, plastic deformation occurs, which causes change in lattice spacing in a particular set of planes. This spacing varies from grain to grain or one part of a grain to another part of the grain. The shifting and broadening of the diffraction line registers high value compressive residual stress on the close proximity of the defect/ring crack due to plastic deformation, irrespective of the stress cycles during the rolling contact fatigue. High residual stresses near the induced ring crack are the result of variation in the lattice spacing due to plastic deformation by impact loading.

Specimen 36 and 27 had geometrically identical ring cracks which were induced at similar impact. The residual stress values for both specimens measured at 0.1 mm distance from the crack are identical. The measured compressive residual stress value for both specimens 36 and 27 were 218 and 243 at stress cycles of 1.07×10^6 and 0.08×10^6 respectively. The lower value of compressive residual stress for both specimen 36 and 27 is understood from the number of stress cycles at which both these specimens were tested. The changes in the values of residual stresses close to and away from the defect during rolling contact are understood by the above phenomenon.

CHAPTER 5

Experimental results of the rolling contact hybrid ceramic/steel contact with refrigerant lubrication and their failure mechanisms due to various induced defects are described. Fatigue life performance of ceramic bearing elements in relation to indents and radial cracks, ring cracks and their ring crack location, position and geometry is discussed. Rolling contact fatigue test programme is provided. The fatigue life performance of the rolling elements with respect to various induced surface defects is discussed. Surface profiles of the failed specimens, using various techniques were obtained during this research and are presented in this chapter.

5. ROLLING CONTACT FATIGUE EXPERIMENTAL TEST RESULTS

5.1. Smooth specimens

Specimens 14 and 15 were tested as smooth specimens. The test results are provided in table 5.1. Both specimens were subjected to a maximum contact Hertz stress of 3 GPa. The spindle speed was 2000 rpm. HC (R600a) refrigerant was used as lubrication. The test for specimen 14 was suspended after 4 hours 44 minutes of test time without any failure. Specimen 15 was tested for 14 hours and 10 minutes. This test was also suspended, since there was no surface failure.

Table 5.1 Test results for smooth specimens

Test Ball	Maximum Contact Pressure (GPa)	Test time	Stress cycles
14	3	4hrs 44min	1.28×10^6
15	3	14hrs 10min	3.83×10^6

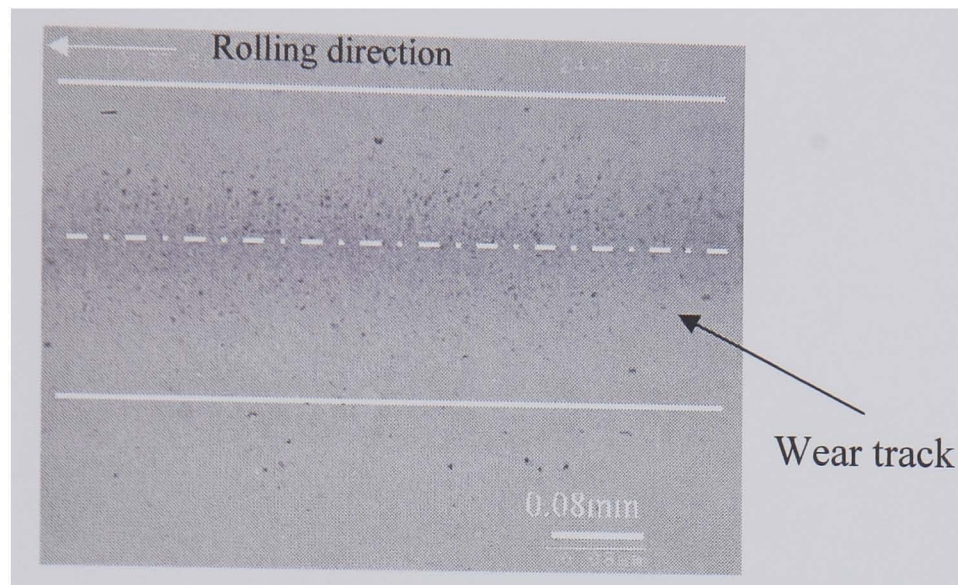


Figure 5.1 Light micrograph;
smooth specimen 15

5.2. Indents and radial cracks

The test programme is detailed in Table 5.2. R600a was used as liquid refrigerant lubrication for all specimens except 3, where R134a was used. The pressure and temperature conditions were recorded during the tests. The system was vacuumed for each test to -1 bar (gauge). This was necessary to eliminate traces of air in the system. The system was then checked for any potential leakage. Once satisfied with the sealing arrangement for the test, the refrigerant was charged into the system. The cooling system was turned on during charging which provided a lower saturation temperature condition for the test. The average chamber pressure was maintained at 3 bar (gauge). The corresponding saturation temperature for R600a is around 29°C and for R134a is 9°C. The initial average temperature of the chamber was -3 to -5°C each time before starting the tests. The maximum bulk temperature for the chamber was no more than 35°C. Figure 5.2 shows a comparison of saturation temperature for R134a with the test temperature. Figure 5.3 shows the saturation temperature for R600a as compared to the observed conditions.

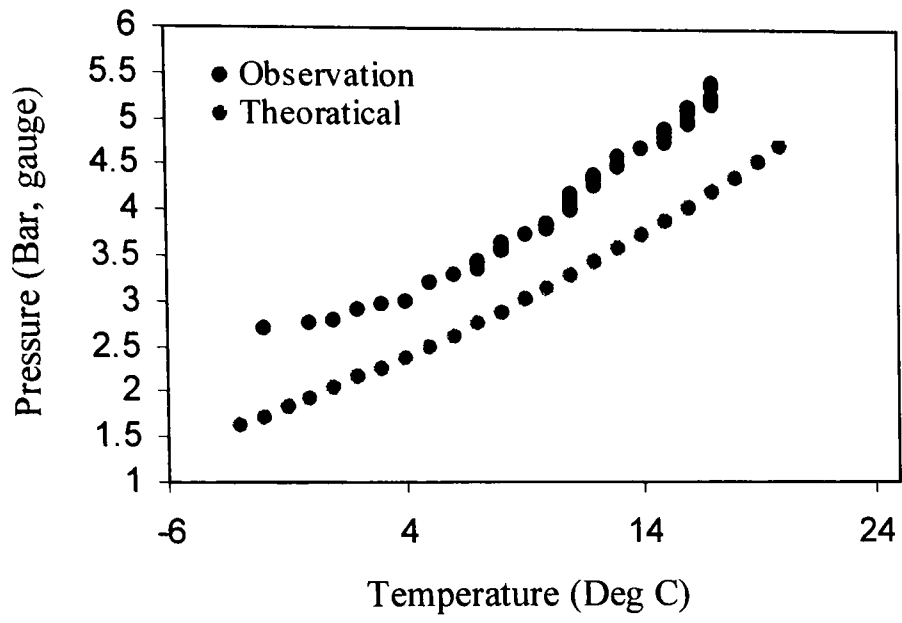


Figure 5.2 Saturation temperatures for R134a

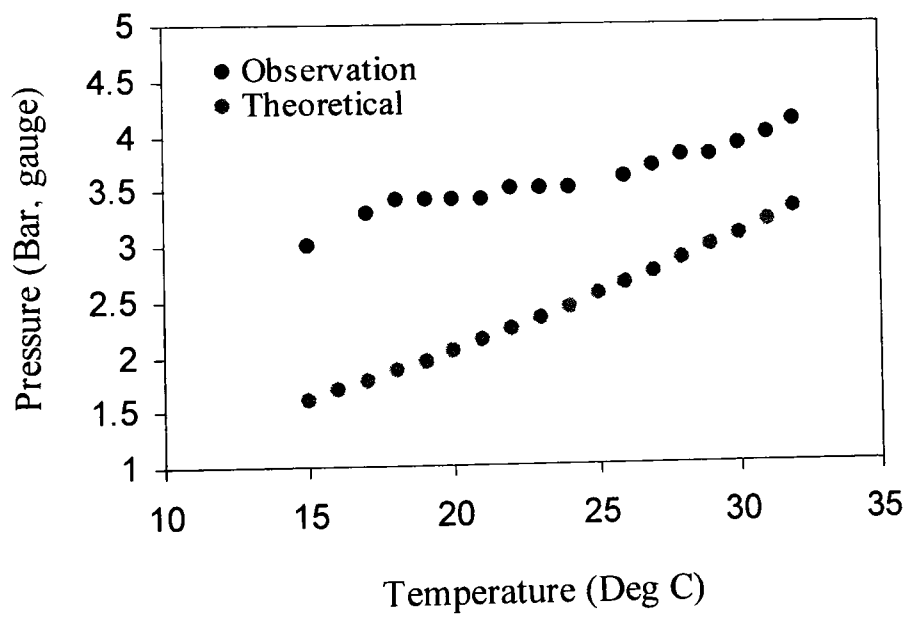


Figure 5.3 Saturation temperatures for R600a

Table 5.2 Test results for specimens with induced indents

Specimen	Lubrication	Contact pressure (GPa)	Shaft speed (rpm)	Time to failure	Stress cycles	Indent load (kg)
1	R600a	3	2000	10min	4.51×10^4	10
2	-	3	2000	3min	1.35×10^4	10
3	R134a	3	2000	4hrs 30min	1.22×10^6	5
4	R600a	3	2000	4hrs 30min	1.22×10^6	5
5	-	3	2000	13hrs 30min	3.65×10^6	1
6	-	5	2000	18min	8.10×10^4	5
7	-	6	2000	5min	2.24×10^4	1
8	-	6	2000	9min	4.05×10^4	1
9	-	6	2000	9min	4.05×10^4	1
10	-	6	2000	7min	3.16×10^4	1
11	-	7	3000	3min	2.03×10^4	5
12	-	7	3000	2min	1.34×10^4	5

The pressurised chamber was used to maintain the liquid state of the refrigerant throughout the tests. The cooling system was employed to ensure lower operating pressures. HC (R600a) was used in test 1 to 12 except for test 3 where R134a refrigerant was used. For test 1 initial temperature of the chamber was 15°C with initial pressure (gauge) of the refrigerant at 3 bar. Temperature gradually rose to 19°C and pressure to 3.35 bar during the test period. Failure occurred in 10 minutes. The actual saturation conditions of the refrigerant are compared in Figure 5.2 for HFC (R134a) and Figure 5.3 for R600a, to theoretical conditions. It is confirmed that the state of the refrigerant was subcooled liquid. An almost similar trend of temperature-pressure variation was observed through tests 1 to 12.

Test 1 was carried out in HC (R600a) refrigerant environment. The results are shown in Figure 5.4. The rolling contact fatigue spall has an elliptical shape. Figure 5.4(c,d) show fatigue crack propagation. After about 10 minutes under 3 GPa contact pressure, the crack growth from the initial indent position is quite significant. The temperature range of the refrigerant environment in this test was 15-19°C while the pressure of the liquid refrigerant was 3-3.5 bar (gauge). The fatigue crack growth change can be seen from Figure 5.4(a) to (b).

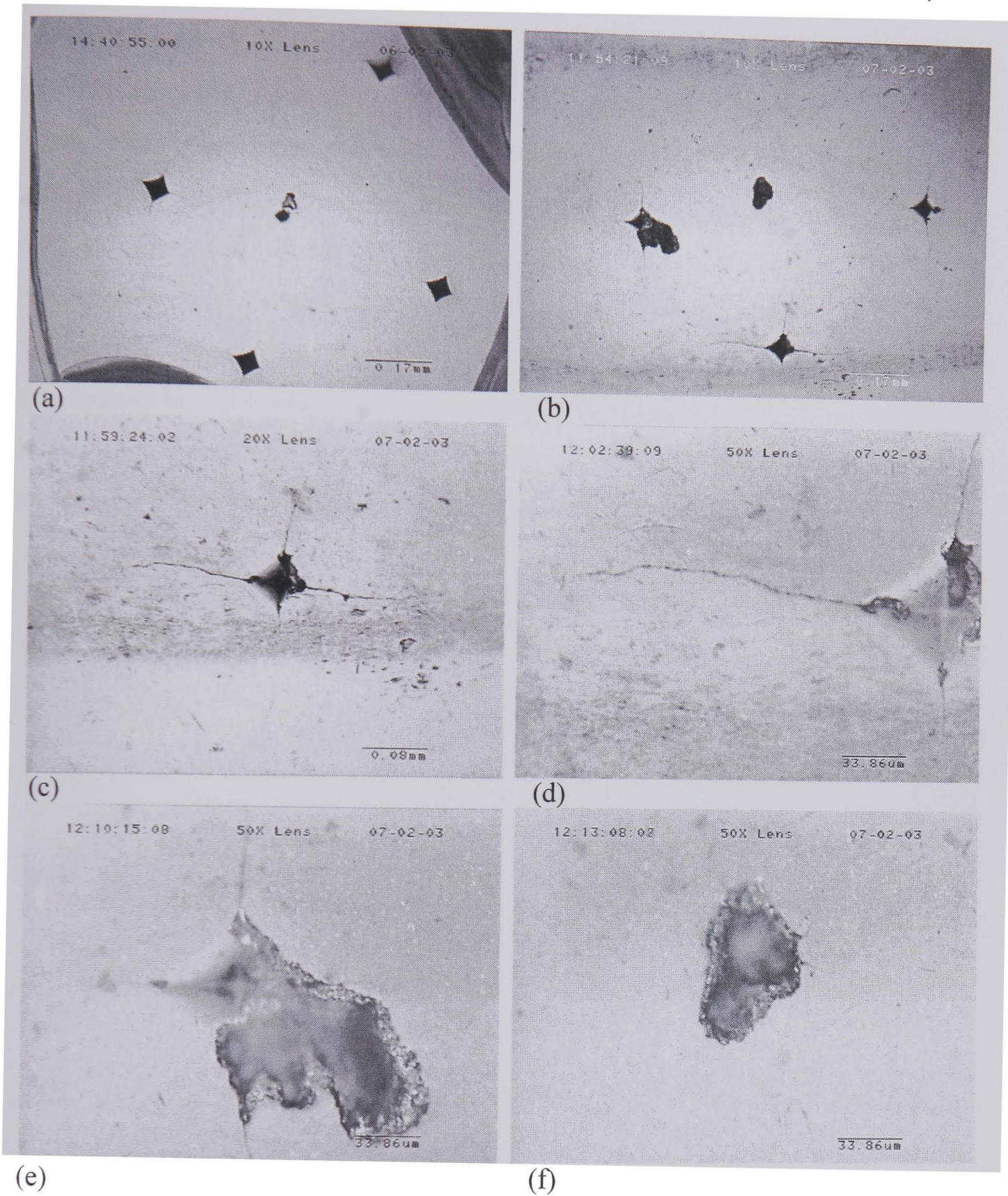


Figure 5.4 Surface damage resulting from ceramic-steel contact. (a) pre-test (b) fatigue spall and crack propagation (c, d) fatigue crack propagation (e, f) fatigue spall; Test 1

Figure 5.5 shows examples from test 2, again carried out in an HC R600a environment. The time to failure was only 3 minutes. Figure 5.4(b) shows a catastrophic failure. The temperature range was 15-20°C while the pressure of the subcooled refrigerant liquid was increased from the initial value of 3 to 3.4 bar (gauge). The shaft speed and maximum pressure were 2000 rpm and 3 GPa respectively. In addition, fatigue spall traces of rolling wear can be seen in Figure 5.4(b). The catastrophic failure in test 2 is the result of a 1°C difference in temperature to test 1 which attributes to 0.05 bars in pressure, orientation of indents in the contact path, the distance between indents and indent load see Figure 5.4(a) and Figure 5.5(a). indent load of 10 kg resulted in low residual stress field.

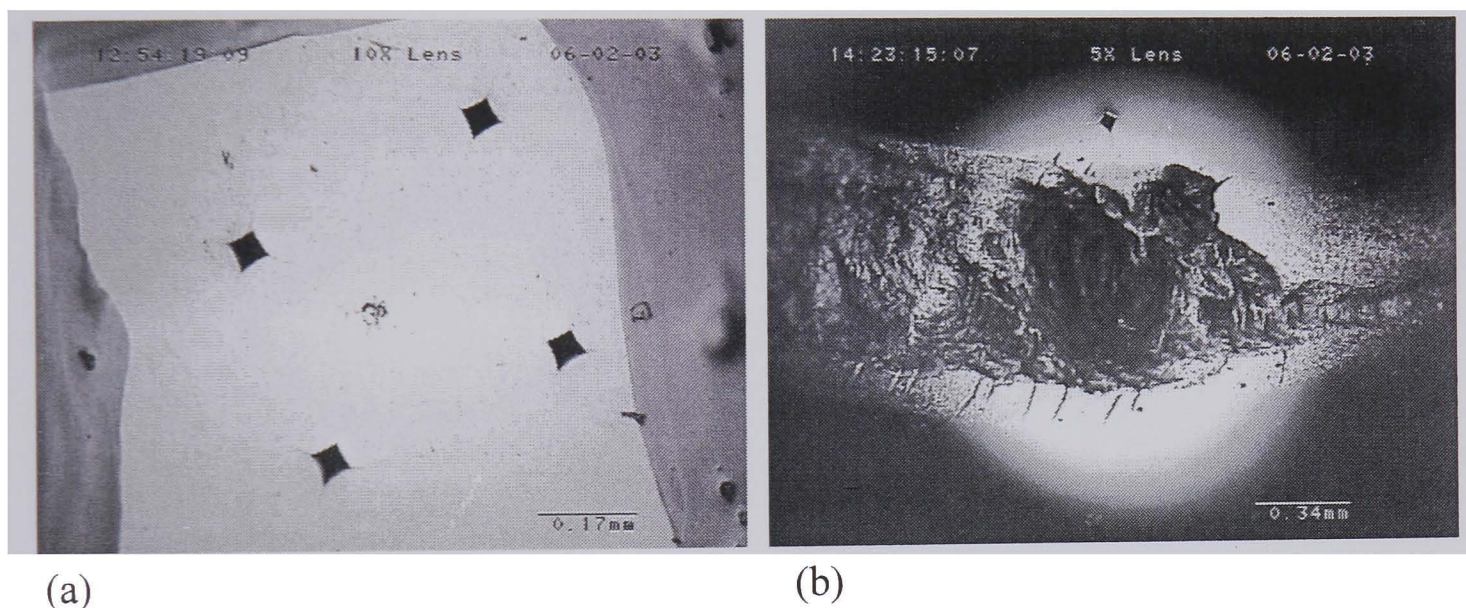


Figure 5.5 Surface damage resulting from ceramic-steel contact. (a) pre-test (b) fatigue spall; Test 2

In test 3 HFC (R134a) was used. The initial minimum temperature of the test was -3°C and the corresponding pressure was 2.58 bar. The temperature increased during the test from its initial value to 17°C and pressure increased to 5.4 bar. The failure was occurred after 4 hours 30 minutes. The saturation conditions of R134a are compared to the experimental conditions in Figure 5.2.

Optical micrographs for test 3 are shown in Figure 5.6(a, b). This test was conducted in the HFC (R134a) refrigerant environment. The maximum pressure was 3 GPa with a shaft speed of 2000 rpm. The minimum temperature was -3°C which

increased to 17°C. The liquid refrigerant pressure increased from 2.58 bar (gauge) to 5.4 bar (gauge). The wear in this case may be erosion which can be seen at the edges of the indents Figure 5.6(a, b). The generation of the secondary crack in Figure 5.6(a) leads to surface removal between cracks and ends in a catastrophic failure. Figure 5.6(b) represents no such situation but the gradual removal of material on the edges of the indent propagates outward. The amount of material removal may be different when the angle and orientation of the indent in the contact path is different. The failure occurred after 4 hours 30 minutes. Here the fatigue life is the same as that of the specimen 4 tested in the R600a environment. The fatigue crack propagation is also a conspicuous phenomenon observed in this case.

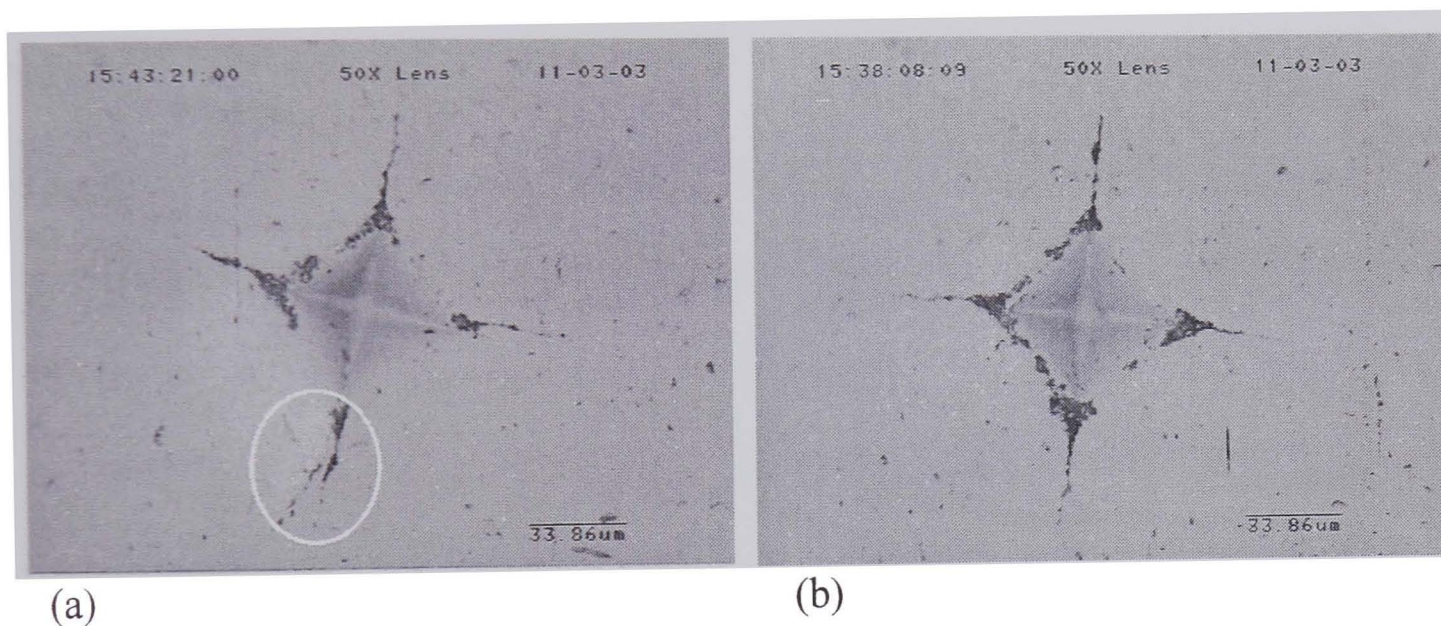


Figure 5.6 Surface damage resulting from ceramic-steel contact in R134a environment; Test 3

In test 4 the initial temperature of the chamber was -3°C with initial pressure of the refrigerant as 1.7 bar (gauge). Temperature gradually rose to 29°C and pressure to 3.88 bar during the test period. Failure occurred after 4 hours and 30 minutes. The actual saturation conditions of the refrigerant are compared in Figure 5.3 to theoretical conditions. It is confirmed that the state of the refrigerant was subcooled liquid. Similarly the refrigerant used in tests 5-12 was R600a.

Figure 5.7 shows light microscopic result of test 4. This result was recorded at 4 hours and 1 minute. The shaft speed was 2000 rpm and shaft load was 3 GPa. An

obvious crack development and propagation leads to delamination. Figure 5.8 shows the failure in the lower indent as delamination.

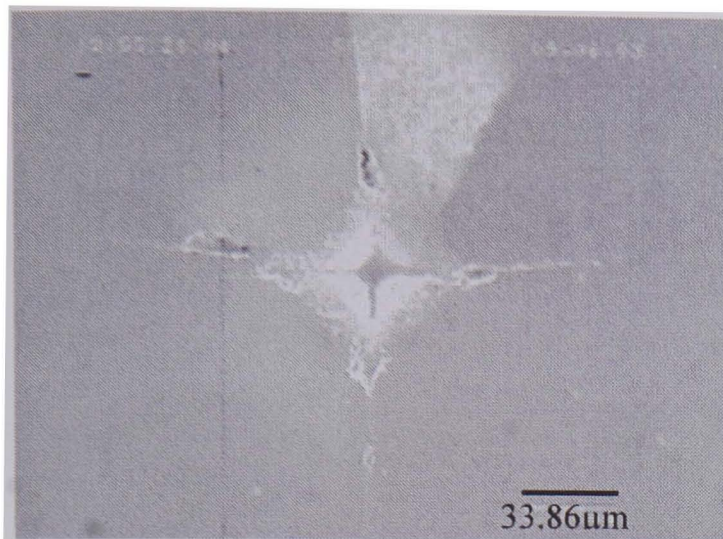


Figure 5.7 Light micrograph showing fatigue crack propagation (specimen-4)

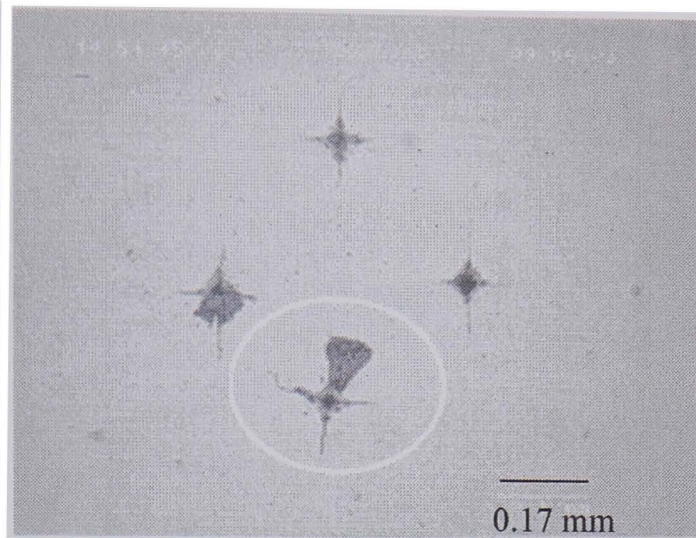


Figure 5.8 Light micrograph failure due to delamination (specimen-4)

Figure 5.9 shows a light micrograph of the specimen 5 before test. This specimen was tested in R600a refrigerant lubrication. The spindle speed for the experiment was set to 2000 rpm. The maximum contact pressure was 3 GPa. The indent loading was 1 kg as set by Vickers' indenter. The specimen failed after 13.5 hours and fatigue cycles were recorded as 1.61×10^6 . A light micrograph of specimen 5 is shown in Figure 5.10 after failure has occurred.

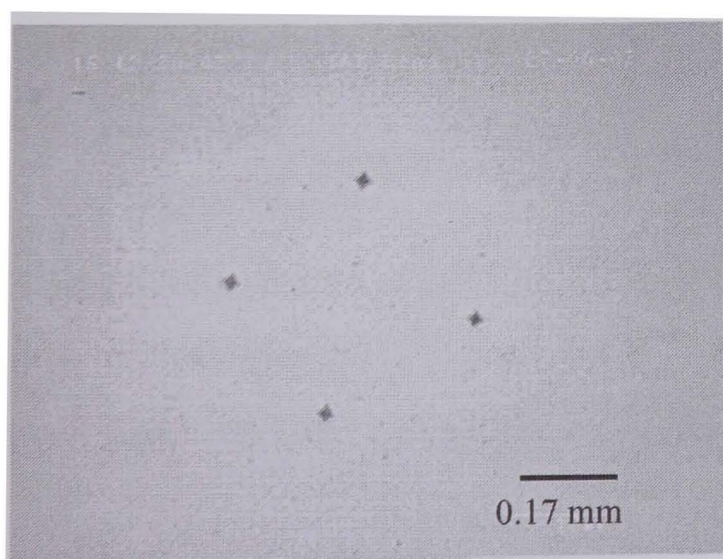


Figure 5.9 Light micrograph before test (specimen-5)

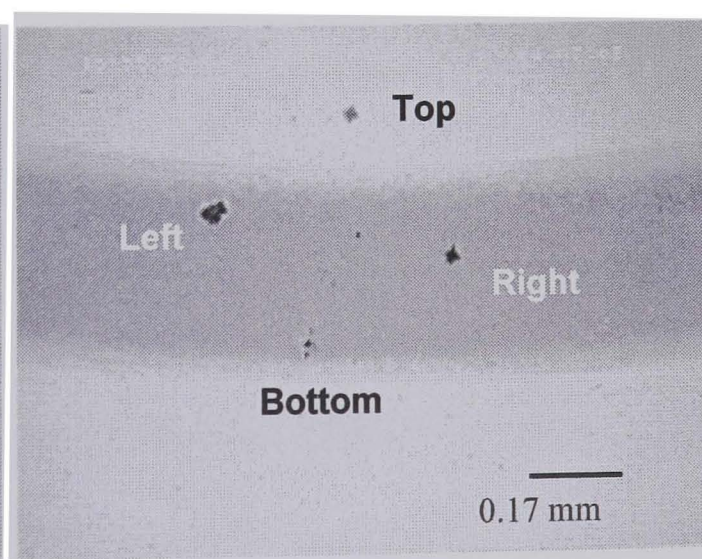


Figure 5.10 Light micrograph after failure (specimen-5)

In test 6 the initial temperature was 1°C and the pressure was 1.9 bar (gauge). Temperature was increased to 17° C while pressure increased to 2.2 bar. Failure happened after 18 minutes. Figure 5.11 shows a light micrograph at 13 minutes of test time. Figure 5.12 shows lower indent failure after 14 minutes.

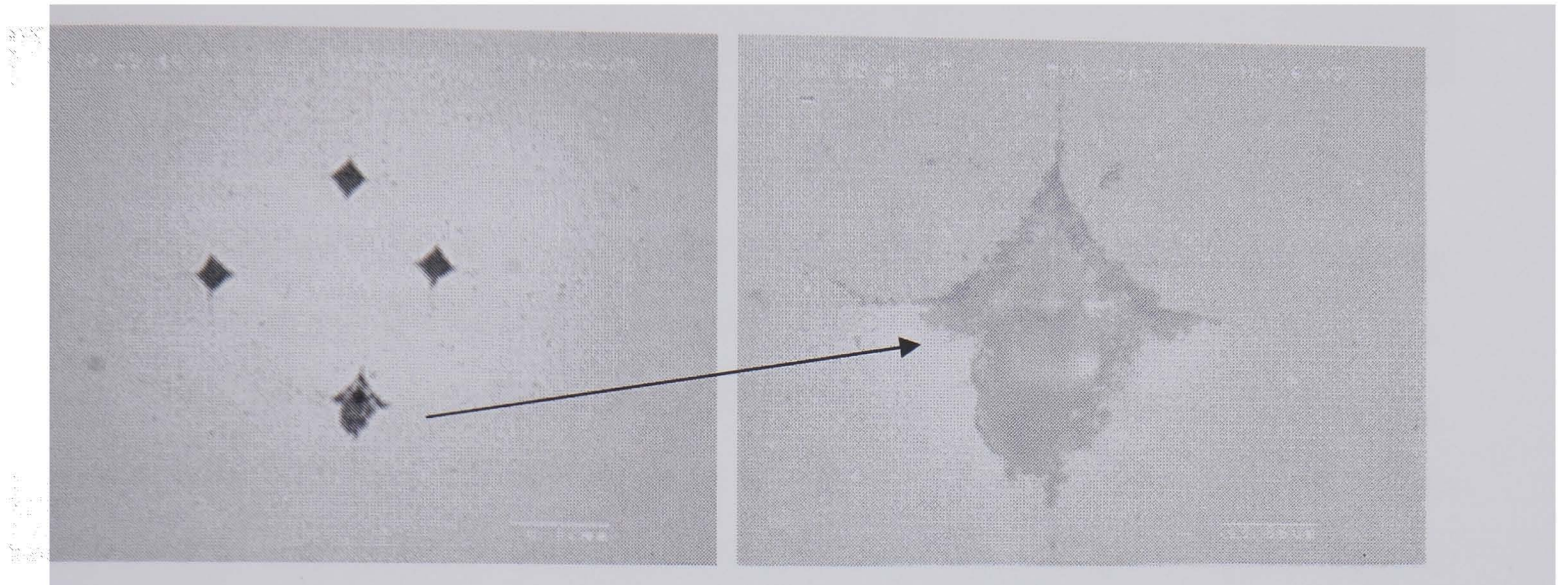


Figure 5.11 Light micrograph for at 13 minutes test time (specimen-6)

Figure 5.12 Light micrograph at 14 minutes test time, lower indent (specimen-6)

In test 7 initial minimum temperature of the test was -1° C and the corresponding pressure was 1.88 bar. The temperature increased during the test from its initial value to 19° C and pressure increased to 3.15 bar. The failure occurred after 5 minutes.

Failure in test 8 occurred after 9 minutes where the initial and final temperatures were 6°C and 14°C respectively and the corresponding pressures were 2.15 and 2.35 bar respectively.

In test 9 and 10 failure occurred at 9 and 7 minutes respectively. In both tests the pressure temperature conditions were at sub-cooled liquid state. Figure 5.13 shows light micrographs for specimen 9. In this specimen a spall failure occurred due to crack initiation and propagation other than the crack from the induced indent.

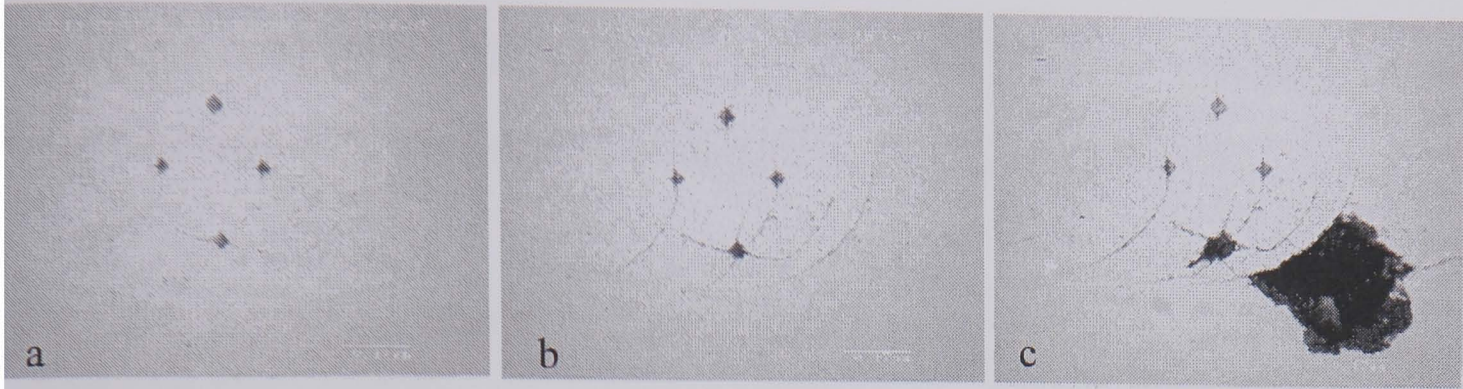


Figure 5.13 Failure process of specimen 9; (a) 5 minutes (b) 8 minutes and (c) 9 minutes

Initial temperature in test 11 increased from -3°C to 14°C while the pressure changed from an initial value of 1.65 bar to 2.3 bar. Failure occurred after 3 minutes. In test 12 initial minimum temperature of the test was -6°C and the corresponding pressure was 1.48 bar. The temperature increased during the test from its initial value to 6°C and pressure increased to 1.95 bar. The failure occurred after 2 minutes. Figure 5.14 is a light micrograph showing positioning and orientation of the induced indent and radial crack defects in the contact path. Figure 5.15 shows radial crack propagation that leads to delamination failure.



Figure 5.14 Light micrograph showing failure in specimen 12

Figure 5.15 Fatigue crack propagation in specimen 12

Table 5.3 is a rearrangement of table 5.2 to show a comparison of fatigue life performance of the rolling contact hybrid ceramic ball bearing with refrigerant R600a (HC refrigerants, $\text{CH}(\text{CH}_3)_3$ 2-Methyl Propane, Isobutane) and R134a (HFC

refrigerants, CH_2FCF_3 , 1,1,1,2-Tetra-Fluoroethane) lubrication. Specimens 1-5 were tested with a spindle speed of 2000 rpm and contact stress of 3 GPa.

Table 5.3 Test programme

Test	Contact Pressure (GPa)	Time to failure (Hrs)	Indent load (kg)	Refrigerant	Shaft speed (rpm)	Fatigue cycles
1	3	0.17	10	R600a	2000	2.00E+04
2	3	0.05	10	R600a	2000	6.00E+03
5	3	13.5	1	R600a	2000	1.61E+06
3	3	4.5	5	R134a	2000	5.35E+05
4	3	4.5	5	R600a	2000	5.39E+05
5	3	13.5	1	R600a	2000	1.61E+06
8	6	0.15	1	R600a	2000	1.77E+04
9	6	0.15	1	R600a	2000	1.93E+04
10	6	0.12	1	R600a	2000	1.33E+04
7	6	0.08	1	R600a	2000	1.06E+04
6	5	0.3	5	R600a	3000	6.08E+04
11	7	0.05	5	R600a	3000	8.93E+03
12	7	0.03	5	R600a	3000	8.34E+03
3	3	4.5	5	R134a	2000	5.35E+05
4	3	4.5	5	R600a	2000	5.39E+05
6	5	0.3	5	R600a	3000	6.08E+04
11	7	0.05	5	R600a	3000	8.93E+03
12	7	0.03	5	R600a	3000	8.34E+03
3	3	4.5	5	R134a	2000	5.35E+05
4	3	4.5	5	R600a	2000	5.39E+05
4	3	4.5	5	R600a	2000	5.39E+05
6	5	0.3	5	R600a	3000	6.08E+04
8	6	0.15	1	R600a	2000	1.77E+04
11	7	0.05	5	R600a	3000	8.93E+03

Specimens 1 and 2 were induced with an indent at 10 kg load by Vickers's indenter. Specimen 3 was tested in R134a refrigerant environment. The induced indent defect for specimens 3 and 4 was induced by Vickers's indenter applying 5 kg load. Specimen 5 was indented with 1 kg indenting load. The fatigue life performance at different indent loads is shown in Figure 5.16.

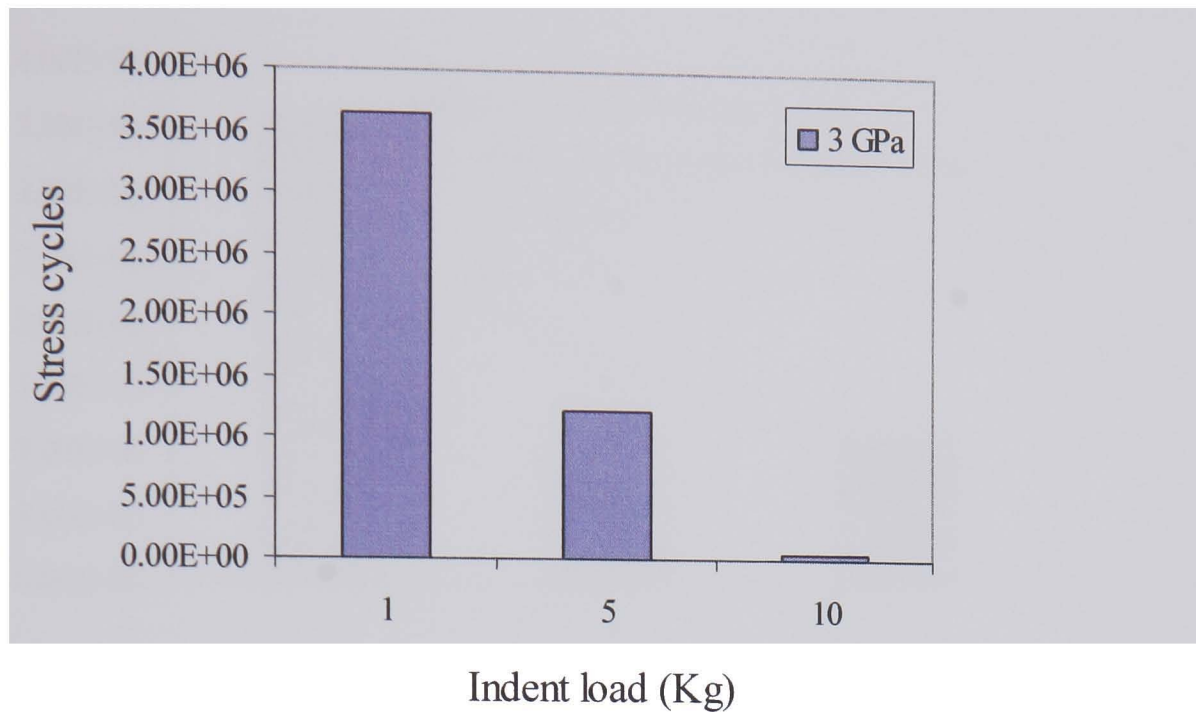


Figure 5.16 Fatigue life performances of specimens 1, 4, and 5 at different indent loading

In Tests 5, 7, 8, 9 and 10 the refrigerant environment was R600a. The induced defect loading was kept constant in these tests as 1 kg and the maximum contact pressure was raised from 3 to 6 GPa. A sharp decline in fatigue lives and fatigue cycles to failure for specimens 7, 8, 9 and 10 can be seen when the contact pressure increased to 6 GPa as compared to maximum contact pressure of 3 GPa for specimen 5.

Specimen 6 was subjected to 5 GPa, specimens 11 and 12 were tested at 7 GPa maximum contact pressure. The indent loading for specimens 6, 11 and 12 was 5 kg with a spindle speed of 3000 rpm. The fatigue life performances of these specimens are shown in Figure 5.17.

For specimens 6, 11 and 12 the indent loading increased to 5 kg and maximum contact pressures 5, 7 and 7 GPa respectively. The spindle speed was also increased and set to 3000 rpm for these tests. The fatigue life performance for specimens 3, 4, 6, 11 and 12 is compared in Figure 5.18. Specimens 4, 5, 6, 11 and 12 were indented by 5 kg test details are provided in Table 5.3.

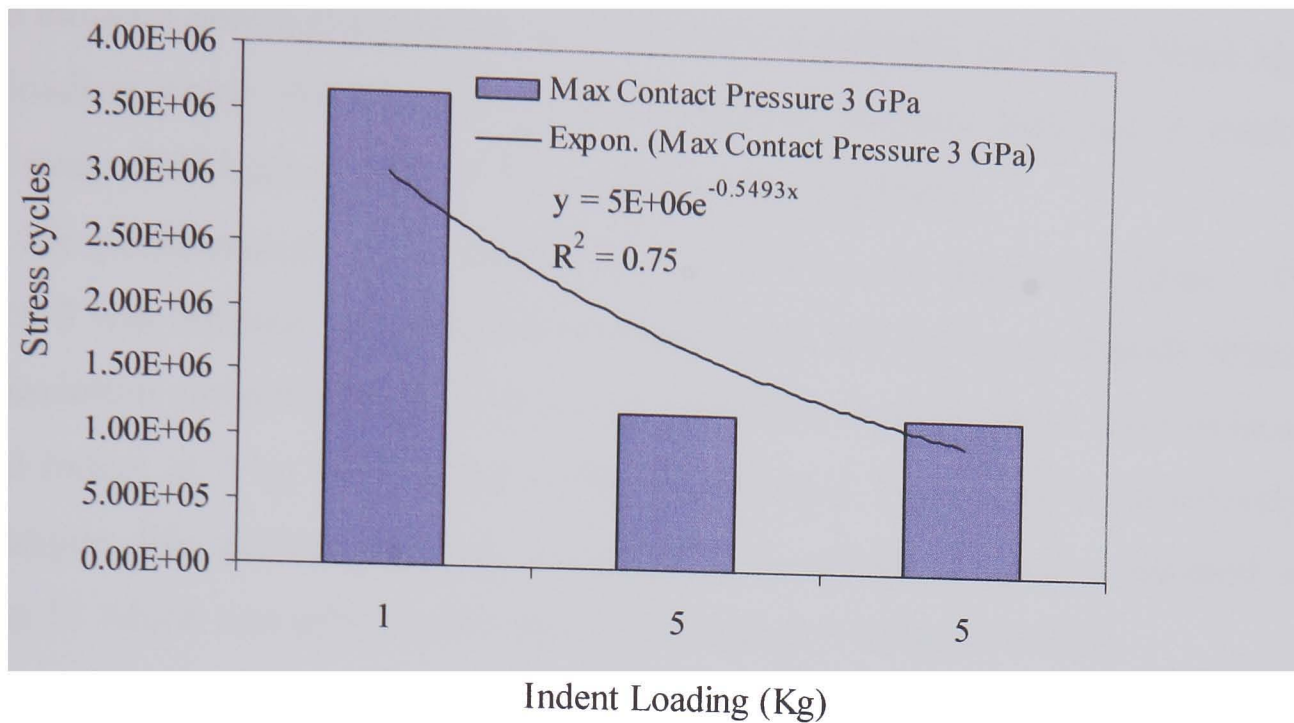


Figure 5.17 Fatigue life performances of specimens 6, 11 and 12 at different indent loading

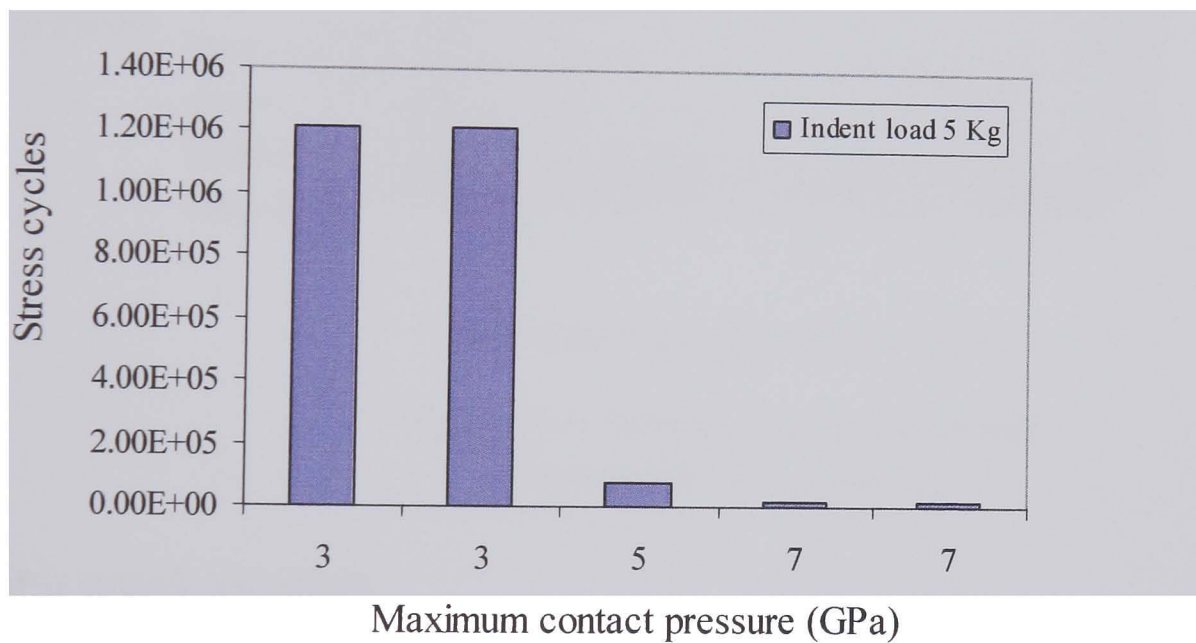


Figure 5.18 Fatigue life performances for specimens 3, 4, 11 and 12

The indent loading has influence on the geometry of the defect being induced, hence a decline in the fatigue life of the specimen occurs when the indent loading has increased to 7 kg. The specimens 3 and 4 were failed in 4.5 hours. Specimen 6 with indent loading of 5 kg failed in 5 hours while 11 and 12 with indent loading of 7 kg failed in 0.05 and 0.03 hours respectively. Other test conditions are provided in table

5.3. The induced defect changes the residual stress magnitude and field. Since high indent loading cause defects with reduced residual stresses therefore a weaker residual stress field leads to shorter fatigue life of the specimens.

Fatigue life performances of specimens 4, 6, 8 and 11 are shown in Figure 5.19. Specimen 8 was induced with 1 kg indent loading; the life decline is directly related to the maximum contact pressure comparing specimens 4 and 6 which were induced with and indent at 5 kg loading but contact pressure at 3 and 5 GPa respectively, while fatigue life performance of specimen 8 is relatively good compared to specimen 11 which was subjected to maximum contact loading of 5 GPa.

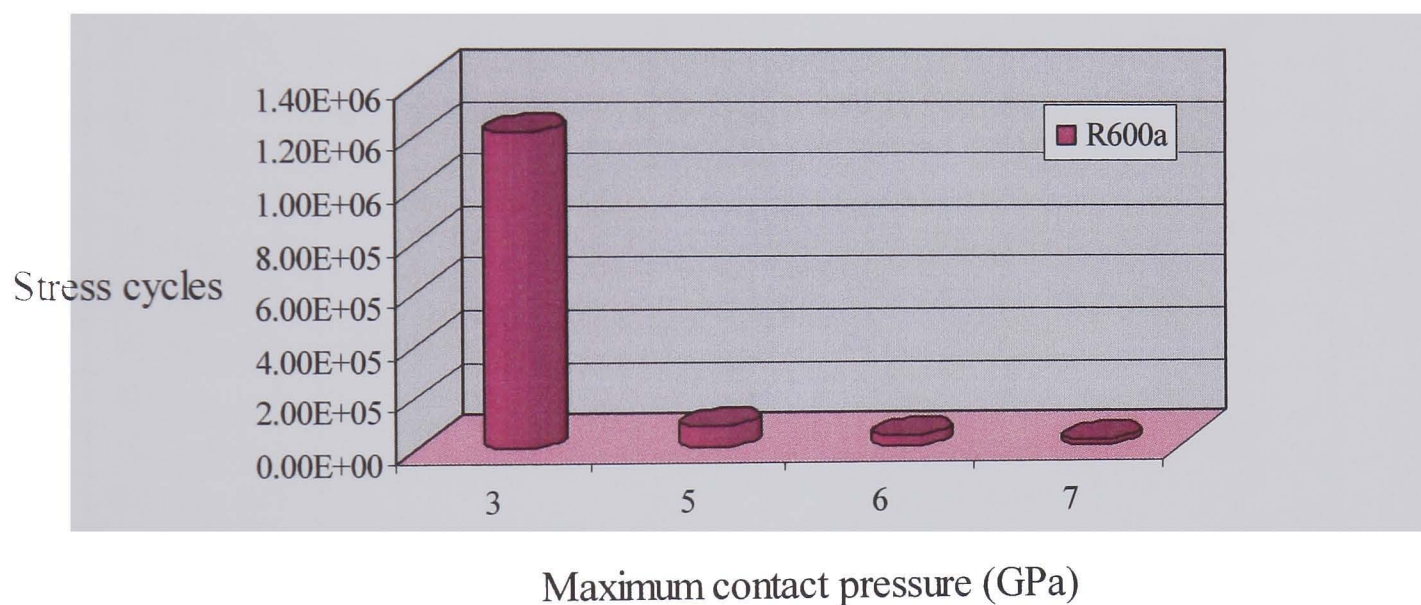


Figure 5.19 Fatigue life performances of specimens 4, 6, 8 and 11

5.3. Ring crack location

Table 5.4 presents test results in the order they were performed. Ring crack location and positioning has an influence on the fatigue life performance. The test programme for comparing fatigue life performance based on the ring crack position and orientation in the contact path is shown in table 5.5 and table 5.6. All the tests were conducted at a shaft speed of 2000 rpm. Hydrocarbon HC (R600a) refrigerant was used as lubricant during the rolling contact fatigue testing. The kinematic viscosity of the saturated liquid R600a at 15° C is $2.759E-07 \text{ m}^2 / \text{s}$.

Table 5.4 Test results at 2000 rpm spindle speed

Test Ball	Test Ball condition	Environment	Max. contact pressure (GPa)	Time to Failure	Stress cycles
13	25 deg (v)	R600a -liquid	3	abandoned	-
14	smooth specimen	-	3	4hrs 44min	1.28×10^6
15	smooth specimen	-	3	14hrs 10min	3.83×10^6
16	30 deg (h)	-	3	6hrs	1.62×10^6
17	30 deg (h)	-	5	18hrs 23min	4.96×10^6
18	30 deg (h)	-	5	1hr 09min	3.11×10^5
19	30 deg (h)	-	6	0hr 42min	1.89×10^5
20	30 deg (h)	-	4	1hr 33min	4.19×10^5
21	30 deg (v)	-	3	17hrs 0min	4.59×10^6
22	30 deg (v)	-	4	4hrs 0min	1.08×10^6
23	30 deg (v)	-	5	0hr 19min	8.55×10^4
24	30 deg (v)	-	6	0hr 04min	1.80×10^4
25	30 deg (v)	R600a - vapour	3	1hr 28min	3.96×10^5
26	30 deg (v)	-	4	0hr 48min	2.16×10^5
27	30 deg (v)	-	5	0hr 17min	7.65×10^4
28	30 deg (v)	-	6	0hr 03min	1.35×10^4
29	30 deg (v)	R600a - liquid	5	1hr 20min	3.60×10^5
30	30 deg (v)	-	6	0hr 53min	2.39×10^5
31	30 deg (h)	-	3	2hr 46min	7.47×10^5
32	30 deg (v)	-	3	11hr 30min	3.11×10^6
33	30 deg (v)	-	3	2hr 41min	7.25×10^5
34	30 deg (v)	-	4	2hr 2min	5.49×10^5
35	30 deg (v)	-	4	0hr 33min	1.49×10^5
36	30 deg (h)	R600a - vapour	3	3hr 57min	1.07×10^6
37	30 deg (h)	-	3	00hr59min	2.66×10^5
38	30 deg (h)	-	4	00hr51min	2.30×10^5
39	30 deg (h)	-	5	00hr21min	9.45×10^4
40	30 deg (h)	-	6	00hr09min	4.05×10^4
41	30 deg (h)	-	3	02hr40min	7.20×10^5
42	18 deg (h)	R600a - liquid	3	12hr49min	3.46×10^6
43	18 deg (h)	-	4	18hr04min	4.88×10^6
44	18 deg (h)	-	5	04hr 17min	1.16×10^6
45	18 deg (h)	-	5	41hr 47min	1.13×10^7
46	18 deg (v)	-	3	20hr 48min	5.62×10^6

Table 5.5 Test Programme (ring crack positioning as figure 5.20a)

Test	Contact Pressure (GPa)	Time to failure	Stress cycles
31	3	2 hr 46 min	7.47×10^5
20	4	1 hr 33 min	4.19×10^5
18	5	1 hr 09 min	3.11×10^5
19	6	0 hr 42 min	1.89×10^5

Table 5.6 Test Programme (ring crack positioning as figure 5.20b)

Test	Contact Pressure (GPa)	Time to failure	Stress cycles
33	3	2 hr 41 min	7.25×10^5
35	4	0 hr 33 min	1.49×10^5
23	5	0 hr 19 min	8.55×10^4
24	6	0 hr 04 min	1.80×10^4

Positioning of the ring crack into the contact path for tests 18, 19, 20 and 31 is shown in figure 5.20(a) and for tests 23, 24, 33 and 35 is shown in figure 5.20(b). The angle of impact for inducing a ring crack on the ball surface was 30° . The refrigerant state was sub-cooled liquid.

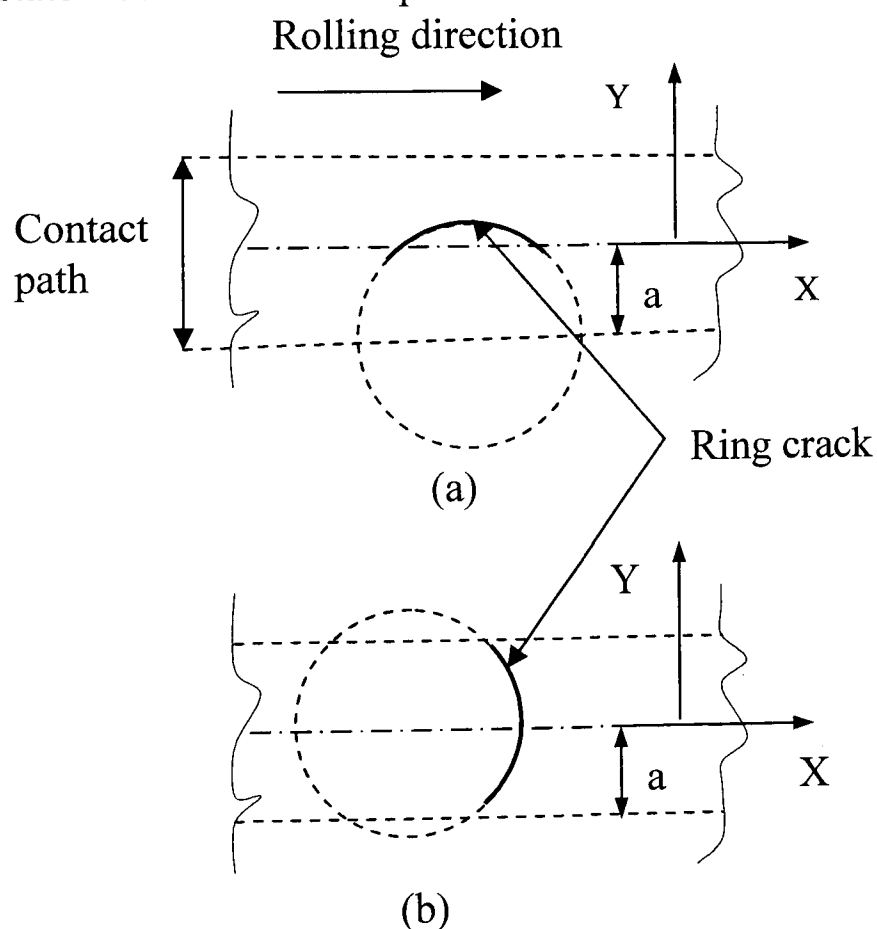


Figure 5.20 Schematic showing, (a, b) ring crack positioning in the contact track

Figure 5.21 shows a light micrograph for specimen 31 showing its ring crack defect positioning in the contact path. Figure 5.22 was recorded at 2 hours and 22 minutes. The secondary crack initiation and propagation due to induced ring crack defect is shown in the light micrograph.

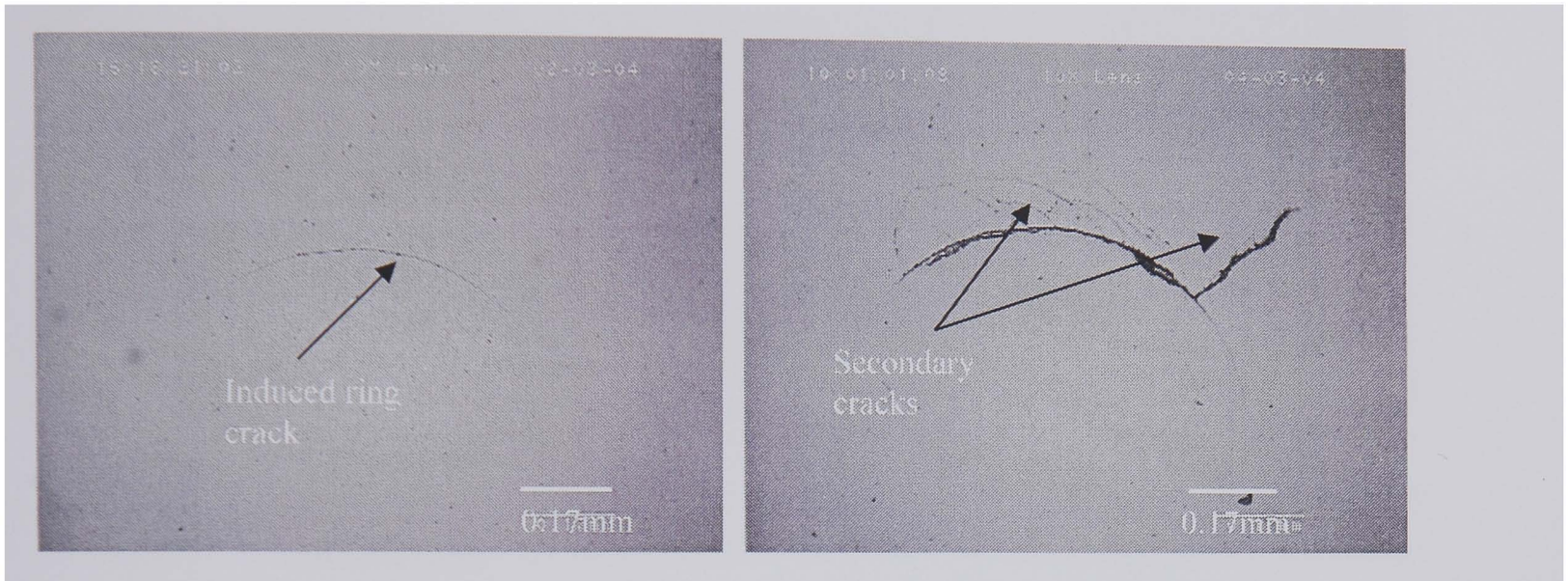


Figure 5.21 Light micrograph; induced ring crack and its positioning in the contact track in specimen 31

Figure 5.22 Light micrograph; secondary cracks initiation and propagation in specimen 31

The specimen failed into a spall after next 24 minutes. Figure 5.23 is a light micrograph of specimen 31 showing fatigue spall after 2 hours and 46 minutes.

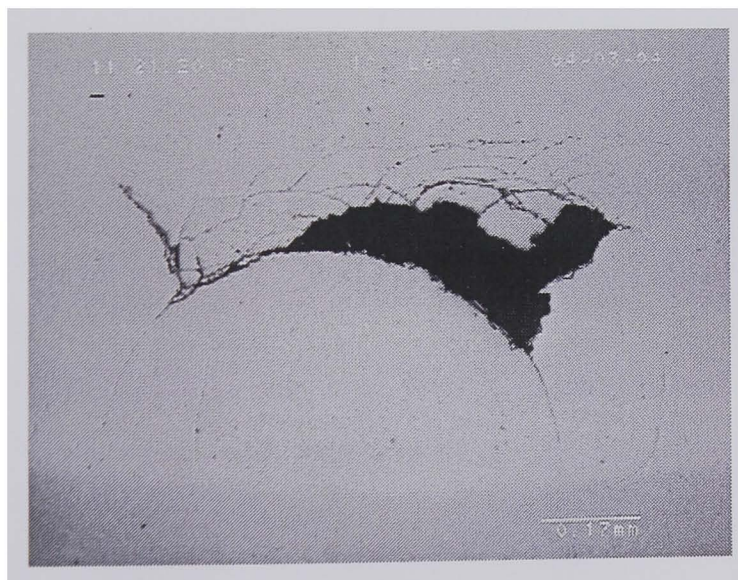


Figure 5.23 Light micrograph; spall failure in specimen 31

Ring crack positioning for specimen 35 is shown in figure 5.24 in the following light micrograph with dark field effects. Secondary crack initiation and propagation is

seen in the light micrograph recorded after 27 minutes of testing in figure 5.25. Specimen 35 failed into a spall after 33 minutes.

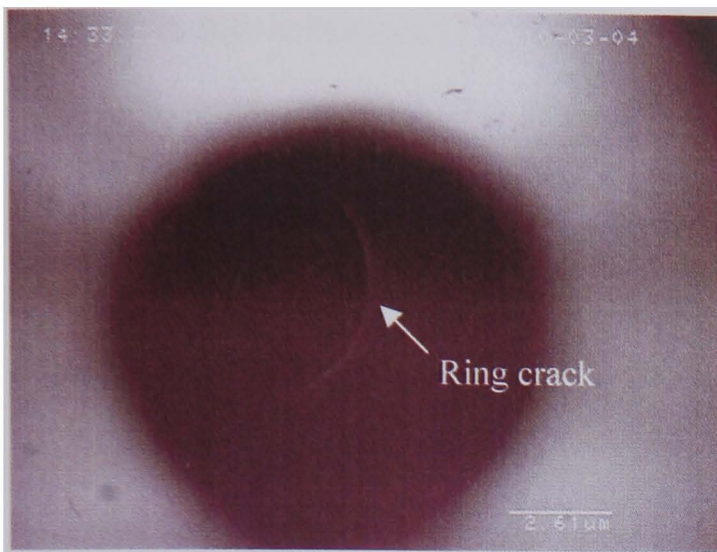


Figure 5.24 Light micrograph; dark field showing crack position in contact path

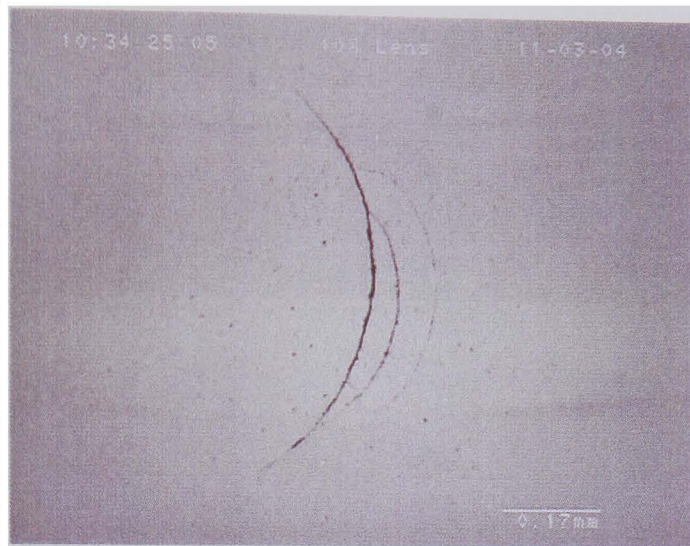


Figure 5.25 Light micrograph; secondary crack initiation and propagation

Fatigue life performance of specimens 18, 19, 20 and 31 with horizontal positioning of the ring crack in the contact path is compared with the specimens 23, 24, 33 and 35 with vertical positioning of the ring crack in the contact path. The comparison of fatigue life performance as influenced by different positioning of the ring crack in the contact path is shown in Figure 5.26.

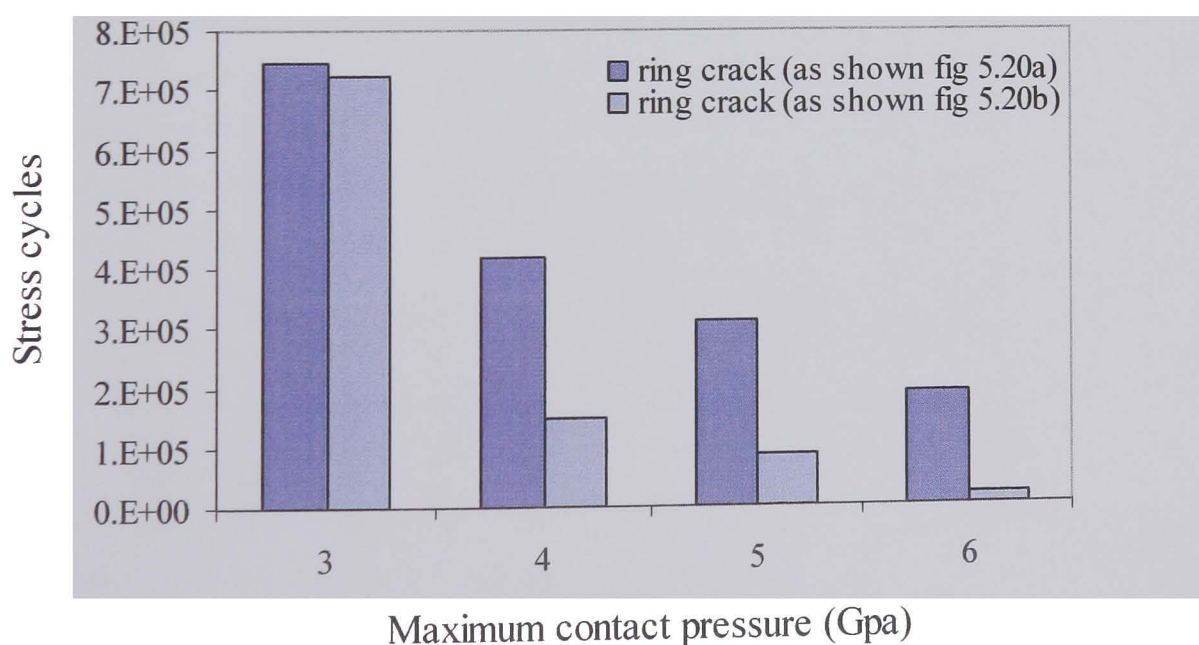


Figure 5.26 Fatigue life performances; influenced by ring crack position in the contact path

5.4. Ring crack geometry

Fatigue life performances of the rolling contact bearing elements with refrigerant lubrication are influenced by the induced ring crack geometry. Table 5.7 showing ring crack geometry details of the tested specimens.

Table 5.7 RCF tested specimens with different ring crack geometry

Specimen	radius (mm)	Arc length	arc area (mm ²)	maximum contact pressure (GPa)	Time to failure (hr)	Stress cycle
32	0.377	0.48757	0.117808	3	11.5	3.11×10^6
33	0.405	0.737959	0.14213	3	2.683	7.24×10^5
34	0.356	0.759273	0.108376	4	2.033	5.49×10^5
35	0.405	0.918915	0.158885	4	0.55	1.49×10^5

The influence of the ring crack radius, length of the ring crack arc and area of the circle of the ring on the fatigue life performance is shown in figure 5.27.

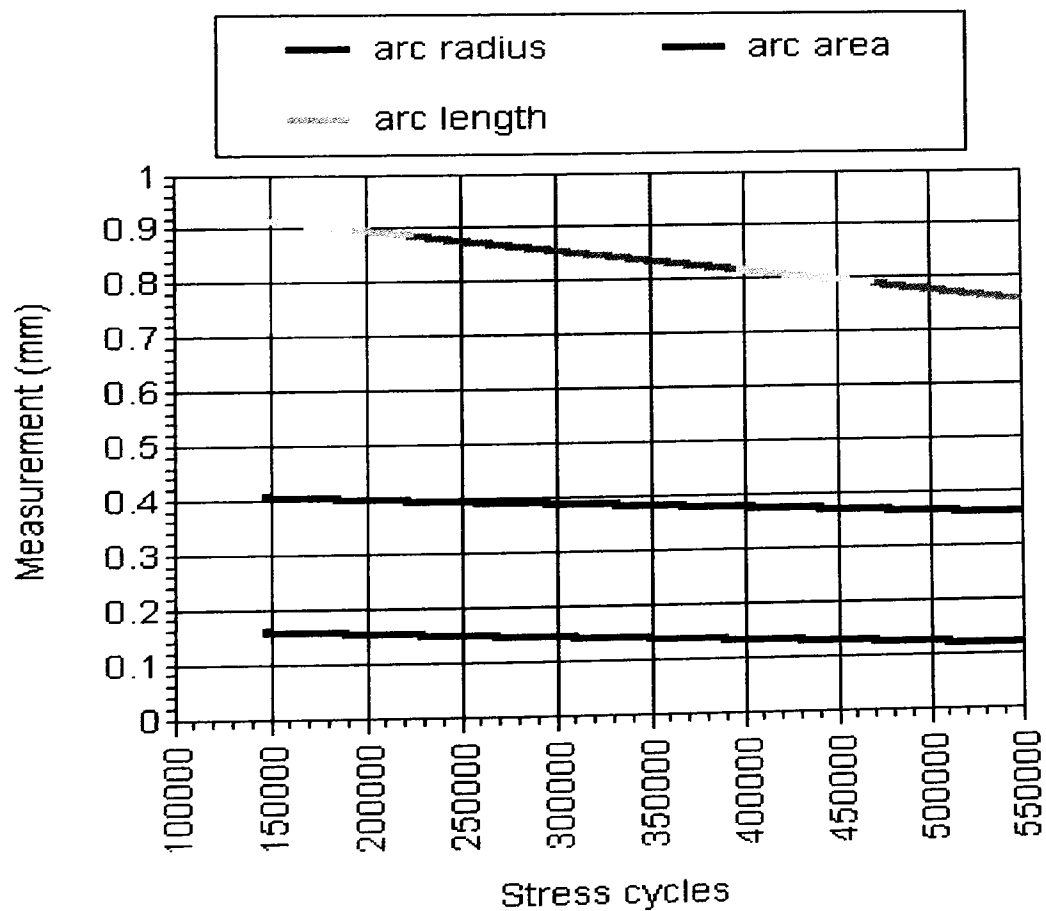


Figure 5.27 Fatigue life performance; as influenced by ring crack geometry

The exponential relationship of the ring crack circle area and radius of the crack circle to the fatigue life performance is shown in figure 5.28.

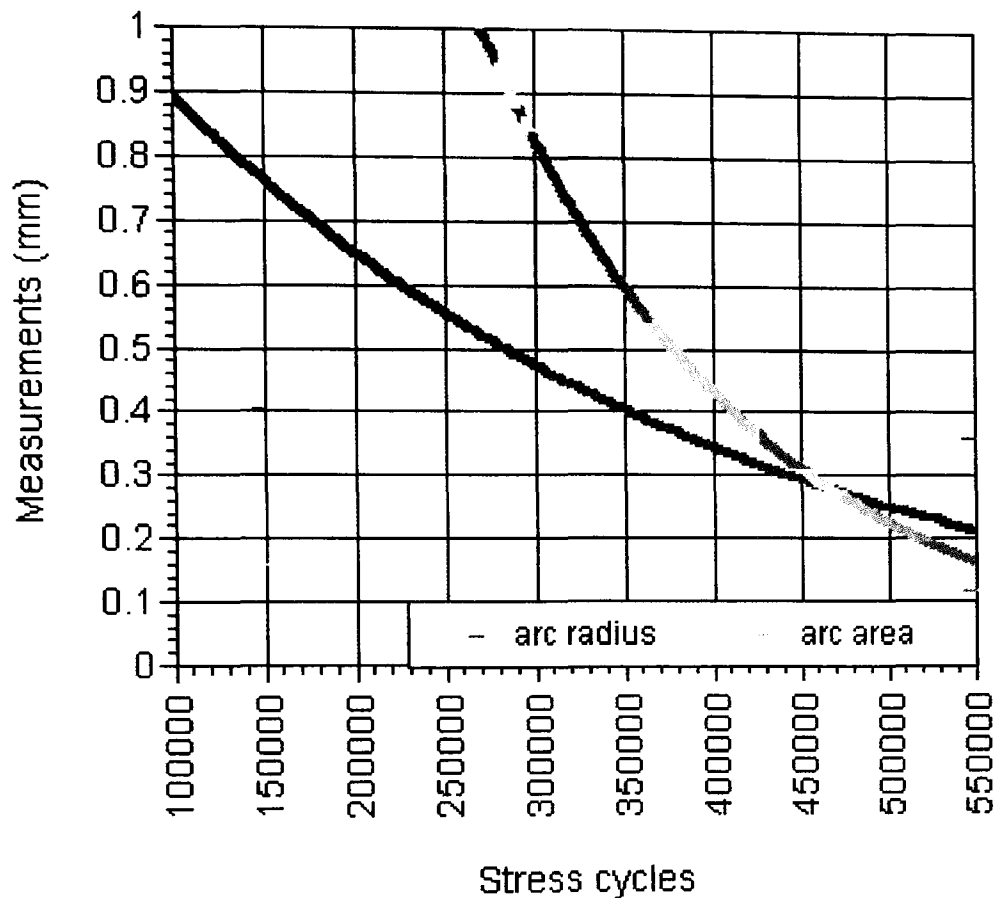


Figure 5.28 Fatigue life performance; as influenced by ring crack geometry

Figure 5.29 shows a light micrograph for specimen 32. This result was recorded at 7 hours and 23 minutes of test time. The maximum contact pressure for the specimen was 3 GPa. The secondary crack initiation and propagation in the contact path led to a mixed failure mechanism of delamination and fatigue spall after 11 hours 30 minutes of test time see figure 5.30.

Specimen 33 with slightly different ring crack geometry compared to specimen 32 was subjected to 3 GPa maximum contact pressure. The specimen failed into a fatigue spall after 2 hours and 41 minutes of test time.

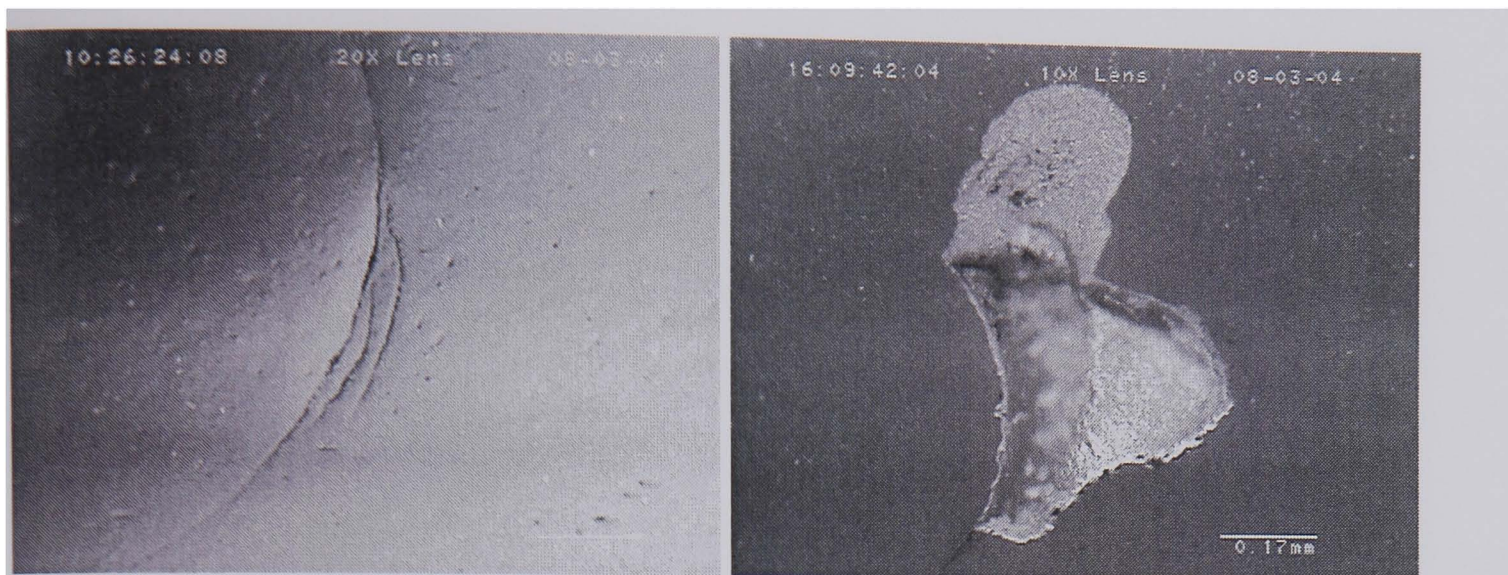


Figure 5.29 Light micrograph;
secondary cracks specimen 32

Figure 5.30 Light micrograph;
delamination and fatigue spall
specimen 32

Specimen 34 was tested with a maximum contact stress of 4 GPa. The ring crack geometry is shown in table 5.7. Secondary crack propagation was recorded at 1 hour 19 minutes of test time figure 5.31. The specimen failed into a fatigue spall at 2 hours and 2 minutes test time shown in a light micrograph figure 5.32.

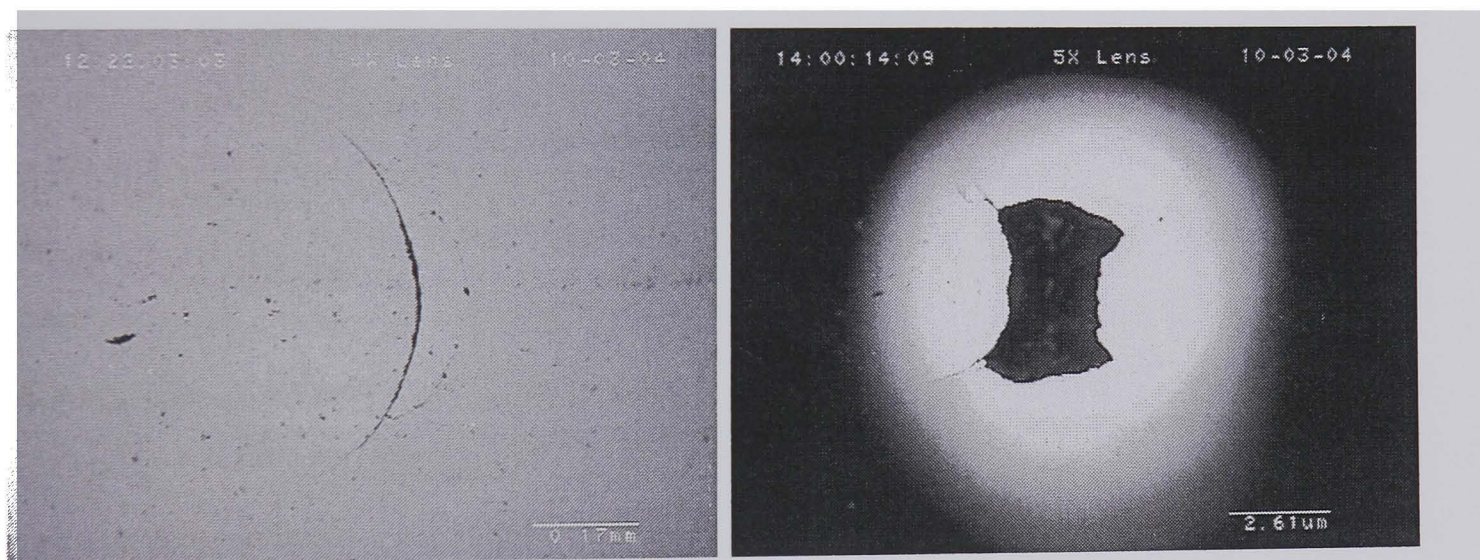


Figure 5.31 Light micrograph;
secondary cracks specimen 34

Figure 5.32 Light micrograph;
fatigue spall failure specimen 34

Specimen 35 was tested at 4 GPa contact stress. Secondary crack propagation is recorded at 27 minutes of test time shown in a light micrograph figure 5.33. The specimen failed into a fatigue spall after 33 minutes of test time. The fatigue spall is shown in figure 5.34 using dark field in the light micrograph.

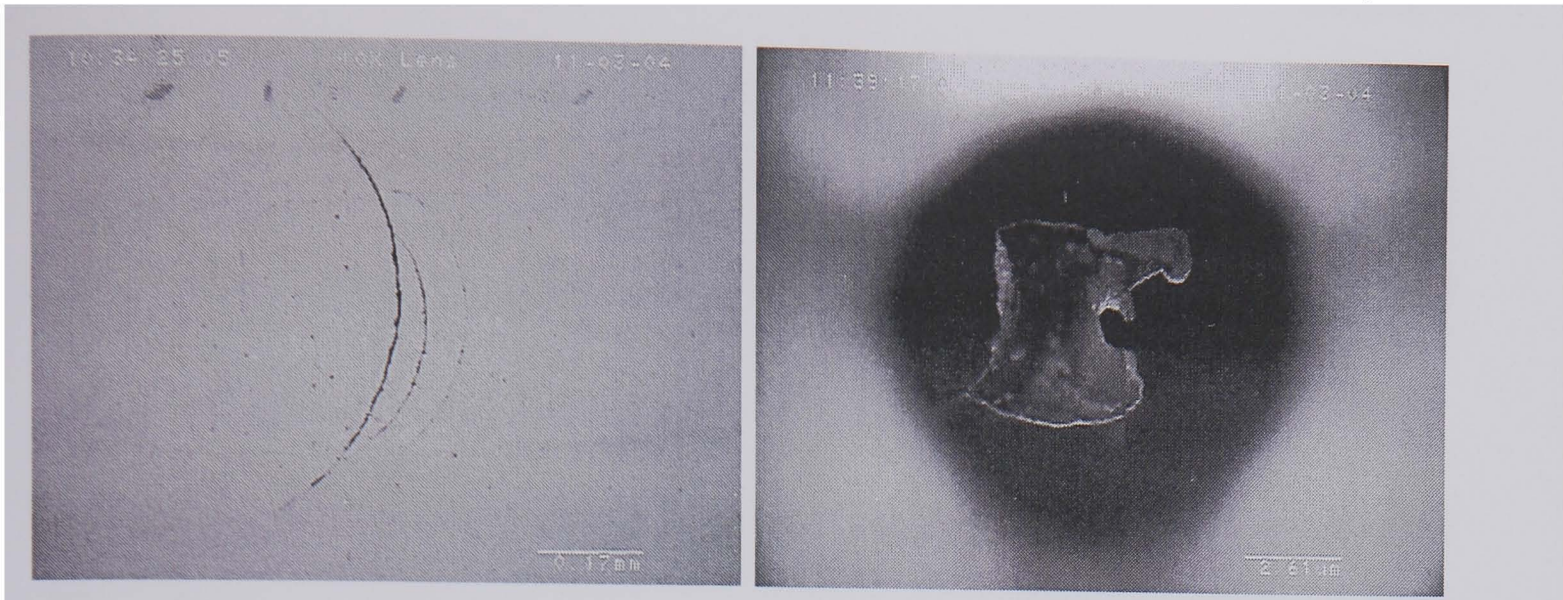


Figure 5.33 Light micrograph; secondary cracks propagation specimen 35

Figure 5.34 Light micrograph; dark field, spall specimen 35

5.5. State of the refrigerant

Refrigerant state has influence on the fatigue life performance. Fatigue life performance of rolling contact silicon nitride bearing elements with liquid refrigerant as lubrication is good in comparison to that tested with vapour state of the refrigerant lubrication. Table 5.8 provides details of the test conditions with liquid and vapour refrigerant lubrication.

The study of the influence of refrigerant state as lubrication is both important and interesting. The vapour state of the refrigerant lubrication has adverse effects on the fatigue life performance. Figure 5.35 shows a comparison of fatigue life performance of specimens 16,20,18,19,25,26,27 and 28. These specimens were tested at 3, 4, 5 and 6 GPa maximum contact stress. The ring crack positioning in the contact path was identical. The impact or swing angle for inducing ring crack was 30°. All tests were carried out at 2000 rpm spindle speed.

Figure 5.36 showing fatigue life performance comparison for specimens 18,19,23,24,27 and 28 and were tested at 2000 rpm spindle speed. The impact angle or swing angle for inducing ring crack was 30°. Fatigue life performance was compared with different positioning of the ring crack and was found to be enhanced when the ring crack is positioned horizontally to the contact path.

Table 5.8 Test results with different refrigerant state

Test	Contact Pressure (GPa)	Time to failure	Stress Cycles	Ring crack position	Refrigerant
16	3	6hrs	1.62×10^6	horizontal	liquid
20	4	1hr 33min	4.19×10^5	horizontal	liquid
18	5	1hr 9min	3.11×10^5	horizontal	liquid
19	6	0hr 42min	1.89×10^5	horizontal	liquid
21	3	17hrs	4.59×10^6	vertical	liquid
22	4	4hrs	1.08×10^6	vertical	liquid
23	5	0hr 91min	8.55×10^4	vertical	liquid
24	6	0hr 4min	1.80×10^4	vertical	liquid
25	3	1hr 28min	3.96×10^5	vertical	vapour
26	4	0hr 48min	2.16×10^5	vertical	vapour
27	5	0hr 17min	7.65×10^4	vertical	vapour
28	6	0hr 3min	1.35×10^4	vertical	vapour

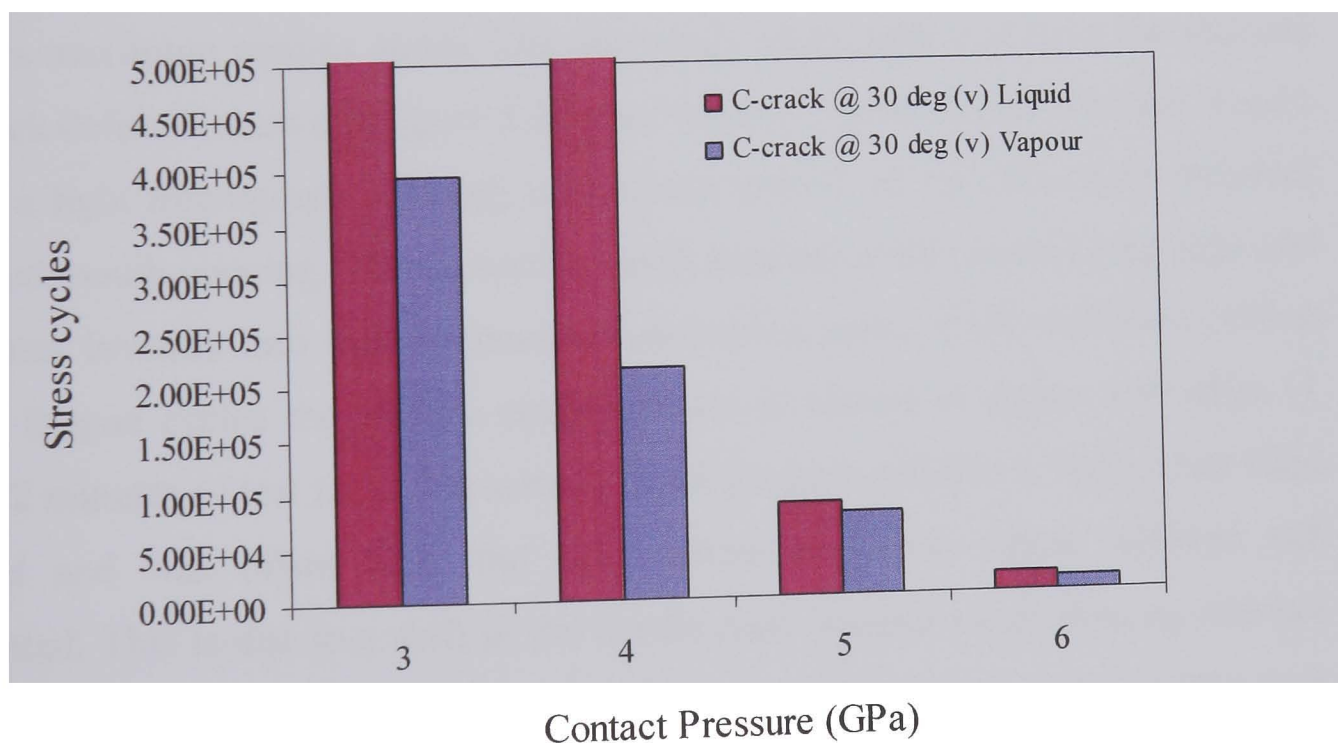


Figure 5.35 Fatigue life performance; liquid and vapour state of refrigerant (specimens 16,18,19,20,25,26,27 and 28)

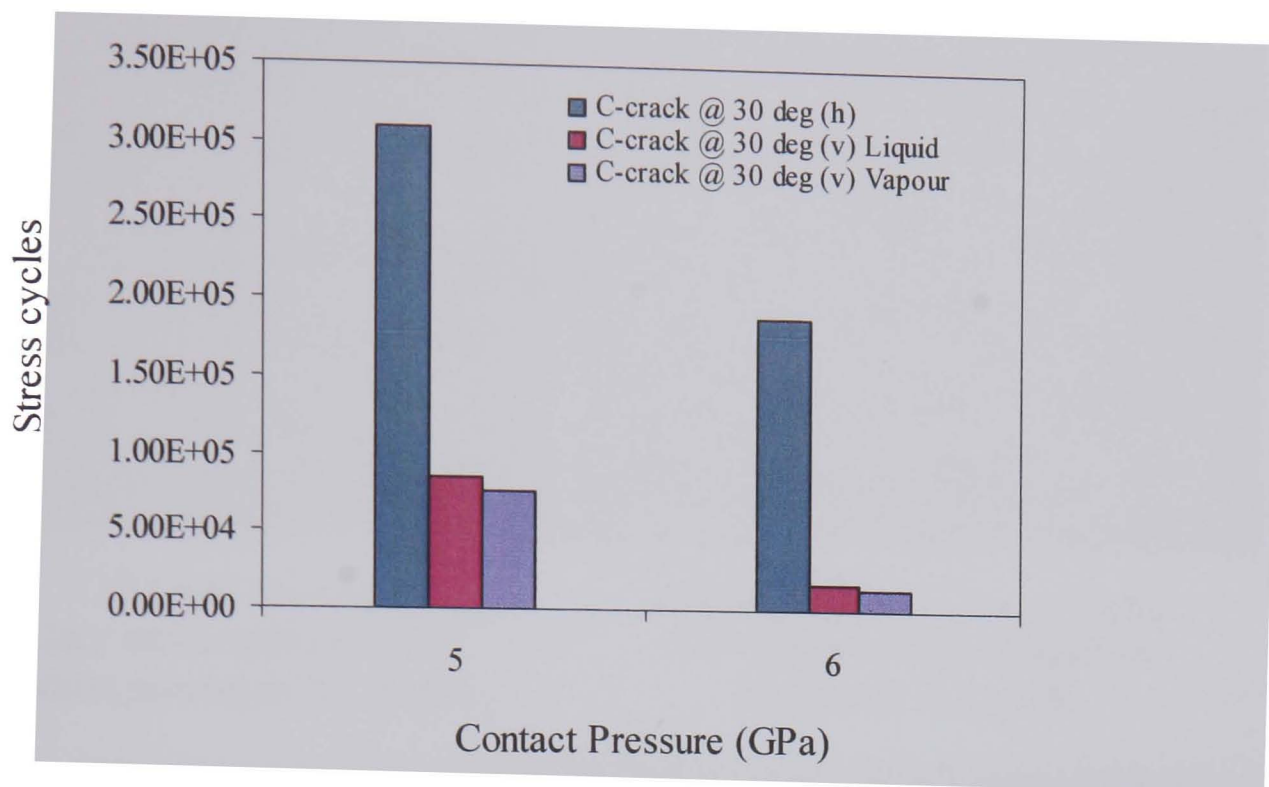


Figure 5.36 Fatigue life performance; liquid and vapour state of refrigerant (specimens 18,19,23,24,27 and 28)

Specimen 21 was tested with liquid refrigerant lubrication. The test was performed at 3 GPa maximum contact stress. The secondary crack initiation from the induced ring crack defect is shown in figure 5.37 after 6 hours 28 minutes of test time. Figure 5.38 is a light micrograph showing consequent growth of the secondary incipient crack and mouth opening. The secondary crack initiates at the contact path edge and propagates inwards into the maximum compression zone. With continued rolling contact fatigue cycles the tertiary crack initiates as shown in figure 5.39 after 11 hours 32 minutes of test time. The tertiary crack position relative to the contact edge changed and was offset from the edge where secondary crack initiated and propagated. This is due to a shift in the tensile zone because of weakening residual stresses within the material. A complete path of the tertiary crack in the contact path is shown in figure 5.40, light micrograph recorded at 17 hours of test time. More cracks in the contact path are initiated and propagated. A shift of these cracks is deeper in the contact path.

Similar mechanisms of failure in specimens tested with vapour state of the refrigerant lubrication exist, fatigue life of the elements was reduced.



Figure 5.37 Light micrograph; secondary crack initiation and propagation specimen 21, at 6hrs

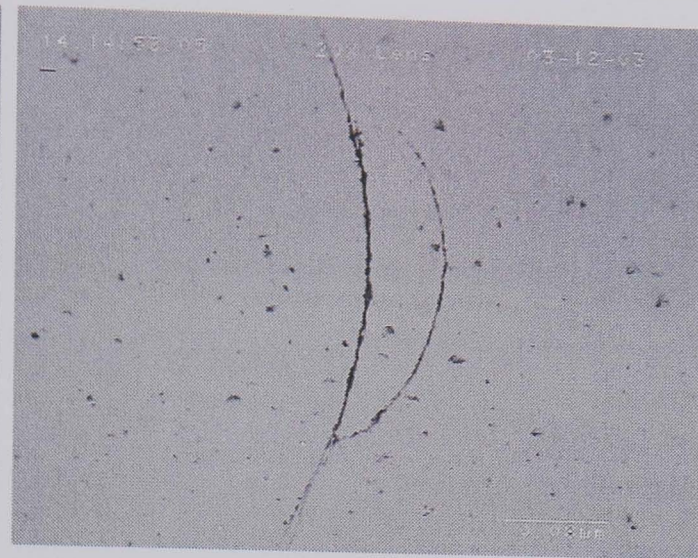


Figure 5.38 Light micrograph; secondary crack propagation specimen 21, at 8 hrs



Figure 5.39 Light micrograph; secondary crack sp 21, at 11 hrs



Figure 5.40 Light micrograph; secondary crack sp 21, at 17 hrs

5.6. Crack propagation

Figure 5.41 is a light micrograph showing surface topography of specimen 35. The ring crack was positioned vertically into the contact path as shown in figure 5.20(b). Secondary cracks are seen after 5.32×10^4 fatigue cycles. Secondary cracks are initiated near the edge of the contact track which is the maximum tensile stress region and are propagated inwards toward the contact circle. The centre of the contact circle is the maximum compression region. The crack initiation is followed by surface and sub-surface crack propagation. The crack opening is in progress and results in relieving material residual stresses. Sub-surface cracks are propagated in

angular fashion and the shallow cracks join the cracks in front. This helps in creating a weak section of material. Due to continuing fatigue cycles, a section of material is eventually removed from the surface thus causing fatigue failure. Figure 5.42 shows a light micrograph for specimen 35 showing spall failure. This result was recorded at 33 minutes. The shaft speed was 2000 rpm and the maximum contact stress was 4 GPa.

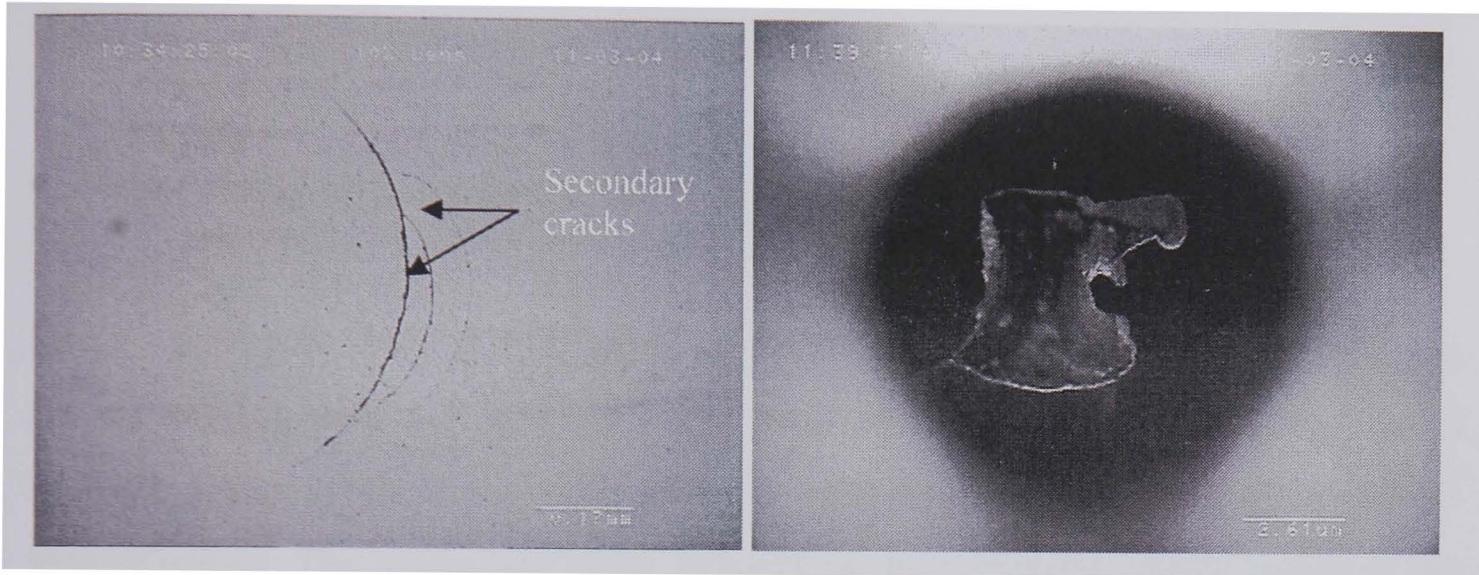


Figure 5.41 Light micrograph showing secondary crack initiation and propagation in specimen 35

Figure 5.42 Scanning electron micrograph showing delamination failure during rolling contact in specimen 35

A light micrograph figure 5.43 shows secondary crack propagation from the induced ring crack on the ball surface for specimen 20. The positioning and orientation of the induced ring crack for this specimen 20 is shown in figure 5.20(a). This result was recorded at 5.9×10^4 fatigue cycles. Initiation and propagation of these secondary cracks results in the loss of material particles due to rolling contact wear. Figure 5.44 is a light micrograph after 1.4×10^4 fatigue cycles. The initial secondary crack initiates in the maximum tensile region in the contact path and propagates into the maximum compression region. Horizontal positioning of the ring crack into the contact path provides a comparatively larger segment of the induced crack in the tensile region and multiple cracks are initiated and propagated in this region forming a network of secondary cracks. This phenomenon causes rolling contact wear due to material particle removal from the surface at adjacent secondary cracks.



Figure 5.43 Light micrograph;
secondary cracks propagation
specimen 20,, at 30 min

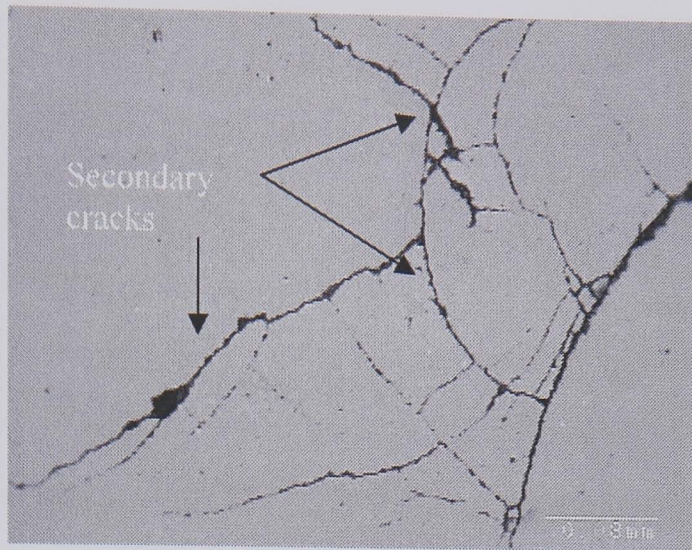


Figure 5.44 Light micrograph
secondary cracks propagation
specimen 20, at 1 hr

Specimen 16 was tested at 3 GPa contact stress. The test conditions for the specimen are provided in table 5.4. The crack was positioned horizontally, see figure 5.20(a) in to the contact path. Figure 5.45 shows a light micrograph obtained after 6.5×10^4 fatigue cycles. The secondary crack initiates in the maximum tensile region at the edge of the contact path. The crack propagation proceeds inwards towards the maximum compression area. In figure 5.46 crack the opening can be seen and material particle has been detached from the surface a wear particle.

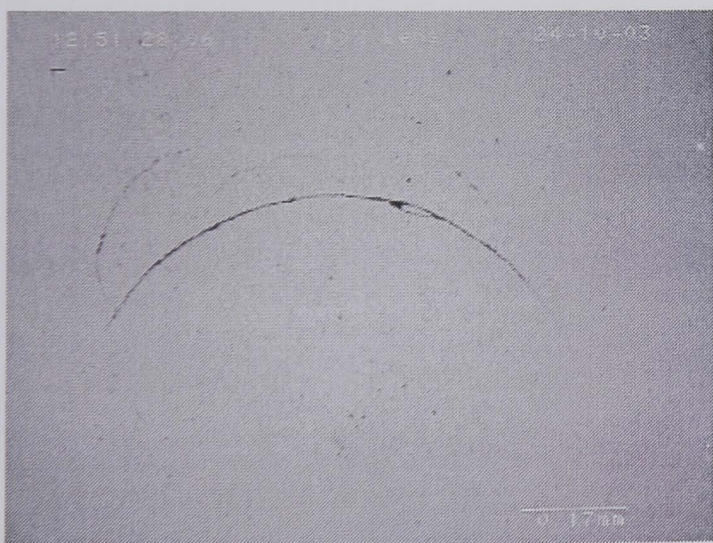


Figure 5.45 Light micrograph;
secondary crack initiation and
propagation specimen 16, at 33 min

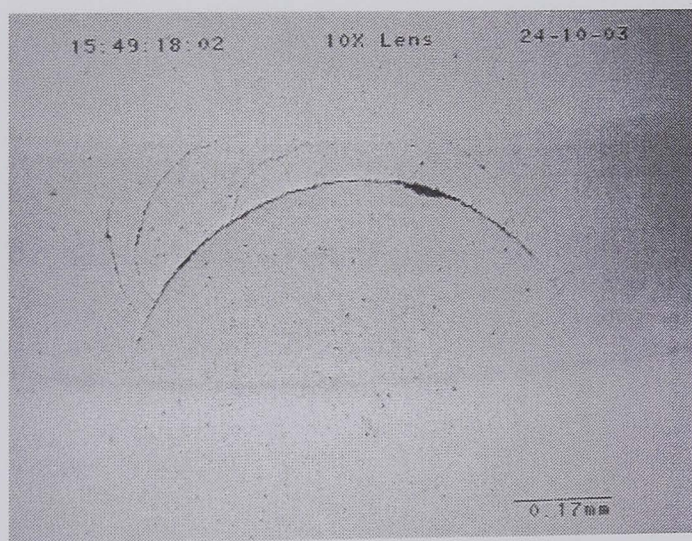


Figure 5.46 Light micrograph;
secondary crack initiation and
propagation specimen 16, at 2 hrs

5.7. Fatigue Spall

Failure due to fatigue spall is one of the common mechanisms of rolling contact fatigue. The sub-surface cracks create a significantly bigger weak zone as compared to delamination. The material removal is gradual and ends in a spall failure.

Figure 5.47 is a light micrograph showing induced ring crack in specimen 31 at zero fatigue cycles. Positioning and orientation of the induced crack is shown in figure 5.20(a). The maximum contact stress for this specimen was 3 GPa. The spindle speed was 2000 rpm. The R600a refrigerant was sub-cooled liquid. A light micrograph figure 5.48 shows secondary cracks were initiated and propagated. This figure was recorded after 2.8×10^5 fatigue cycles. The severity of the sub-surface defect is translated into a spall. Light micrograph figure 5.49 shows river marks in the specimen 31 due to rolling contact fatigue. The consequent propagation of secondary cracks leads to crack opening hence reducing crack edge friction. Scanning electron micrograph in figure 5.50 is spall failure and was recorded at 7.47×10^5 stress cycles. The recorded time to failure was 2 hours 46 minutes.



Figure 5.47 Light micrograph; induced ring crack and its positioning in the contact track in specimen 31

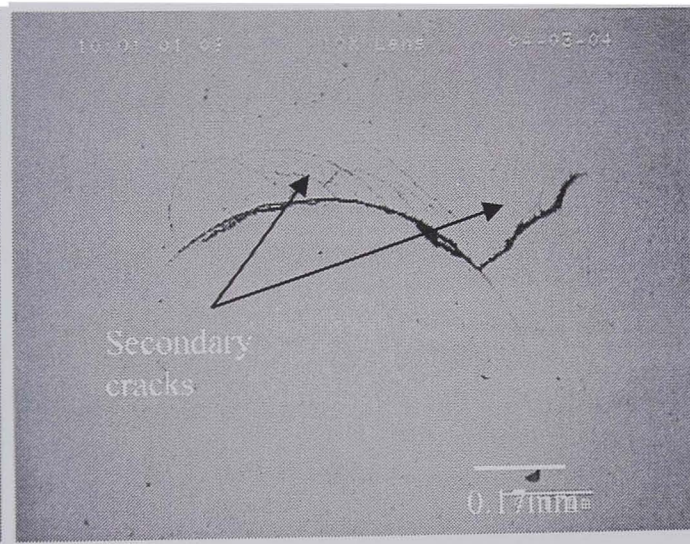


Figure 5.48 Light micrograph; secondary cracks initiation and propagation in specimen 31

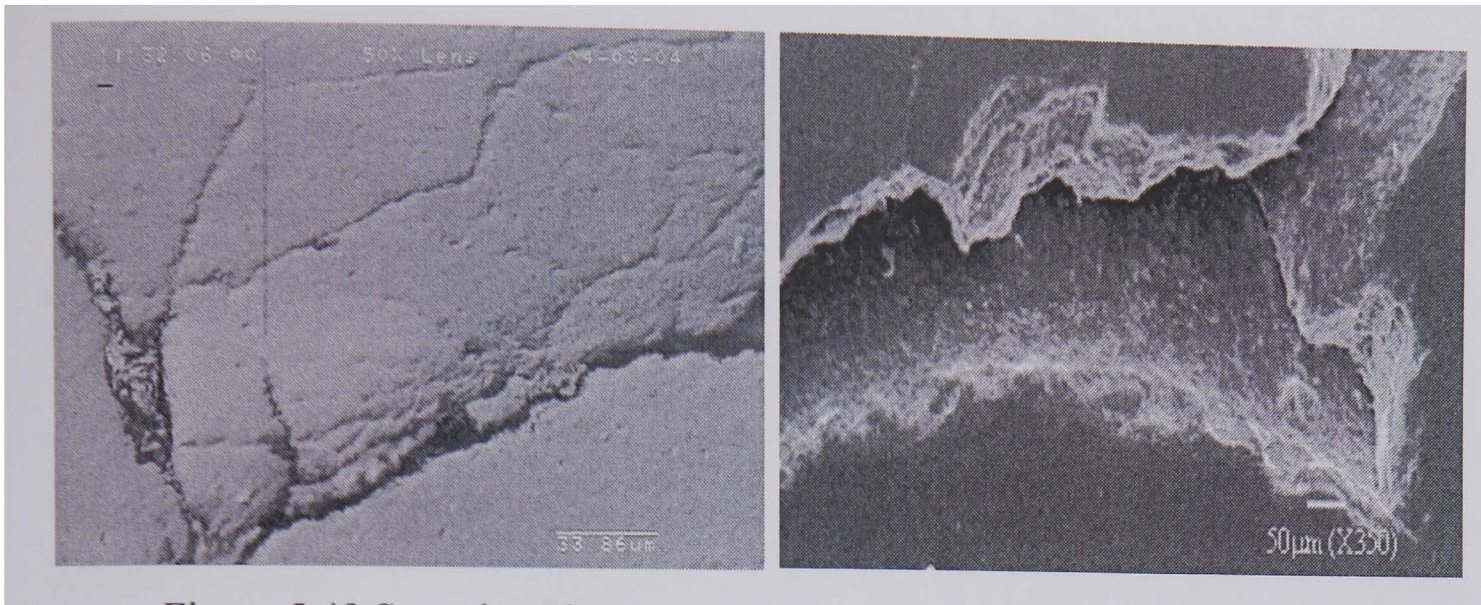


Figure 5.49 Scanning electron micrograph; secondary cracks lead to spall failure in specimen 31

Figure 5.50 Scanning electron micrograph; fatigue spall failure in specimen 31, at 2hrs 46min

Fatigue spall failure in specimens 17 and 23 is shown in scanning electron micrographs figures 5.51 and 5.52 respectively. The test conditions for both specimens are provided in table 5.4. Both specimens were tested in liquid refrigerant lubrication with 5 GPa contact stress. Specimen 17 was failed due to fatigue spall after 18 hours 23 minutes of test time. Specimen 23 was failed into a spall after 19 minutes of test time. The difference in the fatigue life performance is attributed to the positioning of induced ring crack in the contact path.

The induced ring crack for specimen 17 was positioned horizontally to the contact path as shown in figure 5.20(a) and for specimen 23 vertically as figure 5.20(b).

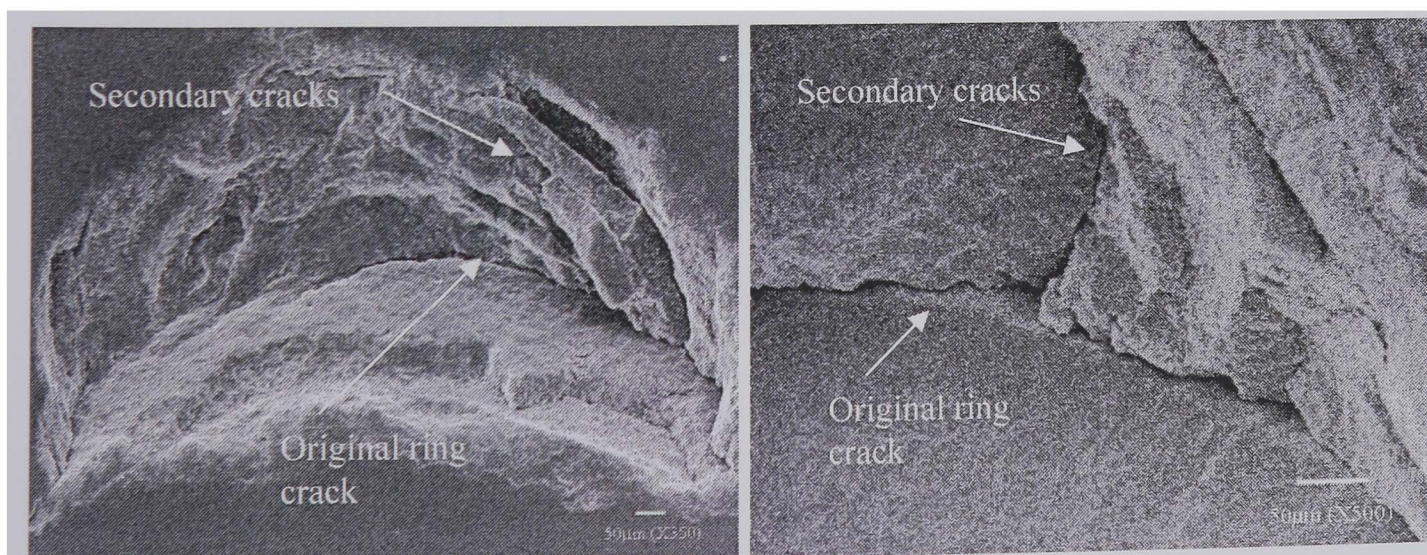


Figure 5.51 Scanning electron micrograph; Spall specimen 17

Figure 5.52 Scanning electron micrograph; Spall specimen 23

A scanning electron micrograph of fatigue spall for specimen 25 is shown in figures 5.53 and 5.54. Specimen 25 was subjected to a maximum contact stress of 3 GPa, the fatigue spall failure in the specimen occurred after 1 hour 28 minutes of test time in 3.96×10^5 stress cycles. Low fatigue life in this case is explained by the vapour state of the refrigerant lubrication compared to 18 hours 23 minutes of test time for specimen 17 with 5 GPa contact stress. The refrigerant lubrication phase has influence on the fatigue life performance. Both phases of the refrigerant have different viscosity. Failure mode in high viscosity is the same as with low viscosity lubricants but the fatigue life performance is different. Fatigue life in high viscosity lubricants is longer than that in low viscosity lubricants. The numerical analysis predicts that the initiation possibility of the secondary surface cracks is decreased as the crack face friction coefficient increases (Wang et al. 2004). Consequently, any factors, which prevent lubricant penetration into the crack, may lead to the increase of the crack face friction coefficient. The use of liquid refrigerant lubrication may inhibit the amount of fluid that can enter a crack, and friction forces acting between the faces of the crack increase. R600a refrigerant was employed as lubrication during these tests. The state of the refrigerant at a temperature of 15°C and pressure of 2.6 bar is subcooled liquid. The kinematic viscosity of saturated liquid refrigerant is 3.08×10^{-7} and saturated gas refrigerant is 1.32×10^{-8} .

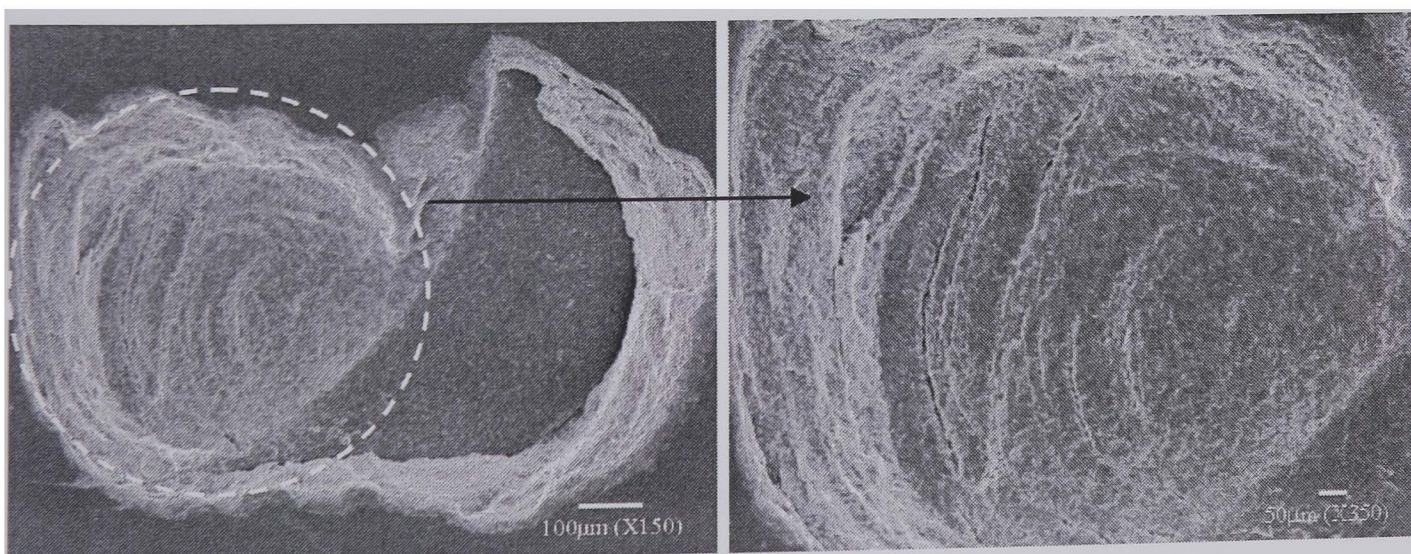


Figure 5.53 Scanning electron micrograph; spall fatigue specimen 25

Figure 5.54 Scanning electron micrograph; spall fatigue specimen 25, close up

Figure 5.55 is a scanning electron micrograph for specimen 43 and shows another example of fatigue spall. This result was recorded at 4.88×10^6 stress cycles after 18 hours + minutes of test time. Specimen 43 was subjected to a maximum Hertz contact stress of 4GPa. The impact angle for inducing ring crack was 18° and positioning of the ring crack into the contact path is shown in figure 5.20(a). Secondary surface cracks which initiate in the high tensile region of the contact circle propagate within the contact circle towards the centre of the contact circle. Residual tensile stress in the element is relieved faster in the contact region. Hence, the crack face friction coefficient decreases followed by subsequent crack opening. The crack then follows a path at the maximum tensile stress region of the contact circle. The induced ring crack and the secondary crack helps in the removal of bulk material leaving a spall failure.

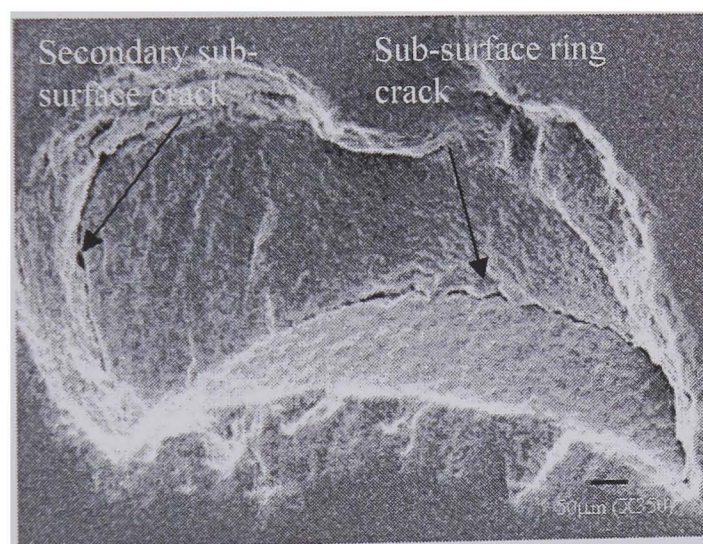


Figure 5.55 Scanning electron micrograph; sub-surface cracks in specimen 43

5.8. Delamination

Figure 5.56 is a light micrograph showing surface topography of specimen 35. Ring crack was positioned vertically to the contact path as shown in figure 5.20(b). Secondary cracks are seen after 1.22×10^5 stress cycles. Secondary cracks are initiated near the edge of the contact track and are propagated inwards. The ends meet near the centre of the track. Simultaneously, sub-surface cracks are propagated.

Contact track is the maximum stress region with an initial material discontinuity. Sub-surface cracks are propagated in angular fashion and the shallow cracks join the cracks in front. This helps in creating a weak section of material. Due to continuing fatigue cycles, the section of material is eventually removed from the surface thus causing delamination failure. Figure 5.57 show scanning electron micrograph for specimen 35 showing delamination failure. This result was recorded at 33 minutes. The shaft speed was 2000 rpm and the maximum contact stress was 4 GPa.

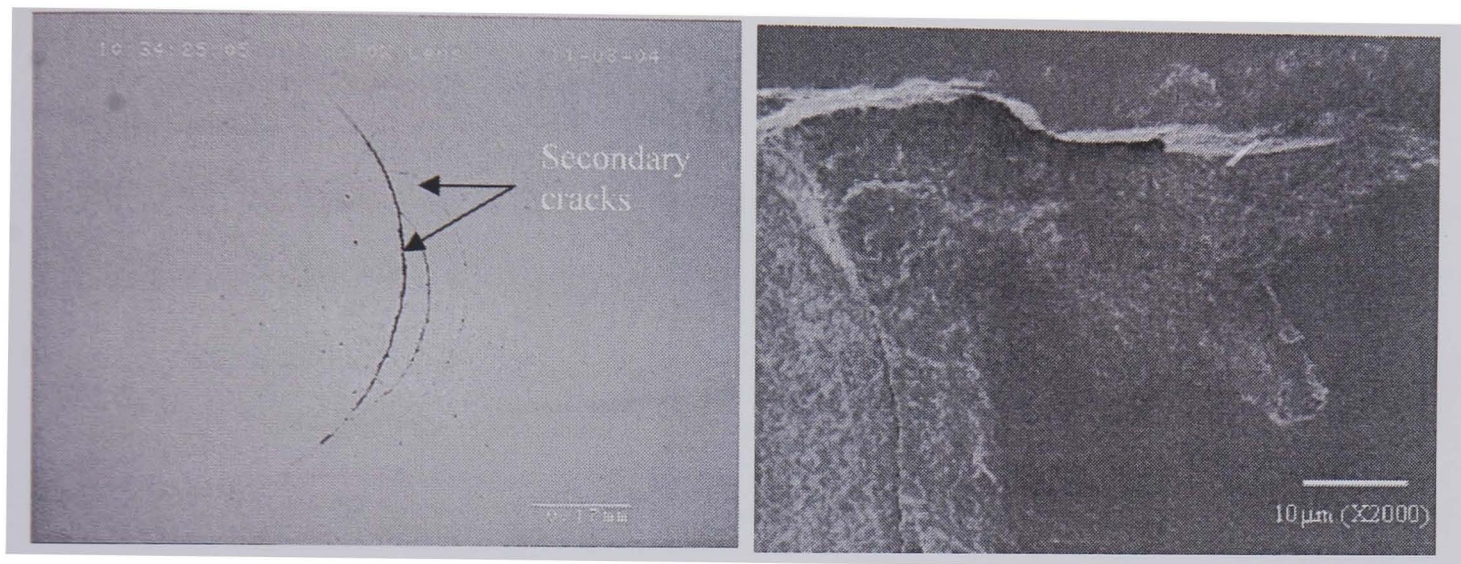


Figure 5.56 Light micrograph; secondary crack initiation and propagation in specimen 35

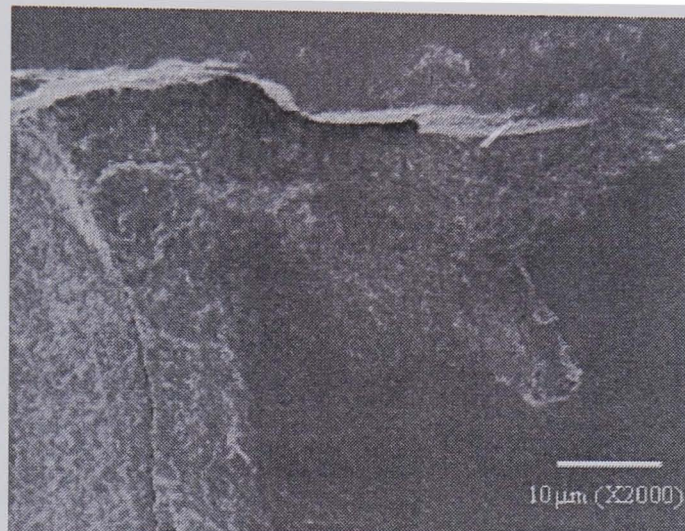


Figure 5.57 Scanning electron micrograph; delamination failure in specimen 35

5.9. Surface wear

Surface wear is one of the most common mechanisms of failure in rolling contact ceramic bearings. In ceramic/ceramic contact, wear particles are generated mechanically without the mechanism of fatigue wear even under elastic contact (Kato et al. 2000). This is the representative wear mechanism of ceramics when specific wear rate is larger than $10^{-6} \text{ mm}^3 / \text{Nm}$ (Adachi et al. 1997). At a critical number of fatigue cycles the break-up of the material surface results in the formation of pitting. The fatigue crack develops and a region of metal is separated from the base metal and eventually detaches and spalls out. Eventually these cracks grow large enough to emerge at the surface and produce wear particles; these particles then become large spalls or flakes. Preliminary work used a modified four-ball

machine to assess hot-pressed silicon nitride as a rolling bearing material (Tourret et al. 1977).

Wear particles are continuously detached from the surface during propagation of surface cracks. When a tangential traction is acting along the contact surfaces, the maximum tensile stresses always occur at the trailing edge of the contact (Wang et al. 2003). The stress field around the contact area is provided by the classical solution from (Hamilton et al. 1966). The maximum tensile stress at the edge of the contact area is given by

$$\sigma_{t,\max} = \frac{1}{8} \pi(4 + \nu)fp_0 + \frac{1}{3}(1 - 2\nu)p_0 \quad (5.1)$$

where f is the friction co-efficient, p_0 the maximum Hertzian contact pressure and ν is Poisson ratio.

A light micrograph figure 5.58 shows secondary cracks propagation from the induced ring crack on the ball surface for specimen 20. The positioning and orientation of the induced ring crack for this specimen 20 is shown in figure 5.20(a). This result was recorded at 4.19×10^5 stress cycles. Initiation and propagation of these secondary cracks results in the loss of material particles due to rolling contact wear. Figure 5.59 is a scanning electron micrograph showing rolling contact wear in specimen 35. This result was recorded at 1.49×10^5 stress cycles.

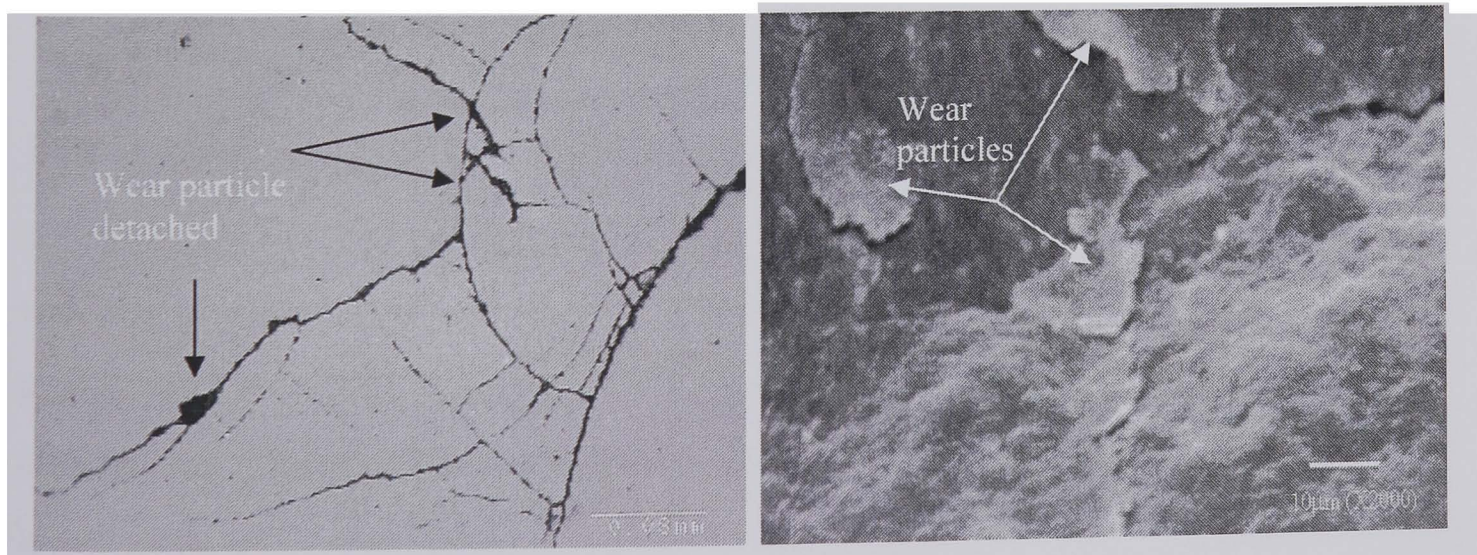


Figure 5.58 Light micrograph; rolling contact wear due to secondary cracks specimen 20

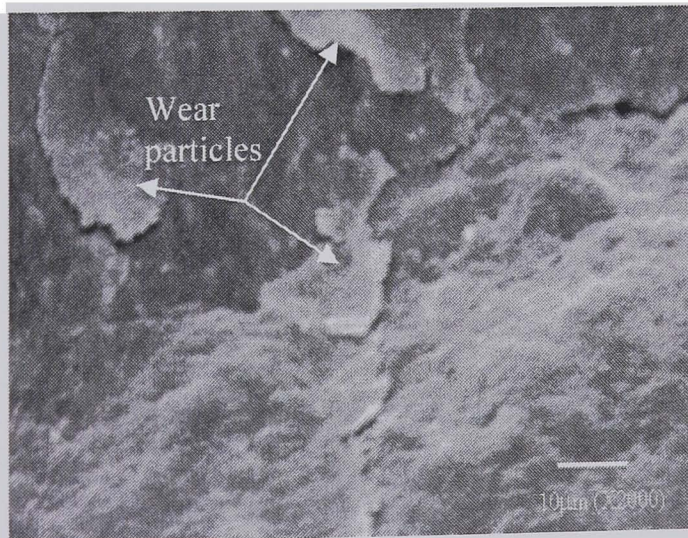


Figure 5.59 Scanning electron micrograph; wear mechanism due to surface initiated cracks specimen 35

Figure 5.60 is an atomic force micrograph (AFM) for specimen 16 showing a 3-dimensional surface profile. Specimen 16 was tested at 3 GPa maximum Hertz contact stress. The positioning of the ring crack for specimen 16 is shown in figure 5.20(a). The surface profile at the contact path was recorded at 6 hours of test time and 1.62×10^6 stress cycles, with liquid refrigerant lubrication. The surface roughness R_a on the contact path was $0.02 \mu\text{m}$. after 6 hours of test time compared to $0.01 \mu\text{m}$ average surface roughness of the ceramic ball.

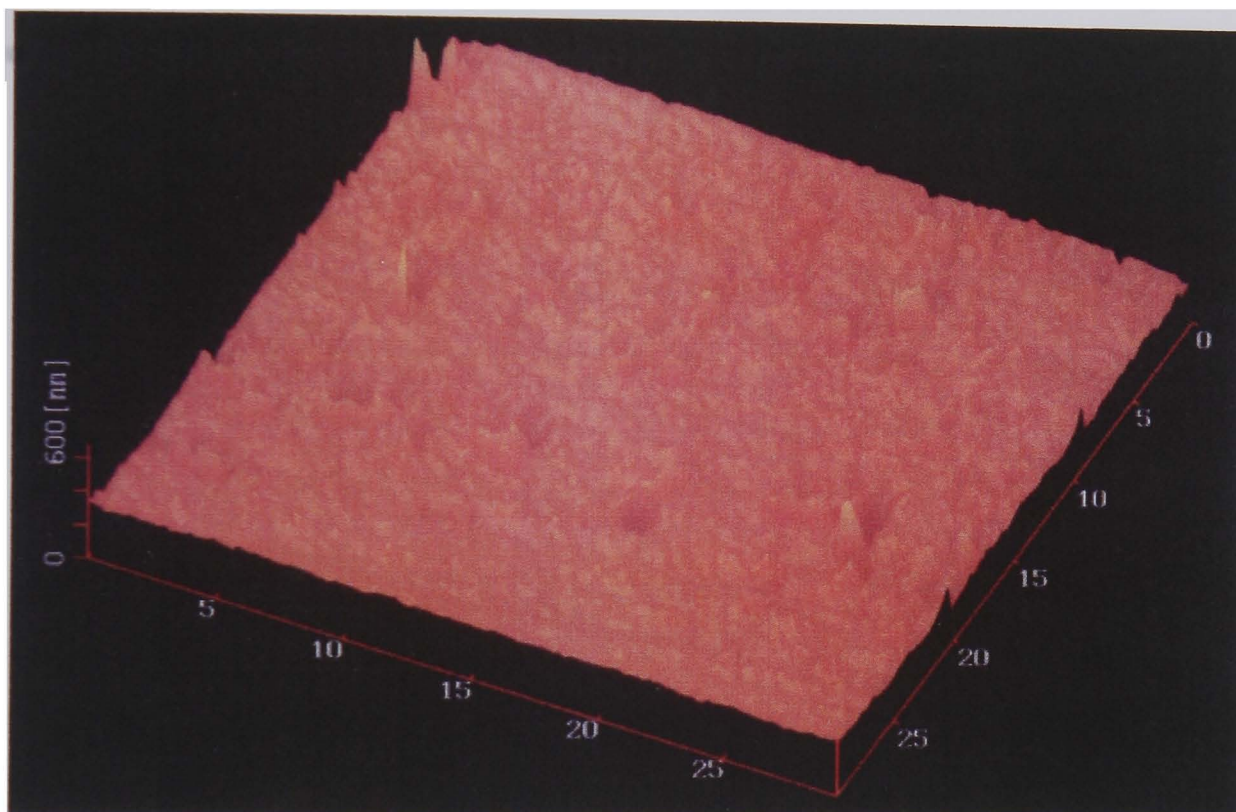


Figure 5.60 Atomic Force Micrograph surface profile; specimen 16

A wear profile of the contact path is shown in figure 5.61 for specimen 46. A contact type Profilometer was used to obtain this result. The probe radius of the Profilometer was $5 \mu\text{m}$. This result was obtained after 20 hours 48 minutes of test time. Wear profile on the contact path with projected edges and centre is generated by differences between steel and ceramic balls according to Young's modulus. The lower steel ball has a Young's modulus of 210 GPa while that of the upper ceramic ball is 320 GPa. Other reasons may be due to stick and slip during rolling contact.

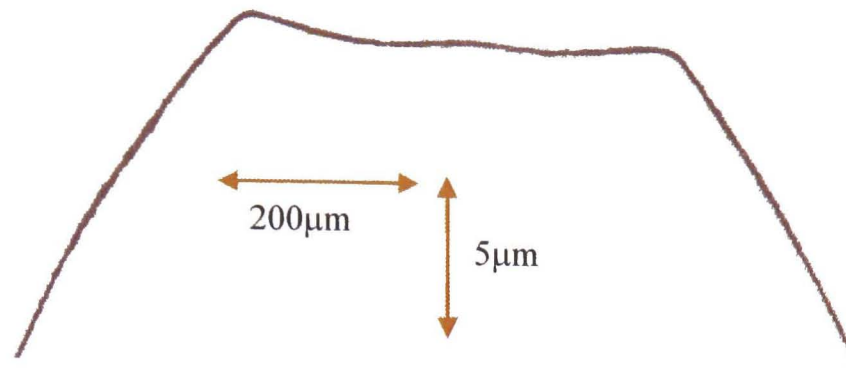


Figure 5.61 Contact path wear profile for specimen 46

Figure 5.62 and 5.63 shows surface profiles of the spall for specimen 17. Specimen 17 was subjected to a maximum contact stress of 5 GPa, spindle speed of 2000 rpm with liquid refrigerant lubrication. The induced ring crack was positioned horizontally to the contact path as in figure 5.20(a). Specimen 28 was subjected to maximum contact stress of 6 GPa, spindle speed of 2000 rpm with vapour state of the refrigerant as lubrication. The induced ring crack for specimen 28 was positioned vertically as in figure 5.20(b).

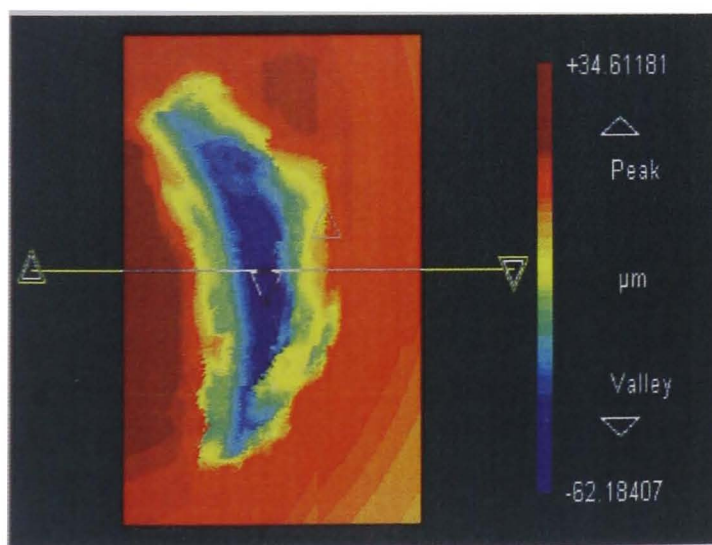


Figure 5.62 Surface profile; spall specimen 17

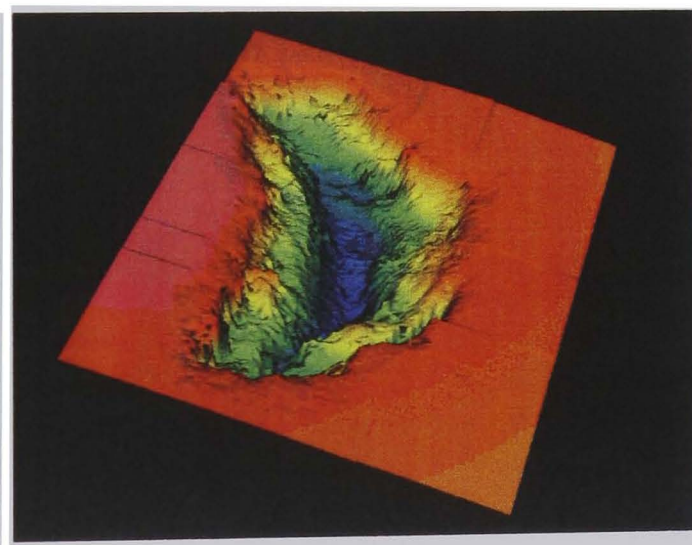


Figure 5.63 3-dimensional surface profile; spall specimen 17

A 3-dimensional surface profile of the spall for specimen 28 is provided in figure 5.64. A comparison of the spall characteristics for specimens 17 and 28 was performed. The comparison of the spall depth (peak valley), rms (root mean square) and roughness (R_a) is compared for specimens 17 and 28 in Figure 5.65.

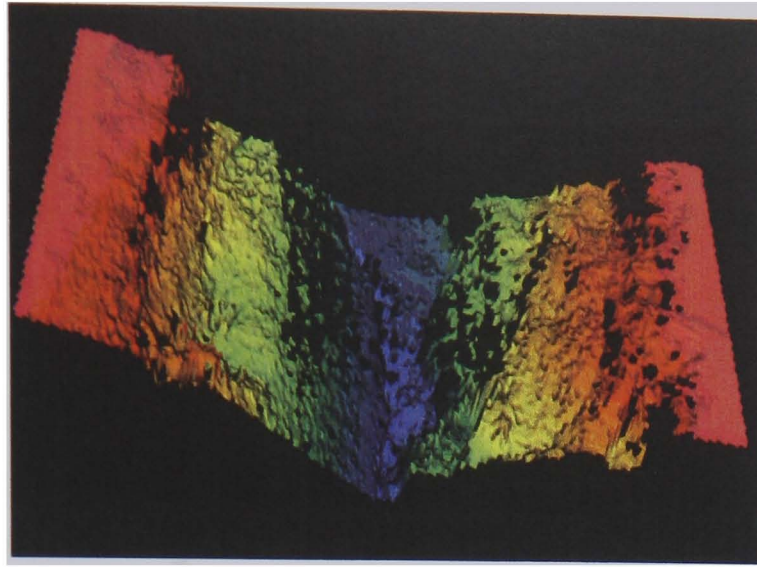


Figure 5.64 3-dimensional surface profile; spall specimen 28

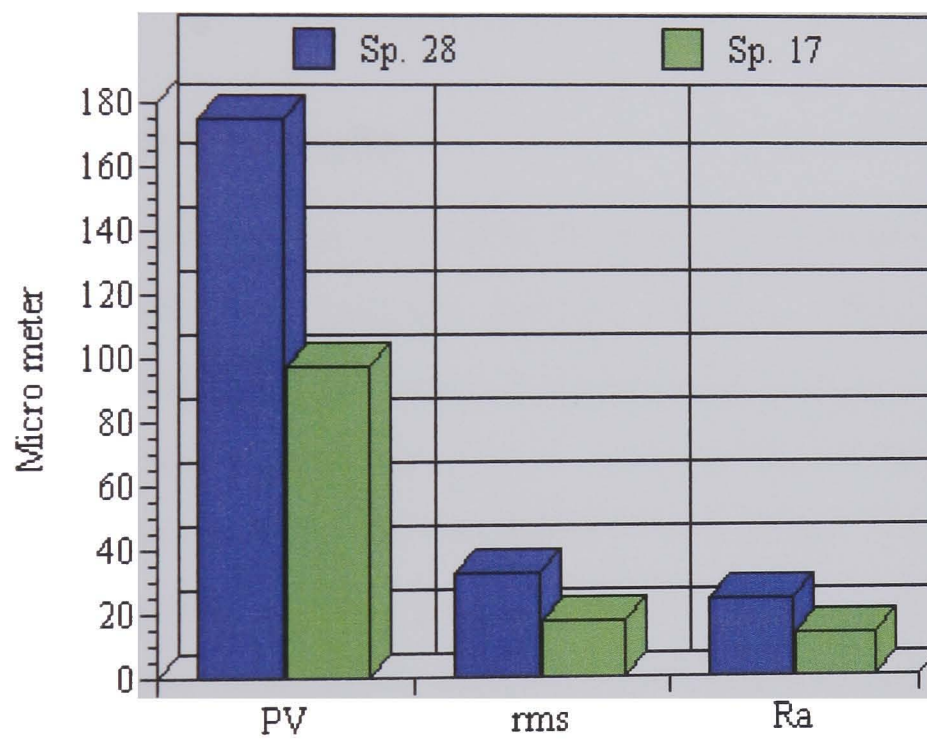


Figure 5.65 Comparison of the fatigue spall characteristics of specimens 28 and 17

CHAPTER 6

Experimental results of the residual stress measurements on failed ceramic elements are provided in this chapter. Residual stress measurement is a key feature of this research and a small volume of irradiation was used to perform residual stress measurement. An experimental study of the residual stress relation to number of stress cycles, distance from induced ring crack, residual stress relation to contact path and measuring direction is presented. Residual stress measurements were performed on fatigue spall. A residual stress survey on the secondary cracks is also provided in this chapter.

6. RESIDUAL STRESS MEASUREMENT RESULTS

6.1. Residual stress results

In this section a residual stress measurement survey is presented for the rolling contact silicon nitride Si_3N_4 /ceramic bearing element. These rolling bearing elements were pre-cracked by inducing a ring crack and indents to analyse the wear mechanisms due to various artificial defects. The loading of impact for inducing these defects and the geometry of the defects are known. The RCF tests were conducted with pressurised HC refrigerant lubrication. The nominal diameter of the silicon nitride ball was 12.67 mm. The RCF tests were conducted for ceramic-ceramic contact (Khan et al. 2003). The RCF maximum contact Hertz stress ranges from 3 to 6 GPa. This section presents 44 RS measurements on 21 ceramic rolling bearing elements. Rolling contact fatigue test details are presented in table 6.1 selected for measuring residual stresses. Table 6.2 and table 6.3 present measured residual stress values. Table 6.4 presents RS measurements on 6 different specimens and shows the number of stress cycles or time to failure in hours for each specimen. Residual stress measurements were taken at various positions with reference to the contact path and fatigue failure. Figure 6.1 shows a general sketch of the of the various RS measuring positions on the rolling bearing element surface. "x" is the

distance of measuring points from a given reference point while "p" indicates the measuring positions. The direction and angle of measuring position to initial reference point is known and is shown in the figure 6.1.

Table 6.1 Specimen RCF details for Residual Stress Measurement

Sp. no	Contact stress (GPa)	Number of hr to failure	Number of stress cycles ($\times 10^6$)	Position of defect	State of refrigerant	defect impact angle (deg)	Type of failure
14	3GPa	13.5	3.6	Indents	Liquid	1 kg	Indents
16	3GPa	6	1.6	Parallel	Liquid	30	crack
31	3GPa	2.77	0.78	Parallel	Liquid	30	crack
33	3GPa	2.68	0.72	Vertical	Liquid	30	Spall
21	3GPa	11.53	3.11	Vertical	Liquid	30	crack
35	4GPa	0.55	0.15	Vertical	Liquid	30	Spall
22	4GPa	4	1.08	Vertical	Liquid	30	crack
23	5GPa	0.32	0.1	Vertical	Liquid	30	Spall
29	5GPa	1.33	0.3591	Vertical	Liquid	30	crack
24	6GPa	0.07	0.02	Vertical	Liquid	30	Spall
36	3GPa	3.95	1.07	Parallel	Vapour	30	crack
27	5GPa	0.28	0.08	Vertical	Vapour	30	crack
46	3GPa	20.8	5.62	Vertical	Liquid	18	crack

Table 6.2 Residual Stress Values

Sp. no	Distance x from the crack								Residual stress (MPa)	Reliability (MPa)
	x1(mm)	x2 (mm)	x							
			1st	2nd	3rd	4th	5th	6th		
14	-	-	0.15	-	-	-	-	-	-29	±44
	-	-	-	0.15	-	-	-	-	-64	±51
	-	-	-	-	0	-	-	-	-84	±49
	-	-	-	-	-	0.15	-	-	-93	±53
16	-	-	0.1	-	-	-	-	-	-164	±44
31	180 deg to the centre of the contact path circle									
	-	-	0	-	-	-	-	-	-41	±15
	-	-	0.1	-	-	-	-	-	-36	±15
33	-	-	-0.1	-	-	-	-	-	-34	±25
	-	-	-	-	-	-	-	-	-48	±10
	-	-	-	-	-	-	-	-	-54	±10
	-	-	-	-	-	-	-	-	-66	±14
21	-	-	-	-	-	-	-	-	-84	±23
	-	-	0.1	-	-	-	-	-	-84	±54
	-	0.1	-	-	-	-	-	-	-213	±64
	0.1	-	-	-	-	-	-	-	-228	±56
	-	0.2	-	-	-	-	-	-	-411	±183
35	0.2	-	-	-	-	-	-	-	-420	±109
	-	-	-	-	-	-	-	-	-3	±13
	-	-	-	-	-	-	-	-	-14	±15
	-	-	-	-	-	-	-	-	-23	±20
	-	-	-	-	-	-	-	-	-61	±26
22	-	-	-	-	-	-	-	-	-	-
	-	-	0.1	-	-	-	-	-	-209	±67
	-	-	-	0.15	-	-	-	-	-36	±34
	-	-	-	-	0.2	-	-	-	-43	±30
23	-	-	-	-	-	0.3	-	-	-48	±45
	-	-	-	-	-	-	-	-	-84	±19
	-	-	-	-	-	-	-	-	-19	±15
	-	-	-	-	-	-	-	-	-33	±25
	-	-	-	-	-	-	-	-	-35	±28
	-	-	-	-	-	-	-	-	-69	±35
29	-	-	-	-	-	-	-	-	4	±18
	-	-	0.1	-	-	-	-	-	-90	±29
	-	-	-	0.2	-	-	-	-	-69	±17
	-	-	-	-	0.3	-	-	-	-24	±20
	-	-	-	-	-	-0.08	-	-	-21	±13
-	-	-	-	-	-	-0.3	-	-65	±25	

Table 6.3 Residual Stress Values

Sp. no	Distance x from the crack								Residual stress (MPa)	Reliability (MPa)	
	x1(mm)	x2 (mm)	x								
			1st	2nd	3rd	4th	5th	6th			
24	-	-	-	-	-	-	-	-	-65	±17	
	-	-	-	-	-	-	-	-	-104	±43	
	-	-	-	-	-	-	-	-	-123	±42	
36	-	-	0.1	-	-	-	-	-	-217	±73	
	-	-	-	0.2	-	-	-	-	-150	±23	
	-	-	-	-	0.3	-	-	-	-146	±29	
	-	-	-	-	-	0.4	-	-	-127	±24	
	-	-	-	-	-	-	0.5	-	-121	±27	
	-	-	-	-	-	-	-	0.6	-38	±9	
27	-	-	0.1	-	-	-	-	-	-242	±57	
	-	-	-	0.2	-	-	-	-	-162	±55	
	-	-	-	-	0.3	-	-	-	-161	±45	
	-	-	-	-	-	0.4	-	-	-144	±35	
	-	-	-	-	-	-	0.5	-	-97	±31	
46	-	-	0	-	-	-	-	-	-73	±26	
	-	-	-	0.1	-	-	-	-	-60	±26	
	-	-	-	-	0.2	-	-	-	-42	±21	
	-	-	-	-	-	0.3	-	-	-32	±16	
	-	-	-	-	-	-	0.4	-	-12	±10	
	-	-	0	-	-	-	-	-	-73	±26	
	-	-	-	0.1	-	-	-	-	-52	±18	
	-	-	-	-	-0.2	-	-	-	-48	±27	
	crack moved 180° CCW										
	-	-	0	-	-	-	-	-	-	-3	±15
	-	-	-	0.1	-	-	-	-	-	3	±11
	-	-	-	-	0.3	-	-	-	-	3	±7
	-	-	-0.1	-	-	-	-	-	-	-13	±7
	-	-	-	0.2	-	-	-	-	-	-24	±11
	-	-	-	-	-0.3	-	-	-	-	-23	±11
-	-	-	-	-	-	0.4	-	-	-11	±9	
180 deg to the centre of the contact path circle											
-	-	0	-	-	-	-	-	-	-41	±20	
-	-	-	0.1	-	-	-	-	-	-36	±15	
-	-	-	-	-0.1	-	-	-	-	-34	±25	

Negative sign for x indicates measurements on right side of the crack

Table 6.4 Residual stress measured values for RCF tested specimens ($x = 0.1$ mm)

specimen	Time to failure (min)	Residual stresses (MPa)	Reliability (MPa)
27	17	-243	± 57
36	237	-218	± 73
22	240	-210	± 67
16	360	-164	± 44
21	692	-85	± 54
46	1248	-60	± 26

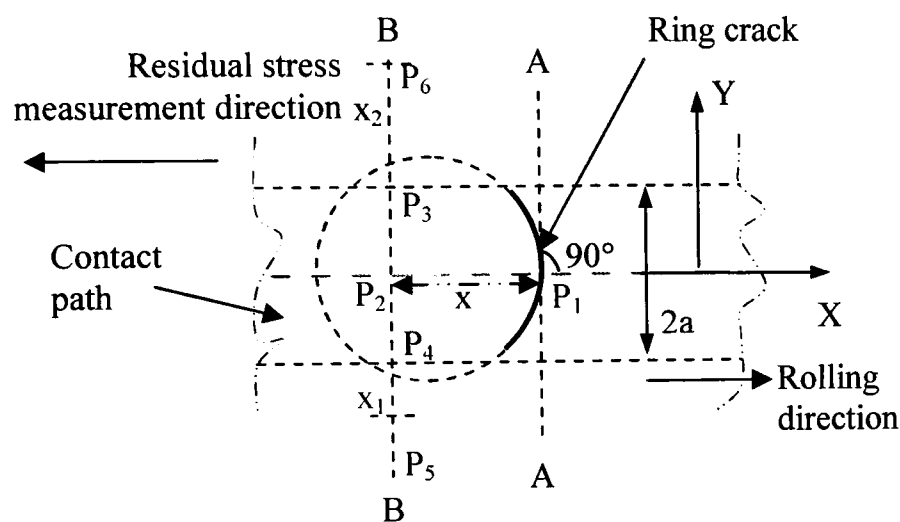


Figure 6.1 Showing residual stress measurement points

6.2. stress cycles

Residual stress measurements for 6 different specimens are presented in table 6.4. The measuring points for these specimens were at 0.1 mm distance from the induced ring crack. A high value of compressive residual stress 243 MPa is measured for specimen 27 with least number of stress cycles table 6.1. While a lowest compressive residual stress value of 60 MPa was measured for specimen 46 with highest RCF stress cycles, table 6.1. These tests clearly demonstrate a consistent relationship of CRS with the RCF stress cycles. The CRS decreases with the increase in the number of RCF stress cycles. This relationship is shown in figure 6.2.

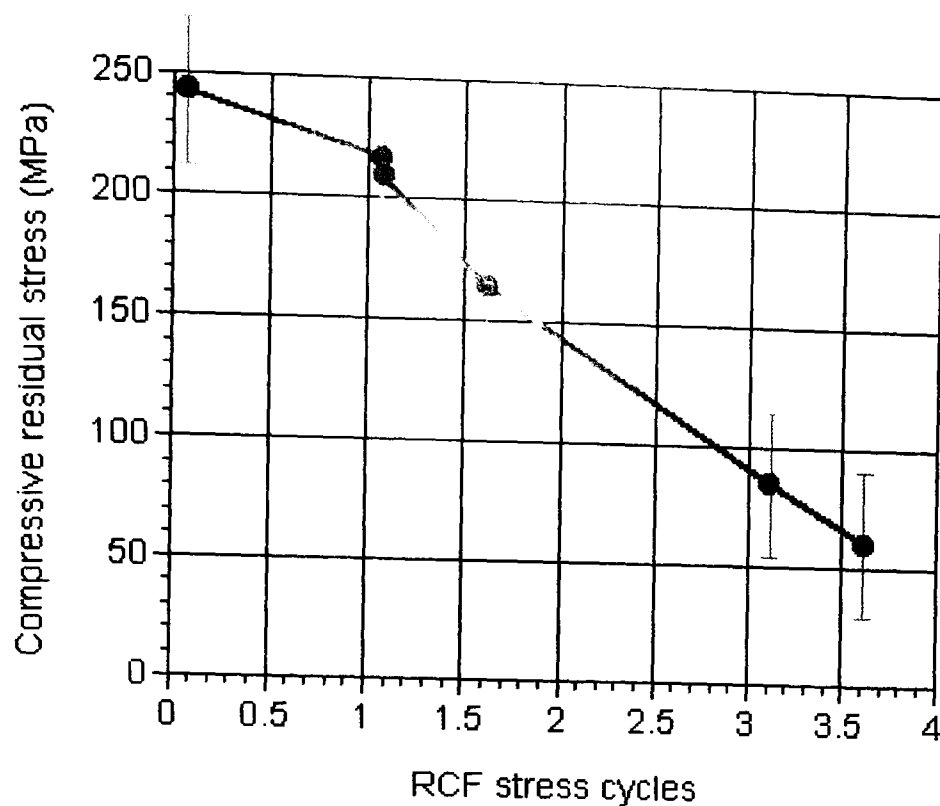


Figure 6.2 Compressive residual stress relation to RCF stress cycles

6.3. Distance from crack

The residual stress measurements for specimen 46 are shown in table 6.5. A ring crack was induced on the ball surface with impact loading. The diameter of the ring crack circle was 0.6 mm. Residual stress measurements are performed within the circle. Specimen 46 was subjected to a maximum Hertz contact stress of 3 GPa.

Table 6.5 compressive residual stress values for Specimen 46

Specimen 46		
x (mm)	Residual stresses (MPa)	Reliability (MPa)
0.0	-73	±26
0.1	-60	±26
0.2	-42	±21
0.3	-32	±16
0.4	-12	±10

Post-test residual stress measurements were performed at 5.6 million stress cycles.

A higher value of the compressive residual stress at the crack could be understood from the plastic deformation due to the impact to induce the ring crack. Previous studies of the residual stress measurements with respect to distance from the induced ring crack on the contact path have shown a similar phenomenon (Khan 2005). This plastic deformation also affects the lattice positioning with respect to the ball surface. The sub-surface crack growth during RCF helps relieve residual stress. A decreasing trend of residual stress within the crack region is recorded (Khan 2005). Figure 6.3 shows residual stress measurement points and measuring direction on the ball surface. Generally, low residual stress values indicate a higher number of stress cycles. The residual stress values decrease with increase in stress cycles. Figure 6.4 shows a relationship of residual stress to distance from the induced ring crack on the contact path for specimens 27 and 36. Figure 6.5 shows compressive residual stress relative to distance from the ring crack for specimen 27 on the contact path. A linear curve fitting has been applied in this case.

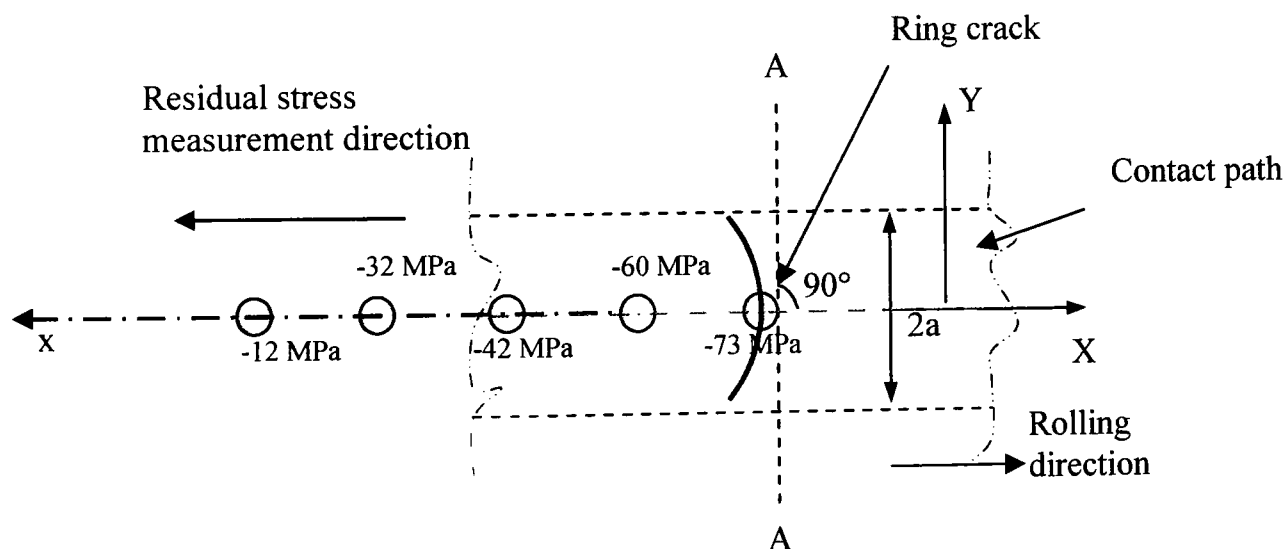


Figure 6.3 Residual stress measurement points, specimen 46

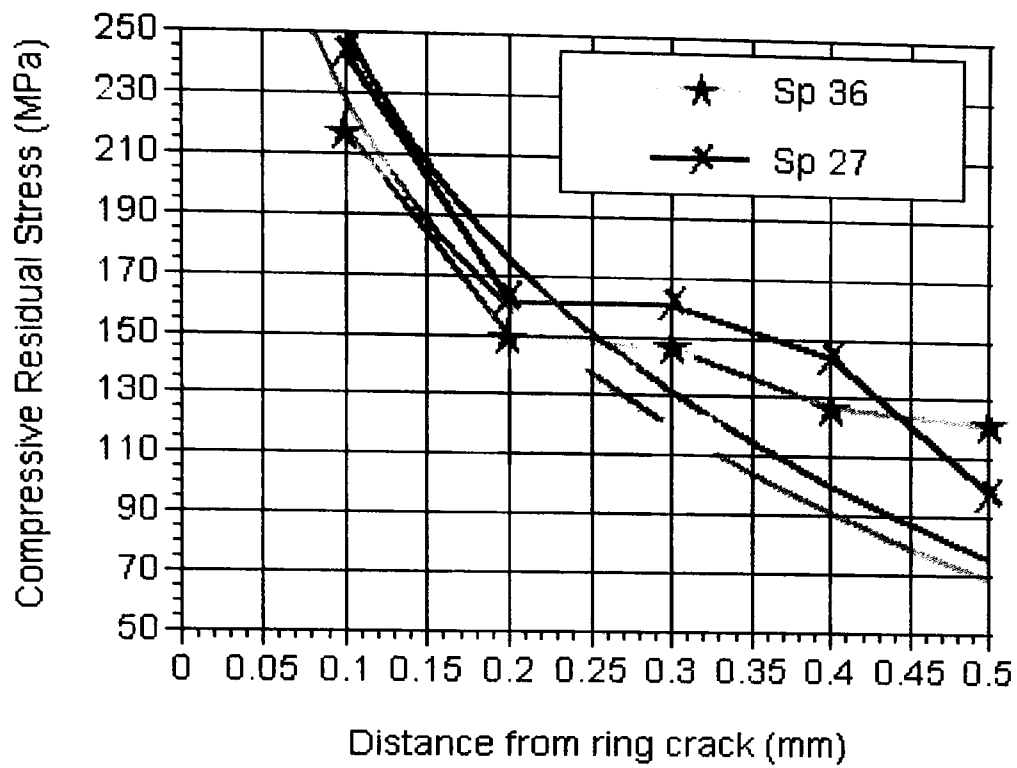


Figure 6.4 Compressive residual stress with distance from crack

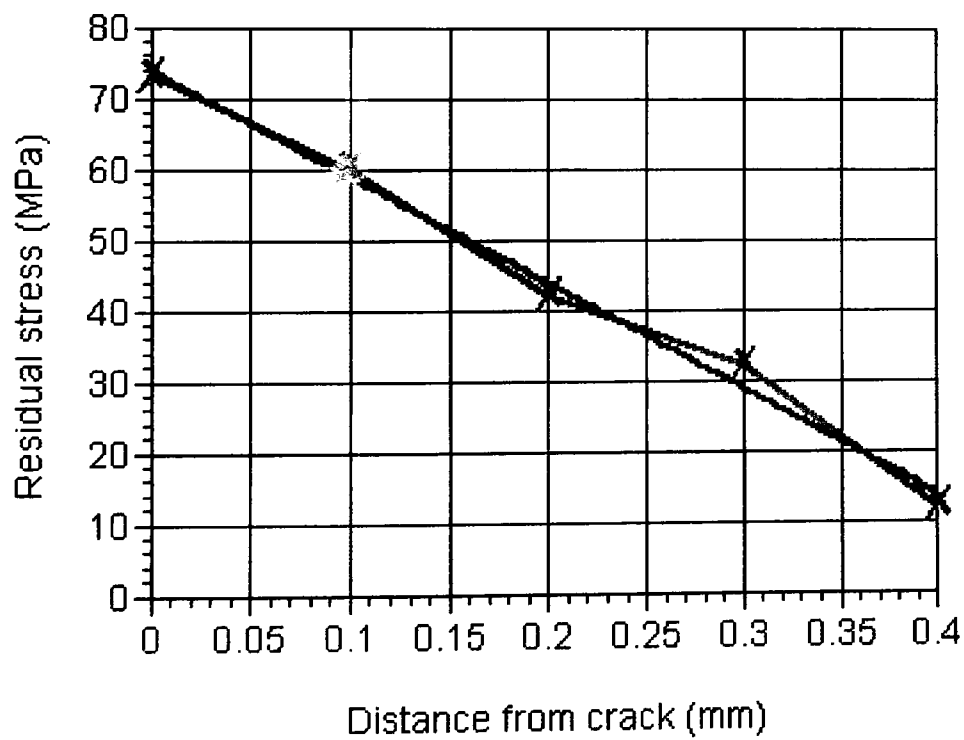


Figure 6.5 Compressive residual stress with distance from ring crack

A schematic of the residual stress measurement direction for specimen 46 is shown in figure 6.6. The residual stress measurements were performed on the right side of

the ring crack. 'x' is the distance of the measuring point on the contact path away from the ring crack.

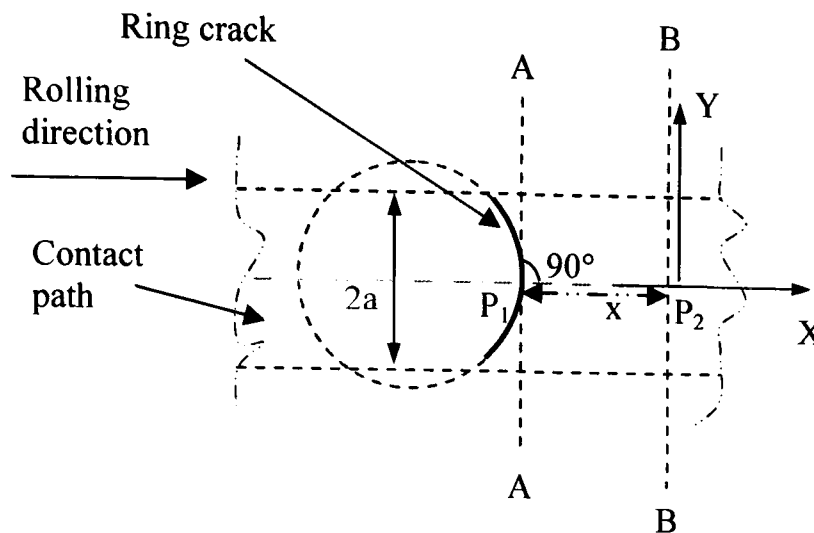


Figure 6.6 Residual stress measurement points

Table 6.6 shows the residual stress values for specimen 46 taken on the right side of the ring crack. A similar phenomenon of residual stress decrease occurred within 0.2 mm of the ring crack. This decrease is due to the sub-surface damage in the vicinity. The value at $x = 0$ was 73 MPa unchanged. While a compressive residual stress value of 52 MPa was measured at $x = 0.1$ mm, compared to a compressive residual stress value of 60 MPa on the left hand side of the ring crack shown in figure 6.3. Similarly, a compressive residual stress value of 48 MPa was measured at a distance of $x = 0.2$ mm from the crack while a corresponding value on the left hand side was 42 MPa, as shown in the figure 6.3. The difference in the compressive residual stress values at the comparing distance is small. The decrease in values indicates the phenomenon of sub-surface crack and the small change in value is due to the change of measuring direction.

Table 6.6 compressive residual stress values for Specimen 46

x (mm)	Residual stresses (MPa)	Reliability (MPa)
0.0	-73	± 26
0.1	-52	± 18
0.2	-48	± 27

Figure 6.7 shows the CRS value measured and the measuring points for specimen 46.

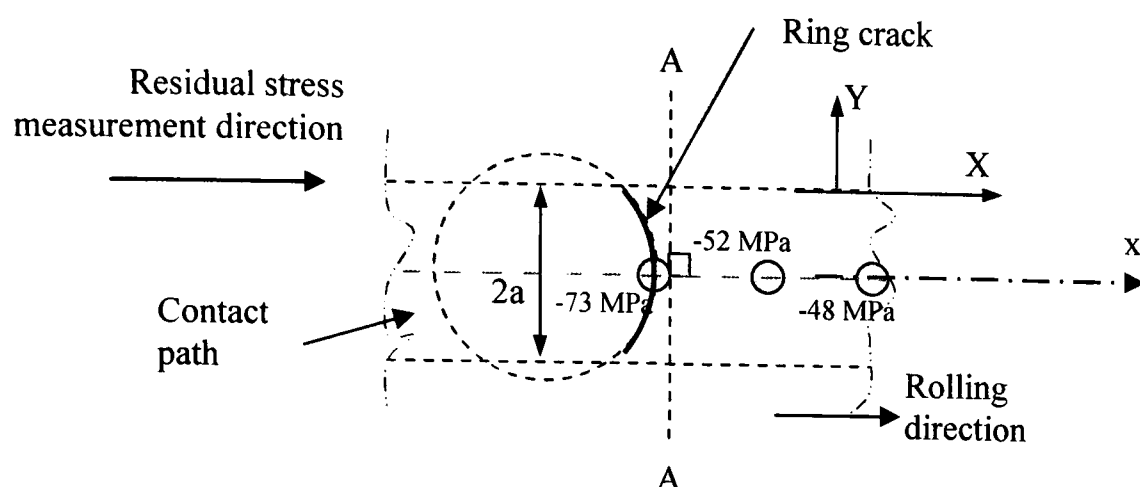


Figure 6.7 Showing residual stress measurement points for specimen 46

6.4. Contact path

Figure 6.6 shows the schematic of the residual stress measuring point for specimen 21 with respect to the pre-test induced ring crack on the ball surface. Specimen 21 was tested at maximum Hertz contact stress of 3 GPa. A ring crack was induced by plastic deformation. The diameter of the arc circle of the ring crack was 0.6 mm. HC liquid refrigerant was employed as lubrication. The residual stress measurements for specimen 21 were performed at 3.2 million stress cycles. Compressive residual stress values for specimen 21 are shown in table 6.7. A lower value of 84 MPa was recorded at the centre of the contact path at a distance of 0.1 mm away from the crack. The corresponding value of compressive residual stress for specimen 46 was 60 MPa, comparatively lower at 5.6 million cycles. The width of the contact path for the specimen was 0.1 mm. The centre of the contact path is the maximum stress region. Two compressive residual stress values of 213 and 228 MPa were recorded on either edge of the contact path, at a right angle to the first point as shown in figure 6.8. These values are higher compared to 84 MPa at the centre of the contact path. This trend indicates that compressive residual stresses are relieved much faster during rolling contact fatigue at higher contact stress level. Two more measuring

points at different distances from the edge of contact path are measured to be 411 and 420 MPa. Compressive residual stress values increased outside of the contact path. These points are further away from the high contact stress region.

Table 6.7. Compressive residual stress values for Specimen 21

Specimen 21				
x (mm)	x ₁ (mm)	x ₂ (mm)	Residual stresses (MPa)	Reliability (MPa)
0.1	-	-	-84	±54
-	-	0.1	-213	±64
-	0.1	-	-228	±56
-	-	0.2	-411	±183
-	0.2	-	-420	±109

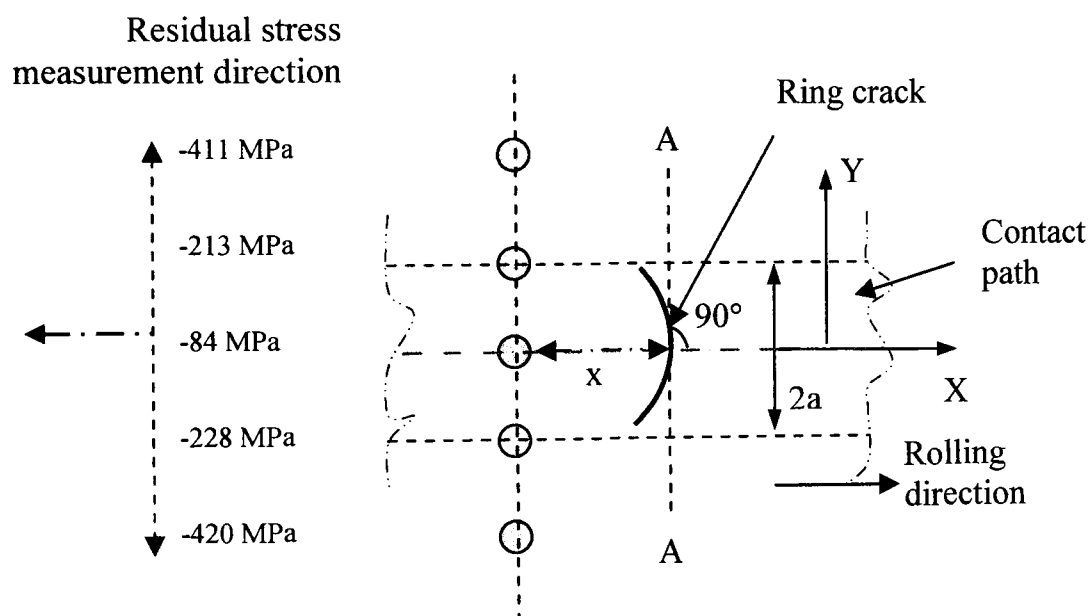


Figure 6.8 Showing residual stress measurement points for specimen 21

6.5. Measuring direction

The direction of the residual stress measurement is shown in figure 6.9. The difference of residual stress measurements can be explained in terms of the stress field and rolling direction although further experimental investigations are required to confirm the directionality of the residual stress (Hadfield et al. 1998). Current investigation suggests that the residual stress measuring direction will cause the

residual stress value to change. Although the change in the residual stress values is not very big, the rolling direction in relation to residual stress measurement direction is significant. This has been demonstrated in the residual stress measurement tests for specimen 46. Residual stress measurements were performed on specimen 46 at three points rotating the ring crack 180° clockwise. These three points were measured at 0.1, 0.2 and 0.3 mm from the ring crack. The compressive residual stress values are provided in table 6.8. The change in compressive residual stress values for specimen 46 was recorded with the change in measuring direction. The change in residual stress values with change in measuring direction could also be the change in orientation of the lattice plane. However, the decrease in the compressive residual stress values within the diameter of the arc circle demonstrates sub-surface crack propagation.

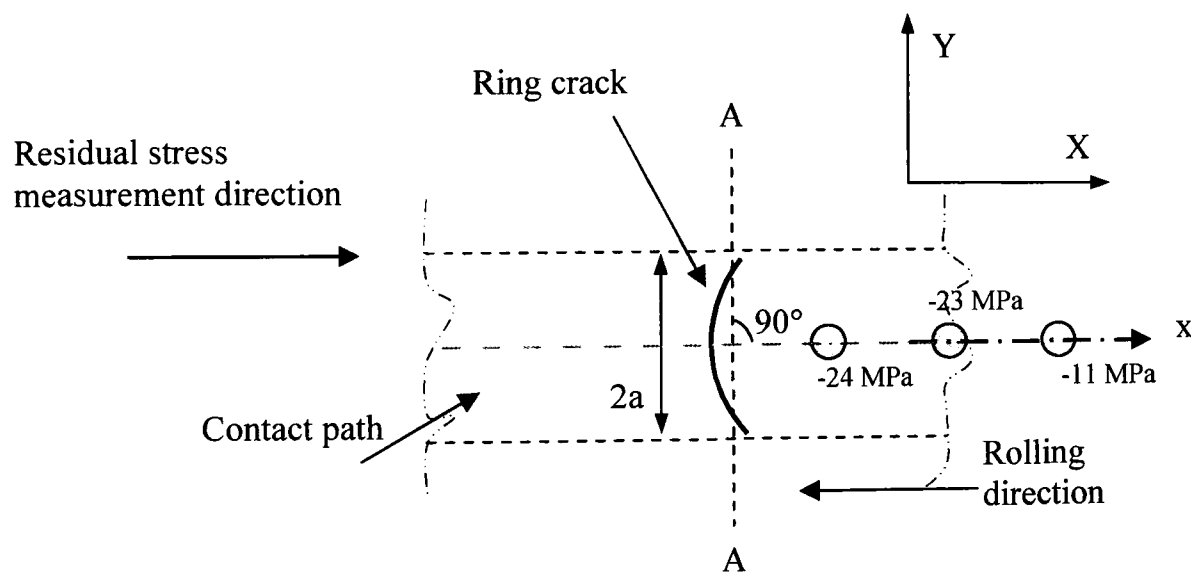


Figure 6.9 Showing residual stress measurement points for specimen 46

Table 6.8 Compressive residual stress values for Specimen 46 with change in measuring direction

Specimen 46		
x (mm)	Residual stresses (MPa)	Reliability (MPa)
0.1	-24	±11
0.2	-23	±11
0.3	-11	±9

6.6. RCF spall

Specimen 24 was subjected to maximum Hertz contact stress of 6 GPa with liquid refrigerant lubrication. The specimen was pre-cracked with a ring crack of known geometry. The surface analysis of the specimen to identify the failure mechanisms was performed by scanning electron micrograph SEM and surface mapping. Three points were selected for measuring residual stress and are provided in table 6.9.

Figure 6.10 shows the rolling and residual stress measuring direction with measured values, showing an increasing trend of residual stress corresponds to increasing depth of failure surface. It should be noted that the residual stress measurements were taken at 30 μm below the surface. The maximum failure depth in specimen 24 was 100 μm , roughness root mean square (rms) is 93.68 μm . It is also known from previous studies (Hadfield et al. 1993) that a high stress gradient exists and maximum shear stress (frictionless) at around 120 μm below the surface of the ball. If significant friction exists during testing, then maximum shear stresses will occur nearer to the surface and tensile stresses will occur on the contact circle edge. The high compressive stresses recorded, coupled with the possibility of high shear forces, favour subsurface initiation, causing original surface damage and consequent fatigue propagation (Hadfield et al. 1993).

Table 6.9 Compressive residual stress for Specimen 24

Specimen 24	
Residual stresses (MPa)	Reliability (MPa)
-65	± 17
-104	± 43
-123	± 42

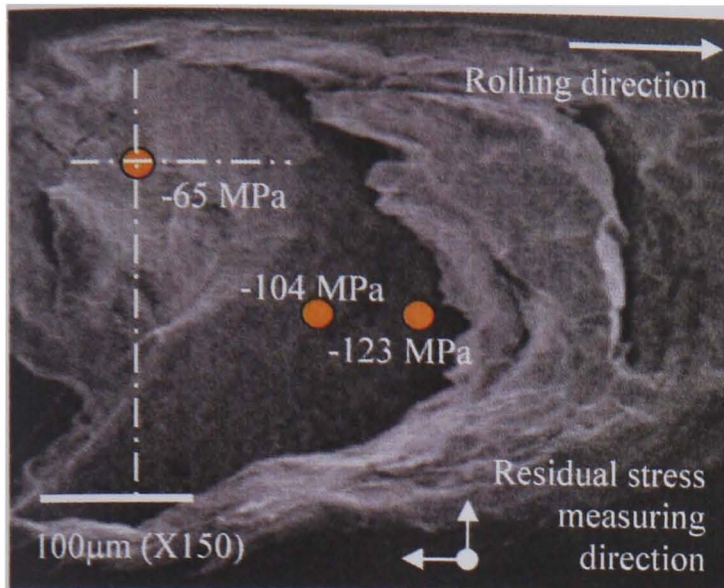


Figure 6.10 Residual stress measurement direction for specimen 24

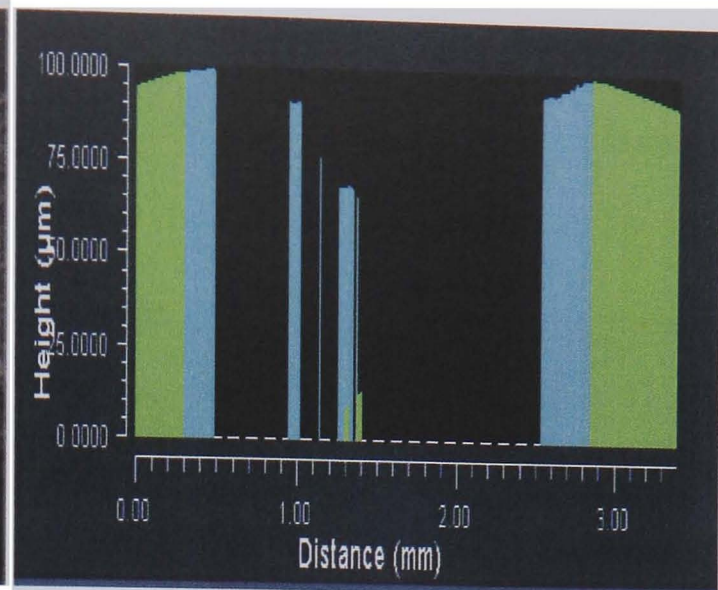


Figure 6.11 3D surface profile of the spall fatigue specimen 24

Figure 6.11 shows 3-dimensional surface mapping of spall in specimen 24. The highest value of compressive residual stress 123 MPa was recorded at a depth of 130 μm (30 μm x-ray depth + 100 μm spall depth). Compressive residual stress in specimen 24 decreases towards the surface and decreasing depth.

Specimen 33 was subjected to a maximum contact stress of 3 GPa at spindle speed of 2000 rpm. The specimen was failed into a spall failure in 2 hr 41 min. The surface analysis was performed by SEM and Zygo surface mapping. The spall depth was recorded to be 122 μm , rms of the spall was 118 μm with an $R_a = 116 \mu\text{m}$. The residual stress values are shown in table 6.10 for specimen 33.

Table 6.10 Compressive residual stress values for Specimen 33

Specimen 33	
Residual stresses (MPa)	Reliability (MPa)
-48	± 10
-54	± 10
-66	± 14
-89	± 23

Figure 6.12 shows the points of measurements with corresponding values. A high value of the compressive residual stress 66 MPa was registered at a depth of 150 μm

(30 μm x-ray depth + 120 μm spall depth) in the spall while the lowest value of 48 MPa was recorded on a region of about 105 μm (30 μm x-ray depth + 75 μm spall depth) deep.

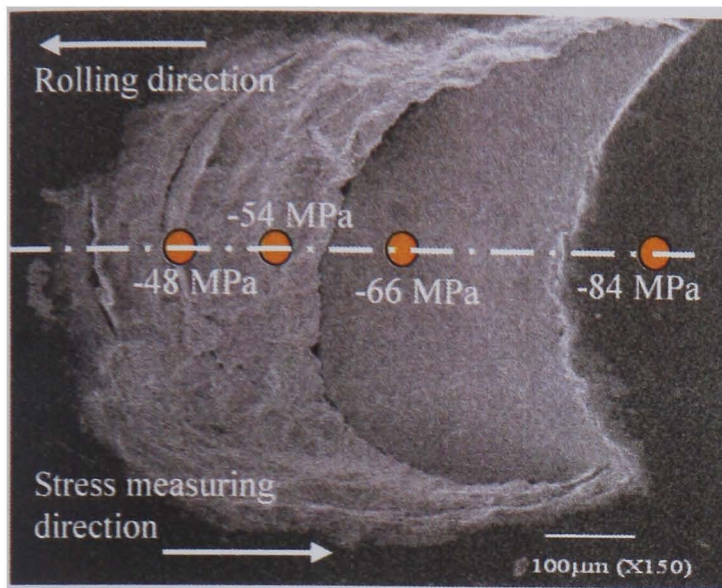


Figure 6.12 Residual stress measuring points for specimen 33

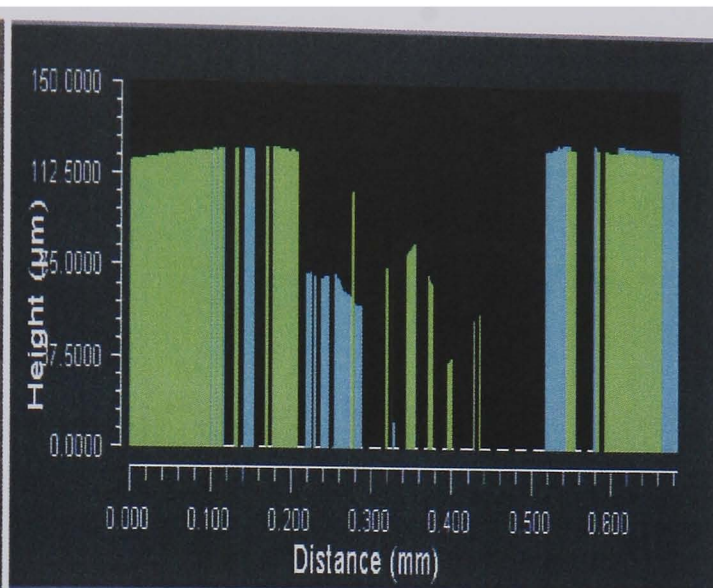


Figure 6.13 3-dimensional surface profile of the spall fatigue specimen 33

Figure 6.13 shows surface profile of the spall fatigue of specimen 33. A high compressive residual stress value of 84 MPa on the surface can be attributed to the number stress cycles. The sub-surface phenomenon of residual stress variations below 30 μm depends on the pre-test conditions of the specimen.

Specimen 23 was tested at a maximum contact stress of 5 GPa which failed due a spall fatigue. The test conditions for specimen 23 are provided in table 5.8. Residual stress measurements were performed on and around the specimen spall area. Six different positions were selected for measuring residual stresses on the specimen. The values measured are provided in table 6.11 and the measuring points are shown in figure 6.14. The surface analysis of the fatigue spall was performed using techniques such as SEM and Zygo surface mapping. A 3-dimensional surface map of the spall area for specimen 23 is shown in figure 6.15. The PV (peak valley) for the spall is 148 μm . The rms (root mean square) is 126.6 μm and Ra (roughness) through the spall is 125 μm .

Table 6.11 Compressive residual stress values for Specimen 23

Specimen 23	
Residual stresses (MPa)	Reliability (MPa)
-8	± 19
-19	± 15
-33	± 25
-35	± 28
-69	± 35
+4	± 18

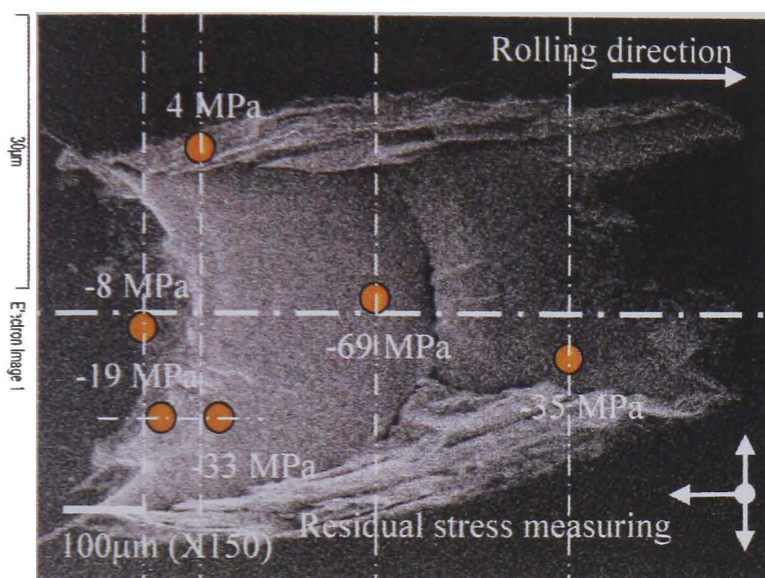


Figure 6.14 Residual stress measuring points for specimen 23

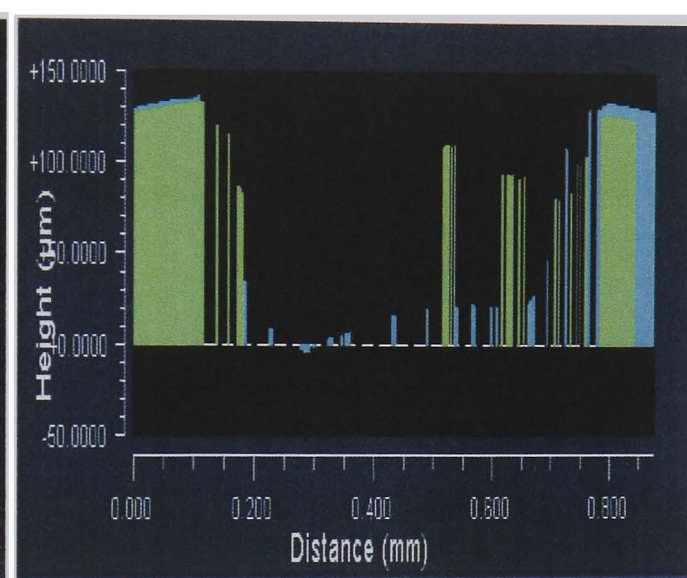


Figure 6.15 3-dimensional surface profile of the spall for specimen 23

Compressive residual stress value of 69 MPa was recorded at a depth of 160 μm (30 μm x-ray depth + 130 μm spall depth below surface). Lower values of compressive residual stress 35, 34 and 19 MPa are measured towards the surface at lower depths. This phenomenon of decreasing compressive residual stress towards the surface indicated major sub-surface deformation and sub-surface crack initiation and propagation. Since the bulk of material is removed during spall fatigue which was the maximum activity region, the lower compressive residual stress values indicate that stress is relieved in the spall region much faster than at a deeper region.

Table 6.12 shows compressive residual stress values for specimen 35 at 4 different positions. Specimen 35 was subjected to a maximum contact stress of 4 GPa and a

spall fatigue resulted in the bearing element failure. The test conditions for specimen 35 are shown in the table 5.8. Figure 6.16 shows the compressive residual stress measuring points on the specimen and figure 6.17 shows a 3-dimensional surface profile of the spall fatigue in specimen 35. The peak valley for the spall is $117.5 \mu\text{m}$, rms is $101 \mu\text{m}$ and Ra is $100.6 \mu\text{m}$.

Table 6.12 Compressive residual stress values for Specimen 35

Specimen 35	
Residual stresses (MPa)	Reliability (MPa)
-3	± 13
-14	± 15
-23	± 20
-61	± 26

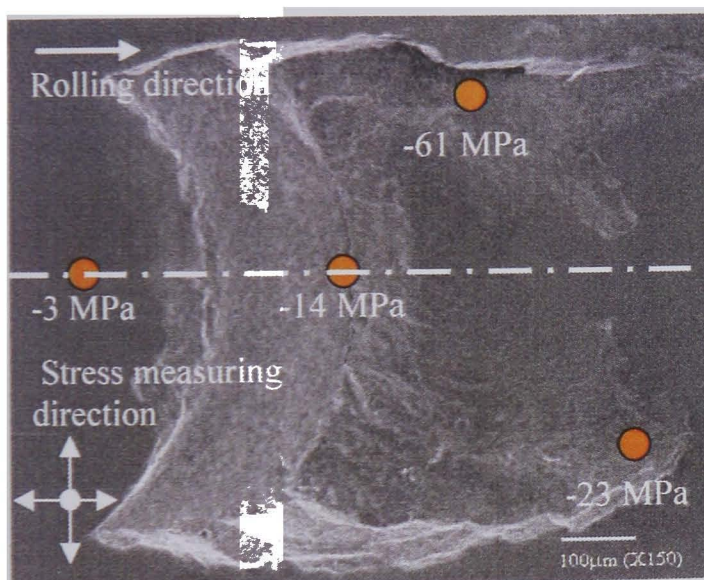


Figure 6.16 Residual stress measurements for specimen 35

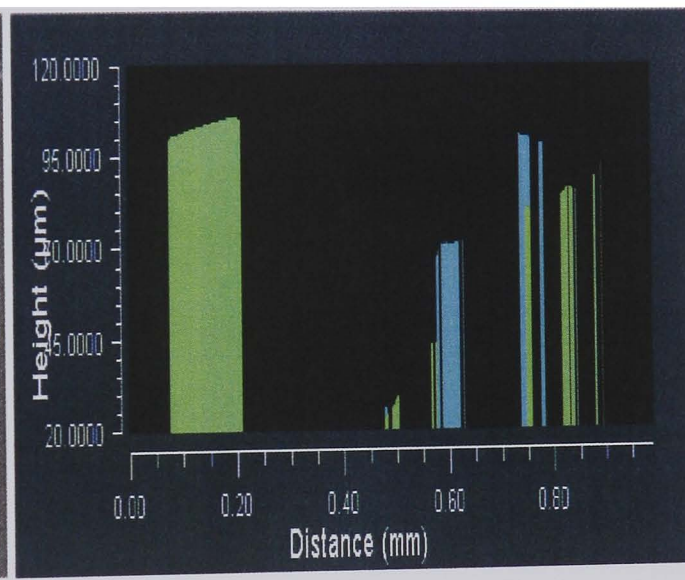


Figure 6.17 3-dimensional surface profile of the spall in specimen 35

A similar phenomenon is found in specimen 35 where a high compressive residual stress value of 61 MPa and low compressive residual stress value of 23 MPa were measured at different depths. The spall depth in specimens 23, 24, 33 and 35 ranges from $100\text{-}148 \mu\text{m}$. The variation of the compressive residual stress values is prominent at this depth. The decrease in the compressive residual stress values is registered in the spall region and demonstrates sub-surface damage in the region.

When the bulk of material has been removed, the sub-surface at a depth $148\ \mu\text{m}$ has been exposed as a fresh metal surface. Any residual stress measurement below this depth at around $130\text{-}178\ \mu\text{m}$ (including $30\ \mu\text{m}$ x-ray depth) registered a comparatively high compressive residual stress value. This indicates no or less sub-surface damage. Figure 6.18 shows a sketch of the ball with spall and the average depth for specimens 23, 24, 33 and 35. Figure 6.19 shows the distribution of sub-surface damage.

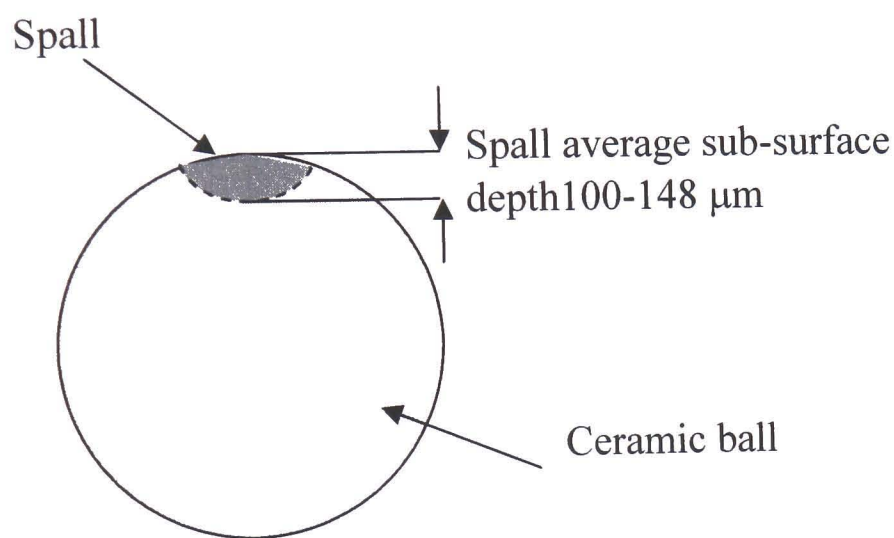


Figure 6.18 Ceramic failed ball showing spall

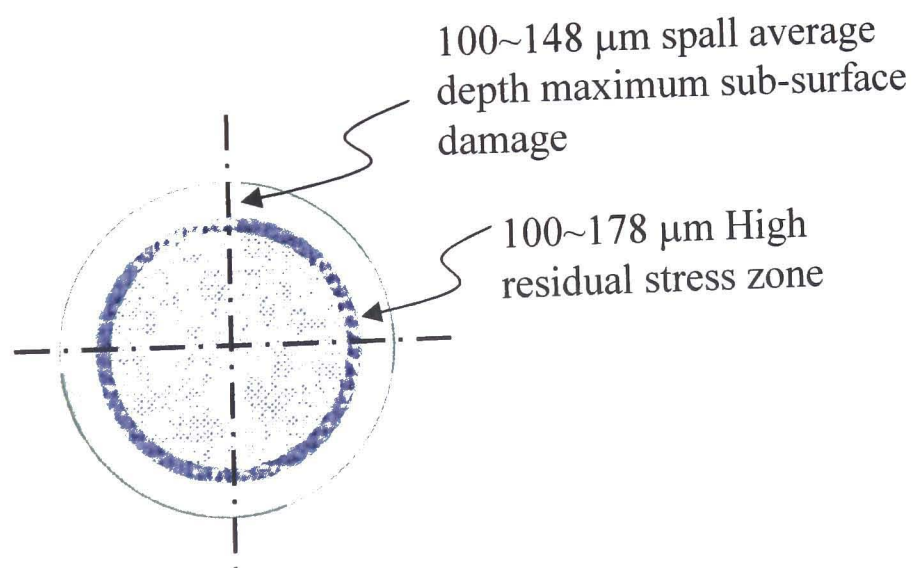


Figure 6.19 Sub surface compressive residual stress distribution

Specimen 14 had four indents. These indents were induced using a Vickers's hardness machine. The indent loading was 1 Kg. The specimen was subjected to a maximum contact stress of 3 GPa. The other test conditions for specimen 14 are provided in table 5.8. Residual stress values for specimen 14 are provided in table 6.13.

Table 6.13 Compressive residual stress values for Specimen 14

Specimen 14	
Residual stresses (MPa)	Reliability (MPa)
-29	± 44
-64	± 51
-88	± 49
-93	± 53

The indent spall has been rotated 90° counter clockwise for residual stress measurement as can be seen from figures 6.20 and 6.21.

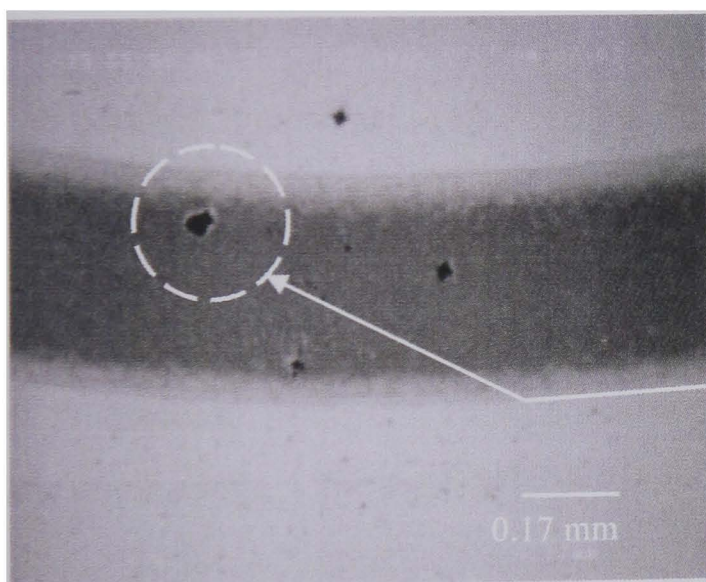


Figure 6.20 Residual stress measuring points for specimen 14

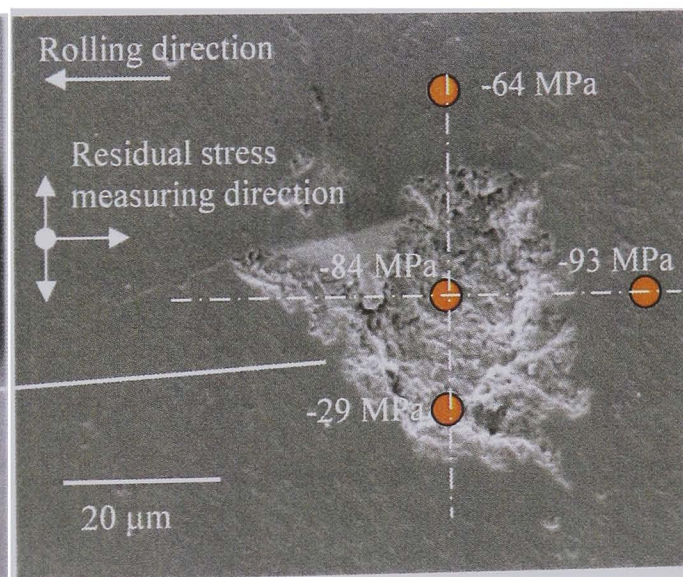


Figure 6.21 Residual stress measuring points for specimen 14

A higher value of 84 MPa is measured at the deep zone in the spall and a lower value of 29 MPa towards the edge of the spall. A lower value 64 MPa of the residual stress was measured at the centre of the contact path. This is because high contact stresses at the centre of the ball relieved the residual stresses more spontaneously. A

comparatively higher value 93 MPa of residual stress away from the contact circle demonstrates lower or non-existent contact stresses in the region. Figure 6.22 shows a schematic of the residual stress measurement points near the spall fatigue and their orientation with respect to the contact path for specimen 14.

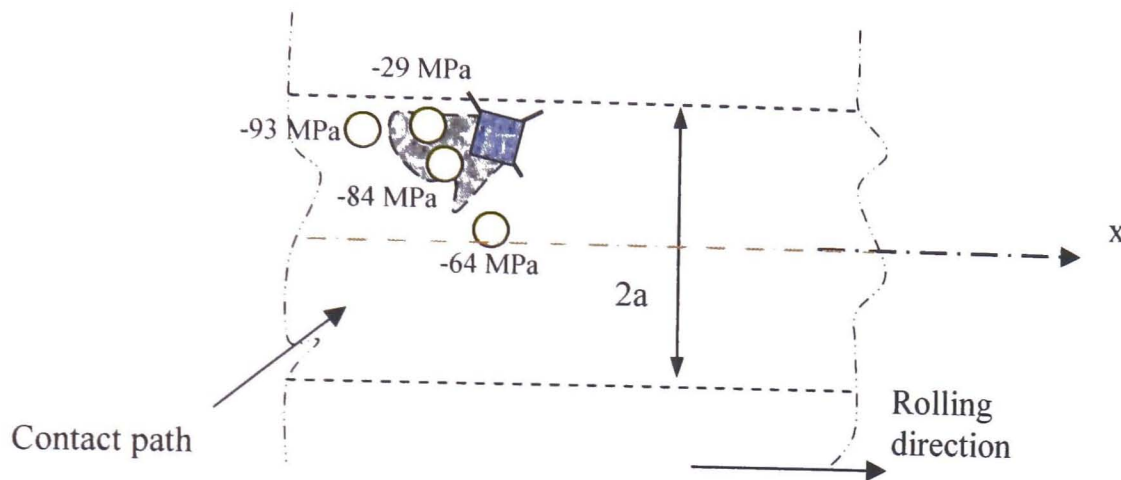


Figure 6.22 Residual stress measurement points for specimen 14

6.7. Secondary cracks

The surface secondary cracks initiate and propagate in the contact path. The influence of these secondary cracks on the residual stress change is not very conspicuous. However, residual stress decreases in the contact area away from the ring crack, as is the case where there are no secondary surface cracks. Table 6.14 shows residual stress measured values for specimen 29. Specimen 29 was tested at a maximum contact stress of 5 GPa. The test conditions are provided in table 5.4.

Table 6.14 Compressive residual stress values for Specimen 29

Specimen 29		
x (mm)	Residual stresses (MPa)	Reliability (MPa)
0.1	-90	±29
0.2	-69	±17
0.3	-24	±20
0.08	-21	±13
0.3	-65	±25

Figure 6.23 shows residual stress measurement points and corresponding values for specimen 29. A higher value 90 MPa of compressive residual stress is measured near the ring crack and shows the decreasing phenomenon away from the ring crack on the contact path. A lower value of 24 MPa residual stress is measured at a distance of 0.3 mm. A comparatively lower value 21 MPa residual stress is measured on the right hand side of the ring crack. Parallel secondary crack initiation and propagation relieves residual stress and lower residual stresses are measured. Residual stresses are relieved at a much faster pace due to secondary surface cracks.

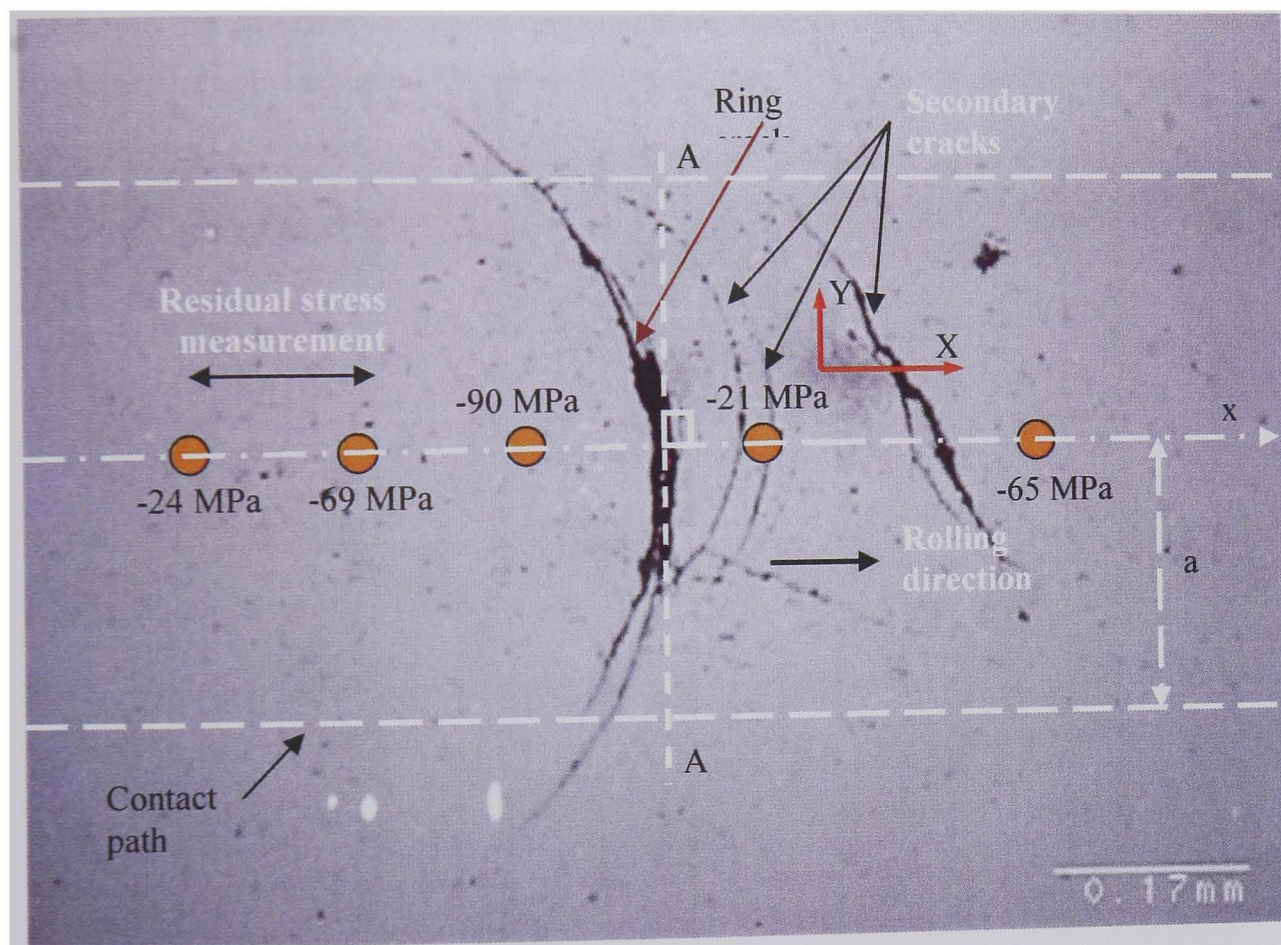


Figure 6.23 Residual stress measurements points for specimen 29

Residual measurements were performed at four points on specimen 22. The highest value of residual stress 209 MPa was recorded at a distance of 0.1 mm away from the induced ring crack. This magnitude of the residual stress decreases sharply and a much lower value of 36 MPa was measured at a distance of 0.15 mm away from the crack. This sharp fall in the residual stress magnitude is due to the secondary surface cracks. A third value 43 MPa residual stress was measured at the secondary surface crack edge at a distance of 0.2 mm away from the ring crack. While a comparatively higher value of 48 MPa residual stress was measured at a distance of 0.3 mm. The two lower values of 36 and 43 MPa are the result of surface cracks.

The residual stress measurement points for specimen 22 and their corresponding values are provided in Figure 6.24. The residual measured stress values for specimen 22 are provided in table 6.15.

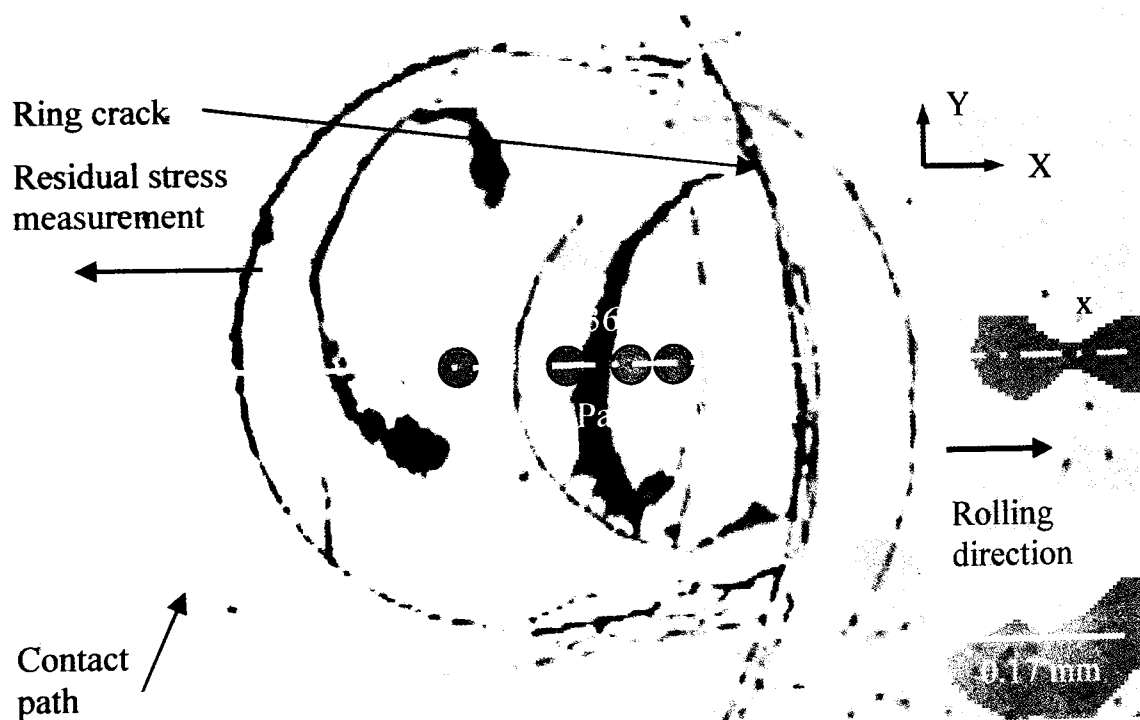


Figure 6.24 Showing residual stress measurements points for specimen 22

Table 6.15 Compressive residual stress values for Specimen 22

Specimen 22		
x (mm)	Residual stresses (MPa)	Reliability (MPa)
0.1	-209	±67
0.15	-36	±34
0.2	-43	±30
0.3	-48	±45

6.8. Tensile residual stresses

Residual stress measurement experiments were performed at 3 different locations on the contact path for specimen 46. These measurements were performed by rotating and positioning the ring crack at 180° CCW. Residual stress measurement values for specimen 46 are provided in table 6.16. The residual stress measuring locations and the corresponding values are provided in figure 6.25. The residual stress measurement for specimen 46 was performed after 5.62 million stress cycles. The residual stress magnitude decreases with the increasing number of stress cycles. The lower compressive residual stresses indicate less time to failure and vice versa. The compressive residual stresses are transformed into tensile residual stresses and will increase with the increasing number of stress cycles. High tensile residual stresses indicate lower fatigue life. The residual stresses are important in predicting the fatigue life of elements in rolling contact.

Table 6.16 Residual stress values for Specimen 46

x (mm)	Residual stresses (MPa)	Reliability (MPa)
0.1	-3	±15
0.2	+3	±11
0.3	+3	±7

The induced value of residual stress depends on the finishing process such as applied lapping load, lapping speed and finishing liquids. The maximum value of

compressive residual stress measured during this research was 420 MPa for specimen 21 at 0.2 mm from the contact circle centre as shown in figure 6.8.

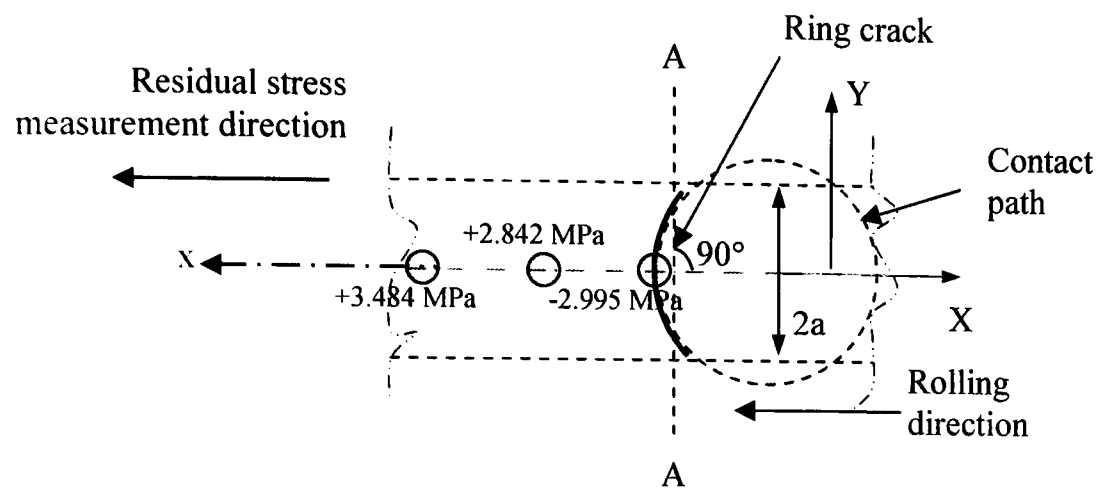


Figure 6.25 Showing residual stress measurements points for specimen 46

This specimen was tested at maximum contact pressure of 5 GPa for 3.11×10^6 stress cycles. The induced value of compressive residual stress for the particular ceramic (Si_3N_4) rolling contact bearing elements under investigation is around 300-350 MPa. This could be different for other silicon nitride rolling contact bearing elements with different lapping conditions.

CHAPTER 7

This research provided design and manufacture of the test rig for conducting pressurised rolling contact fatigue testing both with subcooled liquid and saturated vapour phases of the refrigerant as lubrication. An exhaustive experimental study was performed to study the effect of refrigerant as lubrication. The test specimens were induced with surface defects. State-of-the-art equipment was employed to analyse surface topography of the failed specimens. A comprehensive residual stress survey was performed to understand the residual stress relation to rolling contact test conditions. This chapter summarises the experimental results obtained from rolling contact testing and residual stress measurements.

7. DISCUSSIONS AND CONCLUSION

7.1. RCF test discussions

During rolling contact fatigue testing the secondary crack initiation occurs at the maximum tensile region of the contact path (Khan 2005). The tensile stresses are maximum at the contact path edges. Stress distribution at the contact circle of the rolling contact is shown in figure 7.1. Centre of the contact path is maximum compression. Residual stresses of the element are more vulnerable in the tensile region of the contact path and are relieved faster in that region. The crack initiation takes place as the residual stresses are relieved with increase in rolling contact stress cycles. The crack is subsequently propagated in the contact circle. The decreases of the residual stresses at the edges cause a gradual decrease in the maximum tensile stress circle. The original contact circle stress distribution is changed. The maximum tensile stress circle is reduced by Δx which is proportional to the number of stress cycles. This amount offsets the tensile stress circle and a new secondary crack initiates at the edge of the new circle as shown in figure 7.2. This phenomenon of crack propagation leads to an elliptical spall failure.

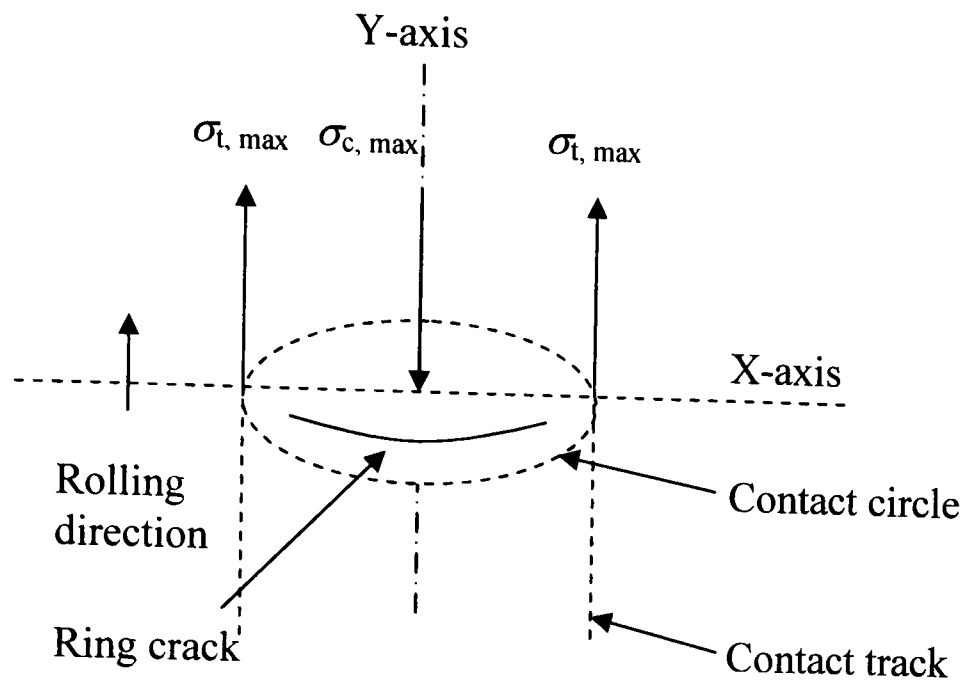


Figure 7.1 Schematic of the stress distribution in the contact circle

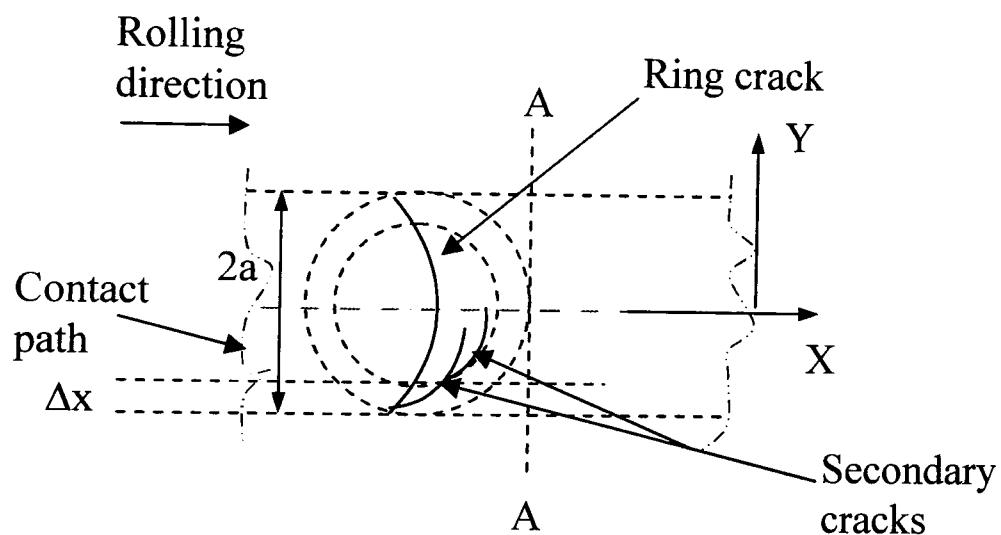


Figure 7.2 Residual stress measurements points

Maximum contact pressure influences fatigue life performance and rolling contact failure mechanisms. The severity of failure is also affected. Similarly, wear state is influenced by the refrigerant liquid or gaseous state. Ring crack positioning and orientation in the contact path influence fatigue life performance as well as the wear in the specimens. A detailed 3-dimensional surface analysis of specimens 17 and 28 was performed using surface mapping by Zygo. Specimen 17 was subjected to a maximum contact stress of 5 GPa and specimen 28 was subjected to a maximum

contact stress of 6 GPa. Both specimens had an induced a ring crack defect caused by impact at a swing angle of 30°. The ring crack was positioned horizontally into the contact path for specimen 17, while vertically for specimen 28. HC refrigerant (R600a) was employed in both tests. The refrigerant state for specimen 17 was subcooled liquid and for specimen 28 was saturated vapour. Both specimens were failed into a fatigue spall. The sub-surface topography was compared for both the specimens.

7.2. Residual stress discussion

A high value of CRS (Compressive Residual Stress) 242 MPa was measured for specimen 27 with the least number of stress cycles. While a lowest CRS value of 60 MPa was registered for specimen 46 with highest RCF stress cycles. These results demonstrate a consistent relationship of CRS with the RCF stress cycles. This relationship is useful in predicting RCF performance of bearing elements.

The maximum value of CRS measured was 242 MPa at a nearest distance of 0.1 mm from the induced ring crack. The lowest value recorded at a distance of 0.5 mm was 97 MPa compressive. These tests suggest a decrease in the CRS with increased distance from the initial crack. RS measurements for specimen 36 show a similar phenomenon to those of specimen 27. A maximum CRS value of 217 MPa was registered at 0.1 mm from the crack on the contact path for specimen 36. A minimum CRS value of 38 MPa at a distance of 0.6 mm was measured.

Higher CRS at or near failure could be due to the subsurface crack propagation releasing HIP (Hot Isostatically Pressed) treatment CRS (Hadfield et al. 1998). The sub-surface crack initiation and propagation causes a weaker residual stress field at the sub-surface crack front (Khan 2005).

The value measured at zero distance from the crack in both directions for specimen 46 MPa remained unchanged. This could be explained in terms of the measuring point being right above the crack opening and measurement being performed at a depth of more than 30 μm . Therefore, changing the direction has no significant influence on the CRS value at that particular point. However, when the direction for

the second measuring point was changed the CRS value changed from 60 to 52 MPa. Taking the difference in values and reliability factor into consideration, this change is not very significant however it does suggest a relationship between the rolling direction and RS measuring direction. RS measurement the on third point for specimen 46 repeats the same change. The CRS value changed from 42 to 48 MPa. The difference of residual stress measurements can be explained in terms of the stress field and rolling direction. Current investigation suggests that the RS measuring direction will cause the RS value to change. Although the change in the RS values is not very big, the rolling direction in relation to RS measurement direction is significant.

7.3. Conclusions

This research was significant from the point of view that refrigerants were used as lubricants. The pressurised chamber is a unique device which ensures the refrigerant is kept in liquid a state without extreme conditions of pressure. The ideal experimental conditions simulate the actual operating condition. Therefore, the experimental results reflect the practical scenarios. The experimental study of the rolling contact of ceramic-steel has shown some significant developments.

1. To satisfy the boundary lubrication conditions, saturated liquid state of the refrigerant must exist. It was possible to achieve the saturated liquid condition of the refrigerant(s) without running the experiments in severe conditions of pressure and temperature that may have caused additional frictional heat, thus not reflecting the practical operating conditions. The design, manufacture and successful commissioning of the pressurised chamber and test rig modification of the Rotary Tribometer provides an opportunity to conduct rolling hybrid (ceramic/steel) contact tests in a sub-cooled refrigerant environment.
2. Fatigue lives of the specimens tested in different refrigerants were different. That suggests that different environmental chemistry significantly affects the wear

mechanisms. The gaseous phase of the refrigerant results in severe wear during rolling contact fatigue of hybrid ceramic/steel contact.

3. Pre-induced defects result in secondary crack initiation and propagation resulting in failure as spalling.
4. Positioning of the crack in the contact track influences fatigue life during rolling contact.
5. Compressive residual stresses are indicative of the rolling contact fatigue life performance. The compressive residual stresses act in a plane opposite to the applied Hertzian contact stresses and therefore, enhance the fatigue life. An inverse relationship of compressive residual stresses to the number of stress cycles during rolling contact fatigue can be used as a measure of the remaining life.
6. Residual stresses are relieved much faster in the fatigue damaged region. The sub-surface crack initiation and propagation develops a weaker residual stress field at the sub-surface crack front. Secondary surface cracks reduce the magnitude of the residual stresses. High residual stress value at the crack could be the result of lower Hertzian contact stresses and the phenomenon of the maximum orthogonal shear stresses at the pre-cracked area.
7. Residual stresses decrease in magnitude in a direction away from the surface ring crack. This phenomenon indicates sub-surface damage i.e. sub-surface crack initiation and propagation. The rolling contact fatigue life is enhanced due to the induced compressive residual stresses. High values of the compressive residual stress indicate a high number of fatigue cycles before failure. Compressive residual stresses transform into tensile residual stresses and lead to fatigue failure. Lower values of CRS are recorded at the maximum contact stress region and within the contact path compared to that exterior to the contact path.
8. When ring crack is induced the residual stress in the element is relieved at the crack tip. The residual stresses are relieved much faster away from the originally

induced ring crack in the contact path, due to sub-surface crack initiation and propagation. The CRS values change when the direction of RS measuring has changed. Therefore, the rolling direction influences the fatigue life. Pre-test residual stress data is vital to predict the fatigue life of a rolling contact element with respect to its rolling direction.

7.4. Future work

1. It has been found that the fatigue life performance of the rolling contact was influenced by the state of refrigerant lubrication. Investigation of the rolling contact fatigue at various temperatures of the subcooled refrigerant lubrication is needed to verify the effects of the lubricant penetration in the crack.
2. A comparative investigation of rolling contact fatigue performance using lubricants of comparable viscosities as of HC and HFC refrigerant will be useful in establishing the tribological properties of the refrigerants as lubricants.
3. A sub-surface crack propagation investigation is necessary to understand the subsequent failure mechanism and prediction of failure.
4. Further experimental study is needed to investigate the implications of the refrigerant lubrication on the bearing life as conventional studies are not suitable to predict remaining life in rolling contact with the new generation of refrigerants as lubrication.
5. RS measurement comparison of specimens produced through different routes of HIPing, Sintering, Doping, etc.
6. Analysis of RS and Hertzian contact stress relationship.
7. Further investigation of RS and validation of the simulation results. Development of an FE model based on the RS relation to RCF life.

1. Experimental Research

There are several test rigs in use to assess rolling contact fatigue failure of silicon nitride bearing elements. These machines are usually coupled with a vibration sensor and will respond to any irregular vibrations due to severe wear or spalling during tests. Any excess vibration due to severe surface damage will result in stopping the machine. The specimen can then be analysed for surface damage. The machine can be stopped intermittently to analyse the surface damage during the course of testing. Failure modes could be changed according to contact geometry (Hadfield et al. 1995a; Hadfield et al. 1995b). The experimental evaluation of silicon nitride bearing elements should be conducted on various model tests prior to predicting its performance for rolling contact application. Various rolling contact test machines are briefly described here.

1.1. Modified Four-Ball Machine

The modified four-ball machine simulates a deep groove ball-bearing environment. This test configuration has three lower balls free to spin and revolve with an upper fixed ball having one degree freedom and only translating spindle motion. The lower three balls revolve in a cup that simulates the bearing outer race, while the upper ball represents the inner bearing race. The lower planetary balls represent the rolling elements within the bearing. Loading geometry for a modified four-ball machine is shown in figure A1.1. This machine has been very useful in the study of RCF performance of materials subjected to various tribological conditions. The influence of lubricants on steel ball RCF was evaluated using this machine (Barwell et al. 1956), (Krivoshein 1960) and (Scott 1963). The Institute of Petroleum compiled numerous papers (Tourret et al. 1977) that describe various test results, kinematics, and ball dynamics using a modified four-ball machine. This machine has been used to study the RCF performance of hot-pressed silicon nitride bearing materials (Scott

et al. 1971) and (Scott et al. 1973). Recently, a modified four-ball machine has been used to simulate the rolling contact in hybrid (ceramic/steel) rolling element bearings (Hadfield et al. 1993a; Hadfield et al. 1993b and Hadfield 1998).

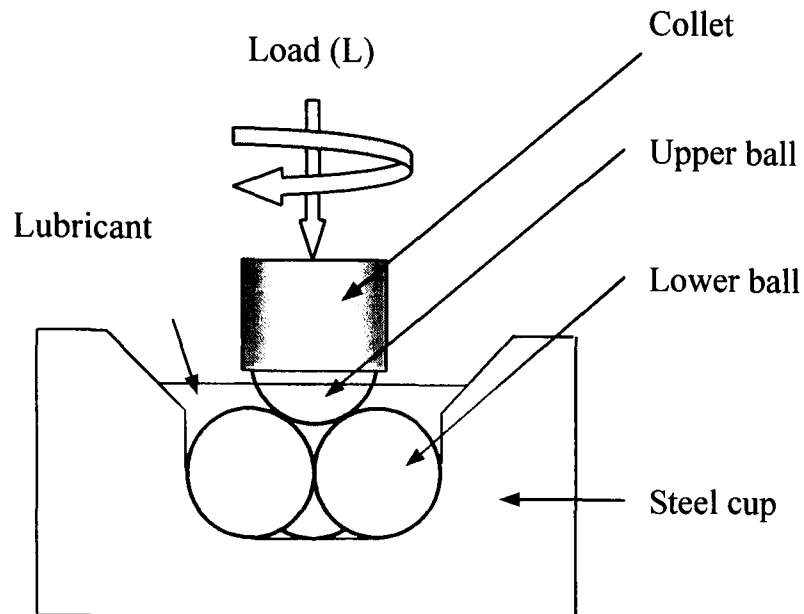


Figure.A1.1 Loading Configuration of Modified Four-Ball Machine

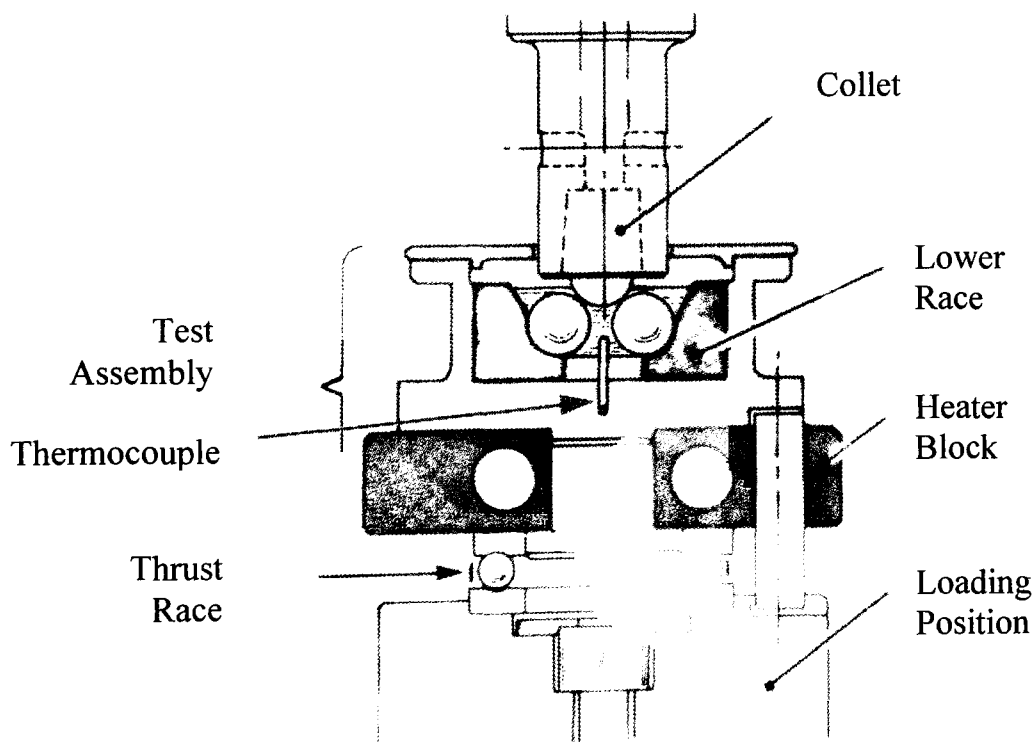


Fig.A1.2 Rolling Contact Fatigue Test Machine, High Speed Test Arrangement (TE92 manual)

A cross-sectional view of the modified four-ball machine is shown in figure A1.2. A thermocouple registers bulk internal temperature of the cup. A heater block is provided to control bulk temperature of the cup. During this research this block was modified to become a part of the cooling system.

1.2. Five-Ball Machine

Figure A1.3 shows contact geometry and rotating mechanism of a five-ball machine. The four lower balls are driven in a race by an upper ball. This arrangement simulates rolling and sliding of angular-contact ball bearings. This machine has been used to investigate the fatigue life of high-speed rolling elements including hot pressed silicon nitride balls (Carter et al. 1960) and (Parker et al. 1975).

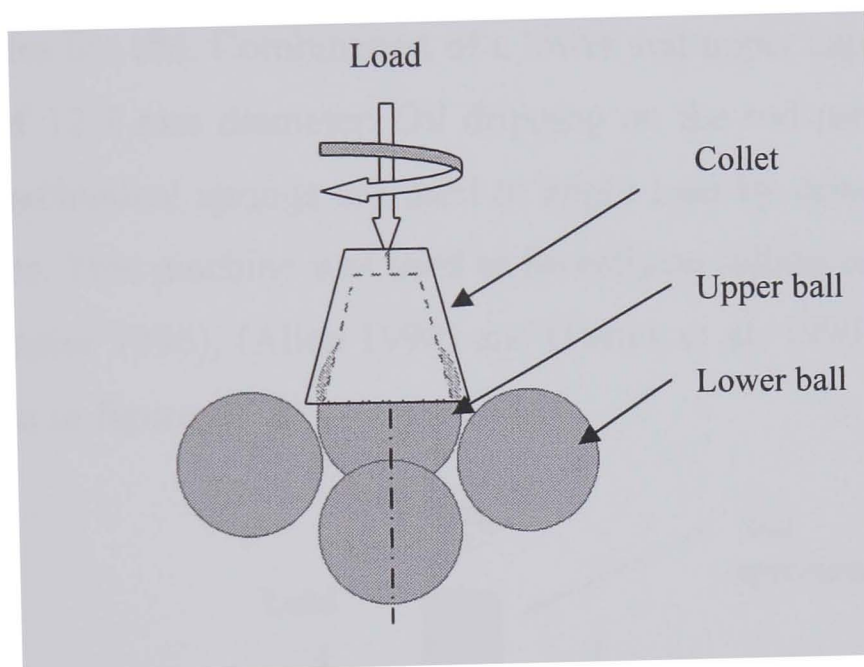


Figure A1.3 Loading configuration of the five-ball machine

1.3. Ball-on-Plate Machine

The ball-on-plate machine shown in figure A1.4 was used to investigate the RCF performance of silicon nitride (Kikuchi et al. 1984) and (Fujiwara et al. 1989). This machine has a unidirectional thrust bearing consisting of three balls or rollers positioned at 120° to each other. The balls/rollers are retained by a retainer and loaded between a stationary flat and a rotating grooved washer. Rotating washers produce motion and transmit load to the rollers/balls and the flat washer.

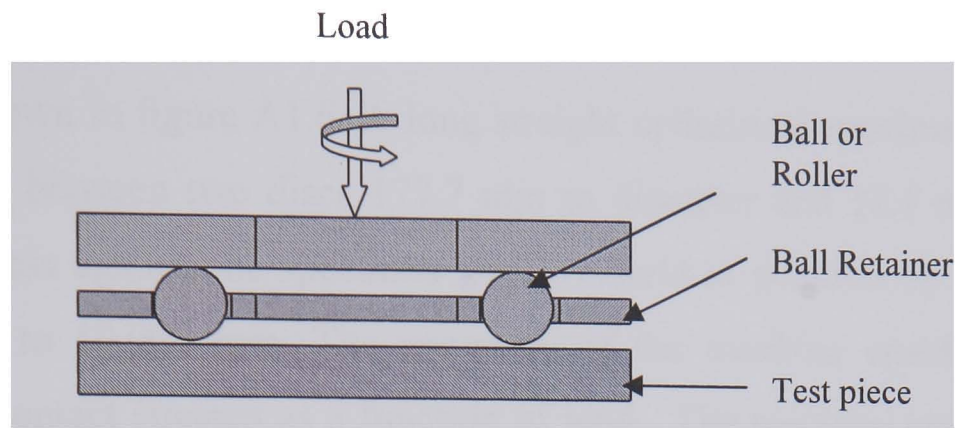


Figure A1.4 Loading configuration of ball-on-plate machine

1.4. Ball-on-Rod Machine

This machine has a cylindrical rod of 9.53 mm in diameter. A motor coupled in line with the rod drives the rod. Combination of a lower and upper cup provides housing for three balls of 12.7 mm diameter. Oil dripping on the rod provides lubrication. Pre-calibrated mechanical springs are used to apply load by driving the upper cup towards the lower. This machine was used to investigate rolling contact wear (Chao et al. 1991), (Burrier 1996), (Allen 1994) and (Lucek et al. 1990). The ball-on-rod machine is shown in figure A1.5.

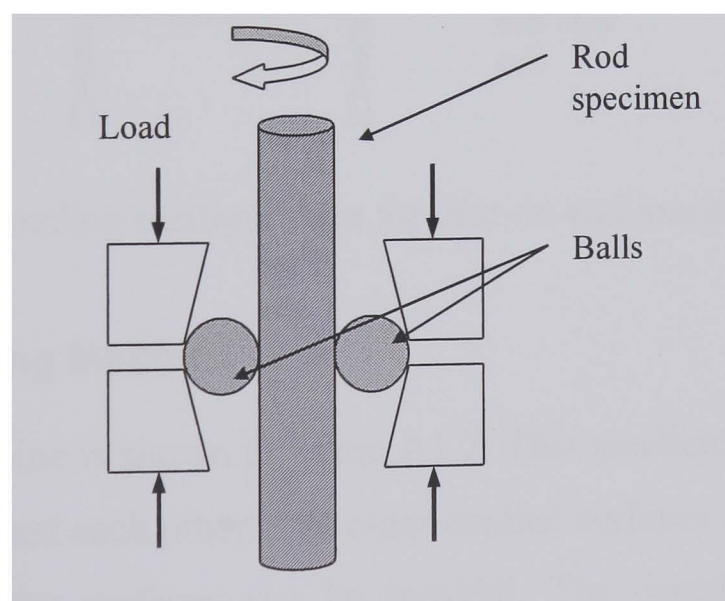


Figure A1.5 Loading configuration of ball-on-rod machine

1.5. Disc-on-Rod Machine

This machine is shown in figure A1.6. A long straight cylindrical specimen 76 mm in diameter is held between two discs 177.7 mm in diameter and 12.7 mm thick. These discs can press against the specimen which is held in position by a spindle and can rotate up to 10,000 rpm. The geometry of the machine enables to the calculation of the contact stresses as a function of load. The machine provides the conditions for rapid testing in almost pure rolling. The specimen undergoes 12×10^5 stress cycles/hour at 10,000 rpm. Some researchers performed earlier work using the disc-on-rod machine (Lucek et al. 1978) and (Baumgartner 1974).

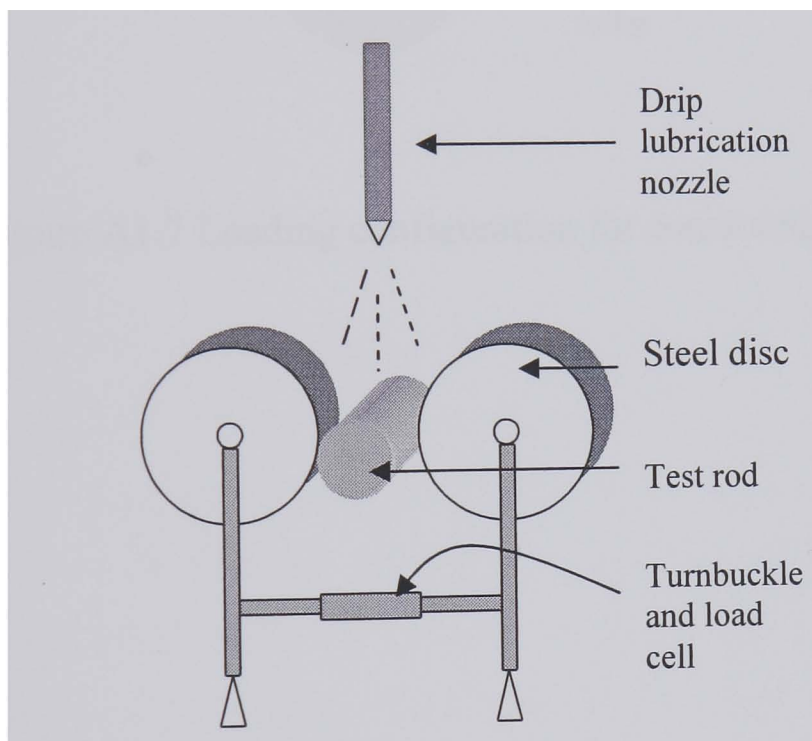


Figure A1.6 Loading configuration for disc-on-rod machine

1.6. Contacting Ring Machine

The contacting ring machine is shown in figure A1.7. This machine has two discs or rings that are rotated against each other. The outer contact surfaces for both the discs may be flat or one of the surfaces can be toroidal. The discs/rings are driven independently by separate motors or a gear mechanism between two discs may be employed thus driving both discs at a different speed. This helps rolling contact with differing sliding/slippage at the surfaces. Load is applied through a compressed coil spring or dead weight mechanism. Dry or lubricated tests can be conducted. The

wear profile on the contact surface helps determine the volume of wear. This machine was used to study the wear performance of ceramics (Akazawa et al. 1986), (Braza 1989) and (Akazawa et al. 1988).

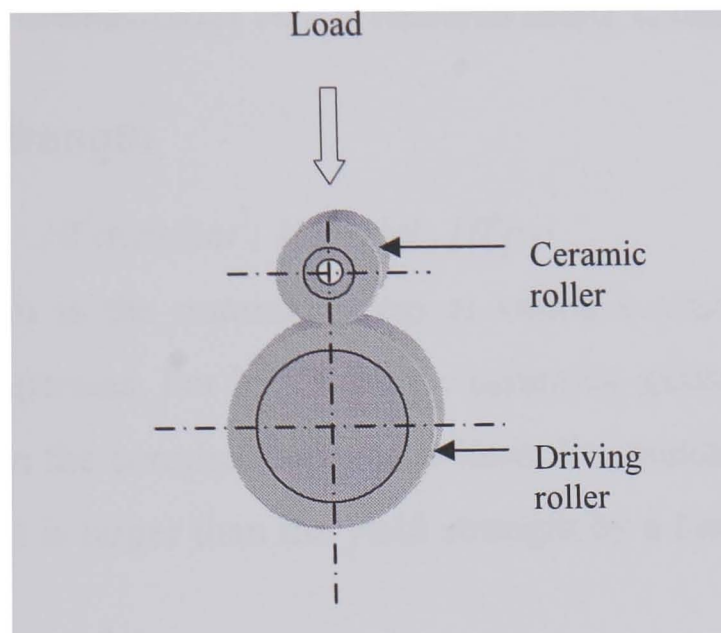


Figure A1.7 Loading configuration for contacting ring

2. Material Selection for Pressurised Chamber

2.1. Tensile Strength

Units: SI: MPa; cgs: 10^7 dyne/cm²; Imperial: 10^3 psi

The Tensile strength is the nominal stress at which a round bar of the material, loaded in tension separates. For brittle solids: ceramics, glasses and brittle polymers - it is much less than the compressive elastic limit. For metals, ductile polymers and most composites - it is larger than the yield strength by a factor ranging from 1.1 to 3.

2.2. Elastic Limit/Yield Strength

Units: SI: MPa; cgs: 10^7 dyne/cm²; Imperial: 10^3 psi

The 'elastic limit' σ_{el} , of a solid requires careful definition.

For metals, the elastic limit is defined as the 0.2% offset yield strength. This represents the stress at which the stress-strain curve for uniaxial tensile loading deviates by a strain of 0.2% from the linear-elastic line. It is the same in tension and compression. It is the stress at which dislocations move large distances through the crystals of the metal.

For polymers, the elastic limit is the stress at which the uniaxial stress-strain curve becomes markedly non-linear: typically, a strain of 1%. This may be caused by 'shear yielding' (irreversible slipping of molecular chains) or by 'crazing' (formation of low density, crack-like volumes which scatter light, making the polymer look white).

For fine ceramics and glasses, the database entry for the elastic limit is an estimate, based on the tensile strength (which is low due to brittle fracture). When based on direct measurements at high pressures, or on hardness measurements, of the stress

required to cause plastic flow, it is very high: higher than the compressive strength, which is lowered by crushing.

For composites, the elastic limit is best defined by a set deviation from linear-elastic uniaxial behaviour: 0.5% is taken in the database.

Elastic limit depends on the mode of loading. For modes of loading other than uniaxial tension, such as shear and multiaxial loading, the strength is related to that in simple tension by a yield function. For metals, the Von Mises yield function works well. It specifies the relationship between the principal stresses σ_1 , σ_2 , σ_3 and the yield strength σ_y (elastic limit):

$$(\sigma_1 - \sigma_2)^2 + (\sigma_2 - \sigma_3)^2 + (\sigma_3 - \sigma_1)^2 = 2\sigma_y^2 \quad (2.1)$$

The Tresca function is sometimes more convenient, because it is less complicated:

For ceramics, a Coulomb flow law is used:

$$\sigma_1 - \sigma_3 = \sigma_y \left(1 + \beta \frac{p}{\sigma_y} \right) \quad (2.2)$$

$$p = -\frac{1}{3}(\sigma_{11} + \sigma_{22} + \sigma_{33}) \quad (2.3)$$

σ_y = yield stress in uniaxial tension, β = constant

For ceramics, a Coulomb flow law is used:

$$\sigma_1 - B\sigma_3 = C \quad (2.4)$$

2.3. Thermal Conductivity

Units: SI: W/m.K; cgs: cal/cm.s.K; Imperial: Btu/h.ft.F

The rate at which heat is conducted through a solid at 'steady state' (meaning that the temperature profile does not change with time) is governed by the thermal conductivity λ . It is measured by recording the heat flux J (W/m²) flowing from surface at temperature T_1 to one at T_2 in the material, separated by a distance X :

$$J = \lambda \frac{(T_1 - T_2)}{X} \quad (2.5)$$

In practice, the measurement is not easy (particularly for materials with low conductivities), but reliable data are now generally available.

2.4. Thermal Expansion Coefficient

Units: SI: $10^{-6}/K$; cgs: $10^{-6}/K$; Imperial: $10^{-6}/F$

Most materials expand when they are heated. The linear thermal expansion coefficient α is the thermal strain per degree K .

If the material is thermally isotropic, the volumetric expansion per degree is 3α . If it is anisotropic, two or more coefficients are required and the volumetric expansion is the sum of the principal thermal strains.

2.5. Temperatures

Units: SI: K ; cgs: K ; Imperial: $^{\circ}R$

The Melting temperature, T_m .

The temperature at which a material turns suddenly from solid to liquid. The melting temperature of an alloy is usually less than the melting temperature of the parent metals.

The Glass temperature, T_g .

A property of non-crystalline solids which do not have a sharp melting point. It characterises the transition from true solid to viscous liquid in these materials.

2.6. Endurance Limit

Units: SI: MPa ; cgs: $10^7 dyne/cm^2$; Imperial: $10^3 psi$

The endurance limit is defined as the maximum applied cyclic stress amplitude for an 'infinite' fatigue life. Generally 'infinite' life means more than 10^7 cycles to failure.

2.7. Loss-Coefficient

Units: Dimensionless

The loss-coefficient measures the degree to which a material dissipates vibrational energy. If a material is loaded elastically to a stress σ_{\max} , it stores elastic energy

$$U = \int_0^{\sigma_{\max}} d\varepsilon \frac{1}{2} \frac{\sigma_{\max}^2}{E} \quad (2.6)$$

per unit volume. If it is loaded and then unloaded, it dissipates energy equivalent to the area of the stress-strain hysteresis loop:

$$\Delta u = \oint \sigma d\varepsilon \quad (2.7)$$

The loss coefficient η is defined as

$$\eta = \frac{\Delta u}{2\pi u} \quad (2.8)$$

The cycle can be applied in many different ways - some fast, some slow. The value of η usually depends on the time-scale or frequency of cycling.

Cast aluminium alloy, A332.0 (c): LM13-TF7¹

General

Designation

Al alloy: A332.0; LM13-TF7 (cast)

Density	2670	-	2730	kg/m ³
Price	0.7547	-	1.223	GBP/kg
CO2 creation	* 11	-	12.1	kg/kg
Production Energy	* 174	-	193	MJ/kg
Recycle Fraction	* 0.8	-	0.9	

Composition

Composition (Summary)

Al/11Si/Mg/Cu

Base	Al (Aluminium)		
Al (Aluminium)	89		%
Cu (Copper)	0		%
Mg (Magnesium)	0		%

¹ Material selection is performed by using Cambridge Engineering Selector (CES)

Si (Silicon)	11		%
Mechanical			
Bulk Modulus	65	- 86	GPa
Compressive Strength	180.5	- 199.5	MPa
Elongation	0.9	- 1.1	%
Elastic Limit	180.5	- 199.5	MPa
Endurance Limit	* 63	- 82	MPa
Fracture Toughness	* 23	- 25	MPa.m ^{1/2}
Hardness - Vickers	74.5	- 75.5	HV
Loss Coefficient	* 1e-4	- 2e-3	
Modulus of Rupture	180.5	- 199.5	MPa
Poisson's Ratio	0.32	- 0.36	
Shape Factor	32		
Shear Modulus	26	- 28	GPa
Tensile Strength	199.5	- 220.5	MPa
Young's Modulus	71	- 75	GPa
Thermal			
Maximum Service Temperature	130	- 180	°C
Melting Point	525	- 560	°C
Minimum Service Temperature	-273		°C
Specific Heat	944	- 982	J/kg.K
Thermal Conductivity	115	- 119	W/m.K
Thermal Expansion	18.5	- 19.5	µstrain/°C
Optical			
Transparency	Opaque		
Environmental Resistance			
Flammability	Good		
Fresh Water	Very Good		
Organic Solvents	Very Good		

Oxidation at 500C	Very Poor
Sea Water	Good
Strong Acid	Very Good
Strong Alkalis	Poor
UV	Very Good
Wear	Average
Weak Acid	Very Good
Weak Alkalis	Good

Notes**Typical Uses**

Pistons

Other Notes

(LM13-TF7) Prices of Aluminium alloys fluctuate greatly and are dependent on batch size, unit size, forming methods, etc. This is the most widely used general purpose, high strength casting alloy.

Reference Sources

Data compiled from multiple sources. See links to the References table.

Rough Machining (Manual)**General****Designation**

Machining: Rough Machining (manual)

The process

Rough machining includes a large group of processes such as cutting, turning, drilling, milling, etc. which are collectively known as machining processes. They have in common the fact that some shape or feature is generated by removing unwanted material.

The workpiece is often held in place using some gripping device and a cutting tool made of a hard material moves in a pre specified way to generate the desired shape.

Rough machining processes, as the name implies, produce liberal tolerances and relatively rough surfaces and are used for removing large amounts of unwanted material. They are often followed by either standard or fine machining processes.

Process Schematic

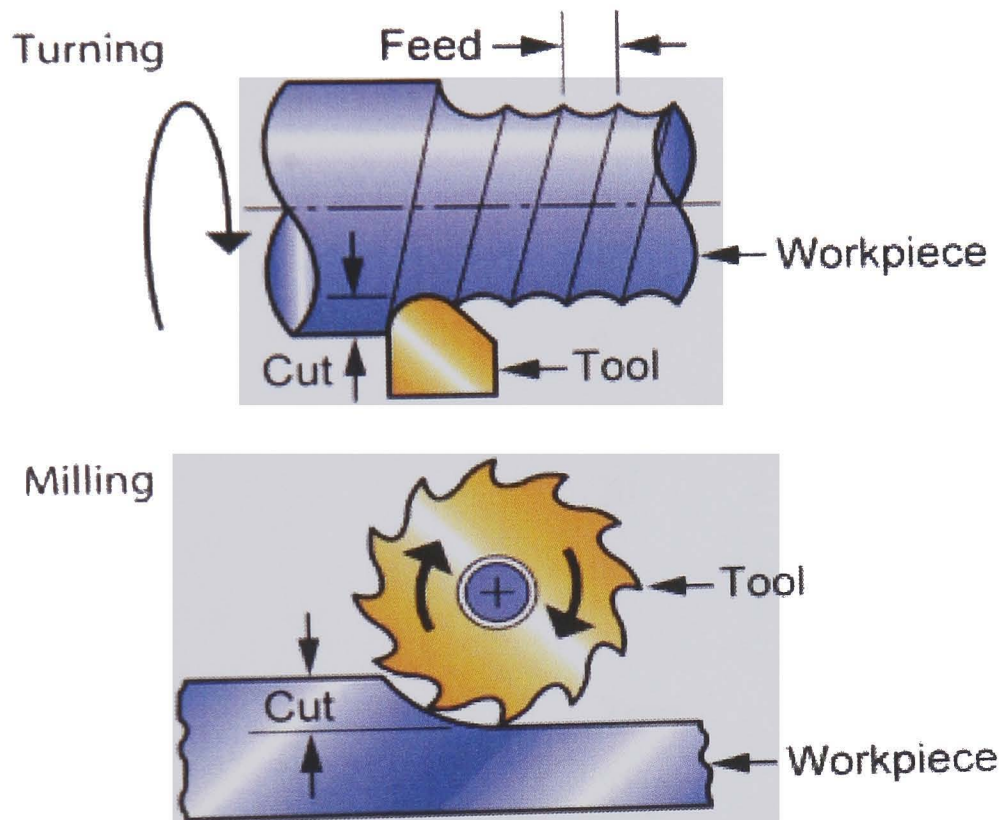


Figure A2.1 Machining process (manual), CES 2005

Physical Attributes

Mass range	0.1	-	1e4	kg
Section thickness	0.1	-	999	mm
Tolerance	0.762	-	1	mm
Roughness	3.2	-	25	μm
Adjacent section ratio	*1	-	10	
Aspect ratio	1	-	1000	
Minimum hole diameter	0.1			mm
Minimum corner radius	1			mm
Quality factor (1-10)	1	-	10	

Economic Attributes

Economic batch size (mass)	10	-	1000	kg
Economic batch size (units)	1	-	1000	

Cost Modelling

Relative Cost Index (per unit)	20.71	-	119.1	
--------------------------------	-------	---	-------	--

Parameters: Material Cost = 5GBP/kg, Component Mass = 1kg, Batch Size = 1000, Overhead Rate = 60GBP/hr, Capital Write-off Time = 5yrs, Load Factor = 0.5

Capital cost	3000	-	3e4	GBP
Lead time	0.1	-	1	week(s)
Material utilisation fraction	0.05	-	0.8	
Production rate (mass)	2	-	50	kg/hr
Production rate (units)	2	-	100	/hr
Tool life (mass)	20	-	100	kg
Tool life (units)	20	-	100	
Tooling cost	5	-	100	GBP

Shape

Circular Prismatic	True
Non-Circular Prismatic	True
Solid 3-D	True
Hollow 3-D	True

Supporting Information**Design guidelines**

Very intricate shapes. Some processes are limited to axisymmetric shapes, some are used for making holes and slots only.

Technical notes

Can be used to machine most materials using suitable tools and techniques

Typical uses

Machinery and structural parts. For example, pistons, pins, gears, shafts, rivets, valves, pipe fittings, etc.

The environment

Most environmental problems are due to lubricants/cutting fluids, overspray and burn off, but there can be metal fumes from the workpiece.

2.8 Chamber Design

2.8.1. External Cooling Design

The assembly statistics² are shown are below.

Total number of components:	2
Parts:	2
Unique parts:	2
Sub-assemblies:	0
Unique sub-assemblies:	0
Resolved components:	2
Suppressed components:	0
Lightweight components:	0
Number of top-level mates:	2
Number of top level components:	2
Maximum depth:	1

Mass properties of the pressurised chamber are given below:

Mass properties of Modified_design_Assembly_1

Output coordinate System : -- default --

Mass = 152 grams

Volume = 152 cm³

Surface area = 45 cm²

Centre of mass: (millimeters)

X = 0.04

Y = 0.05

Z = 20.83

² Components of suppressed sub-assemblies are excluded from these statistics.

Principal axes of inertia and principal moments of inertia: (grams * square millimeters)

Taken at the center of mass.

$$I_x = (1.00, 0.00, 0.00) \quad P_x = 117356.68$$

$$I_y = (0.00, 1.00, 0.00) \quad P_y = 117401.52$$

$$I_z = (0.00, 0.00, 1.00) \quad P_z = 131661.64$$

Moments of inertia: (grams * square millimeters)

Taken at the center of mass and aligned with the output coordinate system.

$$L_{xx} = 117357.55 \quad L_{xy} = -0.31 \quad L_{xz} = 111.76$$

$$L_{yx} = -0.31 \quad L_{yy} = 117402.25 \quad L_{yz} = 102.60$$

$$L_{zx} = 111.76 \quad L_{zy} = 102.60 \quad L_{zz} = 131660.03$$

Moments of inertia: (grams * square millimeters)

Taken at the output coordinate system.

$$I_{xx} = 183525.78 \quad I_{xy} = -0.00 \quad I_{xz} = 233.40$$

$$I_{yx} = -0.00 \quad I_{yy} = 183570.28 \quad I_{yz} = 270.39$$

$$I_{zx} = 233.40 \quad I_{zy} = 270.39 \quad I_{zz} = 131660.68$$

2.8.2. Cooling Fin Design

The assembly statistics³ are shown as below.

Total number of components:	2
Parts:	2
Unique parts:	2
Sub-assemblies:	0
Unique sub-assemblies:	0
Resolved components:	2
Suppressed components:	0
Lightweight components:	0
Number of top-level mates:	2
Number of top level components:	2

³ Components of suppressed sub-assemblies are excluded from these statistics.

Maximum depth: 1

Mass properties of the pressurised chamber are given below:

Mass properties of Cooling_fins_assembly

Output coordinate System : -- default --

Mass = 164.50 grams

Volume = 164 cm³

Surface area = 60 cm²

Centre of mass: (millimeters)

$$X = -0.14$$

$$Y = 0.41$$

$$Z = 21.87$$

Principal axes of inertia and principal moments of inertia: (grams * square millimeters)

Taken at the center of mass.

$$I_x = (1.00, 0.00, 0.00) \quad P_x = 127004.21$$

$$I_y = (0.00, 1.00, 0.00) \quad P_y = 128853.06$$

$$I_z = (0.00, 0.00, 1.00) \quad P_z = 146569.26$$

Moments of inertia: (grams * square millimeters)

Taken at the centre of mass and aligned with the output coordinate system.

$$L_{xx} = 128565.31 \quad L_{xy} = 687.21 \quad L_{xz} = -257.54$$

$$L_{yx} = 687.21 \quad L_{yy} = 127337.07 \quad L_{yz} = 882.18$$

$$L_{zx} = -257.54 \quad L_{zy} = 882.18 \quad L_{zz} = 146524.15$$

Moments of inertia: (grams * square millimeters)

Taken at the output coordinate system.

$$I_{xx} = 207275.11 \quad I_{xy} = 677.79 \quad I_{xz} = -755.36$$

$$I_{yx} = 677.79 \quad I_{yy} = 206021.83 \quad I_{yz} = 2371.28$$

$$I_{zx} = -755.36 \quad I_{zy} = 2371.28 \quad I_{zz} = 146555.48$$

2.8.3. Internal Cooling Design

The assembly statistics⁴ are shown as below.

Total number of components:	2
Parts:	2
Unique parts:	2
Sub-assemblies:	0
Unique sub-assemblies:	0
Resolved components:	2
Suppressed components:	0
Lightweight components:	0
Number of top-level mates:	2
Number of top level components:	2
Maximum depth:	1

Mass properties of the pressurised chamber are given below:

Mass properties of Internal_cooling_assembly

Output coordinate System : -- default --

Mass = 65.15 grams

Volume = 65 cm³

Surface area = 78 cm²

Centre of mass: (millimeters)

$$X = 0.06$$

$$Y = -0.12$$

$$Z = 25.62$$

Principal axes of inertia and principal moments of inertia: (grams * square millimeters)

Taken at the centre of mass.

$$I_x = (1.00, 0.00, 0.00) \quad P_x = 57530.30$$

$$I_y = (0.00, 0.00, 1.00) \quad P_y = 60519.55$$

⁴ Components of suppressed sub-assemblies are excluded from these statistics.

$$I_z = (0.00, 0.00, 1.00) \quad P_z = 60563.54$$

Moments of inertia: (grams * square millimeters)

Taken at the centre of mass and aligned with the output coordinate system.

$$\begin{aligned} L_{xx} &= 128565.31 & L_{xy} &= 687.21 & L_{xz} &= -257.54 \\ L_{yx} &= 687.21 & L_{yy} &= 127337.07 & L_{yz} &= 882.18 \\ L_{zx} &= -257.54 & L_{zy} &= 882.18 & L_{zz} &= 146524.15 \end{aligned}$$

Moments of inertia: (grams * square millimeters)

Taken at the output coordinate system.

$$\begin{aligned} I_{xx} &= 60536.31 & I_{xy} &= -21.53 & I_{xz} &= 8.68 \\ I_{yx} &= -21.53 & I_{yy} &= 60545.83 & I_{yz} &= -52.85 \\ I_{zx} &= 8.68 & I_{zy} &= -52.85 & I_{zz} &= 57531.26 \end{aligned}$$

Table A2.1 Abbreviations

Abbreviation	Description	Common Test Method
EF	Flexural modulus of elasticity	ASTM D 790
E	Tensile modulus of elasticity	ASTM D 638
TSY	Tensile strength at yield	ASTM D 638
FYS	Flexural yield strength	ASTM D 790

Table A2.2 Mechanical properties of polycarbonate

Polymer	Tensile Strength (MPa)	Tensile Modulus (GPa)	Elongation (%)	Max. Temp. (0C)
Polycarbonate	55-65	2.1-2.4	60-100	120

A spring-energised lip seal is shown in Figure A2.2.



Figure A2.2 Spring-Energised Lip seal



Figure A2.3 Shaft Seal

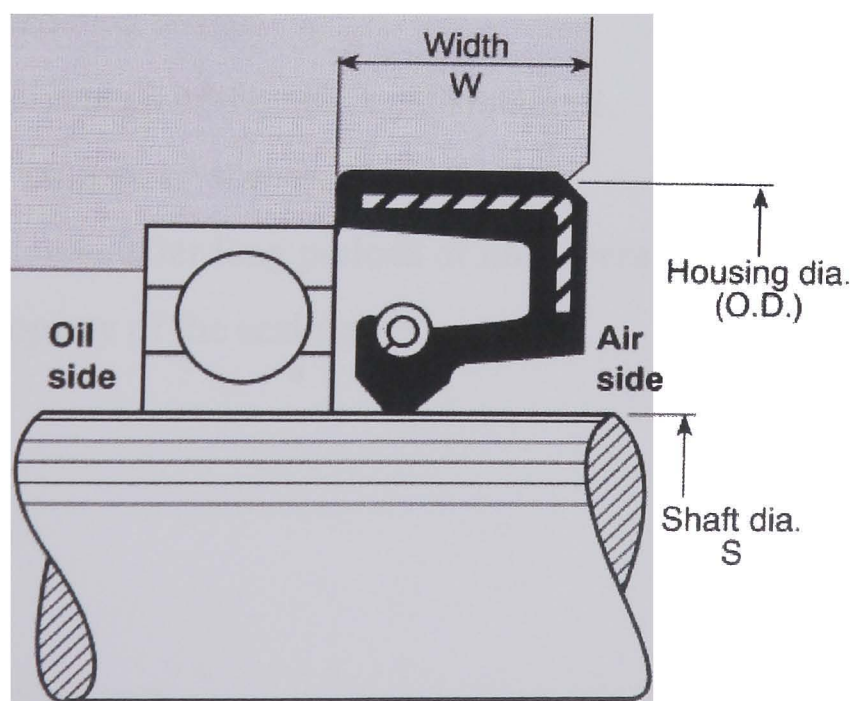


Figure A2.4 Cross-section of a typical Shaft Seal

Figure A2.5 shows some PTFE Rotary Shaft Seals⁵. In order to cover the widest possible range of applications, two standard types have been developed. Type HN 2580 is primarily used for service in unpressurised conditions or where the pressure is only slightly above atmospheric, while type HN 2390 is ideal for pressurised media.

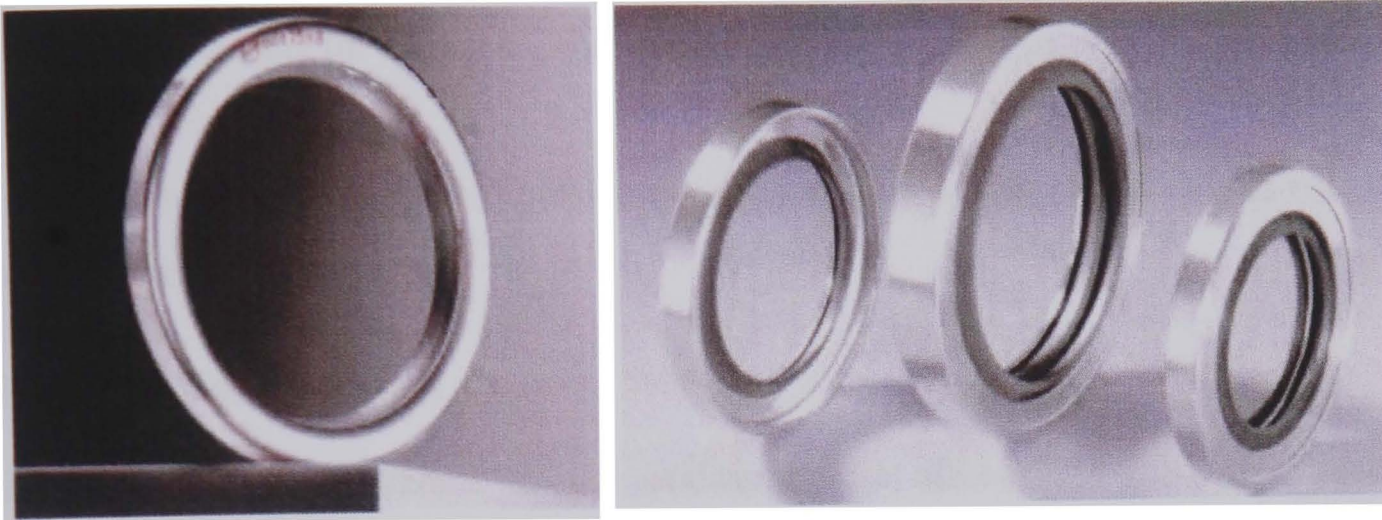


Figure A2.5 PTFE Rotary Shaft Seals

The advantages of the PTFE rotary shaft seals are as follows.

- Outstanding chemical resistance to corrosive media.
- Suitable for high temperature applications from -60 to +220°C.
- Also suitable for lube service and dry running.
- Suitable for unhardened shafts.
- Excellent wear resistance of the sealing lip material.
- Suitable for high peripheral speeds.
- Low breakaway forces after long periods of non-operation.
- Anti-adhesive property of the sealing lip.

⁵ FTL seals technology

Effect of pressure

Pressure affects the seal by forcing it into the gap which exists between toleranced machined parts at the non pressure side of the seal. When the gap is too large the heel of the seal will show "nibbling" and result in premature seal failure. This extrusion will increase if the seal is subjected to side loading. To minimise extrusion while maintaining reasonable machining tolerances seals fitted with anti-extrusion wear rings should be selected. The use of bearing rings will also reduce potential maximum extrusion gaps.

Permissible extrusion gaps / pressure graphs should be consulted for all rod seal applications.

Effect of Temperature

The operating temperature of the sealing media affects the choice of sealing materials. Normal operating temperatures are usually between 80°C to 100°C. The optimum functional temperature for seals and oil stability is between 40°C and 50°C. At low temperatures the seal material will stiffen and may become brittle although it will relax as the temperature rises. At high temperatures the seal material will become more elastic and lose compression set. The higher temperatures will also reduce the viscosity of the oil resulting in accelerated wear of the seals. For PTFE the effect of temperature will be based on the seals energiser.

Effect of Velocity

Seals float on a film of lubricant between the seal lip and moving surface. The fluid is drawn under by movement and is known as hydrodynamic drag. Friction will depend upon the thickness of this lubricating film, which will be squeezed to its minimum thickness when there is no movement, creating stiction. Frictional force begins to decrease with an increase in velocity as more lubricating oil is drawn between the seal and the moving surface. There is a point reached with increasing velocity when the friction force raise and the seal begins to wear. PTFE seals have

an extremely low coefficient of friction when moving on other surfaces and may be a possible exception to this rule.

Effect of Surface Finish

Figure A2.6 shows a diagrammatic representation of average roughness value R_a . The operating life of a seal is greatly influenced by the considerations of the dynamic surface and the method used to produce this surface texture. For instance, honing and roller burnishing may give the same surface finish value but the surface profile would differ. The aim of all types of surface finish is to provide a surface, which causes the minimum wear to the seal. The static surfaces of the seal housing are important as the sealing media may pass over the seal if it is not in the recommended surface finish. The average roughness value R_a (CLA - Centre Line Average Height) is the arithmetic and geometric average value of the profile in "Y" direction from the middle line within the reference length "L".

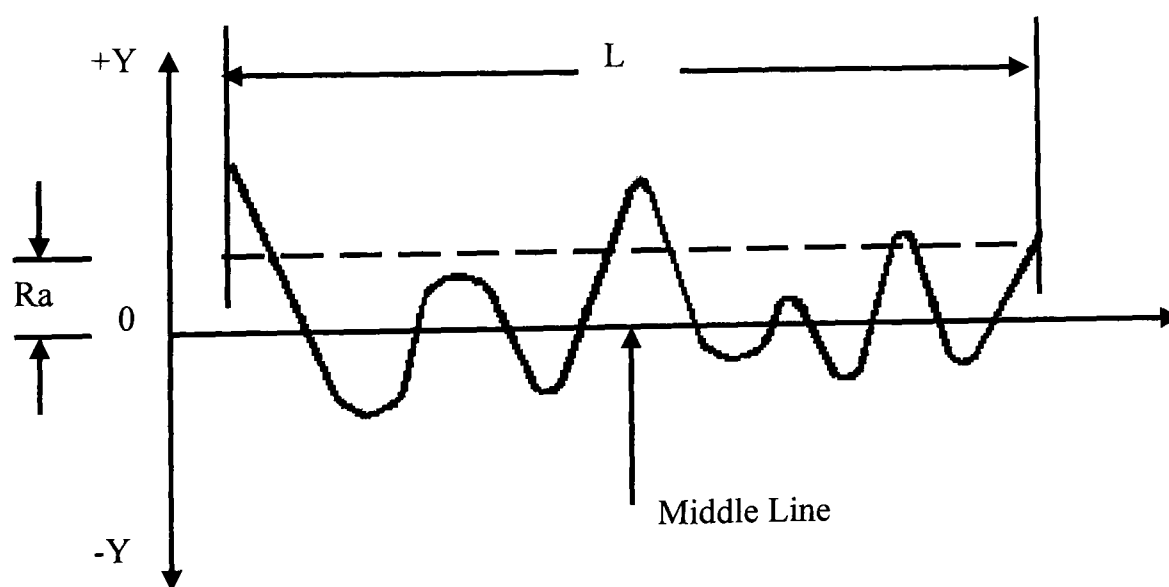


Figure A2.6 Diagrammatic representation of average roughness value, R_a (Courtesy RS online 2005)

Effect of Contamination

Contamination can occur within the system due to inadequate cleaning of parts before assembly or / and due to operational debris from the seal and bearings, with levels of contamination more intensive around the seal area than in the system generally. The effect of contamination is that of seal wear and damage usually in the form of axial scoring. The extent of probability of leakage will depend upon seal materials with PTFE being more prone to leakage when scored. Contaminants may also lodge under the sealing lip allowing a leak path. Bearing materials used in conjunction with seals may also affect oil contamination due to wear debris with metal bearings producing an increase in leakage probability although reducing the surface roughness slightly when used with rods.

Effect of Vapour

Hydraulic fluids contain molecules of air, which is liberated by agitation. Air bubbles then occur and oil vapour collects usually at the highest point in the system. Compression of this mixture will result in a temperature rise causing compression ignition. This process is repeatable and is known as diesel effect, destroying the seal if repeated frequently. The sealing arrangement may be protected with use of phenolic or phosphor bronze rings strategically housed. Sometimes air bubbles will be forced over the seal face, expanding on moving to the low-pressure side of the seal and manifesting themselves as axial grooves, resulting in subsequent seal failure.

PTFE Seal selection

Composite seals were originally designed for low friction or high-temperature applications. The development of PTFE and PTFE compounds in particular, with these capabilities, has greatly extended the useful range of these seals far beyond that of conventional rubber / elastomer based lip-seals. Designs based upon an understanding of lip-geometry and use of the latest development in material technology have allowed composite seals to become acceptable in the normal sphere

of operation of lip-seals, not just in the extremes of duty for which they were originally intended.

Speed and Friction

The optimum speed range for a conventional lip-seal is 0.1 to 0.5 m / sec (RS online 2005). Speeds of up to 4 m / sec can be achieved. Below 0.1 m / sec and above 0.5 m / sec the friction values rise sharply due to the breakdown of lubricant film, causing friction and a build up of heat. At temperatures above 50°C this additional heat can also adversely affect the sealing material, causing swell, hardness and mechanical property changes, with a resultant loss of performance.

Low friction seals are obviously desirable at these extremes of speed or even through the optimum working range of lip-seals when other factors are taken into account.

Frictional heat

The frictional heat developed per second within sliding contact is

$$P_f = f \cdot p \cdot V \cdot A \text{ (Watt)} \quad (2.9)$$

where

f = Co-efficient of friction

p = load (N / mm^2)

V = speed (m/sec)

A = dynamic contact area (mm^2)

Surface Finish

Surface finish is an influencing factor on the performance of seal. For composite seals cylinder bores and rods should have a surface finish between 0.1 - 0.4 μm Ra. Within the housing static sealing surfaces should have a finish better than 0.8 μm Ra. Even after prolonged, bronze filled PTFE will not have any significant effect on surface finish values. Carbon and glass filled PTFE are more abrasive and will slightly reduce the surface roughness. Surface finish can be affected by the use of

hard bearing materials such as Meehanite, Phosphor Bronze or Polyester-Fabric. It is generally recommended that PTFE bearing tape should be used with composite seals.

Bearing materials

PTFE bearing tape is specifically designed for use with PTFE composite seals. The nature of PTFE allows for a manufactured size giving a tighter fit than 'harder' materials such as Meehanite, Phosphor Bronze or Polyester-Fabric. This reduction in radial clearance gives marginal improvement to the pressure capability of the seal but, more importantly, protects the seal from contaminants within the system. A combination of the design of the bearing and the characteristic of PTFE allow the particles to become embedded in the PTFE on the non-working face, thus also protecting the steel counter face from scoring.

During use, bearing materials wear, causing debris and contamination of the fluid. Extensive tests have shown that particle contamination $> 15 \mu\text{m}$ within the fluid increases with the use of Meehanite and Phosphor Bronze and tends to decrease with use of PTFE. The harder debris created by these bearings has a greater effect on seal performance. Particulate contamination in the fluid surrounding the seal can be over 100 times greater than in the main system due to the bearing preventing flushing of the seal space. Increased contamination in this area will increase the probability of a large enough particle gaining access to the seal interface, causing damage and leakage.

Refrigerant: R600a, CH(CH₃)₃, 2-methyl propane (isobutane)

T	P	Vl	Vg	Hl	Hg	R	Sl	Sg
-C	Bar	dm ³ /kg	m ³ /kg	kJ/kg	kJ/kg	kJ/kg	kJ/(kgK)	kJ/(kgK)
-5.00	1.316	1.7011	0.27743	188.74	548.85	360.12	0.9585	2.3015
-4.00	1.366	1.7042	0.26803	190.98	550.20	359.22	0.9669	2.3015
-3.00	1.416	1.7073	0.25902	193.23	551.55	358.32	0.9752	2.3016
-2.00	1.469	1.7104	0.25038	195.48	552.90	357.42	0.9835	2.3016
-1.00	1.522	1.7136	0.24209	197.74	554.25	356.51	0.9917	2.3017
0.00	1.578	1.7168	0.23414	200.00	555.60	355.60	1.0000	2.3019
1.00	1.635	1.7200	0.22650	202.27	556.95	354.69	1.0082	2.3020
2.00	1.693	1.7232	0.21917	204.54	558.31	353.77	1.0165	2.3022
3.00	1.753	1.7264	0.21213	206.81	559.66	352.85	1.0247	2.3024
4.00	1.814	1.7297	0.20536	209.09	561.02	351.92	1.0329	2.3027
5.00	1.878	1.7330	0.19886	211.38	562.37	350.99	1.0411	2.3030
6.00	1.942	1.7363	0.19260	213.67	563.73	350.06	1.0493	2.3033
7.00	2.009	1.7396	0.18659	215.96	565.08	349.12	1.0574	2.3036
8.00	2.077	1.7430	0.18080	218.26	566.44	348.18	1.0656	2.3040
9.00	2.147	1.7464	0.17524	220.57	567.80	347.23	1.0737	2.3044
10.00	2.219	1.7498	0.16988	222.88	569.16	346.28	1.0819	2.3048
11.00	2.293	1.7533	0.16472	225.20	570.51	345.32	1.0900	2.3052
12.00	2.368	1.7568	0.15975	227.52	571.87	344.35	1.0981	2.3057
13.00	2.446	1.7603	0.15496	229.85	573.23	343.38	1.1062	2.3062
14.00	2.525	1.7639	0.15035	232.18	574.59	342.41	1.1143	2.3067
15.00	2.606	1.7674	0.14590	234.52	575.95	341.43	1.1224	2.3073
16.00	2.689	1.7710	0.14162	236.87	577.31	340.44	1.1304	2.3078
17.00	2.775	1.7747	0.13748	239.22	578.67	339.45	1.1385	2.3084
18.00	2.862	1.7784	0.13350	241.58	580.03	338.45	1.1466	2.3090
19.00	2.951	1.7821	0.12965	243.94	581.39	337.45	1.1546	2.3097
20.00	3.042	1.7858	0.12594	246.31	582.75	336.44	1.1627	2.3103
21.00	3.136	1.7896	0.12235	248.69	584.11	335.42	1.1707	2.3110
22.00	3.232	1.7935	0.11889	251.07	585.47	334.40	1.1787	2.3117
23.00	3.329	1.7973	0.11555	253.46	586.83	333.37	1.1867	2.3124
24.00	3.430	1.8012	0.11232	255.85	588.18	332.33	1.1948	2.3132
25.00	3.532	1.8052	0.10920	258.26	589.54	331.29	1.2028	2.3139
26.00	3.636	1.8091	0.10618	260.67	590.90	330.23	1.2108	2.3147
27.00	3.743	1.8132	0.10327	263.08	592.26	329.17	1.2188	2.3155
28.00	3.853	1.8172	0.10045	265.51	593.61	328.11	1.2268	2.3163
29.00	3.964	1.8214	0.09772	267.94	594.97	327.03	1.2348	2.3171
30.00	4.078	1.8255	0.09509	270.38	596.33	325.95	1.2428	2.3180
31.00	4.195	1.8297	0.09253	272.82	597.68	324.86	1.2507	2.3188
32.00	4.314	1.8340	0.09006	275.28	599.03	323.76	1.2587	2.3197
33.00	4.435	1.8383	0.08767	277.74	600.39	322.65	1.2667	2.3206
34.00	4.560	1.8426	0.08536	280.20	601.74	321.53	1.2747	2.3215
35.00	4.686	1.8470	0.08312	282.68	603.09	320.41	1.2826	2.3224

Refrigerant: R134a, CH₂FCF₃, 1,1,1,2-tetrafluoroethane

T	P	Vl	Vg	Hl	Hg	R	Sl	Sg
-C	Bar	dm ³ /kg	m ³ /kg	kJ/kg	kJ/kg	kJ/kg	kJ/(kgK)	kJ/(kgK)
-5.00	2.434	0.7625	0.08230	193.42	394.28	200.86	0.9758	1.7249
-4.00	2.527	0.7644	0.07938	194.73	394.87	200.14	0.9807	1.7243
-3.00	2.623	0.7663	0.07659	196.04	395.46	199.42	0.9855	1.7237
-2.00	2.722	0.7682	0.07391	197.36	396.04	198.68	0.9903	1.7231
-1.00	2.824	0.7701	0.07135	198.68	396.62	197.95	0.9952	1.7225
0.00	2.928	0.7721	0.06889	200.00	397.20	197.20	1.0000	1.7220
1.00	3.036	0.7740	0.06653	201.33	397.78	196.45	1.0048	1.7214
2.00	3.146	0.7760	0.06427	202.66	398.36	195.70	1.0096	1.7209
3.00	3.260	0.7781	0.06210	203.99	398.93	194.94	1.0144	1.7204
4.00	3.376	0.7801	0.06001	205.33	399.50	194.17	1.0192	1.7199
5.00	3.496	0.7821	0.05801	206.67	400.07	193.40	1.0240	1.7194
6.00	3.619	0.7842	0.05609	208.02	400.64	192.62	1.0288	1.7189
7.00	3.746	0.7863	0.05425	209.37	401.21	191.84	1.0336	1.7184
8.00	3.876	0.7884	0.05248	210.72	401.77	191.05	1.0384	1.7179
9.00	4.009	0.7906	0.05077	212.08	402.33	190.25	1.0432	1.7175
10.00	4.145	0.7927	0.04913	213.44	402.89	189.45	1.0480	1.7170
11.00	4.286	0.7949	0.04756	214.80	403.44	188.64	1.0527	1.7166
12.00	4.429	0.7971	0.04604	216.17	404.00	187.83	1.0575	1.7162
13.00	4.577	0.7994	0.04458	217.54	404.55	187.01	1.0623	1.7158
14.00	4.728	0.8016	0.04318	218.92	405.10	186.18	1.0670	1.7154
15.00	4.883	0.8039	0.04183	220.30	405.64	185.34	1.0718	1.7150
16.00	5.042	0.8062	0.04052	221.68	406.18	184.50	1.0765	1.7146
17.00	5.204	0.8085	0.03927	223.07	406.72	183.66	1.0813	1.7142
18.00	5.371	0.8109	0.03806	224.44	407.26	182.82	1.0859	1.7139
19.00	5.541	0.8133	0.03690	225.84	407.80	181.96	1.0907	1.7135
20.00	5.716	0.8157	0.03577	227.23	408.33	181.09	1.0954	1.7132
21.00	5.895	0.8182	0.03469	228.64	408.86	180.22	1.1001	1.7128
22.00	6.078	0.8206	0.03365	230.05	409.38	179.34	1.1049	1.7125
23.00	6.265	0.8231	0.03264	231.46	409.91	178.45	1.1096	1.7122
24.00	6.457	0.8257	0.03166	232.87	410.42	177.55	1.1143	1.7118
25.00	6.653	0.8283	0.03072	234.29	410.94	176.65	1.1190	1.7115
26.00	6.853	0.8309	0.02982	235.72	411.45	175.73	1.1237	1.7112
27.00	7.058	0.8335	0.02894	237.15	411.96	174.81	1.1285	1.7109
28.00	7.267	0.8362	0.02809	238.58	412.47	173.89	1.1332	1.7106
29.00	7.482	0.8389	0.02727	240.02	412.97	172.95	1.1379	1.7103
30.00	7.701	0.8416	0.02648	241.46	413.47	172.00	1.1426	1.7100
31.00	7.924	0.8444	0.02572	242.91	413.96	171.05	1.1473	1.7097
32.00	8.153	0.8473	0.02498	244.36	414.45	170.09	1.1520	1.7094
33.00	8.386	0.8501	0.02426	245.82	414.94	169.12	1.1567	1.7091
34.00	8.625	0.8530	0.02357	247.28	415.42	168.14	1.1614	1.7088
35.00	8.868	0.8560	0.02290	248.75	415.90	167.15	1.1661	1.7085

Table A2.3 Charging HC (R600a) into the System

Date	Time	Vacuum (bar)	Charge (g)	Pressure (bar)	Temp (°C)	State
Tue, 08 Oct 02	1335	-1	-	-	24.3	Vacuum
Tue, 08 Oct 02	1400	-	6.34	3.6	25	Gaseous
Wed, 09 Oct 02	1300	-	6.34	3.4	25	Gaseous
Wed, 09 Oct 02	1450	-	6.34	3.4	24.9	Gaseous
Thu, 10 Oct 02	1220	-	6.34	3.3	23	Gaseous
Thu, 10 Oct 02	1315	-	6.34	3.3	24	Cooling
						Gaseous
Thu, 10 Oct 02	1500	-	-	0	24.8	Discharged
Thu, 10 Oct 02	1500	-	-	3.2	24.8	Air
Thu, 10 Oct 02	1510	-	-	3.1	22.6	Air
Fri, 11 Oct 02	1145	-	-	2.2	20.5	Leak
Mon, 14 Oct 02	1250	-	-	3.2	22.3	Air
Mon, 14 Oct 02	1445	-	-	3.1	22.3	Leak
Mon, 14 Oct 02	1523	-	-	3.05	22.1	Leak
Tue, 15 Oct 02	1300	-	-	3	21.4	No leak
Tue, 15 Oct 02	1540	-	-	3	21.4	No leak
Thu, 17 Oct 02	1310	-	-	2.9	23	No leak
Thu, 17 Oct 02	1310	-	-	2.9	23	Discharged
Thu, 17 Oct 02	1350	-1	0	-1	23.5	Vacuum
Thu, 17 Oct 02	1350	-	3.5	2.5	23.5	Gaseous

Table A2.3 Charging HC (R600a) into the System - continued

Date	Time	Vacuum (bar)	Charge (g)	Pressure (bar)	Temp (°C)	State
Thu, 17 Oct 02	1355	-	3.7	2.5	23.4	Gaseous
Thu, 17 Oct 02	1400	-	3.7	2.8	23.3	Gaseous
Thu, 17 Oct 02	1400	-	3.8	3	23.3	Gaseous
Thu, 17 Oct 02	1420	-	3.8	2.8	20.9	Cooling
						Gaseous
Thu, 17 Oct 02	1430	-	3.8	2.7	19.8	Cooling
						Gaseous
Thu, 17 Oct 02	1435	-	5.3	2.65	19	Cooling
						Gaseous
Thu, 17 Oct 02	1440	-	5.3	2.9	18.9	Cooling
						Gaseous
Thu, 17 Oct 02	1450	-	5.3	2.8	18	Cooling
						Gaseous
Thu, 17 Oct 02	1520	-	5.3	2.75	17.4	Cooling
						Vapour
Mon, 21 Oct 02	1030	-	5.3	3	24.8	Gaseous
Mon, 21 Oct 02	1040	-	5.3	3	24.8	Cooling
						Gaseous
Mon, 21 Oct 02	1130	-	5.3	2.8	20.9	Cooling
						Gaseous

Table A2.4 Charging HC (R600a) into the System - continued

Date	Time	Vacuum (bar)	Charge (g)	Pressure (bar)	Temp (°C)	State
Mon, 21 Oct 02	1245	-	5.3	2.75	19.6	Cooling
						Gaseous
Mon, 4 Nov 02	1100	-	5.3	2.1	25.5	Discharged

Table A2.5 Important Properties of the R600a and R134a Refrigerants⁶

Property (on a weight basis)	R600a	R134a
Boiling point (°C), at 1 atm.	-11.8	-26.1
Ratio of Specific Heats (C_p/C_v), at 1 atm.	1.10	1.12
Density of liquid at 30 °C, Mg/m ³	0.545	1.19
Latent heat of vaporisation at boiling point, kj/kg	362	217
Thermal Conductivity of liquid at 20 °C, W/m °C	0.098	0.08
Surface tension at 25°C, mN/m	9.55	8.4
Viscosity of liquid at 30°C, centipoises	0.14	0.20

⁶ CARE Refrigerants, Training Workshop

Table A2.6 Application ranges for Hydrocarbon Refrigerants⁷

Refrigerant	Application Range	Replacement
R600a (iso-butane)	High/medium temperature; domestic appliances	(R 12, R 134a) ⁸
(R600a/R290blend)	High/medium temperature; commercial, automotive, domestic	R 12, R 134a
R 290 (propane)	High/medium/low temperature; commercial, industrial; freezers, air-conditioning, heat pumps	R 22, R 404A, R 407C, R 507A
R 1270 (propylene or propene)	High/medium/low temperature; commercial, industrial; industrial and process refrigeration, air- conditioning, heat pumps, chillers	R 22, R 404A. R 407C, R 507A
R 290/R 170 blend	High/medium/low temperature; commercial, industrial; industrial and process refrigeration, air- conditioning, heat pumps, chillers	R 22, R 404A. R 407C, R 507A
R 170 (ethane)	Low temperature cascade systems	R 13, R 23, R 503

Table A2.7 Physical Properties of R600a Refrigerant⁹

Refrigerant	R 600a
Mol. Mass (kg/kmol)	58.1
Normal boiling pt. At 1 Atm.	-11.7
Critical temp. (°C)	135.0
Critical pressure (bar, abs.)	36.45
Temp. glide at 25°C (K)	0
Latent heat at 25°C (kJ/kg)	332
Saturation press at 25°C (bar, abs.)	3.5

⁷ ACRIB 2001⁸ R 600a possesses a volumetric refrigerating capacity that is approximately half that of R 12 and R 134a is not a "thermodynamic" replacement for these refrigerants.⁹ ACRIB 2001

Table A2.8 Compatibility of various lubricants with HC refrigerants¹⁰

Lubricant Type ¹¹	Compatibility
Mineral (M)	Fully soluble with hydrocarbons. Excessive solubility at high temperature conditions. Compensate by selection of a high viscosity grade oil.
Alkyl benzene (AB)	Fully soluble and typical viscosity grade applicable to all applications.
Semi-synthetic (AB/M)	A blend of AB and M oils achieving desirable properties for use with hydrocarbons.
Polyester (POE)	Generally exhibits excessive solubility with hydrocarbons. May necessitate higher viscosity grade.
Ployalkylene Glycol (PAG)	Soluble and partially soluble with hydrocarbons depending upon the conditions. Normal grades are generally satisfactory.
Poly-alpha-olefins (PAO)	Soluble with hydrocarbons but typically used for low temperature applications.

¹⁰ ACRIB 2001

¹¹ It is recommended that the compressor manufacturer be consulted to determine the selection of the correct lubricant.

Table A2.9 Refrigerant charging requirements for various categories of occupancy

Category	Example	Requirements
A (domestic/public)	Hospitals, prisons, theatres, school, supermarkets, hotels, dwellings	<ul style="list-style-type: none"> • <1.5kg per sealed system • <5kg in special machinery rooms or in the open air indirect systems
B (commercial/private)	Offices, small shops, restaurants, places for general manufacturing, and where people work.	<ul style="list-style-type: none"> • <2.5kg per sealed system • <10kg in special machinery rooms or open air for indirect systems.
C (industrial/restricted)	Cold stores, dairies, abattoirs, non-public areas of supermarkets, plant rooms.	<ul style="list-style-type: none"> • <10kg in human occupied spaces • <25kg if high pressure side (except air-cooled condenser) is located in a special machinery room or in the open air • No limit if all refrigerant is contained in a special machinery room or in the open air

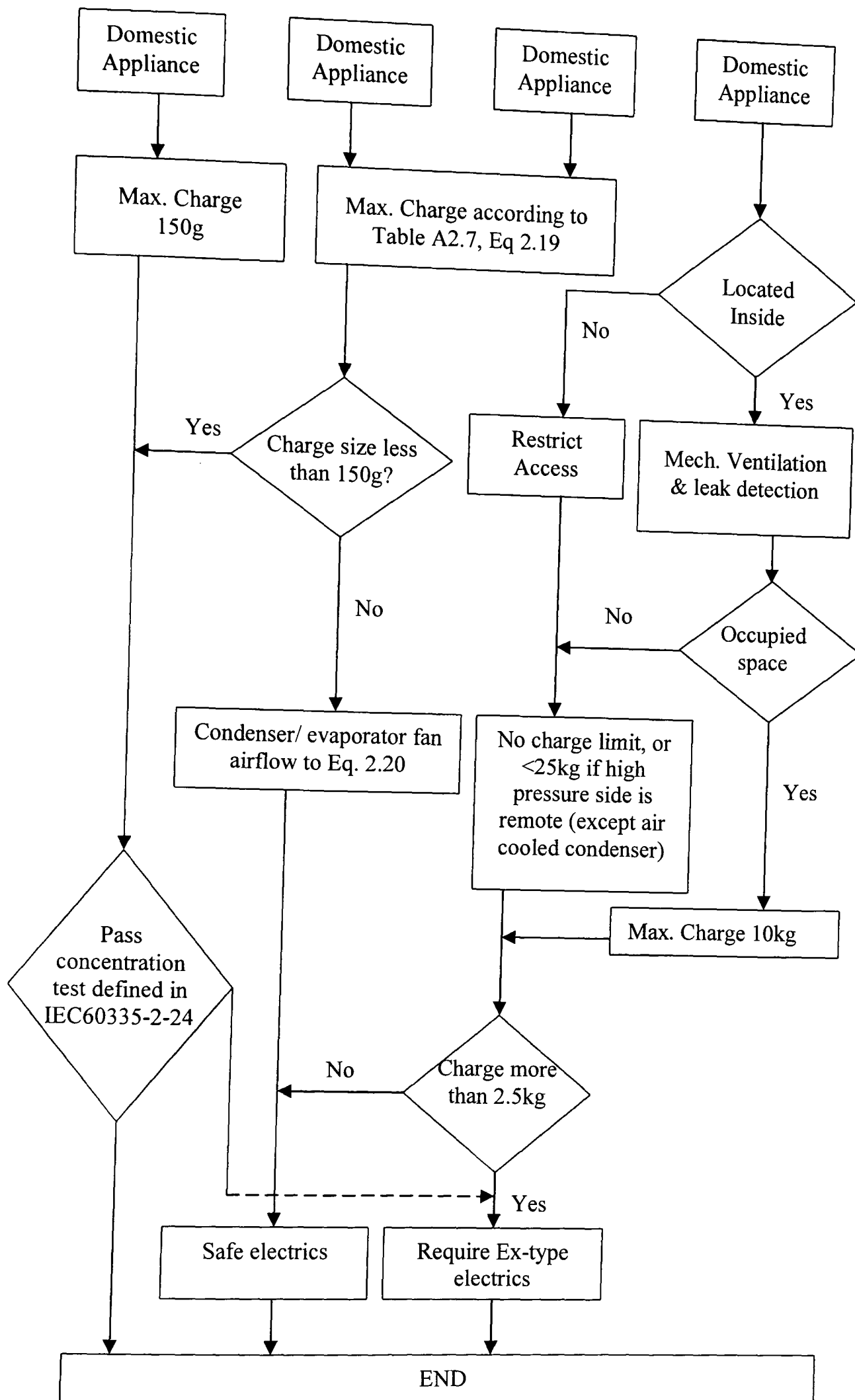


Figure A2.7 Flow chart indicating design routes according to safety standards

Table A2.10 Flammability properties of Selected Hydrocarbon Refrigerants¹²

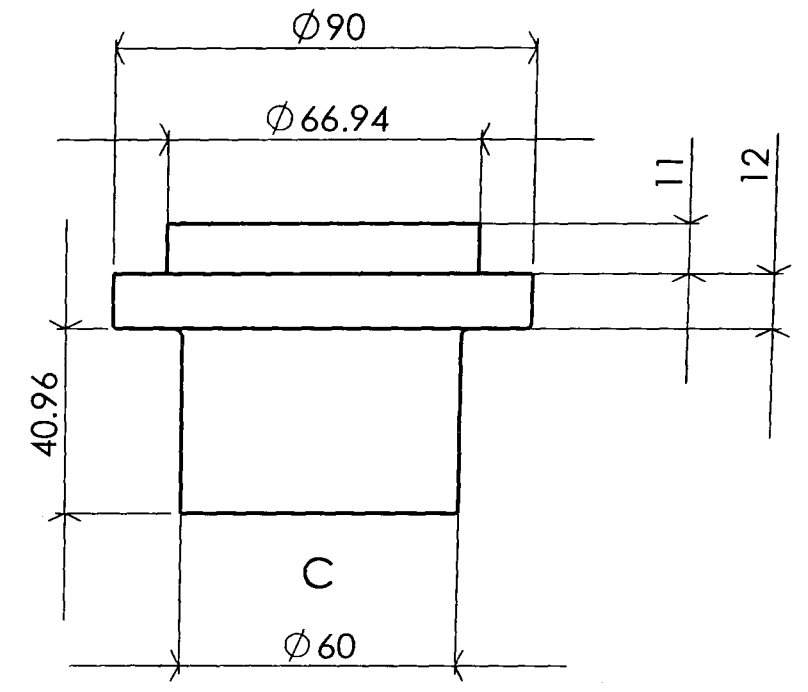
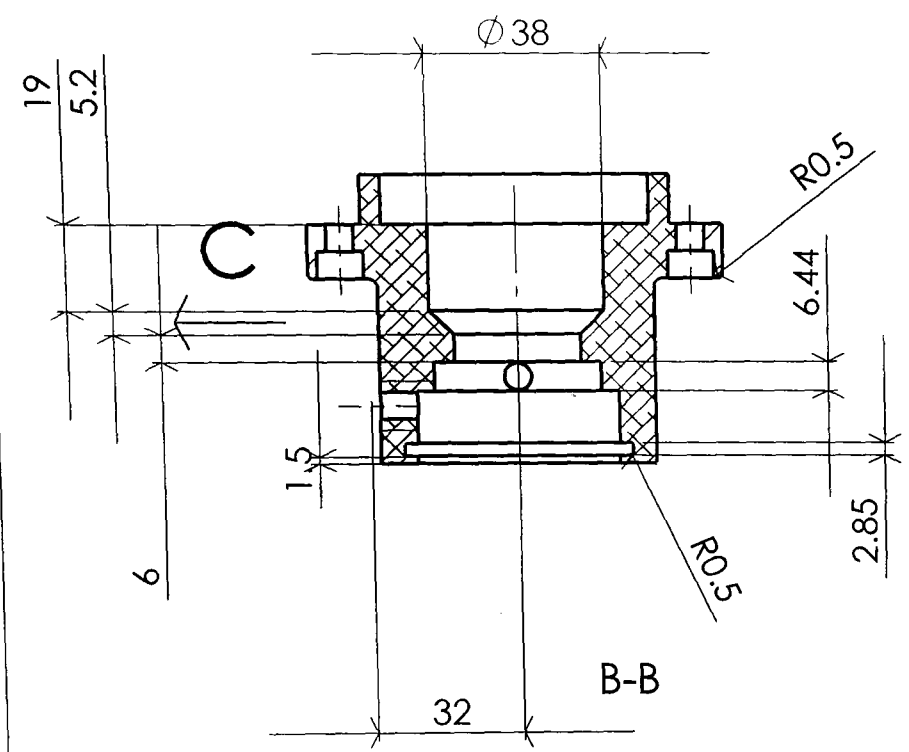
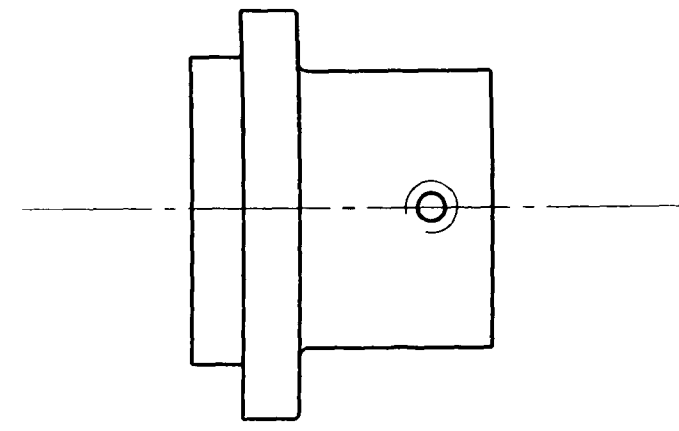
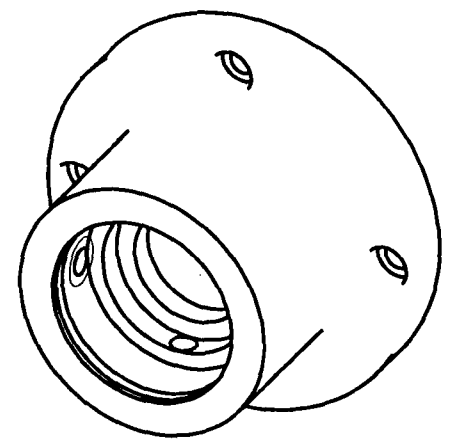
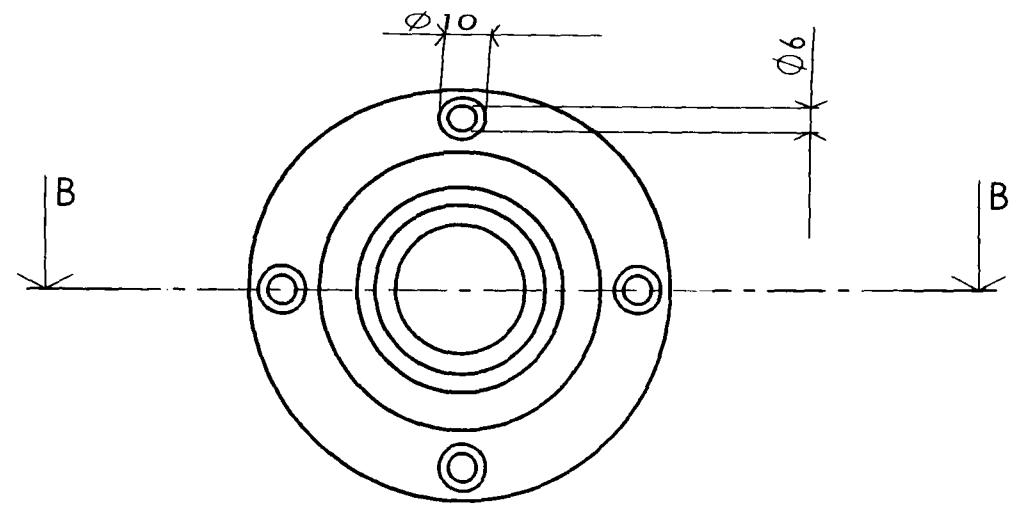
Refrigerant	Number	Lower Flammability Limits (LFL)		Auto-ignition temperature (°C)
		By volume (%)	By mass (kg/m ³)	
Ethane	R 170	3.0	0.037	515
Propane	R 290	2.1	0.038	470
Iso-Butane	R 600a	1.8	0.043	460
Propylene	R 1270	2.5	0.043	455
CARE-30	-	2.0	0.041	460
CARE-50	-	2.2	0.038	460

Table A2.11 Installation/Charges Size Categories

Refrigerant Charge Size								
Occupancy Category	<0.15 kg	0.15-1 kg	1-1.5 kg	1.5-2.5 kg	2.5-5 kg	5-10 kg	10-25 kg	>25 kg
A	A1	A2	A3	A4	A5	A6	N/A	N/A
B	B1	B2	B3	B4	B5	B6	N/A	N/A
C	C1	C2	C3	C4	C5	C6	C7	C8

¹² BS 4434 (1995), BS 5345 (1976), BS EN 1127-1 (1998) & BS EN 378 (2000)

NO.	REV.	REVISIONS DESCRIPTION	DATE	APPROVED

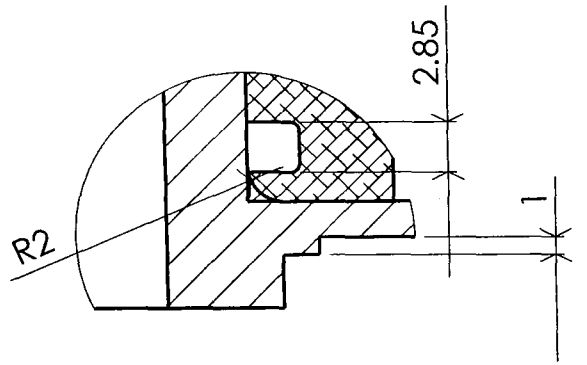
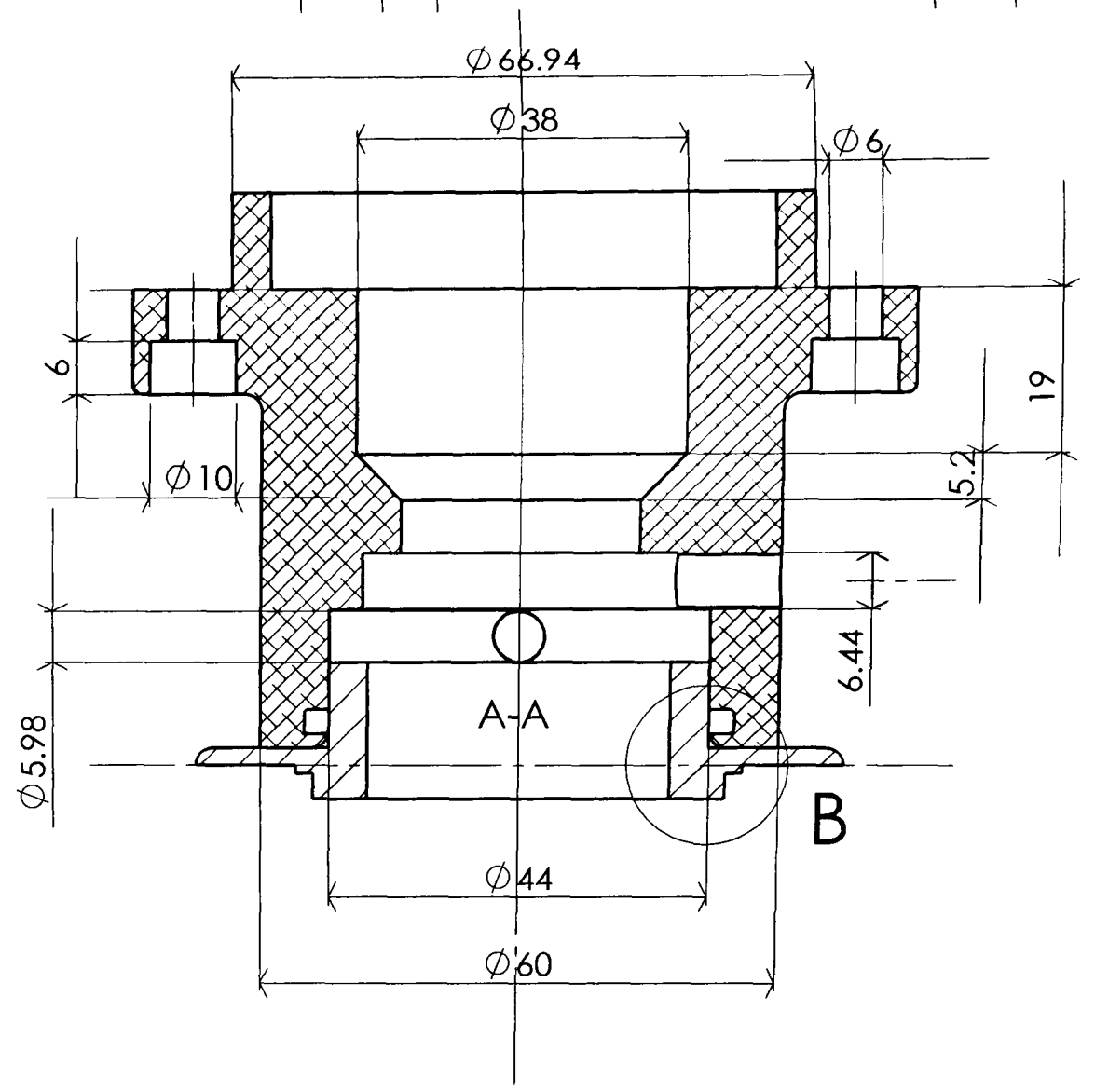
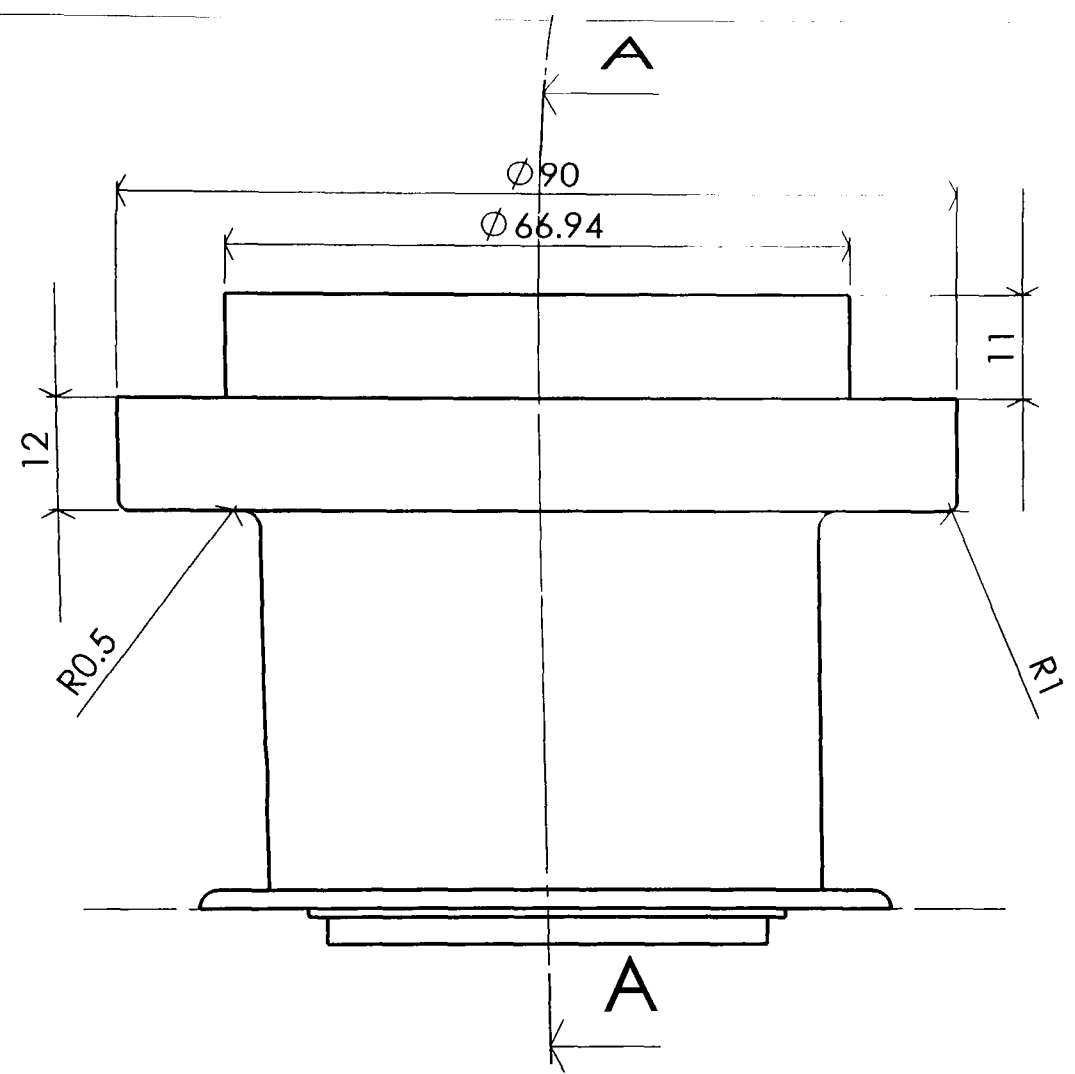


PROPRIETARY AND CONFIDENTIAL
 THE INFORMATION CONTAINED IN THIS DRAWING IS PART OF THIS THESIS ANY REPRODUCTION IN PART OR AS A WHOLE WITHOUT THE WRITTEN PERMISSION OF AUTHOR IS PROHIBITED.

DIMENSIONS ARE IN MILLIMETERS		NAME	DATE	Bournemouth University Pressurised chamber Basic design plan etc
TOLERANCES:		DRAWN	ZULFIQAR 18/06/02	
FRACTIONAL ±0.01		CHECKED	M.HADFIELD 10/07/02	
ANGULAR: MACH ± BEND ±		ENG APPR.		
TWO PLACE DECIMAL ±0.02		MFG APPR.		
THREE PLACE DECIMAL ±0.005		Q.A.		
MATERIAL		COMMENTS:		
AL ALLOY LM13 - TF7				
FINISH				
NEXT ASSY	USED ON			
APPLICATION	DO NOT SCALE DRAWING			

SIZE	DWG. NO.1	REV.1st
A		
SCALE:1:2	WEIGHT:	SHEET 1 OF 1

FORM	REV.	DESCRIPTION	DATE	APPROVED



B (2 : 1)

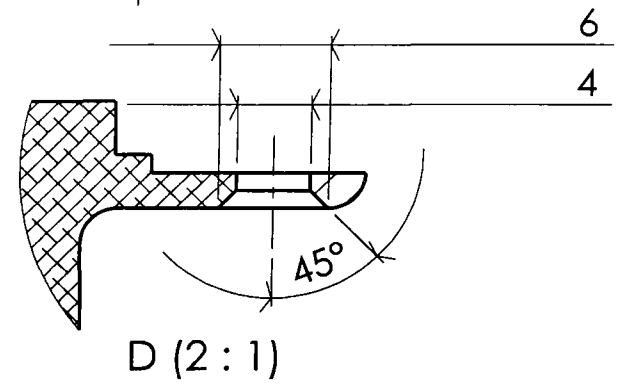
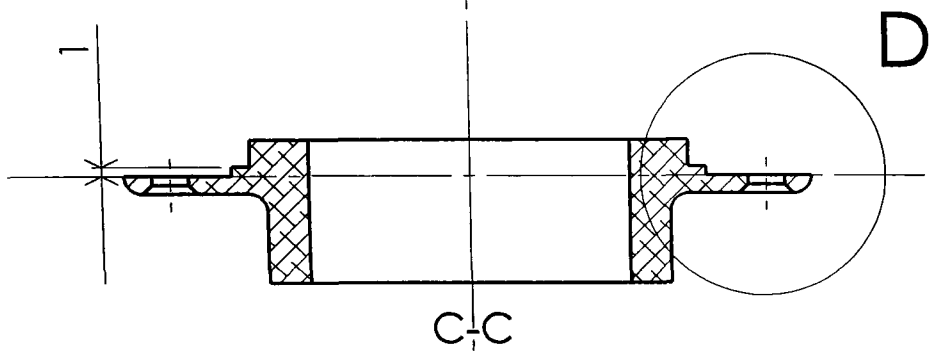
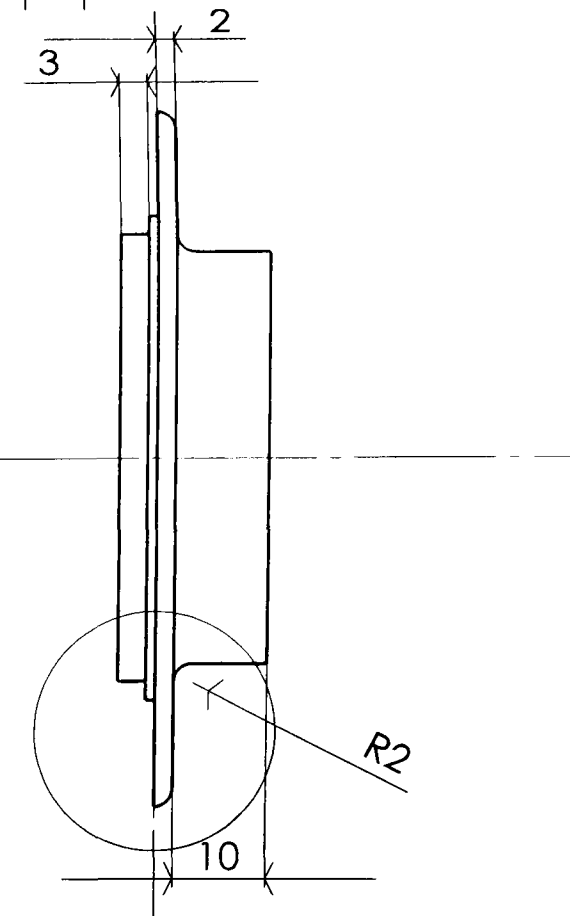
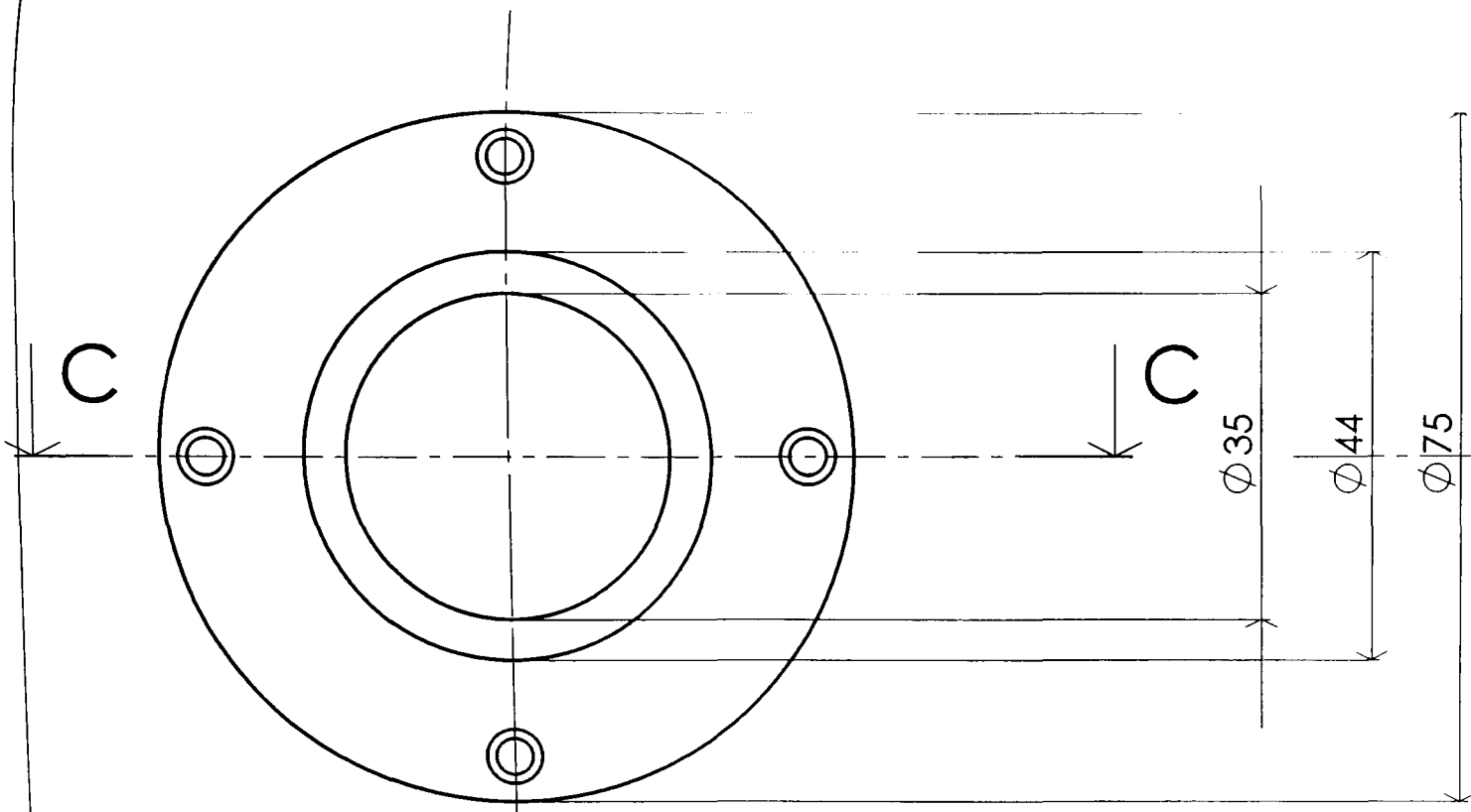
PROPRIETARY AND CONFIDENTIAL
 THE INFORMATION CONTAINED IN THIS DRAWING IS PART OF THIS THESIS ANY REPRODUCTION IN PART OR AS A WHOLE WITHOUT THE WRITTEN PERMISSION OF AUTHOR IS PROHIBITED.

DIMENSIONS ARE IN MILLIMETERS		NAME	DATE
TOLERANCES:		DRAWN	ZULFIQAR 23/06/02
FRACTIONAL ±		CHECKED	M. HADFIELD 10 /07/02
ANGULAR: MACH ± BEND ±		ENG APPR.	
TWO PLACE DECIMAL ±		MFG APPR.	
THREE PLACE DECIMAL ±		Q.A.	
MATERIAL		COMMENTS:	
AL ALLOY LM13 - TF7			
NEXT ASSY	USED ON	FINISH	
APPLICATION		DO NOT SCALE DRAWING	

Bournemouth University
 Presurised chamber
 basic design
 elevation, section

SIZE	DWG. NO.	REV.
A		
SCALE: 1:1	WEIGHT:	SHEET 1 OF 1

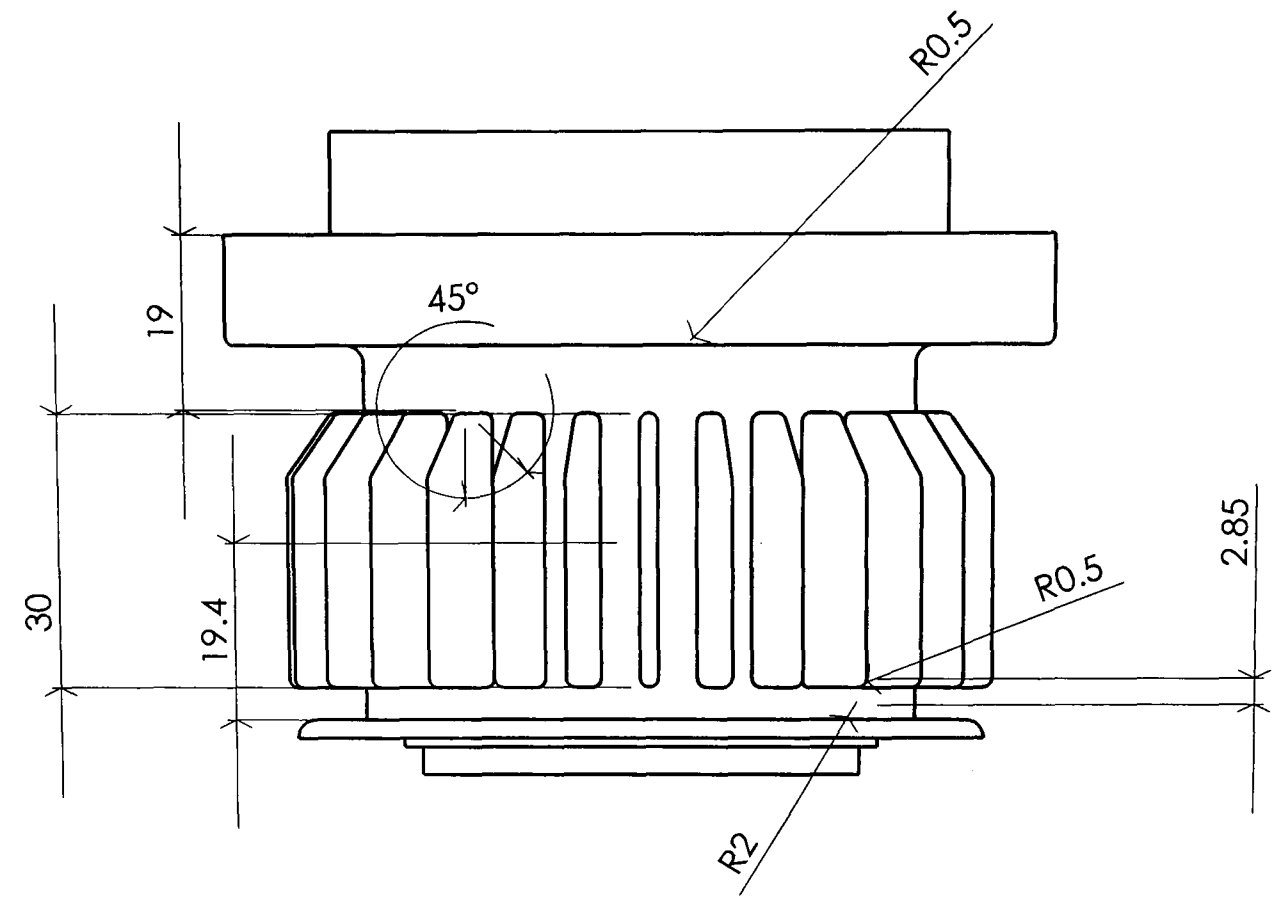
DATE	REV	DESCRIPTION	DATE	APPROVED



PROPRIETARY AND CONFIDENTIAL
 THE INFORMATION CONTAINED IN THIS DRAWING IS PART OF THIS THESIS ANY REPRODUCTION IN PART OR AS A WHOLE WITHOUT THE WRITTEN PERMISSION OF AUTHOR IS PROHIBITED.

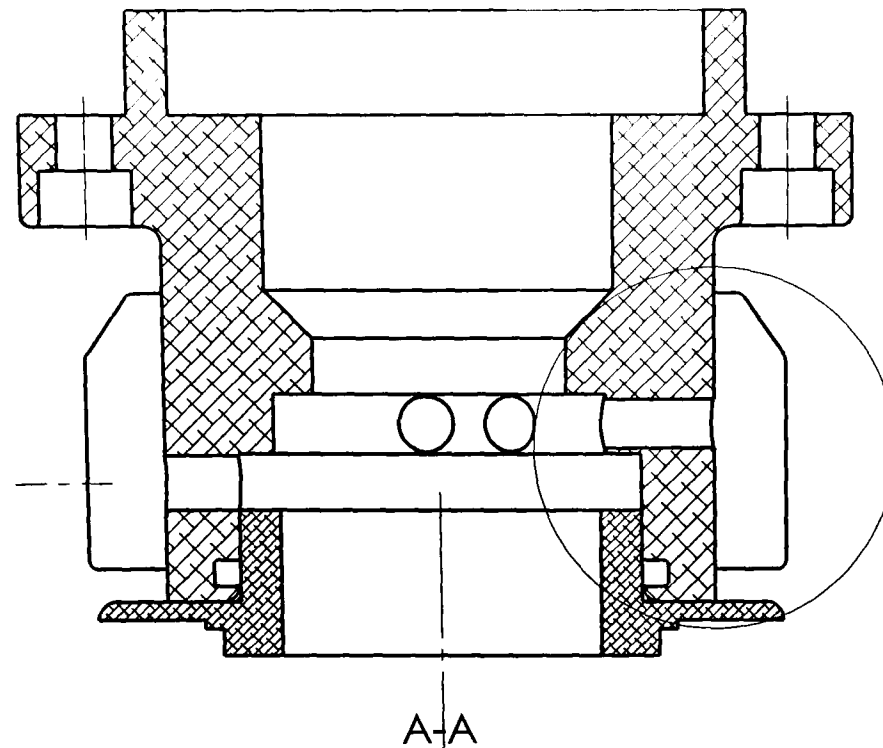
		DIMENSIONS ARE IN MILLIMETERS		NAME	DATE	Bournemouth University
		TOLERANCES:		DRAWN	ZULFIQAR	
		FRACTIONAL ±		CHECKED	M.HADFIELD	10/07/02
		ANGULAR: MACH ± BEND ±		ENG APPR.		Pressurised chamber Basic design lower part
		TWO PLACE DECIMAL ±		MFG APPR.		
		THREE PLACE DECIMAL ±		Q.A.		
		MATERIAL		COMMENTS:		SIZE DWG. NO. REV.
		AL ALLOY LM13 - TF7				
NEXT ASSY	USED ON	FINISH				SCALE: 1:1 WEIGHT: SHEET 1 OF 1
APPLICATION		DO NOT SCALE DRAWING				

DATE	REV	REVISIONS DESCRIPTION	DATE	APPROVED

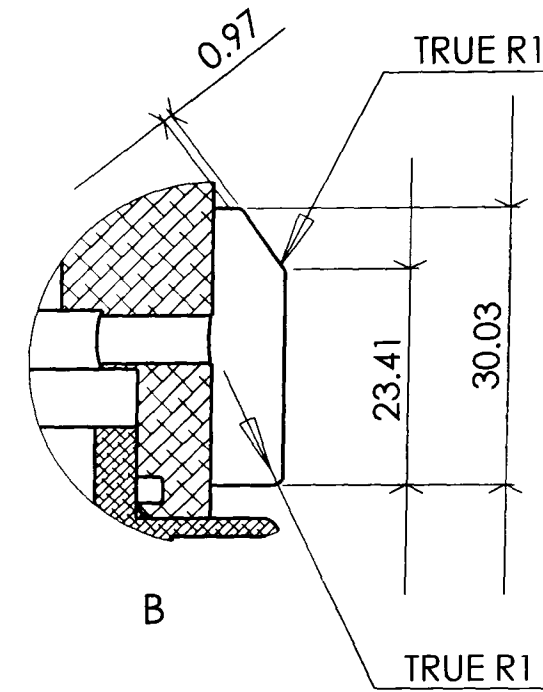


<p>PROPRIETARY AND CONFIDENTIAL THE INFORMATION CONTAINED IN THIS DRAWING IS PART OF THIS THESIS ANY REPRODUCTION IN PART OR AS A WHOLE WITHOUT THE WRITTEN PERMISSION OF AUTHOR IS PROHIBITED.</p>			DIMENSIONS ARE IN MM TOLERANCES: FRACTIONAL ± ANGULAR: MACH ± BEND ± TWO PLACE DECIMAL ± THREE PLACE DECIMAL ±		NAME	DATE	<p>Bournemouth University</p> <p>Pressurised chamber cooling fins elevation</p>
					DRAWN	ZULFIQAR 07/07/02	
					CHECKED	M. HADFIELD	
					ENG APPR.		
					MFG APPR.		
			MATERIAL AL ALLOY LM13 - TF7		Q.A.		
			FINISH --		COMMENTS:		
	NEXT ASSY	USED ON					SIZE A
	APPLICATION		DO NOT SCALE DRAWING				DWG. NO.
							REV
							SCALE: 1:1
							WEIGHT:
							SHEET 1 OF 1

FORM	REV.	REVISIONS DESCRIPTION	DATE	APPROVED



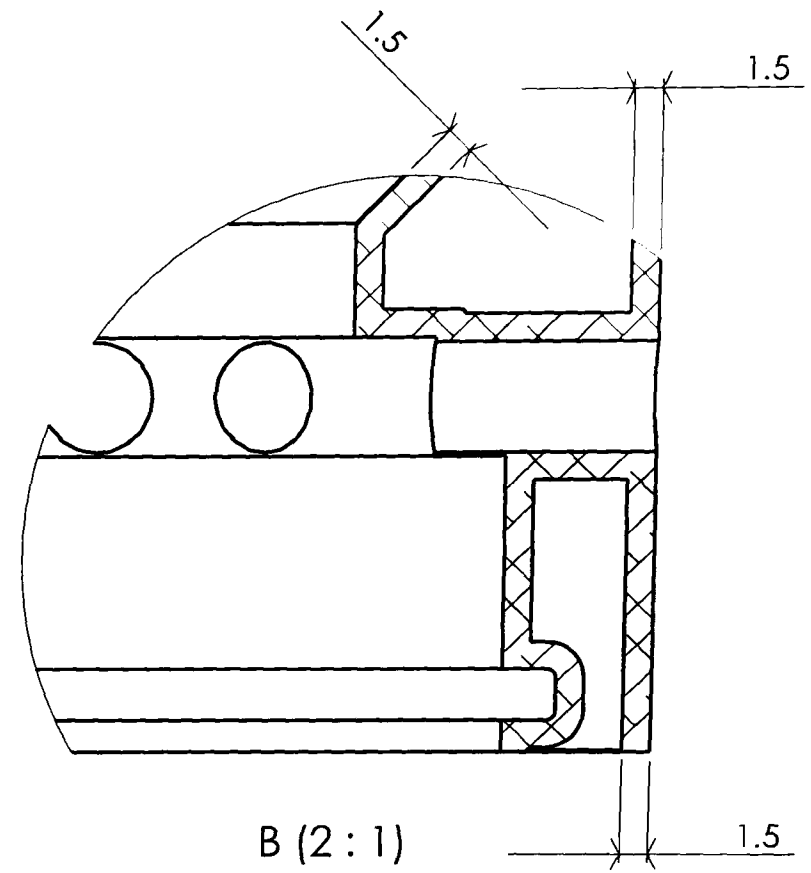
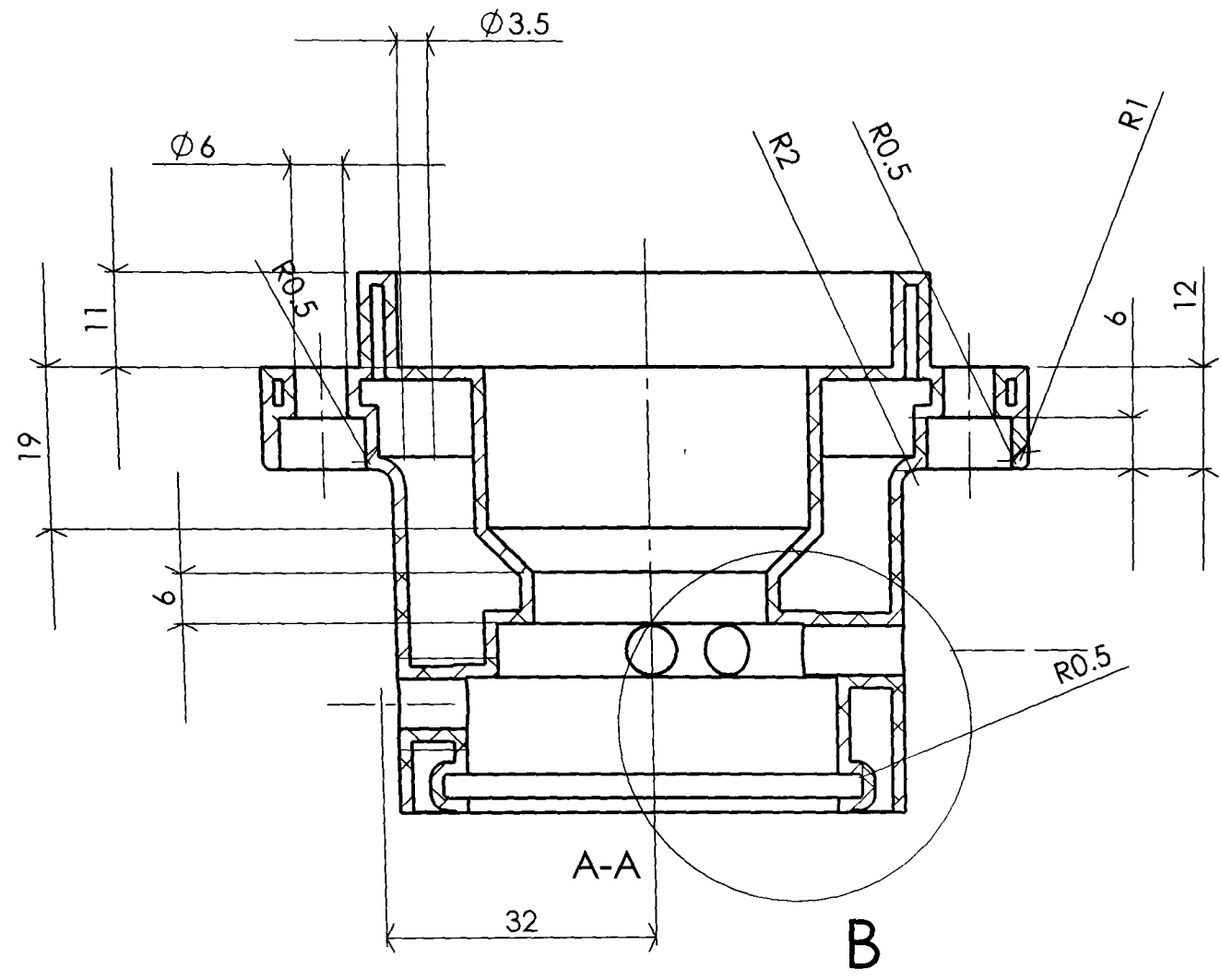
B



PROPRIETARY AND CONFIDENTIAL
THE INFORMATION CONTAINED IN THIS DRAWING IS PART OF THIS THESIS ANY REPRODUCTION IN PART OR AS A WHOLE WITHOUT THE WRITTEN PERMISSION OF AUTHOR IS PROHIBITED.

		DIMENSIONS ARE IN MM		Bournemouth University	
		TOLERANCES:		Pressurised chamber cooling fins Section	
		FRACTIONAL ±		SIZE	DWG. NO.
		ANGULAR: MACH ± BEND ±		A	REV.
		TWO PLACE DECIMAL ±		SCALE: 1:1	WEIGHT:
		THREE PLACE DECIMAL ±		SHEET 1 OF 1	
		MATERIAL	AL ALLOY LM13 - TF7		
NEXT ASSY	USED ON	FINISH	-		
APPLICATION		DO NOT SCALE DRAWING			
		DRAWN	ZULFIQAR	DATE	05/07/02
		CHECKED	M. HADFIELD		
		ENG APPR.			
		MFG APPR.			
		Q.A.			
		COMMENTS:			

DATE	REV.	DESCRIPTION

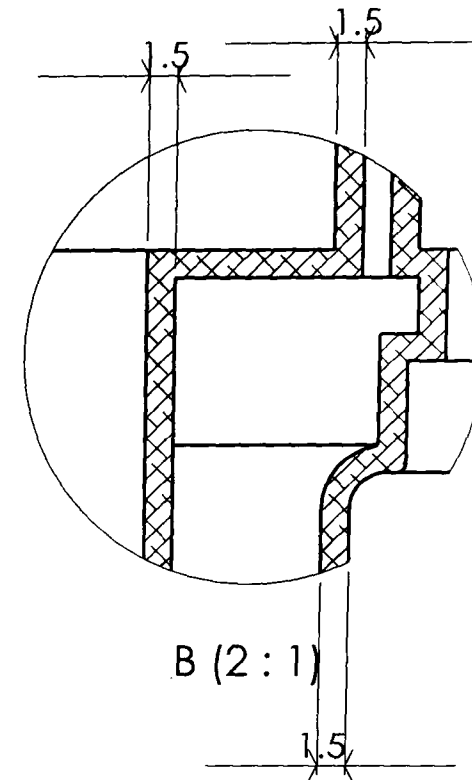
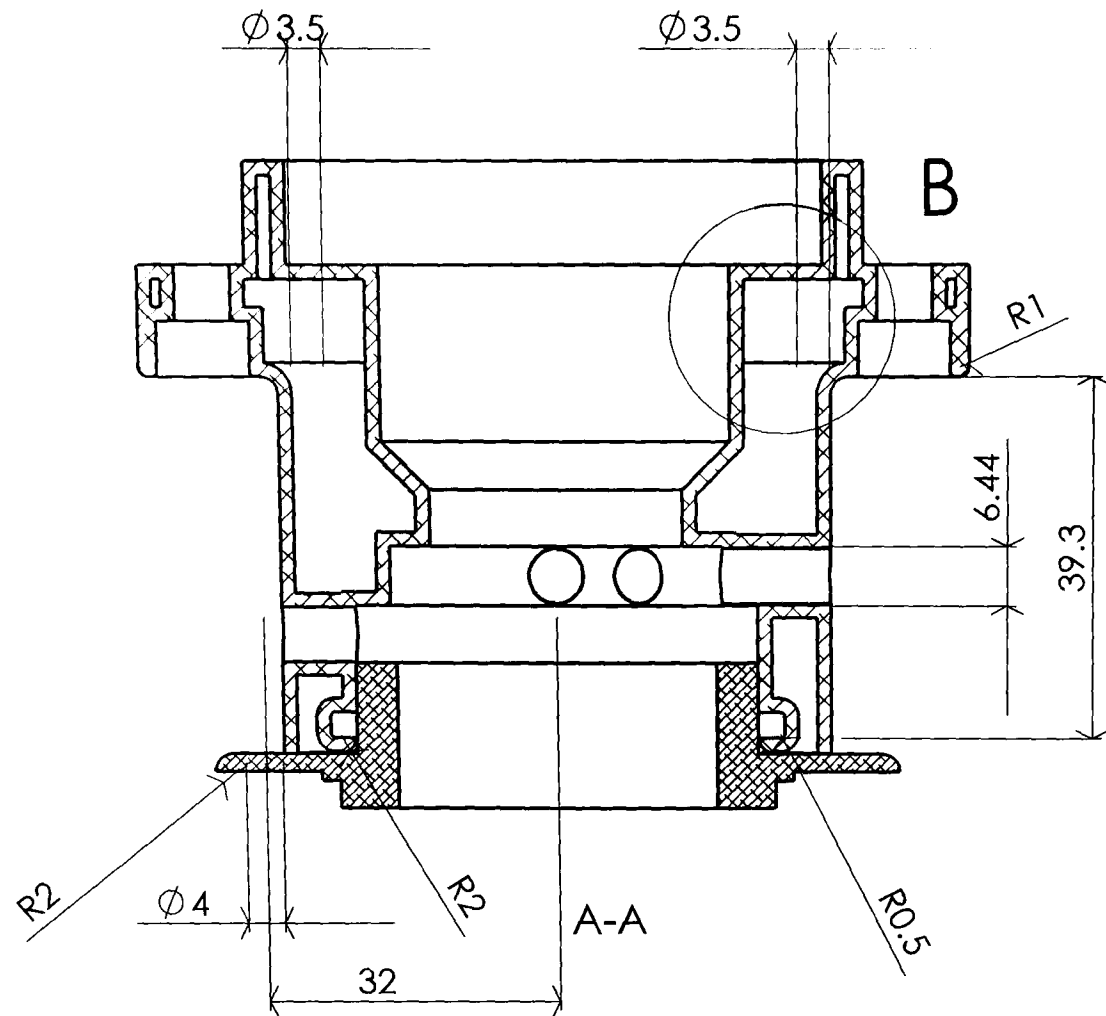


PROPRIETARY AND CONFIDENTIAL
 THE INFORMATION CONTAINED IN THIS DRAWING IS PART OF THIS THESIS ANY REPRODUCTION IN PART OR AS A WHOLE WITHOUT THE WRITTEN PERMISSION OF AUTHOR IS PROHIBITED.

DIMENSIONS ARE IN MM		NAME	DATE
TOLERANCES:		DRAWN	ZULFIQAR 04/07/02
FRACTIONAL \pm		CHECKED	M. HADFIELD
ANGULAR: MACH \pm BEND \pm		ENG APPR.	
TWO PLACE DECIMAL \pm		MFG APPR.	
THREE PLACE DECIMAL \pm		Q.A.	
MATERIAL		COMMENTS:	
AL ALLOY LM13 - TF7			
NEXT ASSY	USED ON		
APPLICATION	DO NOT SCALE DRAWING		

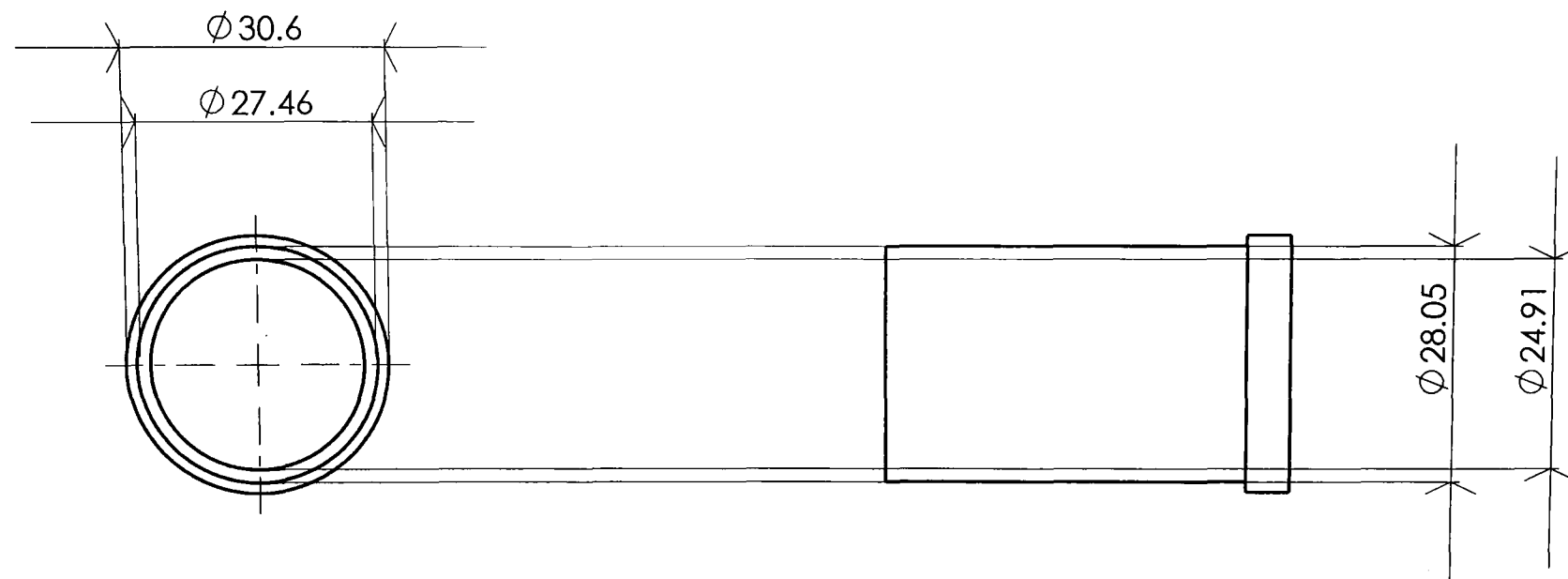
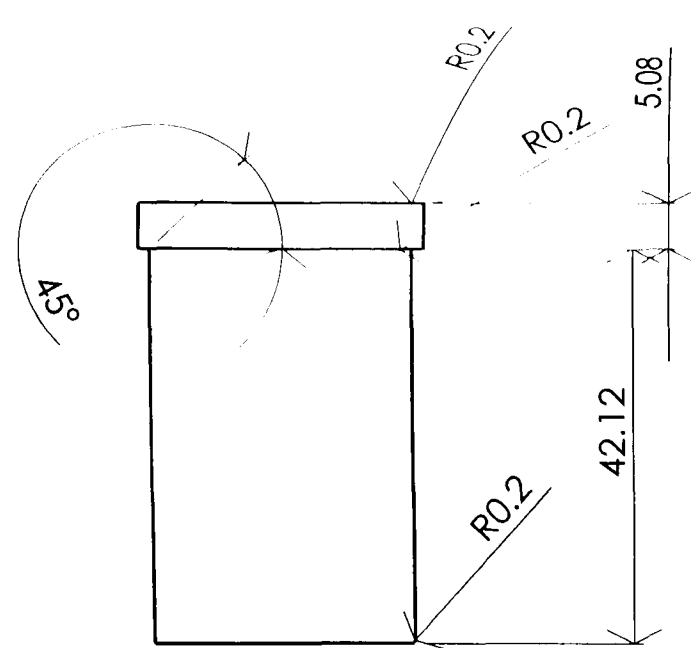
Bournemouth University		
Pressurised chamber internal cooling design Section		
SIZE	DWG. NO.	REV.
A		1
SCALE: 1:1	WEIGHT:	SHEET 1 OF 1

ZONE	REV.	DESCRIPTION



PROPRIETARY AND CONFIDENTIAL
 THE INFORMATION CONTAINED IN THIS DRAWING IS PART OF THIS THESIS ANY REPRODUCTION IN PART OR AS A WHOLE WITHOUT THE WRITTEN PERMISSION OF AUTHOR IS PROHIBITED.

DIMENSIONS ARE IN MM		NAME	DATE	Bournemouth University
TOLERANCES:		DRAWN	ZULFIQAR 05/07/02	
FRACTIONAL ±		CHECKED	M. HADFIELD	Pressurised chamber internal cooling design Assembly
ANGULAR: MACH ± BEND ±		ENG APPR.		
TWO PLACE DECIMAL ±		MFG APPR.		
THREE PLACE DECIMAL ±		Q.A.		
MATERIAL		COMMENTS:		SIZE A
AL ALLOY LM13 - TF7				
NEXT ASSY	USED ON			DWG. NO.
FINISH				REV.
APPLICATION		DO NOT SCALE DRAWING		SCALE: 1:1
				WEIGHT:
				SHEET 1 OF 1



PROPRIETARY AND CONFIDENTIAL
 THE INFORMATION CONTAINED IN THIS
 DRAWING IS PART OF THIS THESIS ANY
 REPRODUCTION IN PART OR AS A WHOLE
 WITHOUT THE WRITTEN PERMISSION OF
 AUTHOR IS PROHIBITED.

		DIMENSIONS ARE IN MILLIMETERS		NAME	DATE	Bournemouth University
		TOLERANCES:		DRAWN	ZULFIQAR	
		FRACTIONAL ±		CHECKED	M. HADFIELD	Spindle sleeve
		ANGULAR: MACH ± BEND ±		ENG APPR.		
		TWO PLACE DECIMAL ±		MFG APPR.		
		THREE PLACE DECIMAL ±		Q.A.		
		MATERIAL		COMMENTS:		
		Alloy steel				
NEXT ASSY	USED ON	FINISH				SIZE
		--				DWG. NO.
APPLICATION		DO NOT SCALE DRAWING.				REV.
						SCALE: 1:1
						WEIGHT:
						SHEET 1 OF 1

3. Surface inspection

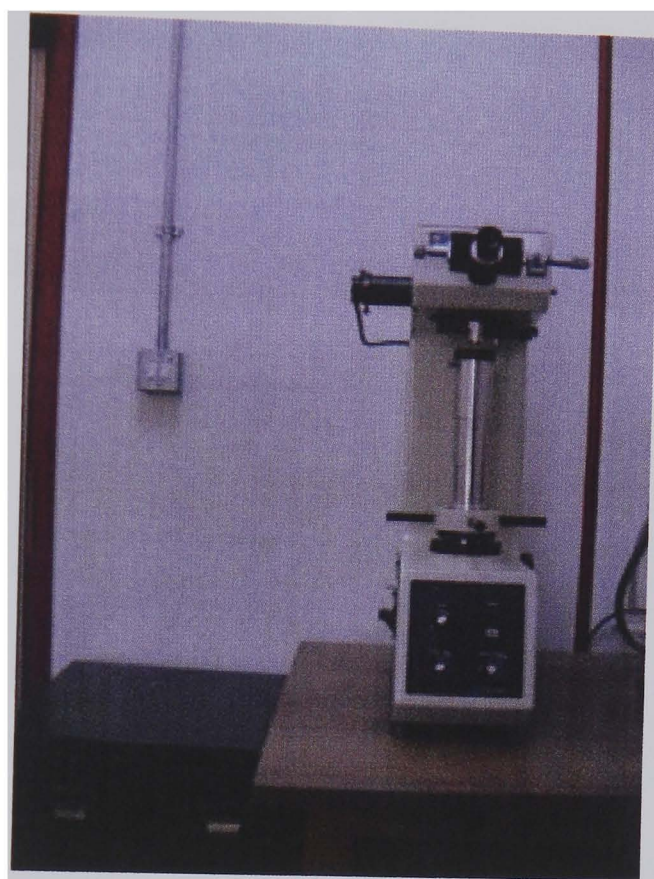


Figure A3.1 Buehler Vickers Indent generating device



Figure A3.2 Digital light microscope used for surface inspection



Figure A3.3 optical microscope used for surface inspection

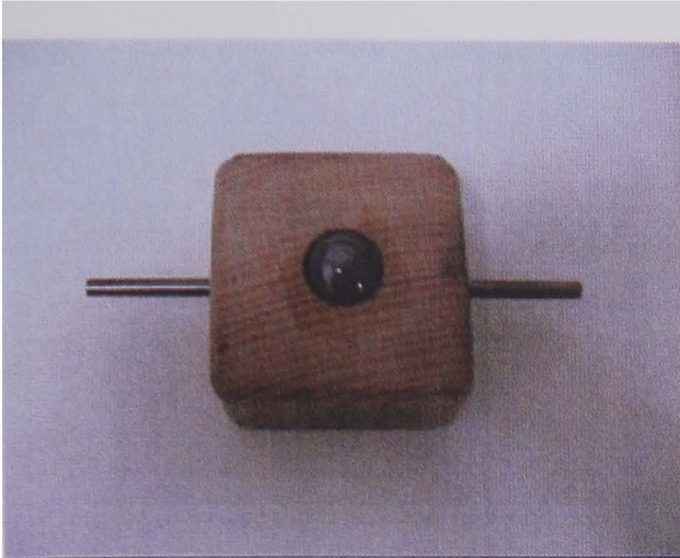


Figure A3.4 Hand free ball rotating manipulator

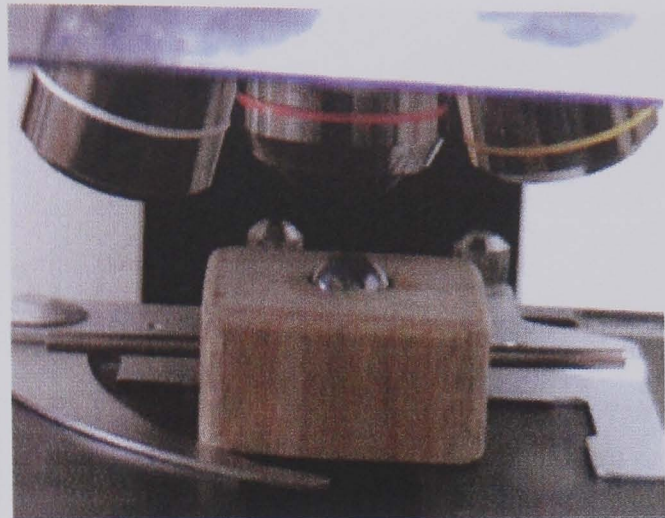


Figure A3.5 Hand free ball rotating manipulator used on light microscope

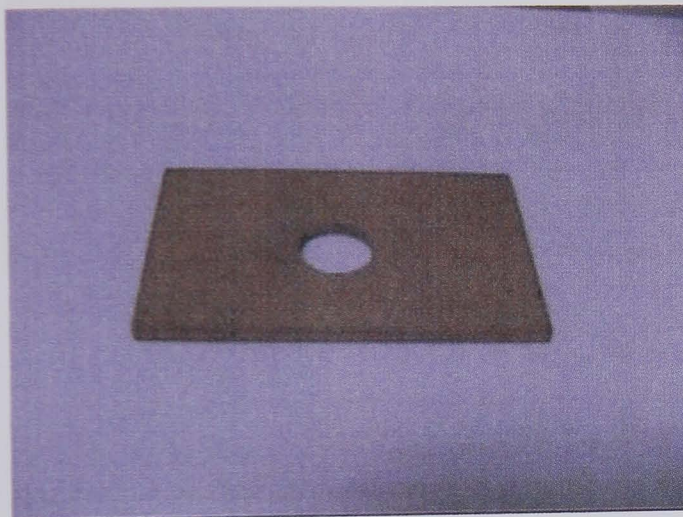


Figure A3.6 Vertical manipulator



Figure A3.7 Vertical manipulator use on light microscope

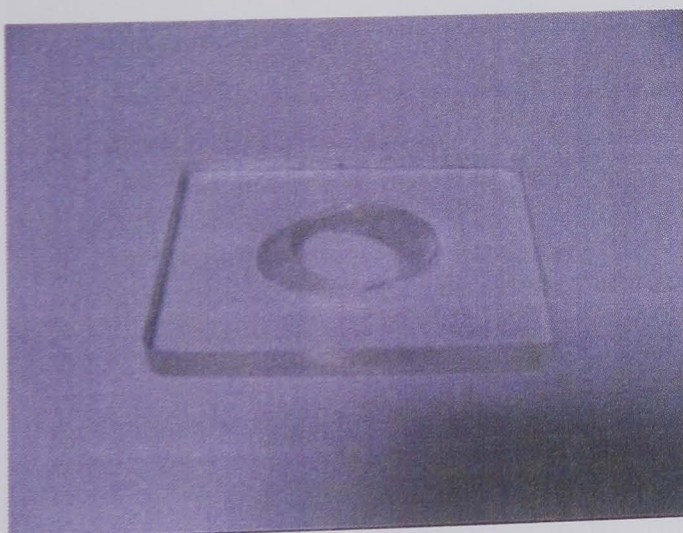


Figure A3.8 Angular manipulator



Figure A3.9 Angular manipulator used on light microscope



Figure A3.10 Determining height of the ball surface tip



Figure A3.11 The tip is offset by h from the top



Figure A3.12 Digital optical microscope



Figure A3.13 Jeol JSM 5300 scanning electron microscope



Figure A3.14 Agar sputter gold surface coater



Figure A3.15 Atomic force microscope

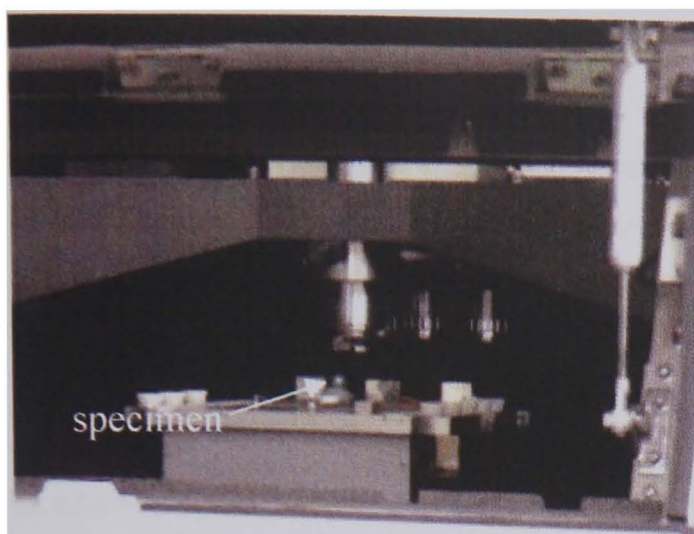


Figure A3.16 Specimen mounted on the AFM stage



Figure A3.17 AFM workstation

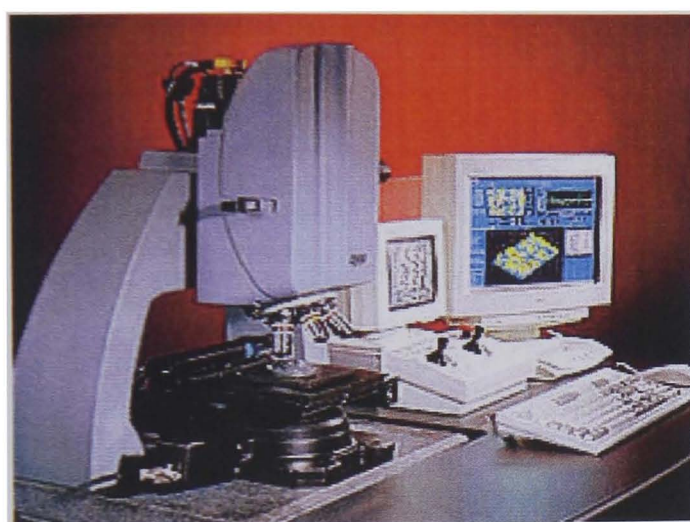


Figure A3.18 Zygo NewView 5000

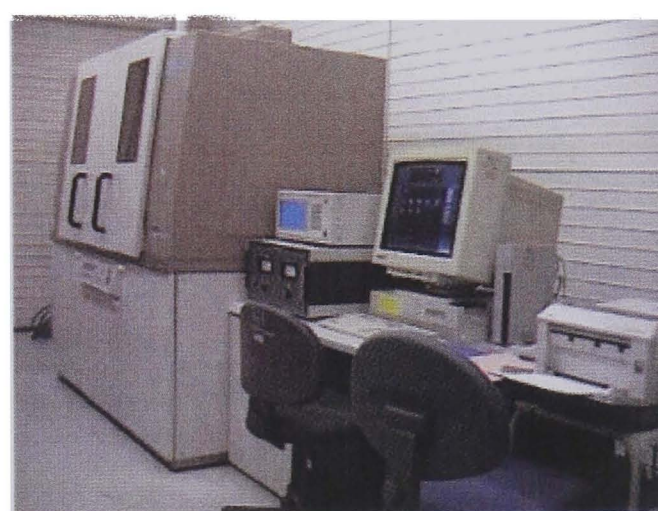


Figure A3.19 Rigaku Rint x-ray diffractometer with Rint 2100 XG control engineering workstation

REFERENCES

- Adachi, K., Kato K., Chen N. (1997). Wear map of ceramics. (2nd Report, Construction of mild-severe wear mode map). **63**(611): pp 2448-2455.
- Ajayi, O. O., Ludema A. J. (1988). Surface Damage of structural Ceramics: Implications for Wear Modeling. *Wear* **124**: pp 142-147
- Akazawa, M., Kato K. (1988). Wear Properties of Silicon Nitride in Rolling-Sliding Contact. *Wear* **124**: pp 123-132.
- Akazawa, M., Kato K., Umeya K. (1986). Wear Properties of Silicon Nitride in Rolling Contact. *WEAR* **110**: pp 285-293.
- Allen, D. L. (1994). Effect of Composition and Physical Properties of Silicon Nitride on Rolling Wear and Fatigue Performance. *Tribol. Trans* **37**: pp 410-414.
- Batdorf, S. B., Crose J. G. (1974). A Statistical Theory for the Fracture Subjected to Non-Uniform Polyaxial Stresses. *Jour. Appl. Mech* **41**(2): pp 459-464.
- Batdorf, S. B., Heinisch H. L. (1978). Weakest Link Theory Reformulated for Arbitrary Fracture Criterion. *Jour. Amer. Ceram. Soc* **61**: pp 355-358.
- Bhushan, B. (2002). *Introduction to Tribology*. 2002 Columbus, John Willey & Sons, Inc.
- Bhushan, B., Sibley L. B. (1981). Silicon Nitride Rolling Bearings for Extreme Operating Conditions. *ASLE Transactions* **25**(4): pp 417-428.
- Braza, J. F., Cheng, H. S., and Fine, M. E (1989). Silicon Nitride Wear Mechanisms: Rolling and Sliding Contact. *Tribology Transactions* **34**(4): pp 173-177
- Burrier, H. I. (1996). Optimising the structure and properties of silicon nitride for rolling contact bearing performance. *Trib. Trans* **39**(2): pp 276-285.
- Burrier, H. I. (1996). Optimizing the Structure and Properties of Silicon Nitride for Rolling Contact Bearing Performance. **39**: pp 276-285.

- Chao, L. Y., Lakshminarayana, R., Iyer, N., Lin, G. Y., and Shetty, D. K (1998). Transient wear of silicon nitride in lubricated rolling contact. *Wear* **223**: pp 58-65.
- Chao, L. Y., Shetty D. K. (1991). Reliability Analysis of Structure Ceramics Subjected to Biaxial Flexure. *Jour. Amer. Ceram. Soc* **74**(2): pp 333-334.
- Chen, S. S., Rodgers A. S., Chao J., Wilhoit R. C., Zwolinski B. J. (1975). Ideal Gas Thermodynamic Properties of Six Fluoroethanes. *J. Phys. Chem* **4**(2): pp 441-456.
- Chen, S. S., Wilhoit R. C., Zwolinski B. J. (1976). Ideal Gas Thermodynamic Properties of Six Chlorofluoromethanes. *J. Phys. Chem* **5**(3): pp 571-580.
- Chiu, Y. P. (1999). Approach for fatigue cracking failure prediction of ceramic rolling elements under Hertzian loading. *Tribology Transactions* **42**(2): pp 289-295.
- Fleming, J. R., Suh N. P. (1977). Mechanics of crack propagation in delamination wear. *Wear* **44**: pp 39-56.
- Fujiwara, T., Yoshioka T., Kitahara T., Koizumi H., Takebayashi H., Tada T. (1989). Study on Load Rating Property of Silicon Nitride for Rolling Bearing Material. *J. JSLE, Int. Ed.*: pp 81-86.
- Fujiwara, T., Yoshioka, T., Kitahara, T., Koizumi, S., Takebayashi, H., Tada, T (1989). Study on load rating property of silicon nitride for rolling bearing material. *Journal of JSLE International Edition* **10**: pp 81-86.
- Hadfield, M. (1998). Failure of Silicon Nitride Rolling Elements with Ring Crack Defects. *Ceramics International* **24**(5): pp 371-377.
- Hadfield, M., Cundill R. T., Stolarski T. A. (1993a). Delamination of ceramic balls in rolling contact. *Ceramics International* **19**: pp 151-158.
- Hadfield, M., Fujinawa G., Stolarski T. A., Tobe S. (1993b). Residual Stresses in Failed Ceramic Rolling-Contact Balls. *Ceramics International* **19**(5): pp 307-313.

- Hadfield, M.,Stolarski T. A. (1995a). The effect of the test machine on the failure mode in lubricated rolling contact of silicon nitride. *Tribology International* **28**(6): pp 377-382.
- Hadfield, M.,Stolarski T. A. (1995b). Observations of delamination fatigue on pre-cracked ceramic elements in rolling-contact. *Ceramics International* **21**(2): pp 125-130.
- Hadfield, M., Stolarski T. A.,Cundill R. T. (1993). Failure modes of ceramics in rolling contact. *Proc. R. Soc.* **A443**: pp 607-621.
- Hadfield, M., Stolarski T. A., Cundill R. T.,Horton S. (1993). Failure Modes of Ceramic Elements with Ring-Crack Defects. *Tribol. Int* **26**: pp 157-164.
- Hadfield, M., Stolarski T. A., Cundill R. T.,Horton S. (1993). Failure modes of pre-cracked ceramic elements under rolling-contact. *Wear* **169**: pp 69-75.
- Hadfield, M., Tobe, S., Stolarski, T. A (1994). Subsurface crack investigation on delaminated ceramic elements. *Tribology International* **27**(5): pp 359-367.
- Hadfield, M., Stolarski, T A (1995). Observations of lubricated rolling contact fatigue on silicon nitride rods. *Ceramics International* **21**(1): pp 13-19.
- Hadfield, M.,Tobe S. (1998). Residual stress measurements of hot isostatically pressed silicon nitride rolling element. *Ceramic International* **24**: pp 387-392.
- Hamilton, G. M.,Goodman L. E. (1966). The stress field cracted by a circular sliding contact. *J. Appl. Mech.* **33**: pp 371-376.
- Hon-Ma, Y.,Komatsuzaki S. (1983). Problems in Lubrication of Refrigerating Compressor Lubricant. *J. JSLE* **28**(12): pp 887-890.
- Itoh, T. (1966). Experimental Study of Lubrication for Refrigeration Compressors. *Refrigeration (J. Japanese Assn. of Refrigeration)* **50**(571): pp 969-972.
- Jonsson, U. J.,Hansson N. (1999). Lubrication limits of rolling element bearings in refrigeration compressors. *Tribologia*, Publisher: Finnish Soc Tribol, Helsinki, Finland **18**(1): pp 23-30.
- Kang, J., Hadfield M.,Tobe S. (2002). Residual stress field of HIPed silicon nitride rolling elemnets. *Ceramics International* **28**: pp 645-650.

- Kang, J., Stolarski T. A.,Gawne D. T. (1996). Tribochemically assisted wear of silicon nitride. *J. Eur. Ceram. Soc* **16**: pp 25-34.
- Kato, K. (1986). Wear Mechanisms of Ceramic Materials in Dry Rolling Friction. *ASME Transaction* **108**: pp 522-526.
- Kato, K. (1990). Tribology of ceramics. *Wear* **136**: pp 117-133.
- Kato, K., a,b (1988). Wear Properties of Silicon Nitride in Rolling Sliding Contact. *Wear* **124**: pp 241-249.
- Katz, R. N.,Hannoosh J. G. (1985). Ceramic for High Performance Rolling Element Bearings: A Review and Assessment. *Int'l. Jour. High Tech. Ceramics* **1**: pp 69-79.
- Katz, R. N.,Jahanmir S. e. (1991). Effects of Composition, Microstructure and Processing on Ceramic Rolling Element Bearing Performance. *Ceramic Bearing Technology* **824**: pp 121-130.
- Keer, L. M., Worden R. E. (1990). A qualitative model to describe the microchipping wear mode in ceramic rollers. *Tribol. Trans* **33**: pp 411-417.
- Khan, Z.,Hadfield M. (2004). Design and Finite Element Analysis of a Novel Pressurised Chamber to Conduct Rolling Contact Experiments using Refrigerant Lubrication. In: Special House of Commons' Reception for Younger Researchers, London, House of Commons. L2-8.
- Khan, Z., Hadfield M.,Wang Y. (2003). Rolling Wear of Silicon Nitride Bearing Material in a Simulated Refrigerant Environment using a Novel Pressurised Chamber. In: *Tribology in Environmental Design*, Bournemouth, UK, **ISBN 1 86058 415 2** Professional Engineering Publishing Limited, Bury St Edmunds and London, UK. 337-346.
- Khan, Z., Hadfield M.,Wang Y. (2004). Design of a Novel Pressurised Chamber to Assess in-use Durability Performance of Rolling Contact Elements using Refrigerant Lubrication. In: *4th Intl. Conf. Advanced Engineering Design*, Scotland, **ISBN 80-86059-41-3** University of Glasgow.
- Khan, Z., Hadfield M.,Wang Y. (2005). Pressurised Chamber Design for Conducting Rolling Contact Experiments with Liquid Refrigerant Lubrication. *Materials and Design* **26(8)**: pp 680-689.

- Khan, Z., Hadfield, M., Tobe, S., Inaba, F., Wang, Y. (2005). An experimental study of refrigerant lubricated ceramic rolling elements wear with ring crack defects. In: *Tribology in Environmental Design 3*, Bournemouth, UK, Professional Engineering Publishing Limited, Bury St Edmunds. (submitted).
- Khan, Z., Hadfield, M., Tobe, S., Wang, Y. (2005). Ceramic rolling elements with ring crack defects - a residual stress approach. *Materials Science and Engineering A* **404**: pp 221-226.
- Khan, Z., Hadfield, M., Tobe, S., Wang, Y. (2005). Residual stress variations during rolling contact fatigue of refrigerant lubricated silicon nitride bearing elements. *Ceramics International*: pp (in press).
- Khan, Z., Hadfield, M., Wang, Y. (2005). Rolling wear of silicon nitride bearing materials with refrigerant lubrication. In: *Tribology Group's Mission*, London, UK, Institution of Mechanical Engineers. (submitted).
- Kikuchi, K., Yoshioka T., Kitahara T., Ozaki K., Nakayama K., Fujiwara T. (1984). Rolling Contact Fatigue Life of Ceramics for Rolling Bearing Materials. *J. JSLE, Int. Ed.*: pp 137-142.
- Kim, S., Kato K., Hokkirigawa K., Abe H. (Oct 1986). Wear Mechanisms of Ceramic Materials in Dry Rolling Friction. *ASME Transaction* **108**: pp 522-526.
- Kim, S. S., Kato, K., Hokkirigawa, K., and Abe, H (1986). Wear mechanism of ceramic materials in dry rolling friction. *Trans. ASME(108)*: pp 522-526.
- Kobayashi, H. (1992). Evaluation of Fatigue, Stress Corrosion Crack Properties of Ceramics. Tokyo, Heisei san nendo kagaku kenkyuhi: 51-75.
- Komatsuzaki, S., Homma Y. (1991). Antiseizure and antiwear properties of lubricating oils under refrigerant gas environments. *Source: Lubrication Engineering* **47(3)**: pp 193-198.
- Komatsuzaki, S., Tomobe T., Hon-Ma Y. (1987). Additive effects on lubricity and thermal stability of refrigerator oils. *Lubrication Engineering* **43(1)**: pp 31-36.
- Krivoshein, G. S. (1960). On Evaluating the Effect of Lubricants on the Fatigue Pitting of Steel. *Ind.Lab.*, **26**: pp 405-407.

- Mizuhara, K., Matsuzaki T. (1994). The friction and wear behaviour in Controlled Alternative Refrigerant Atmosphere. *Trib. Trans* **37**(1): pp 120-128.
- Mori, S., Sera H., H A., Komatsuzaki S., Homma Y. (1991). Activity of Aluminum and Aluminum Alloy Fresh Surfaces. In: *Pro. Of JAST Trib. Conf.*
- Morrison, F. R., Mc Cool, J. I., Yonushonis, T. M (1982). The Load-Life Relationship for M-50 Steel Bearing with Silicon Nitride Ceramic Balls. *ASLE Preprints* **82-LC-3C**(4): pp 1-7.
- Murry, S. F., Johnson R. L., Swikert M. A. (1956). Difluorodichloromethane as a Boundary Lubricant for Steel and Other Metals. *Mech. Eng* **78**: pp 233-236.
- Parker, R., Zaretsky E. V. (1975). Fatigue life of high-speed ball bearings with silicon nitride balls. *Trans. of the ASME, J. of Lub. Tech*: pp 350-357.
- Parker, R., Zaretsky E. V. (1975). Fatigue Life of High-Speed Ball Bearings with Silicon Nitride Balls. *J. Lubr. Technol.*: pp 350-357.
- Rosenfield, A. R. (1980). A fracture mechanics approach to wear. *Wear* **61**: pp 125-132.
- Scott, A., Blackwell, J., McCullagh P. J. (1971). Silicon nitride as a rolling bearing material - A preliminary assessment. *Wear*(17): pp 73-82.
- Scott, D. (1963). Study of the Effect of Lubricant on Pitting Failure of Balls. In: *Lubrication and Wear Convention, I Mech E.* 463-468.
- Scott, D., Blackwell J. (1973). Hot Pressed Silicon Nitride as a Rolling Bearing Material-A Preliminary Assessment. *WEAR* **24**: pp 61-67.
- Scott, D., Blackwell J., McCullagh P. J. (1971). Silicon Nitride as a Rolling Bearing Material-A Preliminary Assessment. *Wear* **17**: pp 73-82.
- Sturmer, G., Schutz A., Witting S. (1992). Lifetime Prediction for Ceramic Gas Turbine Components. *ASME. Jour. Eng. For Gas Turbine and Power* **115**: pp 70-75.
- Suh, N. P. (1977). An overview of the delamination theory of wear. *Wear* **44**: pp 1-16.

- Sutor (1984). Tribology of Silicon Nitride and Silicon Nitride-Steel Sliding Pairs. Ceramic Engineering and Science Proceedings(July-August).
- Walker, W.,Levy S., L (1962). Stability of Mixtures of Refrigerants and Refrigerating Oils. ASHRAE Trans **68**: pp 360-389.
- Wang, L., Snidle R. W.,Gu L. (2000). Rolling contact silicon nitride bearing technology: A review of recent research. Wear **246**(1-2): pp 159-173.
- Wang, Y.,Hadfield M. (2000a). The influence of ring crack location on the rolling contact fatigue failure of lubricated silicon nitride: experimental studies. Wear **243**: pp 167-174.
- Wang, Y.,Hadfield M. (2000b). The influence of ring crack location on the rolling contact fatigue failure of lubricated silicon nitride: fracture mechanics analysis. Wear **243**: pp 157-166.
- Wang, Y.,Hadfield M. (2001). Ring crack propagation in silicon nitride under rolling contact. Wear **250**: pp 282-292.
- Wang, Y.,Hadfield M. (2003). A mechanism for nucleating secondary fractures near a pre-existing flaw subjected to contact loading. Wear **254**: pp 597-605.
- Wang, Y.,Hadfield M. (2004). Failure modes of ceramic rolling elements with surface crack defects. Wear **256**(1-2): pp 208-219.
- Wedevan, L. F., et al (1988). Tribological Examination of Unlubricated and Graphite Lubricated Silicon Nitride under Traction Stress. Wear: pp.241-247

BIBLIOGRAPHY

- ACRIB (October, 2000). EU Ozone Depleting Substances Regulation.
- Akazawa, M.,Kato K. (1988). Wear properties of silicon nitride in rolling-sliding contact. *WEAR*(124): pp 123-132.
- Allen, D. L. (1994). Effect of composition and physical properties of silicon nitride on rolling wear and fatigue performance. *Trib. Trans*(37): pp 410-414.
- Barwell, F. T.,Scott D. (1956). Effect of Lubricant on Pitting Failure of Ball Bearings. *Eng*: pp 9 -12.
- Baumgartner, H. R. (1974). Evaluation of Roller Bearings Containing Hot-Pressed Silicon Nitride Elements. J. J. Burke, A. E. Gorum and R. N. Katz, Brook Hill Publishing.
- Baumgartner, H. R.,Cowley P. E. (1975). Silicon Nitride in Rolling Contact Bearings, U.S. Navy NASC Norton Company, Industrial Ceramic Division, Worcester, MA.
- Carter, T. L.,Zarretsky E. V. (1960). Rolling Contact Fatigue Life of a Crystallized Glass Ceramic, National Aeronautics and Space Administration.
- Ciantar, C. (2001). Sustainable Development of Mechanical Systems Using Replacement Environmentally Acceptable Refrigerants. Ph.D. thesis. UK, Bournemouth University.
- Cullity, B. D. (1978). Elements of x-ray diffraction. pp 447-476.
- Cullity, B. D. (1996). Elements of X-ray diffraction. 2nd Massachusetts, Addison-Wesley.
- Duffy, P. E. (1991). Exploratory Testing and Analysis of Full Ceramic Ball Bearings. SAE Paper(911800)
- Fisher, T. E.,Tomizawa H. (1985). Tribochemistry and Microfracture in the Friction and Wear of Silicon Nitride. *WEAR* **105**: pp.

- Johnson, G. L. (1964). *The Statistical Treatment of Fatigue Experiments*. Elsevier Publishing Company.
- Johnson, K. L. (1985). *Contact Mechanics*. 1st Cambridge, University Press.
- Kato, K., Adachi K. (2000). *Modern Tribology Handbook*. CRC press.
- Kato, K., Umehara N. (1980). A study on magnetic fluid grinding. *Trans. JSME* **54**: pp 1.
- Lucek, J. W., Cowley P. E. (1978). *Investigation of the Use of the Ceramic Material in Aircraft Engine Bearings*, US Dept. of Navy.
- Lucek, John W. (1990). Rolling wear of silicon nitride bearing materials. In: *International Gas Turbine and Aeroengine Congress and Exposition, CERBEC Ceramic Bearing Co, East Granby, USA, 0402-1215 Belg, GT165 7p Publisher: Publ by ASME, New York, NY, USA. 11-14.*
- Miyoshi, K., et al (1989). *Plasma-Deposited Amorphous Hydrogenated Carbon Films and their Tribological Properties*. NASA Technical Memorandum(102379).
- Nemeth, N. N., Gyekenyesi J. P. (1992). *Probabilistic Design of Ceramic Components with NASA/CARES Computer Program*. SAE, Warrendale PA.
- Randles, S., Heavers A. (1996). Optimization of ester technology for high performance industrial oils. In: *Presented at the 10th International Colloquium on Tribology, Esslingen, Germany.*
- Spauschus, H., O, Doderer G., C (1961). Reaction of Refrigerant 12 with Petroleum Oils. *ASHRAE J* **2**: pp 65-69.
- Touret, R., Wright E. P. (1977). *Rolling Contact Fatigue: Performance Testing of Lubricants*. Heyden & Son Limited.
- Thomsen, N. B., Karihaloo B. L. (1996). Subsurface and surface cracks under contact loading in transformation-toughened ceramics. *J. Mech. Phys. Solids* **44**